



Available online at www.sciencedirect.com



Materials Science and Engineering R 55 (2006) 57–149



Reports: A Review Journal

www.elsevier.com/locate/mser

Charged point defects in semiconductors

Edmund G. Seebauer ^{*}, Meredith C. Kratzer

*Department of Chemical and Biomolecular Engineering, University of Illinois at Urbana-Champaign,
600 S. Mathews Avenue, Urbana, IL 61801, United States*

Accepted 5 January 2006

Abstract

Native point defects control many aspects of semiconductor behavior. Such defects can be electrically charged, both in the bulk and on the surface. This charging can affect numerous defect properties such as structure, thermal diffusion rates, trapping and recombination rates for electrons and holes, and luminescence quenching rates. Charging also introduces new phenomena such as nonthermally photostimulated diffusion, thereby offering distinctive mechanisms for defect engineering. The present work incorporates the first comprehensive account of semiconductor defect charging, identifying correspondences and contrasts between surfaces and the bulk as well as among semiconductor classes (group IV, groups III–V, and metal oxides). For example, small lattice parameters, close-packed unit cells, and basis atoms with large atomic radii all inhibit the formation of ionized interstitials and antisites. The charged defects that exist in III–V and oxide semiconductors can be predicted with surprising accuracy from the chemical potential and oxygen partial pressure of the ambient. The symmetry-lowering relaxations, formation energies, and diffusion mechanisms of bulk and surface defect structures often depend strongly on charge state with similar qualitative behavior, although for a given material surface defects do not typically take on the same configurations or range of stable charge states as their counterparts in the bulk.

© 2007 Elsevier B.V. All rights reserved.

Keywords: Point defects; Semiconductor; Diffusion; Defect levels; Surface defects

Contents

1. Introduction	59
2. Fundamentals of defect ionization and transport	60
2.1. Thermodynamics of defect charging	60
2.1.1. Free energies, ionization levels, and charged defect concentrations	61
2.1.2. Ionization entropy	63
2.1.3. Effects of oxygen pressure on oxides	65
2.2. Thermal diffusion	66
2.3. Drift in electric fields	69
2.4. Direct surface-bulk coupling	69

* Corresponding author. Tel.: +1 217 333 4402; fax: +1 217 333 5052.
E-mail address: eseebaue@uiuc.edu (E.G. Seebauer).

3.	Experimental and theoretical characterization of charged defects	70
3.1.	Experimental characterization	70
3.1.1.	Direct detection of bulk defects	70
3.1.2.	Diffusion in the bulk	71
3.1.3.	Direct detection of surface defects	71
3.1.4.	Diffusion on the surface	72
3.2.	Computational prediction	72
3.2.1.	Density functional theory	72
3.2.2.	Other atomistic methods	74
3.2.3.	Systems-based methods	74
3.2.4.	Surfaces and interfaces	75
4.	Effects of crystal structure, atomic properties, and stoichiometry on charged defects	75
5.	Geometry and structure of charged defects	78
5.1.	Bulk defects	78
5.1.1.	Silicon	80
5.1.2.	Germanium	81
5.1.3.	Gallium arsenide	82
5.1.4.	Other III–V semiconductors	84
5.1.5.	Titanium dioxide	85
5.1.6.	Other oxide semiconductors	87
5.2.	Surface defects	88
5.2.1.	Silicon	88
5.2.2.	Germanium	90
5.2.3.	Gallium arsenide	90
5.2.4.	Other III–V semiconductors	92
5.2.5.	Titanium dioxide	93
5.2.6.	Other oxide semiconductors	93
6.	Energetics and ionization levels of charged defects	94
6.1.	Bulk defects	94
6.1.1.	Silicon	94
6.1.2.	Germanium	98
6.1.3.	Gallium arsenide	101
6.1.4.	Other III–V semiconductors	105
6.1.5.	Titanium dioxide	107
6.1.6.	Other oxide semiconductors	111
6.2.	Surface defects	114
6.2.1.	Silicon	114
6.2.2.	Germanium	115
6.2.3.	Gallium arsenide	116
6.2.4.	Other III–V semiconductors	118
6.2.5.	Titanium dioxide	119
6.2.6.	Other oxide semiconductors	121
7.	Diffusion of charged defects	122
7.1.	Bulk defects	122
7.1.1.	Silicon	122
7.1.2.	Photostimulated diffusion in silicon	124
7.1.3.	Germanium	125
7.1.4.	Gallium arsenide	125
7.1.5.	Other III–V semiconductors	127
7.1.6.	Titanium dioxide	128
7.1.7.	Other oxide semiconductors	129
7.2.	Surface defects	131
7.2.1.	Silicon	131
7.2.2.	Photostimulated diffusion on silicon	133
7.2.3.	Germanium	133
7.2.4.	Gallium arsenide	134

7.2.5. Other III–V semiconductors	735
7.2.6. Titanium dioxide	735
8. Summary	136
Acknowledgements	137
References	137

1. Introduction

The technologically useful properties of a semiconductor often depend upon the types and concentrations of the defects it contains. For example, defects such as vacancies and interstitial atoms mediate dopant diffusion in microelectronic devices [1–5]. Such devices would be nearly impossible to fabricate without the diffusion of these atoms. In other applications, defects also affect the performance of photo-active devices [6–8] and sensors [9], the effectiveness of oxide catalysts [10,11], and the efficiency of devices for converting sunlight to electrical power [12,13]. To improve material performance, various forms of “defect engineering” have been developed to control defect behavior within the solid [14], particularly for applications in microelectronics. Examples include surface oxidation [15], various protocols for ion implantation and annealing [16–20], and the incorporation of impurity atoms [21].

Crystalline surfaces support native defects in the same way that the bulk solid does [22], with many close analogies between the two cases. Table 1 shows examples of some of these correspondences, focused primarily on point defects. Understanding surface defects is becoming increasingly important in practical applications—for example, as electronic devices shrink closer to the atomic scale (with the attendant increase in surface-to-volume ratios), and as molecular-level control of catalytic reactions becomes increasingly feasible. Of particular importance is defect-mediated surface diffusion, which plays an important role in crystal growth, heterogeneous catalysis, sintering, corrosion, and microelectronics fabrication. Considerably less is known about the behavior of surface defects than bulk defects. (Even less is known about defects at solid–solid interfaces, but some analogies with the bulk and free surface still hold.) Recent research has also indicated that surfaces or interfaces can directly influence point defect behavior in the bulk [23,24], and that bulk properties can couple directly into the behavior of surface defects [25,26] (Table 1).

It has long been known that bulk defects in semiconductors can be electrically charged. Charging of surface defects has been identified and studied rather more recently. In either case, this charging can affect defect structure [27,28], thermal diffusion rates [29–31], trapping rates of electrons and holes [32,33], and luminescence quenching rates [34]. More interestingly, defect charging also introduces new phenomena such as nonthermally photostimulated diffusion [25,26,35]. Such phenomena offer completely new mechanisms for defect engineering, as well as new means to study the charging phenomenon itself.

Semiconductors contain not only native atomic defects, but also defects that arise from the incorporation of foreign atoms into the crystal lattice. This review will focus upon native point defects, however. Although numerous reviews articles and books have been published on the general subject of semiconductor defect structure and behavior for both the bulk [1,5,36–43] and the surface [44–46], a comprehensive treatment of semiconductor defect charging is lacking. Correspondences and contrasts in charging behavior on surfaces and in the bulk have not been clearly delineated. The same lacuna exists for the various semiconductor types (group IV, groups III–V, and oxide semiconductors). The present work fills those gaps, and in so doing, identifies trends in behavior that may not have been previously evident. For example, certain crystal properties such as small lattice parameters, close-packed cells, and basis atoms with large atomic radii inhibit the formation of ionized interstitials and antisites. The charged defects that exist in III–V and oxide

Table 1
Correspondence in defect structure and behavior for the bulk and surface

Bulk	Surface
Interstitial atom	Adatom
Vacancy	Vacancy
Interstitial cluster	Adatom island
Vacancy cluster	Vacancy island
Kick-in/kick-out	Exchange diffusion
Vacancy–interstitial formation	Vacancy–adatom formation

semiconductors can be predicted with surprising accuracy based on the chemical potential and oxygen partial pressure of the ambient. The symmetry-lowering relaxations, formation energies, and diffusion mechanisms of bulk and surface defect structures often depend strongly on charge state with similar qualitative behavior, although for a given material surface defects do not typically take on the same configurations or range of stable charge states as their counterparts in the bulk.

The notation for describing point defects varies widely through the literature. For example, most literature for oxide semiconductors uses “Kroger–Vink” notation to represent charged crystal defects [47]. The literature for silicon and III–V defects employs a substantially different notation. To foster a uniform treatment, this article will employ a single notation for all types of charged defects in all types of materials.

2. Fundamentals of defect ionization and transport

Native atomic defects include vacancies, empty lattice sites, interstitials, excess atoms present in the lattice, and antistructure defects. Antistructure (or antisite) defects, where native atoms are misplaced but remain on lattice sites, are relevant only for binary compounds such as III–V or oxide semiconductors. One such example is a gallium atom occupying an arsenic atom lattice site, denoted as Ga_{As} , rather than its proper location, Ga_{Ga} .

2.1. Thermodynamics of defect charging

The thermodynamics of defect charging have been discussed in numerous journal articles and books [5,36,40,48–50]. Note that the thermodynamic parameters, including band gaps, ionization energies, and energies of defect formation and/or migration, are not the eigenvalues of a Schrodinger equation describing the crystal [48]. The thermodynamic parameters are defined statistically in terms of reactions occurring among ensembles of all possible configurations of the system. Confusion over this distinction sometimes exists particularly with reference to ionization levels.

When thermally generated or artificial point defects are introduced into a perfect semiconductor crystal, they increase the Gibbs free energy G of the system. The equilibrium concentration $[X]$ of a point-defect species X can be expressed as

$$\frac{[X]}{[S]} = \theta_X \exp \left[\frac{-G_X^f}{kT} \right] = \theta_X \exp \left[\frac{S_X^f}{k} \right] \exp \left[\frac{-H_X^f}{kT} \right] \quad (1)$$

where $[S]$ is the concentration of available lattice sites in the crystal, θ_X the number of degrees of internal freedom of the defect on a lattice site, and G_X^f , H_X^f and S_X^f are respectively the free energy, enthalpy, and entropy of formation [5,51,52]. The parameters k and T respectively represent Boltzmann’s constant and temperature. A defect may have several degrees of freedom due to spin degeneracy or equivalent geometric configurations at the same site [40]. Typically only the spin degeneracy is of direct interest for defect charging. For simplicity, therefore, the discussion henceforth will focus upon the spin-degeneracy g rather than other degrees of internal freedom of the defect. For oxide semiconductors, which typically exhibit small deviations from stoichiometry, it should be possible to rewrite Eq. (1) to explicitly reflect the dependence of $[X]$ upon the ambient oxygen pressure P_{O_2} . In practice, it typically becomes necessary to define several additional variables including N_M , the number of sites in the metal sublattice, and N_O , the number of sites in the oxygen sublattice [36]. It then follows that the concentration of vacancies in the metal sublattice is given by

$$[V_M] = P_{\text{O}_2}^\alpha N_M \exp \left[\frac{\Delta S_1}{k} \right] \exp \left[- \frac{\Delta H_1}{kT} \right] \quad (2)$$

and that of vacancies in the oxygen sublattice by

$$[V_O] = P_{\text{O}_2}^{-\alpha} N_O \exp \left[\frac{\Delta S_2 - \Delta S_1}{k} \right] \exp \left[- \frac{\Delta H_2 - \Delta H_1}{kT} \right] \quad (3)$$

where the constant α derives from the ratio of oxygen to metal in the MO or MO_2 crystal [36]. ΔS_1 and ΔS_2 may contain contributions from the vibrational entropy of the crystal resulting from the addition of V_M , V_O , and extra

oxygen atoms, as well as the standard value of the entropy of the oxygen molecule in the gas phase $\Delta S_{O_2}^\circ$. The ΔH parameters contain the enthalpies associated with the same defect processes [36].

For neutral defects, the equilibrium concentration of point defects does not depend upon the position of the chemical potential (or more colloquially, “Fermi energy” E_F , even for $T > 0$ K) in the bulk. This is not the case for charged defects.

2.1.1. Free energies, ionization levels, and charged defect concentrations

Neutral native defects almost always have unsaturated bonding capabilities (e.g. dangling bonds). These capabilities facilitate the transfer of electronic charge between the host matrix and the defect, and often occur to the point that the defect becomes fully ionized. The degree and direction of electron transfer (toward or away from the defect, respectively, for acceptors and donors) naturally depend upon the electron richness of the host, as quantified by the host’s Fermi energy (i.e. chemical potential) in the vicinity of the defect. In semiconductors, the host’s electron richness can be adjusted readily by doping, imposed electric fields, photostimulation, and other factors. Thus, the ionization state of the defect can often be controlled. If the defect possesses significant capacity to store excess charge within its structure, the range of ionization states can be quite large. For example, a monovacancy in silicon nominally incorporates four unsaturated dangling bonds, and permits charge states ranging from (2−) to (2+) [5,53].

Some defects have eigenstates close to the edges of the valence band or conduction band; these states can be described by a hydrogenic model with a ground state and a series of bound excited states described by hydrogen atom wavefunctions, with full ionization occurring into the energy continuum of the valence or conduction band. This simple picture must, of course, be modified to account for the interactions of the electrons and holes with the lattice, which alters their effective mass. Also, the crystal reduces the binding potential, which is described with a dielectric constant [54]. For defects having eigenstates deeper within the band gap of the semiconductor, a more detailed quantum mechanical treatment is needed.

For many purposes, the concentration of defects that are charged must be known. This concentration can be calculated through the concept of an ionization level together with Fermi statistics. The ionization of an acceptor defect X can be represented by the reaction:



Sometimes it proves helpful to compare the concentration of charged defects to those in the neutral state. For this purpose, with the assumption that the ionization levels and E_F differ significantly, the concentration of X^{1-} can be described by

$$\frac{[X^{1-}]}{[X^0]} = g \exp \left[-\frac{E_{X^{1-}} - E_F}{kT} \right] \quad (5)$$

Here, $[X]$ is the total concentration of the defect X in all charge states ($[X] = [X^0] + [X^{1-}] + [X^{2-}] + \dots + [X^{1+}] + [X^{2+}] + \dots$), g is a degeneracy factor, and $E_{X^{1-}}$ represents the ionization level for the singly ionized acceptor state. The degeneracy factor g is the ratio of the degeneracy of X^{1-} to that of X^0 , or $g_{X^{1-}}/g_{X^0}$. Both $E_{X^{1-}}$ and the Fermi energy are referenced to the energy of the valence band maximum. When considering the multiply charged acceptor X^{2-} , Eq. (5) is recast as

$$\frac{[X^{2-}]}{[X^0]} = g \exp \left[-\frac{E_{X^{2-}} + E_{X^{1-}} - 2E_F}{kT} \right] \quad (6)$$

In the same way, the ionization of a donor defect can be represented by the reaction:



where the concentration of X^{+1} can be determined from Eq. (8):

$$\frac{[X^{+1}]}{[X^0]} = g \exp \left[-\frac{E_F - E_{X^{+1}}}{kT} \right] \quad (8)$$

and that of X^{2+} from Eq. (9):

$$\frac{[X^{2+}]}{[X^0]} = g \exp \left[-\frac{2E_F - E_{X^{2+}} - E_{X^{1+}}}{kT} \right] \quad (9)$$

For both acceptor and donor defects, the value of the degeneracy factor g can be deduced by applying the principle of equal occupation of states when $E_F = E_{X^{1-}}$. As an example, neutral vacancy defects have no spin degeneracy, as they have no bound carriers. However, if one additional singly charged state exists (either V^{1+} or V^{1-}), that singly charged state is two-fold spin degenerate with electron spins that can be either up or down. Thus, for the specific case of the positive vacancy, we must have $[V^{1+}] = 2[X^0]$ or alternatively $[V^{1+}] = 2/3 [X]$, so $g(V^{1+}) = 1/2$. The same argument gives $g(V^{1-}) = 1/2$. The relative concentrations of the various defect ionization states, taking into account the spin-degeneracy factors, are then calculated with the Fermi–Dirac expressions:

$$[X^{1-}] = \frac{[X]}{1 + g(X^{1-}) \exp((E_{X^{1-}} - E_F)/kT)} \quad (10)$$

and

$$[X^{1+}] = \frac{[X]}{1 + g(X^{1+}) \exp((E_F - E_{X^{1+}})/kT)} \quad (11)$$

Clearly the charged defect concentrations vary with T . Fig. 1 shows the concentration of charged vacancies in silicon at 300 and 1400 K as determined by Van Vechten and Thurmond [50].

In addition, the concentration of a charged defect depends upon its charge state and the position of the Fermi energy, which implies related dependencies in its formation energy. After all, there is work involved in moving an electron from the Fermi energy into the energy state associated with the defect. This is perhaps more evident when the energy of formation of X^{1-} is written as

$$G_{X^{1-}}^f = G_{X^0}^f + E_{X^{1-}} - E_F \quad (12)$$

where $G_{X^0}^f = H_{X^0}^f - TS_{X^0}^f$ [5]. When considering a surface defect as opposed to a bulk defect, all the same basic principles apply except that the position of the Fermi energy at the surface (which often differs from that in the bulk) is the key factor in determining the concentrations of various ionization states.

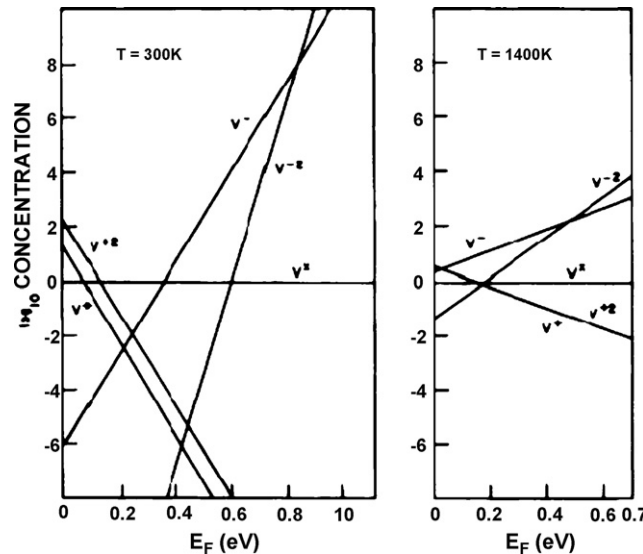


Fig. 1. Variation with E_F of the concentrations of various vacancy charge states in silicon relative to the neutral. The majority species change with temperature. For example, the neutral state exists at 300 K for E_F between $E_v + 0.14$ (ionization level for $(2+0)$) and $E_v + 0.35$ (ionization level for $(0/1-)$). However, at 1400 K only the neutral vacancy is never the majority charge state. Note that a smaller range of E_F is shown for 1400 K than for 300 K because of band gap narrowing with increasing temperature.

Although these equations describing the formation energy have their place, for practical purposes it is often more useful to examine the work (or Gibbs free energy) associated with ionizing the defect. For the single ionization of an acceptor, the free energy $\Delta E_I(X^-)$ needed to transfer an electron from X^0 to the conduction band at E_c is

$$\Delta E_I(X^{1-}) = E_c - E_{X^0} \quad (13)$$

As donor ionization levels are typically referenced to the valence band maximum rather than the conduction band minimum, the corresponding free energy of ionization for the singly ionized donor is given by

$$\Delta E_I(X^{1+}) = E_{X^{1+}} - E_v \quad (14)$$

These ionization free energies can be decomposed into corresponding enthalpies and entropies of ionization, ΔH_I and ΔS_I :

$$\Delta E_I(X^{1-}) = \Delta H_I(X^{1-}) - T\Delta S_I(X^{1-}) \quad (15)$$

$$\Delta E_I(X^{1+}) = \Delta H_I(X^{1+}) - T\Delta S_I(X^{1+}) \quad (16)$$

Note that ΔE_I , ΔH_I , and ΔS_I all depend on temperature. The enthalpy of ionization is strongly affected by the degree of localization of the remaining bound carrier of the ionized state. A greater value of ΔH_I corresponds to an ionization level deeper within the band gap and a remaining carrier that is more loosely bound to the defect center. The value of ΔH_I at non-zero temperatures can be obtained from an empirical expression due to Varshni [55] for the band gap energy ΔE_{cv} (equivalent to the free energy of electron–hole pair formation):

$$\Delta E_{cv}(T) = \frac{\Delta E_{cv}(0) - \alpha T^2}{T + \beta} \quad (17)$$

where α and β are empirical constants. Since ΔE_{cv} is the increase in free energy, ΔG , when one more electron–hole pair is excited across the fundamental gap, its temperature derivative is the negative standard entropy of that reaction [48]:

$$\frac{\partial E_{cv}}{\partial T} \equiv -\Delta S_{cv} \quad (18)$$

Then the definition $\Delta G = \Delta H - T\Delta S$ implies:

$$\Delta H_{cv}(T) = \frac{\Delta E_{cv}(T) - T \partial E_{cv}(T)}{\partial T} \quad (19)$$

Substitution of the derivative of Eq. (17) into the expression above yields the following empirical expression for enthalpy of electron–hole pair formation at non-zero temperatures:

$$\Delta H_{cv}(T) = \frac{\Delta E_{cv}(0) + \alpha \beta T^2}{(T + \beta)^2} \quad (20)$$

As an example, for Si the relevant constants are $\alpha = 0.000473$ eV/K, $\Delta E_{cv}(0) = 1.17$ eV and $\beta = 636$ K [56]. The enthalpy of ionization obtained from Eq. (20), when combined with ΔH_I at $T = 0$ as deduced from experiment, is then used to describe the variation in enthalpy as a function of charge state according to

$$\Delta H_I(T) = \Delta H_I(0) + \Delta H_{cv}(T) \quad (21)$$

The enthalpy of ionization at 0 K, $\Delta H_I(0)$, is charge state-dependent, thus the enthalpies of multiply charged defects phenomenologically track with each other as a function of temperature, yet have different maxima and minima, as shown in Fig. 2 [396].

2.1.2. Ionization entropy

Formation entropies for defects can contain several contributions, including configurational degeneracy, lattice mode softening due to bond cleavage, and ionization [49,50]. Our principal concern here is the ionization contribution, which helps govern charge-mediated effects. There exists significant theoretical and experimental evidence to suggest that the ionization entropy ΔS_I can be very large for certain kinds of native defects such as vacancies. The main contribution to ΔS_I originates from electron–phonon coupling near the vacancy, leading to lattice-mode softening

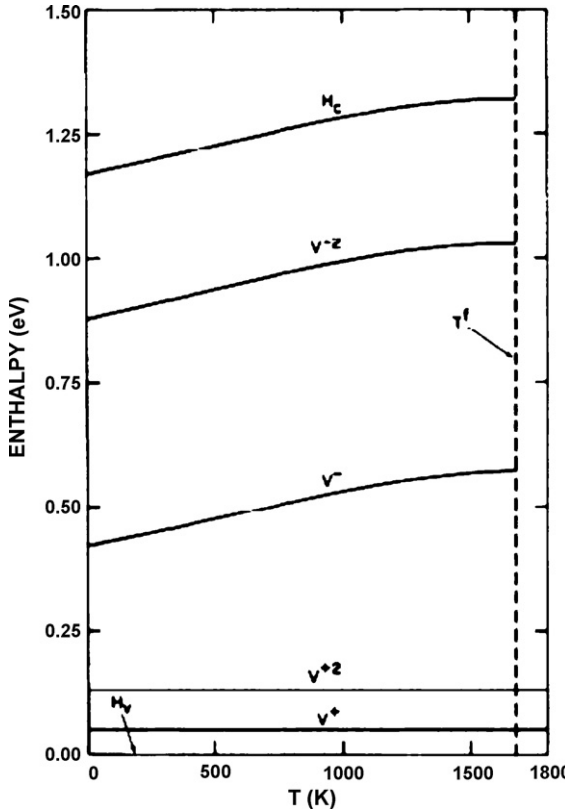


Fig. 2. Variation of the enthalpies of silicon vacancy ionization levels (and of the band gap) as a function of temperature.

[49,57]. The magnitude can be calculated by considering either the effect of thermal vibrations upon the electronic defect levels or the effect of the thermally excited electronic states upon the lattice vibration mode frequencies [48], although the latter method has proven more useful for simple estimates [49].

In this perspective, the band gap energy ΔE_{cv} of a bulk semiconductor crystal corresponds to the standard chemical potential for creating a delocalized hole at the valence band maximum and a delocalized electron at the conduction band minimum. Such creation might occur thermally or by photoexcitation. The magnitude of ΔE_{cv} can be obtained from the empirical Varshni relation given above in Eq. (17).

Standard thermodynamic relations require that the entropy change ΔS_{cv} for formation of the $e^- - h^+$ pair obeys [56]:

$$\Delta S_{cv}(T) = -\frac{\partial \Delta E_{cv}}{\partial T} = \frac{\alpha T(T + 2\beta)}{(T + \beta)^2} \quad (22)$$

Ionization of a defect represents another mechanism for creating two new carriers of opposite charge. One of the carriers roams the crystal in a delocalized way, while the other remains bound in the vicinity of the defect. The delocalized carrier contributes to ΔS_{cv} the way any delocalized carrier would. The effect of the bound carrier depends upon its degree of localization, however. If that carrier is loosely bound to the defect and therefore largely delocalized, the entropy for the ionization event clearly matches ΔS_{cv} .

If the carrier is tightly bound to the defect, however, and hovers close to it, the contribution to ΔS_{cv} is more difficult to estimate *a priori*. To make such an estimate, Van Vechten and Thurmond examined experimental data for the entropies of optical transitions in Si, Ge, GaAs and GaP between various points in the Brillouin zone. These data were derived from the temperature dependence of the various gaps as determined by optical reflectance. For Si the reported entropies suffered considerable uncertainties, but values remained within a factor of two of ΔS_{cv} . Since that compilation, more data have become available for Si that confirm the early results, including data for the E_2 and E'_0 direct gaps up to 1000 K [58] and for the E_2, E'_0, E_1 and E'_1 critical points up to 600 K [59]. The optical results indicate

that, at least for the four semiconductors examined, mode-softening effects from $e^- - h^+$ pair formation are insensitive to the final state charge distribution, so that, like the case of charges loosely bound to the defect:

$$\Delta S_I(T) \approx \Delta S_{cv}(T) \quad (23)$$

for single ionization events regardless of whether ionization results in a positive or negative vacancy [49]. Note that this argument should apply quite directly to the surface as well as the bulk, since the reflectance data on which the argument rests are sensitive primarily to surface optical susceptibilities. (Linear optical susceptibilities typically lie close to those of the bulk in any case.) Unlike the argument used for loosely bound carriers, however, Eq. (23) depends on data only for specific semiconductors—data that verify the conclusion only approximately.

These arguments suggest that $\Delta S_{cv}(T)$ can be used to estimate $\Delta S_I(T)$ regardless of the degree of localization of the bound charge. However, the reliability of the estimate does depend upon the degree of localization, which fortunately can be obtained with ease from DFT calculations.

A consequence of the correspondence between $\Delta S_{cv}(T)$ and $\Delta S_I(T)$ is that, as T increases and ΔE_{cv} decreases, free energies referenced to the valence band maximum for vacancy ionization levels remain at a constant energy below the conduction band for negatively charged vacancies and remain a constant energy above the valence band for positively charged vacancies [49]. This consequence makes the ionization levels quite easy to calculate from DFT results. An example for the divacancy on the Si(1 0 0) surface is shown in Fig. 3 [28,57,60].

2.1.3. Effects of oxygen pressure on oxides

For oxide semiconductor crystals, the relative concentration of charged defects is affected by the partial pressure of the oxygen ambient [47,61,62]. The law of mass action can be used to calculate the equilibrium constants of defect formation reactions and concentrations of charged defects in the crystal [36,61]. For example, for a metal M having a crystalline oxide MO, the following metal vacancy formation reaction may occur:



The concentration of singly ionized metal vacancies is a function of oxygen partial pressure according to

$$[V_M^{1-}] = \frac{K_1 P_{O_2}^{1/2}}{p[O_O]} \quad (25)$$

where K_1 is the equilibrium constant for Eq. (25) and p is the concentration of free hole carriers. The charge state dependence arises from the equilibrium constant; no separate contribution to the free energy, entropy, or enthalpy of ionization is broken out. The reader should make note that this approach is decidedly different from that of Van Vechten, who explicitly references concentrations of charged species to the concentration of neutral species.

Similarly, the exchange reaction that results in the formation of oxygen vacancies:

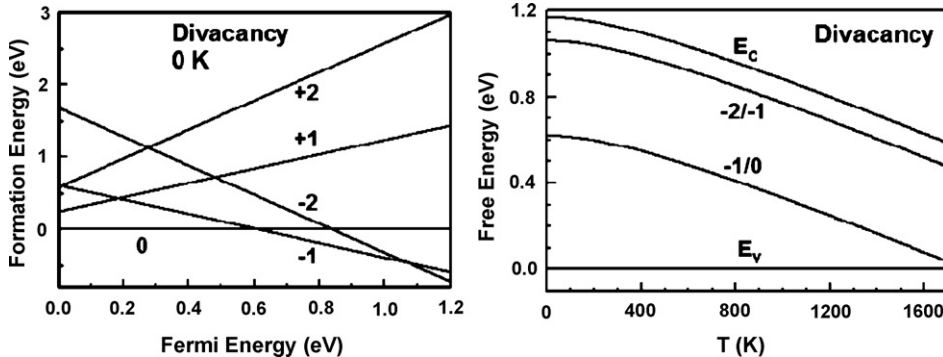


Fig. 3. (Left) Formation energies of various dimer vacancy charge states on Si(1 0 0)-(2 \times 1) as a function of Fermi energy. The formation energy is referenced to the neutral dimer vacancy and the Fermi energy is referenced to the valence band maximum. The charge state with the lowest formation energy at a given Fermi energy has the highest concentration. (Right) Variation of the dimer vacancy ionization levels with temperature.

has a corresponding concentration of singly positively charged oxygen vacancies given by [61]:

$$[\text{VO}^{1+}] = \frac{K_2 P_M}{n [\text{M}_M^0]} \quad (27)$$

The equilibrium between the semiconductor MO and its vapor is described by the following equation and equilibrium expression:



$$[\text{M}_M^0][\text{O}_O^0] = \frac{P_M P_{\text{O}_2}}{K_3} \quad (29)$$

The neutrality condition, which accounts for the fact that the overall crystal has no electrical charge, is

$$n + [\text{V}_M^{1-}] = p + [\text{V}_O^{1+}] \quad (30)$$

and one final equilibrium expression:

$$np = K_i \quad (31)$$

arises from the intrinsic equilibrium of electrons and holes in the crystal. The ionized defects in MO are now described by a series of five equations containing seven variables: n , p , $[\text{V}_M^{1-}]$, $[\text{V}_O^{1+}]$, P_M , P_{O_2} , and T , where T is the absolute temperature of the system. Normally P_{O_2} is taken as an independent variable; P_M is then a dependent variable. The whole range of oxygen partial pressures is subdivided into regions in which the two types of defects occurring at the neutrality condition predominate. To make this subdivision, it is necessary to know (either exactly or approximately) the values of all of the equilibrium constants at a given temperature. This complicated system of equations is often solved by applying the graphical method proposed by Brouwer [63]. It is thus common to find the concentration of charged defects in TiO_2 , ZnO , UO_2 , and CoO plotted as a function of oxygen partial pressure, where either the valence band maximum or conduction band minimum is used as the reference for the Fermi energy (Fig. 4).

2.2. Thermal diffusion

Bulk diffusion is typically mediated by point defects such as vacancies and interstitials, which may exchange with the lattice and defect clusters (which sometimes play a role as reservoirs of defects) [40,64–68]. The situation is similar for surface diffusion, although the relevant defects are typically surface vacancies and adatoms, which can exchange with surface lattice sites and islands.

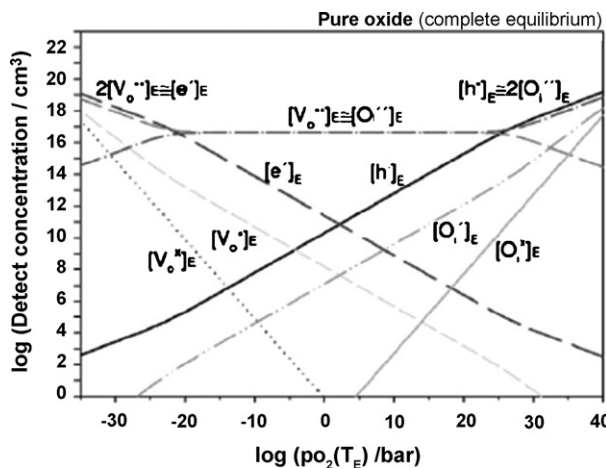


Fig. 4. Brouwer diagram of a pure oxide in complete equilibrium, where the concentrations of charged and neutral oxygen vacancies and interstitials as a function of oxygen partial pressure are shown.

For both the bulk and the surface, an atomistic description of the diffusion rate exists for native point defects, based on the work of Einstein and Smoluchowski. That description quantifies the motion in terms of a diffusion coefficient D . In a single dimension (say, x), component D_x of the diffusion coefficient in that direction is defined in terms of the mean square x -displacement $\overline{\Delta x^2}$ of the diffusing atoms and the time interval t during which diffusion takes place, according to

$$D_x = \frac{\overline{\Delta x^2}}{2t} \quad (32)$$

In the case of diffusion in n dimensions (2 for surface, 3 for bulk) with mean square displacement $\overline{\Delta r^2}$, this equation generalizes to

$$D = \frac{\overline{\Delta r^2}}{2nt} \quad (33)$$

Treatments of diffusion in this context often examine the random hopping motion of atoms between well-defined, energetically favorable sites [40]. Such hops lead to motion of individual atoms, but when time-averaged, lead to no net displacement of the ensemble. If Γ represents the hopping frequency between sites and L is the hop length between them, then the diffusion coefficient can be recast as

$$D = \frac{\Gamma L^2}{2n} \quad (34)$$

Since thermal diffusion of defects on or within semiconductors typically involves some form of bond stretching or breakage, the hopping frequency typically incorporates a temperature dependence in Arrhenius form. Zener, Vineyard, Rice, and Flynn have all presented theories for the jump frequency of a diffusing atom in the bulk, where Γ can be expressed as (for temperatures above the Debye temperature) [69–72]:

$$\Gamma = \Gamma_0 \exp\left(\frac{\Delta S_m}{k}\right) \exp\left(-\frac{\Delta H_m}{kT}\right) \quad (35)$$

where Γ_0 stands for a weighted mean frequency, often called an “attempt frequency,” and ΔS_m and ΔH_m respectively represent the entropy and enthalpy of migration, T is the absolute temperature, and k is Boltzmann’s constant. Similar descriptions exist for surface diffusion [73]. Alternatively, D is sometimes written in simpler Arrhenius form:

$$D(T) = D_0 \exp\left(\frac{-E_a}{kT}\right) \quad (36)$$

where E_a is the activation energy for diffusion and D_0 is the pre-exponential factor. Comparing Eqs. (35) and (36) indicates that

$$D_0 = \frac{\Gamma_0 \exp(\Delta S_m/k)L^2}{2n} \quad (37)$$

For both bulk and surface diffusion, Γ_0 usually lies near a vibrational frequency (about the Debye frequency), while L is typically an atomic bonding distance near 0.3 nm. Thus, in the absence of significant entropy effects during diffusion, the pre-exponential factor lies near $10^{-3} \text{ cm}^2/\text{s}$. Significant deviations from this value are often observed, however, particularly for surface diffusion [74]. Clearly $E_a = \Delta H_m$ in this treatment.

The atomistic perspective constitutes the basis of most theoretical methods for determining diffusion coefficients, as well as experimental methods that directly image atomic motion. However, a continuum approach often proves more useful for quantifying diffusion in most other kinds of experimental measurements taken at length scales longer than a few atoms [66]. The rate of mass transport on these length scales depends upon the total number of mobile defects, and also upon the rate at which these defects move from site to site.

In principle, several types of defects can contribute to the overall motion. Such behavior has been reported for bulk silicon, where some measurements have been interpreted in terms of separate diffusional pathways involving vacancies and interstitial atoms [75–77]. However, more typically a single defect type dominates the transport. For example, bulk diffusion can be mediated by the directional migration of vacancies or interstitials, the displacement of lattice atoms into interstitial sites, or the interchange of diffusing atoms between substitutional and interstitial sites in

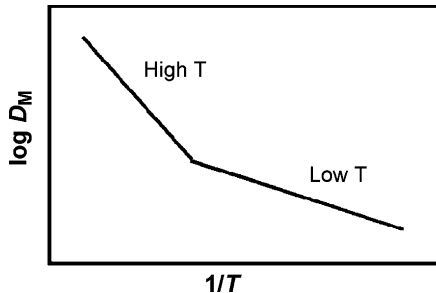


Fig. 5. Sketch of an Arrhenius plot for mesoscale surface mass transport showing two temperature regimes.

the crystal lattice [78]. The latter mechanism is often referred to as “kick-out” diffusion. Interstitials can also bind to intrinsic or extrinsic defects and migrate via a “pair diffusion” mechanism, where the atoms diffuse as a bound complex. Sometimes, a defect can diffuse through the crystal lattice by more than one pathway. Self-diffusion of the silicon interstitial is a primary example, where numerous possible pathways have been identified [30,79–81]. For the case of oxide semiconductors, where significant deviations from stoichiometry often occur, the pertinent diffusion mechanism may depend on the partial pressure of the ambient [82–90].

Similar principles apply to surface diffusion. Migration on these substrates has not been studied to the extent of that in the bulk. In analogy to bulk diffusion, however, different migration mechanisms dominate on the surface as a function of temperature, Fermi energy, and stoichiometry. A large body of aggregated experimental data for nickel, tungsten, silicon, germanium, aluminum oxide, and other materials indicates that two distinct temperature regimes of Arrhenius behavior exist for surface self-diffusion [74,91–98], as sketched schematically in Fig. 5. The trends appear to arise from adatom-dominated transport at low temperatures and vacancy-dominated transport at high temperatures [24].

When an inhomogeneous distribution of defects exists in the bulk or on the surface, the species migrates to reestablish equilibrium. In a continuum description, a diffusion coefficient D can be defined assuming that the chemical potential of the diffusing species scales linearly with its concentration C . (Note that other factors sometimes influence the chemical potential gradient, such as strong curvature in surface scratch decay experiments.) In the absence of electric fields, the flux J of the diffusing species obeys Fick's 1st law:

$$J = -D\nabla C \quad (38)$$

The dependence of C on time and space is described by Fick's 2nd law:

$$\frac{\partial C}{\partial t} = \nabla(D\nabla C) \quad (39)$$

Note that “species” must be defined carefully. For example, for purposes of Fick's laws, an interstitial dopant atom constitutes a different species than a substitutional one. Failure to make this distinction sometimes leads to erroneous discussion of “non-Fickian diffusion” when kick-in/kick-out reactions interconvert the interstitial and substitutional species.

Regardless of the specific mechanism, the charge state of the primary diffusing defect can affect its rate of hopping. For example, changing the charge state of a bulk interstitial atom affects not only its effective size (and therefore its ability to squeeze between lattice atoms) but also its ability to chemically bond to the surrounding atoms. In silicon, the energy barrier for the migration of V^{2+} differs from that of V^{2-} [99–104]. Such effects can, in principle, show up in the pre-exponential factor as well as the activation energy.

Thus, there are two ways for charge state to affect the rate of motion of a defect over length scales greater than atomic: changes in concentration and changes in hopping rate. When multiple charge states for a defect exist simultaneously, their effects are typically additive. For example, an effective diffusivity of self-interstitials can be expressed as

$$D_i^{\text{eff}} = D_{i^0} \left(\frac{C_{i^0}}{C_{i,\text{Total}}} \right) + D_{i^{1+}} \left(\frac{C_{i^{1+}}}{C_{i,\text{Total}}} \right) + D_{i^{1-}} \left(\frac{C_{i^{1-}}}{C_{i,\text{Total}}} \right) + \dots \quad (40)$$

The relative importance of each of these terms depends upon the position of the Fermi energy.

2.3. Drift in electric fields

Since pn junctions and heterojunctions are the foundation of most major semiconductor devices, an internal electric field often acts on mobile charged defects [105] during processing and subsequent device use. These fields, as well as their interactions with electrically active defects introduced during the fabrication process, can dramatically degrade device performance [106]. The reduction in size scale of these devices has caused the magnitudes of these electric fields to progressively rise.

When an electric field E of 10^4 to 10^6 V/cm is applied along with thermal diffusion from a constant source, field-aided diffusion takes place [78] according to

$$J = -D \frac{\partial C}{\partial x} + z\mu CE(x) \quad (41)$$

The mobility μ can be approximated roughly as qD/kT . The transport rate of charged defects can be either retarded or enhanced depending on the direction of the field. For a complete solution of the equations of motion for the defects, this transport equation must be solved together with Poisson's equation for the electrostatic potential Ψ :

$$\nabla^2 \Psi = \frac{q}{\epsilon} \left(n - p + \sum_i z_i C_i \right) \quad (42)$$

where n and p are the number of electrons and holes in the conduction and valence bands, respectively, and the variable z_i denotes the charge associated with the defect i with concentration C_i . For example, z_i would take on a nominal charge of (1+) for singly ionized acceptors and (1-) for singly ionized donors.

Field-assisted diffusion also occurs on semiconductor surfaces. Such behavior has been observed most notably in the imaging of charged defects with scanning tunneling microscopy. Tip-induced electric fields affect the electronic structure of a semiconductor surface containing native defects [107].

2.4. Direct surface-bulk coupling

Researchers have expended substantial effort comparing the physics of bulk solids with those of free surfaces and solid interfaces. Curiously, much less attention has focused upon the direct coupling between these phenomena. Only a handful of papers have considered topics such as bulk quenching of surface exciton emission [108], bulk-influenced surface state behavior at steps on metals [109], and bulk doping effects on surface band bending in semiconductors [110]. While the latter authors considered the effects of the semiconductor bulk on surface electronic properties, other work has shown that surface and interface electronic properties affect bulk semiconductor behavior. Two mechanisms can lead to direct surface-bulk coupling: near-surface band bending and defect exchange with dangling bonds.

Band bending near a free surface or solid-solid interface occurs when dangling bonds in those regions exchange charge with the semiconductor bulk. This charge exchange sets up a space charge region (and associated electric field) within the semiconductor. When point defects within the semiconductor are charged, this electric field provides an electrostatic coupling mechanism between the surface or interface and the bulk defects [23]. For a semiconductor such as silicon, for which surfaces and interfaces typically support Fermi level pinning near the middle of the band gap, the direction of the electric field typically repels charged defects within the bulk. At high semiconductor doping levels, the electric field within the space charge region is so strong that field-induced drift dominates diffusion of the defects. Thus, the ability of the surface or interface to absorb defects from deep within the bulk is greatly diminished. However, the variation in Fermi level near the surface or interface can also change the average charge state of charged defects in that vicinity, leading to complex effects such as the pileup of implanted dopants [4]. The degree of band bending can, in principle, be controlled through adsorption at a free surface [173] and ion bombardment at a solid-solid interface [23,173].

Defect exchange with dangling bonds at a surface also provides a method to withdraw defects from the underlying semiconductor bulk [111]. An atomically clean surface can annihilate interstitial atoms by simple addition of the interstitials to dangling bonds. But if the surface is decorated with a strongly bound adsorbed species, defect annihilation requires the insertion of interstitials into existing bonds. This process should have a higher activation barrier and a correspondingly reduced probability of occurrence [112]. Such effects have been demonstrated recently

in silicon implanted with silicon isotopes [24] and arsenic [112]. The latter case points to the possibility of creating very shallow pn junctions with exceptionally high levels of electrically active dopant.

This exchange mechanism can also inject defects into the semiconductor whose defect concentration is below that indicated by thermodynamics. Seebauer et al. recently showed that point defect concentrations as deep as 0.5 μm within a semiconductor can be controlled over several orders of magnitude through gas adsorption [24].

3. Experimental and theoretical characterization of charged defects

3.1. Experimental characterization

3.1.1. Direct detection of bulk defects

Defect properties, including thermodynamic ionization levels, can be derived from electron paramagnetic resonance, positron annihilation spectroscopy, and deep level transient spectroscopy experiments [113]. Each of these techniques provides distinct information, and not all of them are well suited to every semiconductor. Experiments are often hampered because most point and extended defects exist at low concentrations and are therefore difficult to observe.

Electron paramagnetic resonance (EPR) spectra provide detailed structural information about a semiconductor defect, including its symmetry, atomic, and lattice configuration [114–118]. The technique, based upon the absorption of electromagnetic waves in the microwave frequency domain, involves the creation of magnetic dipoles in crystals subjected to magnetic fields [116]. The point symmetry of a defect can be deduced from the angular dependence of its spectrum, while its atomic and lattice structure are inferred from hyperfine interactions [115]. Long spin-lattice relaxation times and low defect concentrations place stringent conditions on the experimental techniques required to observe defects in silicon with EPR. For example, the defects in silicon are observable only at low sample temperatures (4–40 K) and magnetic field modulation frequencies of less than 1 kHz [119]. Up until the mid-1980s, the use of EPR for the characterization of groups III–V semiconductors was also not as widespread; the high nuclear spins of the constituent atoms in a III–V lattice cause experimental difficulties [118].

Several reviews have been written about the application of positron annihilation lifetime spectroscopy (PAS) to the identification of defects in solids [120–125]. Positrons injected into a semiconductor become preferentially trapped in features such as vacancies, vacancy clusters, and negative charge centers, where they subsequently annihilate from the trapped state in the defect. Thus, the lifetime of positrons trapped in defects is long in comparison to those that annihilate at defect-free regions [126]. The lifetime of positrons trapped at a defect varies with the defect charge state [127,128]. Additionally, annihilation characteristics can be used to shed light upon the nature, structure, and abundance of defects in the bulk [120,126,129,130].

Deep level transient spectroscopy (DLTS), introduced by Lang [131], is widely used to study electrically active deep level defects in semiconductors. Under ideal circumstances, it can be used to detect defect concentrations as low as 10^{-6} times the carrier concentration of the semiconductor [132–135]. It can also be used for the identification of near-surface defects, where the technique is instead influenced by the position and shape of the Fermi energy at the Schottky diode interface [132]. The experimentally obtained DLTS signature can be compared to libraries of known electronic signatures in order to positively identify a specific defect. DLTS is a space charge technique requiring the formation of p⁺n (n⁺p) or Schottky barrier junctions. As the voltage applied over the junction is pulsed, capacitance transients are measured [136]. These transients occur because carriers trapped at deep levels in the band gap are thermally emitted when the junction bias returns to the steady state value. As the transients display an exponential time dependence, the activation energies for electronic transitions, capture cross sections, and concentrations of defects within the band gap can be resolved. Small uncertainties in the determination of the position of a DLTS peak can cause significant errors in the evaluation of the parameters of electronic states deep within the band gap; it is difficult to distinguish defects that are very close in energy. Several modifications have been developed to improve the accuracy of the analysis and its sensitivity to noise, including fitting and correlation methods [137–141]. Also, “positron-DLTS,” high resolution Laplace DLTS (LDLTS), and synchrotron radiation DLTS (SR-DLTS) can be used in place of the conventional technique to overcome sensitivity issues and glean information about closely spaced electronic levels in the band gap and the origin of deep-level defects [142–144].

3.1.2. Diffusion in the bulk

As the direct detection of semiconductor defects is often not feasible, diffusion measurements can serve as a valuable tool for inferring information about the type and concentration of bulk point defects. Techniques for diffusion measurement are typically easier to use than those for direct defect detection. For example, self-diffusion within a semiconductor can be measured directly with the use of an isotopic tracer together with secondary ion mass spectroscopy [24,75,145]. The diffusion coefficient is obtained by fitting the distribution of tracer atoms resulting from a heat treatment to theoretical distribution profiles [66]. These experiments can be performed on both intrinsic and doped material. When a tracer method is used, an allowance is made for a correlation factor, f , where the self-diffusion D_{SD} coefficient is related to the tracer diffusion coefficient D_T according to

$$D_T = f D_{SD} \quad (43)$$

Correlation factors are related to both defect type and crystal lattice structure. For example, f is equal to 0.5 and 0.78 for the vacancy mechanism in the diamond and face-centered cubic lattice, respectively [36,146,147]. The total tracer diffusion coefficient can be broken down into contributions of vacancies and self-interstitials [40]:

$$D_T = f^I D^I + f^V D^V \quad (44)$$

The respective contributions of interstitial and vacancy diffusion can be identified by an assortment of experimental methods. Early investigations were based on oxidation-enhanced diffusion, in which surface oxidation injects excess interstitials into the bulk. The oversaturation of self-interstitials can be estimated from the growth of stacking faults [40]. Gosele and Tan developed a method that correlates the retarded migration of extrinsic dopants to the fraction of self-interstitials contributing to diffusion [148]. Also, it is possible to compare the diffusivities of multiple dopants under non-equilibrium conditions in the bulk of the semiconductor. The best example of this technique, including how to extract numerical diffusivity values from experimental measurements, has been described by Fahey et al. [149].

Self-diffusion in silicon has been monitored using both the stable isotopes ^{29}Si and ^{30}Si and the unstable isotope ^{31}Si [40]. Compound semiconductors can be probed with isotopes of either one of their constituent elements. For example, the diffusion of Ga and As tracers in GaAs has been studied, as well as that of dopants such as aluminum, sulfur, and antimony, typically as constituents of a superlattice [150,151]. Similarly, measurements of the diffusion kinetics of both metal and oxide can be obtained for the metal oxide semiconductors such as TiO_2 , ZnO , UO_2 , and CoO . An alternate method for the determination of point-defect migration energies involves high-energy electron, photon, or ion irradiation. The irradiation creates point defects at temperatures low enough to prevent their migration in the bulk. By monitoring the annealing behavior of these excess defects at high temperatures, one can deduce their migration energies [5]. Point defects created in the bulk by the ion implantation of dopant atoms can also be monitored to obtain information about the energetics of diffusion. During annealing, transient enhanced diffusion occurs in the bulk. If this phenomenon is caused by the point defects created by implantation, the migration energy of the defect responsible for diffusion equals the activation energy of diffusion at the beginning of the transient time period [5].

3.1.3. Direct detection of surface defects

Experimental methods exist for probing the nature of both ideal and defected semiconductor free surfaces. The surface geometries and reconstructions of defect-free semiconductor surfaces have been investigated with low-energy-electron-diffraction (LEED) [152], reflection high-energy electron diffraction (RHEED) [153–155], electron energy loss spectroscopy (EELS) [156,157], inelastic electron tunneling spectroscopy (IETS) [158–163], scanning tunneling microscopy (STM), and transmission electron microscopy (TEM). Defects can be explored by both averaging and targeted imaging methods. Averaging methods examine the whole surface, while targeted imaging methods examine individual surface defects, and include techniques such as STM. Surface diffusion measurements have been used in a fashion akin to bulk diffusion measurements to shed light upon surface charging effects.

Optical spectroscopies based on the reflectance of ultraviolet and visible light, such as photoemission spectroscopy, surface differential reflectance spectroscopy (SDRS), and reflectance anisotropy spectroscopy (RAS, also called reflectance difference spectroscopy (RDS) by some authors), and photoreflectance spectroscopy (PR) provide information on the structure and electronic nature of large-area surfaces, including changes induced by temperature or adsorption [164,165]. Conventional photoemission spectroscopy, based on the energy analysis of photoelectrons emitted by a surface bombarded with ultraviolet or X-ray photons, sheds light upon the localized electronic states that

are responsible for Fermi energy pinning at certain semiconductor device interfaces and chemisorption bonds [166]. Photoemission spectroscopy can also be coupled with a synchrotron radiation source to explore electronic band structure, surface sensitivity, surface core-level shifts, and the nature of electronic surface states [166]. SDRS can be used only with samples that display a crystalline or morphological anisotropy on a dimension range equivalent to the size of the optical beam. As such, its use is limited to surfaces on which adsorption induces a change in surface optical anisotropy [167]. Photoreflectance is one of a class of modulation spectroscopies in which a semiconductor is periodically perturbed and the resulting change in dielectric constant is detected by reflectance [168]. The presence of a non-zero PR spectrum demonstrates unequivocally the existence of surface band bending, and experiments as a function of temperature and pump intensity can yield useful information about the electronic band structure of the surface. For example, this laboratory has used photoreflectance to probe the band bending, or defect-induced changes in the position of the surface Fermi energy, at Si(1 0 0)–SiO₂, Si(1 1 1)–SiO₂, and Si(1 0 0)–Si₃N₄ interfaces [23,169,170].

The atomic resolution afforded by scanning tunneling microscopy enables the characterization of defects, including their atomic configuration and real-time migration, on semiconductor surfaces [171]. Researchers have also recently demonstrated the applicability of Kelvin probe force microscopy (KPFM) to obtaining high-resolution defect images and local surface charge densities [172,173]. As point defects induce localized perturbations that give rise to shallow or deep ionization levels in the band gap, voltage-dependent depressions surrounding STM and KPFM-imaged surface defects serve as charge state signatures [174,175]. Attention has to be paid to the interaction between the substrate and the tip-sample system, however, as the charge state of the defect can be influenced by the presence of the tip [175]. Also, electrons can tunnel directly between the defect gap states and the tip states, causing a permanent current between the electrodes and affecting the spectroscopy of the charged defect [175]. Kubby and Boland have published an extensive review article on the principles, experimental methods, and characterization of semiconductor surfaces with STM [176]. A more pertinent discussion on the theory and issues behind imaging charged defects can be found in an article by de la Broise et al. [175]. STM images of neutral and charged surface defects on silicon, germanium, gallium arsenide, and other III–V semiconductors will appear throughout this review [177–181].

3.1.4. Diffusion on the surface

Numerous methods exist to measure surface diffusion [74], although only a few have been employed to examine surface charging on semiconductors. Indeed, most methods for measuring diffusion on Si, Ge, and GaAs surface carry serious drawbacks [29]. Standard electron or ion probes often lack sufficient spatial resolution or induce structural damage. While several authors have explored the diffusion of surface vacancies with STM, the migration is sometimes artificially triggered by the STM tip [182]. In addition, high-resolution, non-damaging probes such as STM cannot follow coverage dependence in the diffusivity. Second harmonic microscopy (SHM) has been used to measure concentration-dependent diffusivities on semiconductor surfaces [183,184]. SHM uses spatially resolved surface second harmonic generation (SHG) to monitor, without damage, adsorbate coverages at a resolution approaching the optical diffraction limit ($\sim 1 \mu\text{m}$) [29].

3.2. Computational prediction

3.2.1. Density functional theory

Ab initio density functional theory is one of the most frequently used atomic scale tools for investigating the properties of defects in semiconductors. Within this framework, the key quantity to calculate is the defect formation energy:

$$E_d^C = E_T^C(\text{defect}^q) - E_T^C(\text{no defect}) + \sum \mu_i n_i - q(\varepsilon_v + \varepsilon_F) \quad (45)$$

where $E_T^C(\text{defect}^q)$ and $E_T^C(\text{no defect})$ denote the total energy of the supercell C with and without the defect of charge q , respectively. The defect is typically formed in the computational domain by the addition or removal of n_i atoms of chemical potential μ_i . The quantity ε_F represents the Fermi energy referenced to ε_v , the valence band edge. A supercell geometry is generally used, whereby the defect is surrounded by a finite number of semiconductor atoms, with a periodic repetition of the whole structure. The advantage of this method is that it typically describes the band structure of the host crystal more accurately than cluster calculations, which often suffer from spurious quantum confinement effects that alter the band structure [113].

Approximations are invoked to deal with the small number of atoms considered in the computation, many of which lead to unwanted effects of their own. The local density (LDA), local spin density (LSDA), and generalized gradient approximation (GGA) are commonly used approximations for exchange and correlation [185,186]. Two major errors arise due to the use of these approximations: a significant ($\sim 50\%$) underestimation of the semiconductor band gap and imposition of system boundary conditions [187]. By implication, deep electronic levels associated with point defects incur similar errors [188,189]. As DFT calculations typically consider only 100–1000 atoms, boundary conditions acquire relatively high importance. One of the most common approaches is to use periodic boundary conditions together with a plane wave basis set [190]. Alternatively, calculations can be performed in “real space,” where no supercell geometry is introduced to describe the localized system [191]. When periodic boundary conditions are imposed, they lead to artificial long-range defect interactions that can only be eliminated in the limit of an infinitely large supercell; these interactions have a large effect on the calculated defect formation energies [192]. For charged defects, the supercell approximation leads to a divergence of the Coulomb energy [193]. This can be expressed as

$$E_{\text{def}}^q(L) = E_{\text{d}}^q(L) - E_{\text{b}}(L) \quad (46)$$

where $E_{\text{def}}^q(L)$ is the difference in the supercell energies as a function of L , which arises due to the size-dependent defect–defect Coulomb interaction energy [193]. Errors in E_{def}^q directly affect the defect formation energies and depend on the defect charge state according to q^2 [193]. Ionization level errors scale directly with the charge, q [193]. It is known that studies performed with small supercells typically overestimate ionization level positions with respect to the valence band maximum [194]. Fig. 6, found in Puska et al. [194], illustrates how the ionization levels of the silicon vacancy vary with 64-, 128-, and 216-atom supercells (experimental values from Watkins are included for purposes of comparison [195]).

Also, most quantum calculations are valid only at 0 K, but mechanisms can change at higher temperatures. For example, diffusion in Si at processing temperatures appears to be governed by collective atomic motions that do not operate at lower temperatures [188]. Moreover, DFT calculations typically ignore entropic effects, some of which can change pre-exponential factors by many orders of magnitude [188].

Correction schemes to improve these errors have been proposed by numerous authors, many of which have been reviewed and assessed in a recent article by Castleton et al. [187]. The Coulomb divergence of the charged defects is traditionally circumvented with the use of a uniform, neutralizing “jellium” background charge [193]. The Perdew–Zunger self-interaction correction to account for the LD and LSD approximations yields improved values of total energy, binding energy, electron density, and orbital eigenvalues [28,196]. The Makov–Payne correction scheme, published in 1995, works well for atomic or molecular systems calculated in otherwise empty supercells, although it often leads to overly high corrections for defects in semiconductors [113,197–203]. A multipole expansion can be employed to reduce the effect of the interactions between the actual defect and its images imposed by the periodic boundary conditions [204]. Unfortunately, for charged and neutral defects, electrostatic errors arising from multipole interactions affect the accuracy of the formation energy [198,205]. Schultz developed the local moment countercharge (LMCC) method, based on the linearity of the Poisson equation, to eliminate the unphysical interactions of charges between supercells, and calculate the properties of charged defects in extended systems [200,201]. He has also just published an alternate supercell modification method that identifies a common electron reservoir for net charge for all defects, deals with defect banding, and incorporates bulk polarization [53]. Even though these correction schemes

Size	(2+/+)	(2+/0)	(+/0)	(0/-)	(-/2-)	(0/2-)
64 & Γ	(0.50)	0.43	(0.35)	(0.70)	(0.59)	0.65
64 & $\Gamma + L$	(0.40)	0.39	(0.38)	0.62	0.66	(0.64)
64 & 2^3	–	–	–	0.26	0.33	(0.30)
64 & 3^3	–	–	0.05	0.41	0.53	(0.47)
128 & Γ	(0.32)	0.28	(0.24)	0.39	0.52	(0.64)
216 & Γ	(0.19)	0.15	(0.11)	(0.57)	(0.40)	0.49
EXPT.	(0.13)	0.09	(0.05)		–	

Fig. 6. Ionization levels of the Si vacancy from Ref. [194], where the experimental results are from Ref. [195]. Notice how the computational defect ionization levels change as a function of supercell size.

pervade the computational literature, it has been suggested that they still introduce large errors in the calculated total energies for charged defects in semiconductors [113,193].

3.2.2. Other atomistic methods

The shortcomings of the DFT approach have been addressed by an assortment of other computational techniques, although most are only valid for the investigation of neutral defects. Classical molecular dynamics and total-energy pseudopotential calculations of neutral defects are also often limited to systems of less than 10^6 atoms and nanoscale-order time scales [113,206–212]. Green's function calculations of the electronic structure of neutral defects in solids were popular during the 1980s and early 1990s [213–215]. More recently, Green's function implementation in linear muffin-tin orbital calculations has been demonstrated by Gorczyca et al., although these authors only considered unrelaxed substitutional defects in GaN, AlN, and BN [216–218]. By combining the supercell approach with the full-potential version of the linear-muffin-tin-orbital method, defect ionization levels in the band gap can be estimated as the center of gravity of the impurity band determined by means of the density-of-states functions [216].

Hartree–Fock (HF) based models seek to approximately solve the electronic Schrödinger equation for quantum many-body systems. For example, Nolte has considered the discrete charge states associated with mesoscopic point-like semiconductor defects using the unrestricted Hartree–Fock approximation [219]. *Ab initio* HF calculations are highly resource demanding, fail to consider correlation effects, and can only be applied to system with small numbers of atoms [113]. More recently, the *ab initio* HF approach has been largely replaced by less rigorous tight-binding (TB) schemes for the investigation of charged defects in semiconductors [113,220–224]. Monte Carlo calculations, which were first used to study diffusion processes, have also been utilized to explore the properties of defects and impurities in semiconductors [113,225,226]. For instance, Martin-Bragado et al. have recently detailed an approach for the modeling of dopant diffusion in Si for implementation in an atomistic KMC process simulator that accounts for multiply charged defects and a local Fermi energy-dependent electric bias [227,228]. Also, Alfe and Gillan have reported quantum Monte Carlo calculations of the formation energies of (2+) Mg vacancies and (2–) oxygen vacancies in MgO [229].

3.2.3. Systems-based methods

Despite the variety of experimental and computational methods for studying defects and their charging behavior, the results have often proven conflicting and unreliable. For example, experimental results have been used to justify diffusion coefficients for the Si self-interstitial that vary by more than 10 orders of magnitude at typical processing temperatures [188]. In light of these problems, rationally defensible procedures for estimating ionization levels and other thermodynamic and kinetic parameters must be accepted in place of certain truth about their values. One method that deals directly with this problem is the statistical technique of maximum likelihood parameter estimation [230]. This approach gives the most likely value for each parameter based on the available literature, and estimates the corresponding uncertainty. The maximum likelihood approach has proven quite useful in predicting ionization levels for interstitial atoms in Si [4], as well as their diffusion coefficients [231] and rate constants for their exchange with the lattice [231] and the surface [24,232]. This approach can be extended by a combination of parameter sensitivity analysis [233] and the method of maximum *a posteriori* estimation [234] to yield further refinements of these quantities for use in predictive models for phenomena such as transient enhanced diffusion in ion implantation technology [235].

The most likely value \bar{y} for a given parameter is obtained by minimizing the objective function [234]:

$$\Phi(\bar{y}) = \sum_i w_i (y_i - \bar{y})^2 \quad (47)$$

where y_i denotes the estimate for the parameter drawn from a particular paper i in the literature, and w_i is a weighting factor that accounts for the accuracy of y_i . Setting the derivative of $\Phi(\bar{y})$ with respect to \bar{y} equal to zero yields an analytic formula for \bar{y} :

$$\bar{y} = \frac{\sum_i w_i y_i}{\sum_i w_i} \quad (48)$$

Computational papers (particularly by DFT) often produce several estimates for a parameter using a family of closely related methods (such as the local density approximation and the generalized gradient approximation). In such

cases, y_i can be taken as the average of the individual estimates y_{ij} . This procedure tacitly assumes that all estimates reported by a particular laboratory have equal probability.

The weighting factors w_i can be computed based on the common assumption [230] that the uncertainty in y_i obeys a normal (Gaussian) distribution. Thus, w_i is set to equal the inverse of the variance σ_i^2 , where σ_i is the standard deviation of y_i . Assuming that errors are additive and satisfy standard Gauss–Markov assumptions (i.e. that the errors are uncorrelated, have zero mean, and have constant variance), σ_i obeys [234]:

$$\sigma_i = \sqrt{\frac{\min_{b_1, b_0} \sum (Y_k - b_1 X_k - b_0)^2}{(m - 2) \sum (X_k - \bar{X})^2}} \quad (49)$$

where \bar{X} denotes the mean of X , m denotes the total number of data points, and b_1 and b_0 represent the fitting parameters.

In computational papers offering multiple estimates y_{ij} , the standard deviation can be calculated using the formula:

$$\sigma_i = \sqrt{\frac{\sum_j (y_{ij} - y_i)^2}{n - 1}} \quad (50)$$

where n is the total number of estimates in the paper. The uncertainty in the most likely value \bar{y} is quantified as a standard deviation given by

$$\bar{\sigma} = \frac{1}{\sqrt{\sum_i (1/\sigma_i^2)}} \quad (51)$$

Parameter estimates can then be reported in the form of $\bar{y} \pm \bar{\sigma}$.

3.2.4. Surfaces and interfaces

Computational methods can apply in equal measure to surface defect phenomenology, though their application for this purpose is comparatively recent. DFT has been the method of choice. For example, the charging of surface vacancies on Si(1 0 0) and Si(1 1 1) has been explored with density-functional theory by Dev and co-workers [28,59,62,243]. This laboratory adapted the approach of Van Vechten and Thurmond for estimating ionization entropies to estimate surface vacancy ionization levels at processing temperatures [57,60,236]. With regard to other materials, considerable attention has focused upon III–V surfaces such as GaAs(1 1 0), InP(1 1 0), InAs(1 1 0), and InSb(1 1 0) [197,237–243]. Models of scanning tunneling microscopy images for III–V surfaces have been proposed [237,241] that seek to replicate the experimentally observed surface defect geometries and electronic structure. The defect chemistry of oxide semiconductor surfaces is still poorly understood, although recent DFT investigations have yielded some preliminary results [244–247]. Spin-polarized calculations performed using the generalized gradient approximation and the embedded-cluster numerical discrete variational method have also been used to explore oxide semiconductor surface defects [248–250].

4. Effects of crystal structure, atomic properties, and stoichiometry on charged defects

Many bulk and surface defects have charge state-dependent structural forms and symmetry-lowering relaxations. In the case of the latter, the charge on the defect can affect both the magnitude and direction of the relaxations. Although both bulk and surface defects can be ionized, for a given semiconductor the two types do not necessarily take on the same range of charge states. There are typically fewer stable charge states on the surface than in the bulk; sometimes donor or acceptor states present in the bulk will not be manifested on the surface. The kinetics of defect diffusion depend upon charge state both in the bulk and on the surface. Defects in silicon and germanium take on the stable charge states summarized in Table 2.

The geometry and structure of charged defects depend on the crystal lattice structure and, in the case of surfaces, reconstructions that may be present. For example, crystals described by small lattice parameters, especially those comprised of atoms with large atomic radii, are unlikely to contain significant concentrations of interstitial defects. In the case that multiple crystal structures exist for a given semiconductor, certain defects may be favored by a structure that is either more open or has higher bond coordination. Both silicon and germanium have a diamond crystal lattice

Table 2

Summary of the silicon and germanium defect charge states that have been proposed to be stable in the bulk and on the surface

Material	Regime	Vacancy	Interstitial
Silicon	Bulk	2+, 0, 1-, 2-	2+, 0, 1-
	Surface	2+, 0, 1- (lower), 2- (upper)	—
Germanium	Bulk	0, 1-, 2-	1+, 0, 1-
	Surface	<0	—

structure that can be described in terms of two interpenetrating face centered cubic crystal lattices. Whereas most gallium-containing III–V semiconductors have a zinc-blende structure, those containing nitrogen and boron tend towards greater stability in a hexagonal structure. Monoxides, MO, typically crystallize in the rocksalt structure, although some of them, e.g. ZnO and BeO, show the structure of wurtzite [36]. The rocksalt lattice is composed of two face-centered cubic sublattices, and both the anions and cations are six-fold coordinated. The wurtzite lattice has hexagonal symmetry and the coordination number for both kinds of atoms is four. Dioxides having formula MO₂ usually possess either a rutile or fluorite crystal structure. The rutile structure has tetragonal symmetry; each cation is six-fold coordinated whereas each anion is surrounded by three cations. The rutile structure is found with oxides of tetravalent metals such as Ti, Nb, Ta, Cr, Mo, W, Mn, Ru, Os, Ir, Ge, Sn, Pb, and Te. The fluorite structure is composed of close-packed, face-centered cubic sublattices of cations; each cation is eight-fold coordinated, while the anions are only four-fold-coordinated. The fluorite structure is found with tetravalent atoms with large radii such as Zr, Hf, Ce, Pr, Tb, Po, Th, Pa, U, Np, Pu, and Am [36]. The easily or normally grown crystal structures for the semiconductors discussed within this review are tabulated in Table 3.

Interesting exceptions to typical charged defect behavior occur in zinc-blende AlN ($a = 4.38 \text{ \AA}$) and wurtzitic BN, two less-stable, yet obtainable, crystal phases of these nitride compounds. In zb-AlN, the Al_i³⁺ has a lower formation energy than V_N¹⁺ or V_N³⁺, the dominant defect in p-type wurtzitic AlN [113,251]. Also, for zinc-blende AlN, the vacancy defect level is resonant in the conduction band, causing it to act as a shallow donor, while in wurtzite (which has a larger band gap), the level lies well below the conduction band minimum, causing the vacancy to act as a deep donor [113]. Orellana and Chacham found N_i in the (2+) or (3+) charge state to be the most stable defect for wurtzitic BN under N-rich conditions. For the same conditions when looking at the cubic phase of the compound, positively charged nitrogen vacancies and negatively charged boron vacancies dominate for p-type and n-type material, respectively [252]. These phenomena can be justified by the different bonding configurations, band gap values, and covalent radii involved with the two crystal structures and compounds. In wurtzitic material the interstitial can only

Table 3

Summary of easily or normally grown crystal structures for group IV, III–V, and oxide semiconductors

Material	Crystal structure	$a (\text{\AA})$	$c (\text{\AA})$
Si	Diamond	5.431	—
Ge	Diamond	5.6579	—
GaAs	Zinc-blende	5.6533	—
GaP	Zinc-blende	5.4508	—
GaSb	Zinc-blende	6.09593	—
c-BN	Zinc-blende	3.6155	—
h-BN	Hexagonal	2.504	6.6612
w-AlN	Hexagonal	3.112	4.982
α -GaN	Hexagonal	3.1896	5.1855
InN	Hexagonal	3.548	5.76
TiO ₂	Rutile	4.59–4.64	2.95–2.97
TiO ₂	Anatase	3.764	9.46646
ZnO	Wurtzite	3.2495	5.2069
UO ₂	Fluorite	5.471	—
CoO	Rocksalt	4.26	—

The lattice constants a and c ($T = 300 \text{ K}$) in angstroms are also included. Data taken from Adachi's "Properties of group IV, III–V and II–VI semiconductors" [443].

interact with three nitrogen neighbors, whereas in zinc-blende it can form bonds with four nitrogen atoms [113,251]. In comparing rutile versus anatase titanium dioxide, consider the temperature at which titanium interstitials overtake oxygen vacancies as the dominant defect in the bulk. At 10^{-1} Pa, the switch occurs at 1100 °C in rutile in comparison to 580 °C in anatase. The more favorable formation of interstitials in anatase is attributed to the fact that the crystal lattice structure has a 10 % lower density than rutile [253].

Energy-lowering surface reconstructions impact the type and stability of defects observed on groups IV, III–V, and oxide surfaces. For a prototypical III–V semiconductor such as GaAs, reconstructions that minimize the number of anion and cation dangling bonds and surface dimers occur under cation- and anion-rich conditions, respectively. In some cases, surface defects actually lower the energy of the cleaved surface; divacancies on Si(1 0 0)-(2 × 1) stabilize the dimer buckling of the undefected surface. Alternatively, the existence of a high concentration of defects can induce energetically favorable surface reconstructions [254]. Depending on the stability of the reconstruction, different types of defects can form. For example, the defect chemistry of the stable natural cleavage plane of silicon is considerably different than that of the Si(0 0 1) surface; monovacancies, rather than divacancies, are the dominant defects on Si(1 1 1)-(7 × 7). These adatom vacancies can occur in four different locations on the surface, where the local geometry is described by unfaulted and faulted triangular units of six adatoms [60,255]. Similarly, the rutile (1 1 0)-(1 × 1) surface is adorned with rows of two-fold coordinated bridging oxygen atoms, all of which are missing one Ti bond, stretch along the [0 0 1] direction; this unsaturated coordination encourages the formation of bridging and in-plane oxygen vacancies.

In order to discuss the electronic and structural properties of III–V semiconductors, the compounds will be classified into two groups. The classification system arises naturally, a consequence of the unusual behavior of the semiconductors containing boron and nitrogen, or the elements from the second row of the periodic table. While groups III–V compounds containing elements from the third, fourth, and fifth rows of the periodic table behave somewhat similarly to GaAs, the same cannot be said for those containing 2nd row elements. Boron and nitrogen atoms have small atomic and covalent radii, an absence of p electrons in the core, and are expected to have deep and localized pseudopotentials in comparison to those of atoms from other rows [256,257] (Table 4). Subsequently, the semiconductors formed from boron and nitrogen have small lattice parameters and ionicity [256]. As deep atomic potentials and a small lattice constant are two important criteria for obtaining a wide band gap, the large band gaps of BA_x, BN, BP, BSb, AlN, GaN, and InN are not unexpected [256]. The small radius of the nitrogen atom, especially in comparison to the large radii of aluminum, gallium, or indium has an important effect on the defect chemistry in the bulk. The mismatch in covalent radii between the group III element and the nitrogen atom leads to high self-interstitial and antisite formation energies; only vacancies have formation energies that are low enough to ensure that their concentration affects the electronic properties in the bulk [113]. When a large gallium atom seeks to form a defect such as Ga_i or Ga_N (for the case of GaN), the atoms move away from the defect and cause large lattice strains. Similarly, when a small nitrogen atom is introduced into the crystal, large displacements, and thus significant strains, are required to form the low-symmetry bonding configuration. Large strains within the crystal, although slightly diminished by atomic relaxations, lead to high formation energies [113].

For compound and oxide semiconductors, the chemical potential and oxygen partial pressure of the system critically affect the nature of charged bulk and surface defects. The important defects in III–V materials vary from

Table 4

The atomic radius and electron configuration of the elements found in III–V semiconductors can be correlated to the types of defects found in the bulk

Element	Atomic radius (pm)	Electron configuration
Al	143.1	3s ² 3p ¹
As	125	4s ² 3d ¹⁰ 4p ³
B	83	2s ² 2p ¹
Ga	122.1	4s ² 3d ¹⁰ 4p ¹
In	162.6	5s ² 4d ¹⁰ 5p ¹
N	71	2s ² 2p ³
P	93	3s ² 3p ³
Sb	142	5s ² 4d ¹⁰ 5p ³

Notice the comparatively small radii of boron and nitrogen.

Table 5

Semiconducting properties of binary metal oxide of non-stoichiometric composition as detailed by Bak et al. [258]

p-Type semiconductors	
Deficit of metal	Excess of oxygen
CoO, NiO, FeO, MnO, Cu ₂ O	UO ₂
n-Type semiconductors	
Excess of metal	Deficit of oxygen
TiO ₂ , ZnO, CdO	TiO ₂ , ZrO ₂ , Nb ₂ O ₅ , Ta ₂ O ₅ , WO ₃ , CeO ₂ , PuO ₂ , SnO ₂ , Bi ₂ O ₃ , PbO ₂

group III element-rich to group element-rich conditions. For example, Ga-rich GaAs contains a negligible amount of arsenic interstitials and arsenic antisites; the crystal lattice is described by the presence of gallium interstitials and antisites. Under arsenic-rich conditions, the arsenic antisite increases in concentration, as does the gallium vacancy. Most metal oxides are naturally non-stoichiometric, and the extent and nature of their non-stoichiometry alters the electrical properties of the material. They can be classified into two main categories, p-type and n-type, and four subcategories, metal deficient, metal excess, oxygen deficient, and oxygen excess [258] (Table 5).

For example, in reducing atmospheres, TiO₂ loses oxygen and becomes an oxygen-deficient compound according to the following equilibrium:



where x is the deviation from stoichiometry in the oxygen sublattice [259]. The relationship between the concentration of defects in the bulk and the deviation from stoichiometry, x , in TiO_{2-x}, is then given in its most thorough form by

$$x = \frac{2([\text{Ti}_i^{3+}] + [\text{Ti}_i^{4+}] - [\text{V}_{\text{Ti}}^{4-}]) + [\text{V}_\text{O}^{2+}]}{1 + [\text{Ti}_i^{3+}] + [\text{Ti}_i^{4+}] - [\text{V}_{\text{Ti}}^{4-}]} \quad (53)$$

Titanium dioxide falls into both the metal excess and oxygen deficient categories, however; its defect chemistry is characterized by a predominance of Ti_i³⁺ at low P_{O₂} and V_O²⁺ at high P_{O₂}, respectively. A metal-deficient p-type semiconductor such as CoO, for example, is typically represented as Co_{1-x}O, where for any non-zero value of x , the crystal has an assortment of atomic defects. For the case of $x > 0$, the crystal has metal vacancies, V_M, whereas for the case of $x < 0$, the crystal has extra metal atoms that are situated at interstitial positions, M_i [43]. Charged metal vacancies, V_{Zn} and V_U, are the predominant defects in O-rich ZnO and UO₂. Under metal rich or stoichiometric conditions, these semiconductors are more likely to contain ionized oxygen vacancies and interstitials. Kosuge and Jarzebski have discussed these phenomenon in more detail in “Chemistry of Non-Stoichiometric Compounds” and “Oxide Semiconductors” [36,43]. Both include valuable portions on the derivation of Kröger–Vink diagrams, which employ principles of chemical equilibria to depict the concentration of ionized defects in the bulk as a function of oxygen partial pressure, as well as oxide semiconductor case studies.

Having now discussed the effect of crystal structure, atomic properties, and chemical potential on semiconductor defects (and their charge states), a summary is in order. Table 6 lists the defect charge states that are thought to be stable for several compound and oxide semiconductors. Notice that GaP holds more in common with GaAs than GaN. Also, the fact that defects in ZnO have ionization levels within the forbidden band gap, while those in TiO₂ do not. Such commonalities and differences will be discussed in more detail in the body of this review.

5. Geometry and structure of charged defects

5.1. Bulk defects

When an atom is removed from or introduced into a semiconductor crystal lattice, the defect that is formed may take on one of an assortment of possible geometries (Fig. 7). Isolated vacancies in the semiconductor crystal structure can be described by two geometric configurations. A simple lattice vacancy, V_L, results when an atom is removed from the lattice, leaving a void in its place (Fig. 7a). A “split” vacancy, V_B, results when an atom resides at the bond center between two empty sites (Fig. 7d) [27,260]. In most semiconductors V_L is the dominant geometric configuration for the ionized vacancy defect, whereas V_B is often important primarily to help describe the transition state in vacancy

Table 6

Summary of the group III–V and oxide semiconductor defect charge states that have been proposed to be stable in the bulk and on the surface

Material	Regime	$V_{\text{III/metal}}$	$V_{\text{v/oxygen}}$	$I_{\text{III/metal}}$	$I_{\text{v/oxygen}}$	V_{III}	III_{v}
GaAs	Bulk	0, 1–, 2–, 3–	1+, 1–, 3–	3+, 2+, 1+, 0	1+, 0, 1–	2+, 1+, 0	0, 1–, 2–
	Surface	1+, 0, 1–	1+, 0, 1–	–	–	–	–
GaP	Bulk	1+, 0, 1–, 2–, 3–	1+, 1–, 3–, 5–	3+, 2+, 1+	3+, 1+, 0, 1–	2+, 0	2+, 0, 1–, 2–
	Surface	–	1+, 0, 1– (InP)	–	–	–	–
GaN	Bulk	0, 1–, 2–, 3–	3+, 1+, 1–, 2–, 3–	3+, 1+	3+, 2+, 1+, 0, 1–	2+, 1+, 0, 1–	3+, 2+, 1+, 0, 1–
	Surface	–	–	–	–	–	–
TiO_2	Bulk	4–	2	3+ or 4+	n/a	–	–
	Surface	–	2+, 1+, 0	–	–	–	–
ZnO	Bulk	0, 1–, 2–	2+, 0	2+, 1+, 0	1+, 0, 1–, 2–	–	2+, 1+, 0
	Surface	–	2	–	–	–	–

Proposed charge states of vacancies, interstitials, and antisites are included, where the subscript indicates whether the defect is comprised of an anion or cation. As the GaP surface is not well characterized, the charge states of its surface vacancies are instead given by those on InP.

migration [27]. For simplicity, the present exposition will drop the “L” subscript for the lattice vacancy but retain the “B” subscript.

Analogs to the lattice and “split” vacancy exist for interstitial defects, although self-interstitials can occupy a considerably larger number of geometries than vacancies. Well known examples in silicon include tetrahedral (Fig. 7e), split- $\langle 1\ 1\ 0 \rangle$ (Fig. 7c), hexagonal (Fig. 7f), extended, split- $\langle 1\ 0\ 0 \rangle$, and bond-centered [27,81,261] configurations. In addition, several lower-symmetry configurations have been postulated based mainly upon evidence from quantum calculations. In particular, a highly asymmetric “caged” silicon self-interstitial was identified by Clark et al. in 1997 [261–264]. Marques et al. have found evidence for an extended self-interstitial in silicon, consisting of four displaced atoms and three empty lattice sites along the $\langle 1\ 1\ 0 \rangle$ plane, and a newly identified asymmetric configuration, formed from three displaced atoms and two lattice sites [265].

For many defects, both neutral and ionized, the Jahn–Teller distortions responsible for structural relaxation lead to a breaking of local tetrahedral (T_d) symmetry, in which all six interatomic distances are equal [266–268]. The distortions occur when a degenerate set of orbitals is occupied unevenly with electrons, leading to unevenly balanced forces. The distortions can lead to point symmetries such as D_{2d} , where the tetragonal lattice distortion has two equal and shorter interatomic distances and four approximately equal and longer distances, and C_{2v} , where the orthorhombic lattice distortion has one shorter interatomic distance and five approximately equal and longer distances [267]. The final point-symmetry of the defect, as well as the magnitude and direction of the relaxations, typically depends upon charge

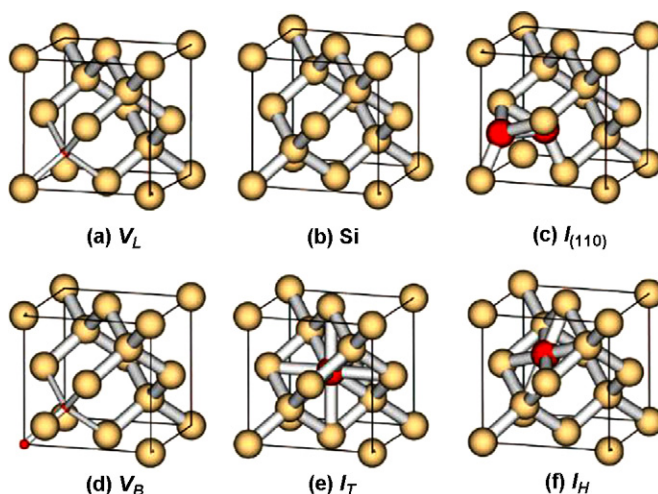


Fig. 7. Geometries of defects in relation to a conventional cubic unit cell of Si.

state. In general, the direction of atomic relaxations caused by the charged defects reflect the effects of electrostatic attraction or repulsion. Sometimes, the symmetry-lowering relaxations are so energetically favorable that negative-U behavior is observed [27,213,269,270]. For a negative-U system, the capture of an electron or hole is immediately followed by a capture of a second carrier of the same type; thus, the intermediate charge state is energetically unstable at all possible chemical potentials [271].

5.1.1. Silicon

When a single atom is removed from the diamond crystal lattice, it leaves behind four dangling bonds located at the vertices of a tetrahedron [27]. Nominally, each of these dangling bonds contains one unpaired electron, so that the associated silicon atoms can be conceptualized as free radicals. Except under strongly n-type conditions, the vacancy defect in silicon assumes an energetically favorable lattice configuration; i.e. the lattice vacancy, rather than the split vacancy, is the preferred configuration for V^{1+} , V^0 , and V^{1-} [27]. As early as 1974, Bourgoin and Corbett suggested that the split vacancy V_B^{2-} would replace the lattice vacancy as the ground state of the defect in heavily donor-doped material [272]. The reversed stability in the highly n-type region can be attributed to the greater number of bonds on V_B . The displaced atom in the split vacancy, illustrated in Fig. 8, has four valence electrons and six neighbors, or two additional electrons with which to form six equally strained bonds, so it can accept electrons with greater ease [27]. Centoni et al. have recently confirmed the fact that the vacancy in strongly n-type material exists in the split, rather than lattice, configuration via first-principles calculations; they posit that many researchers are unaware of this phenomenon because it only occurs at low temperatures, whereas most technologically useful processes involve elevated temperatures [27]. Still, many computational studies consider only the lattice configuration of the defect that has been observed in experimental studies, which occur at temperatures above 0 K.

The lattice monovacancy in bulk Si can support charge states of (2−), (1−), (0) and (2+) [273]. Experiments and computations have shown that strong Jahn–Teller distortions lead to a breaking of T_d symmetry for all charge states except (2+) [274–276]. According to Watkins' linear combination of atomic orbitals model, when electrons are added to V_{Si}^{2+} , the symmetry is reduced to D_{2d} for V_{Si}^{1+} and V_{Si}^0 and then to C_{2v} for V_{Si}^{1-} and V_{Si}^{2-} [27,271,274]. Using DFT, Lento et al. have calculated transitions to tetragonal D_{2d} symmetry for all but V_{Si}^{1-} , which adopts a D_2 configuration. In both approaches, the symmetry lowering lattice relaxation from T_d to D_{2d} for the (2+) to (0) charge state transition leads to negative-U behavior, destabilizing the (1+) charge state of the defect; this phenomenon has been predicted since the 1970s [27,213,269,270]. With a 256-atom supercell, Lento et al. observed large inward relaxations of 32.3–47.6% for charge states from (1+) to (2−). 256- and 33-atomic supercells give a −9.7 and 12.9% contraction for V_{Si}^{2+} , respectively; the inward relaxation of the doubly positively charged vacancy is only obtained with supercells larger than ~200 atoms [194,271,275]. Interestingly, Centoni et al. found that V_B does not experience symmetry-breaking distortions [27] as the lattice vacancy does.

For interstitials in silicon, the question of which structures are most stable is still under debate. The relatively symmetric tetrahedral, hexagonal, and split-⟨1 1 0⟩ configurations have received the most attention [30,264,277–281]. An alternative, low-symmetry caged interstitial structure has been proposed by Clark and Ackland, although

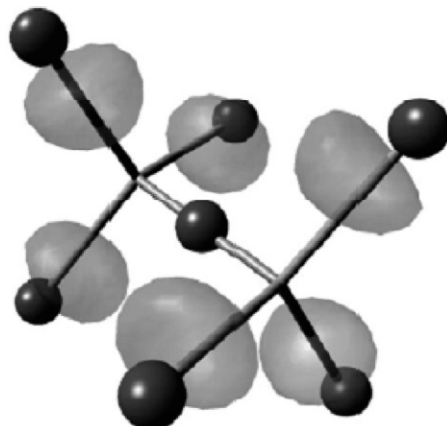


Fig. 8. Doubly negative silicon vacancy, where the spheres give the relaxed positions of the ions with respect to ideal bulk bonds denoted by sticks.

subsequent investigators have questioned its stability [261,262,264]. The tetrahedral interstitial atom is four-fold coordinated with four 5-fold-coordinated nearest-neighbor atoms. The atoms that form the $\langle 1\ 1\ 0 \rangle$ -split interstitial are also four-fold coordinated, although only two of the neighboring atoms are five-fold coordinated. The pair of Si atoms at a substitutional site directed in the $\langle 1\ 1\ 0 \rangle$ direction has been shifted from the ideal lattice site by 0.76 Å in the $\langle 0\ 0\ 1 \rangle$ direction [30]. The displacement is energetically favorable because it minimizes the relaxations associated with the neutral defect. Most computational investigations suggest that tetrahedral Si_i^{2+} dominates in p-type silicon, with a switch to Si_i^0 , Si_i^{1-} , or Si_i^{2-} in a $\langle 1\ 1\ 0 \rangle$ -split configuration for n-type material [4,30,281]. While some workers have found the highly symmetric hexagonal geometry to be energetically favorable for Si_i^{2+} , regardless of defect charge state, the hexagonal configuration is usually assumed to be the saddle point for interstitial diffusion [27,30,261,263,282]. Among the high-symmetry configurations, the $\langle 1\ 0\ 0 \rangle$ -split and bond-centered configurations are generally acknowledged to be unstable [261,263,264].

Little quantitative discussion exists in the literature on the relaxations associated with the different charge states of these defects [261,283]. According to Lee et al., small, charge state-independent relaxations (~ 1 Å) are associated with the tetrahedral and hexagonal self-interstitial sites [30]. Centoni et al. calculated relaxation volume tensors only for neutral defects, which are pertinent to $I_{\langle 1\ 1\ 0 \rangle}$ but not I_T [27]. For the split-interstitial, the two 5-fold-coordinated neighbors expand outwards in the $\langle 1\ 1\ 0 \rangle$ direction by approximately 5%, while the two 4-fold-coordinated neighbors are almost the same as the bulk bond length [27,30].

5.1.2. Germanium

The vacancy defect in germanium behaves differently from that in silicon; no negative-U behavior is observed, and V^{1-} and V^{2-} relax to different point symmetries. To date, it appears that only the lattice vacancy has been considered; there has been no investigation of V_B^{2-} in Ge. For V^0 and V^{1+} , the distortions in the bond lengths that induce a reduction to D_{2d} point symmetry are three times smaller in Ge than in Si. This is due to the weak electron-lattice coupling in germanium, which is about six times smaller than in silicon, and causes the charge states (2+), (+), and (0) to *not* form a negative-U system [267,284]. Both Janotti et al. and Fazzio et al. proposed C_{2v} symmetry for the negatively charged vacancy states using density functional theory with the LDA, a 128-atom supercell, an energy cutoff of 12 Ry, and Brillouin zone sampling using one k -point [268]. However, in a spin density functional study using the AIMPRO code, Coutinho et al. recently published results suggesting that V^{1-} relaxes to the D_2 or T_d structure, while V^{2-} undergoes a tetragonal Jahn-Teller distortion that leads to D_{2d} symmetry [266]. For V^{1-} the proposed D_2 deformation follows the occupancy of a bonding state between atom pairs whereas for V^{2-} , the distorted D_{2d} structure allows the four available electrons to be accommodated in the t_2 state. The method utilized by Coutinho et al. may provide more realistic results, as vacancy dangling bonds induce long range strain fields that cause the structures predicted by DFT to depend heavily on supercell size and shape, as well as the Brillouin zone sampling scheme [266]. A schematic of their calculated structural distortions in Ge for several charge states of interest is shown in Fig. 9 [266].

In contrast to the vacancy, the germanium interstitial resembles silicon in many respects. For example, similar to Si_i^0 , the split- $\langle 1\ 1\ 0 \rangle$ (or dumbbell) configuration of Ge_i^0 has a lower formation energy than both the tetrahedral and hexagonal configurations [268,285–287]. The stable geometry of the self-interstitial, the $\langle 1\ 1\ 0 \rangle$ dumbbell, has also been called a “kite-defect” due to its symmetrical configuration. da Silva et al. arrived at this designation based on the delocalization of the charge density among the four-atom ring formed by the two Ge atoms in the dumbbell and their

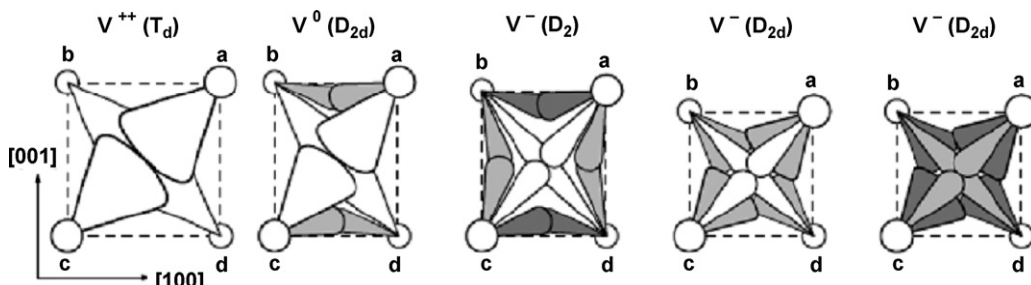


Fig. 9. Scheme of the structural distortions in a Ge vacancy for several charge states of interest. The symmetry of each structure is shown within parentheses.

two nearest neighbors along the zig-zag [285]. For the neutral charge state of the germanium dumbbell self-interstitial, these authors find that all of the atoms along the $\langle 1\ 1\ 0 \rangle$ zigzag direction relax outward. The relaxations for the first-, second-, and third-neighbor atoms to the dumbbell are about 2.9, 5.4, 3.7% of the nearest-neighbor distance, respectively [288]. The comparative stability of the split- $\langle 1\ 1\ 0 \rangle$ versus tetrahedral configurations for Ge_i^{1+} is a subject of much debate. da Silva et al. found that the former is always the lowest energy configuration of Ge_i , regardless of charge state, while Birner et al. proposed that the tetrahedral site was more favorable for Ge_i^{1+} [285,289]. The (1-) charge state, on the other hand, has been considered primarily in the split- $\langle 1\ 1\ 0 \rangle$ configuration [287,288].

5.1.3. Gallium arsenide

The picture of charged defects in gallium arsenide, a group III–V binary semiconductor having the zinc-blende structure, differs from that of silicon and germanium because there exist two different types of vacancies, interstitials, and antisite defects. The vacancies and interstitials are symbolized by V_{Ga} , V_{As} , Ga_i , As_i , and antisite defects by Ga_{As} and As_{Ga} .

An ideal Ga vacancy in GaAs is surrounded by four As atoms that remain in their bulk crystalline positions; defect creation results in four broken bonds pointing out from the four As atoms towards the Ga vacancy [290]. The As dangling bonds do not form pairs in any charge state, and the defect maintains the same configuration for all charge states. All of the atoms move significantly inwards while maintaining T_d symmetry, with charge state-independent volumetric relaxations on the order of 35% for the stable defects V_{Ga}^0 , V_{Ga}^{1-} , V_{Ga}^{2-} , and V_{Ga}^{3-} [291–293]. By contrast, the geometric and electronic structure of the arsenic vacancy is far different. Except for the positively charged vacancy, there are substantial departures from the initial local symmetry; for V_{As}^{1+} tetrahedral symmetry is preserved with an associated inward 17.1% volume change [291–293]. For the (1+) charge state of the arsenic vacancy, in contrast to the other stable charge states, there is no breathing mode displacement to break the local symmetry and no bond stretching and pairing to cause large volume deformations [293]. For the neutral and (2-) vacancy, large Jahn–Teller distortions destabilize the defect, and negative-U behavior is observed [293,294]. El-Mellouhi et al. calculated the point symmetries and percent volume changes for the stable (1-) and (3-) charge states as $\sim D_{2d}$ and D_{2d} -resonant and –51.2 and –62.9, respectively [293]. Fig. 10 serves to summarize the volumetric relaxations of the charged gallium vacancy in comparison to those of the charged arsenic vacancy.

Gallium and arsenic interstitials can exist in several structural forms. The $\langle 1\ 1\ 0 \rangle$ split-interstitial, two-fold coordinated bridge-bond geometry, and tetrahedral–interstitial configurations are preferred for Ga_i^0 , Ga_i^{1+} , and $\text{Ga}_i^{2+,3+}$, respectively [281]. The configuration for Ga_i^{1+} results when the interstitial breaks a bulk Ga–As bond and forms bridge bonds to the two resulting broken bonds [281] (Fig. 11). The T_{d1} tetrahedral–interstitial site that is favored for the (2+) and (3+) charge states is described by a gallium interstitial surrounded by four Ga atoms. This structure differs from the T_{d2} form, which is 0.14 eV higher in energy for the (2+) interstitial. Upon relaxation, the stable T_{d1} form expands outwards by 5%, whereas in the T_{d2} form, the As–Ga bond lengths are increased by about

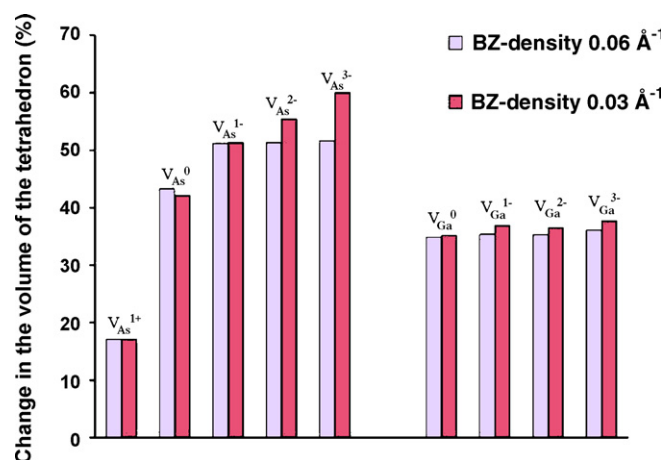


Fig. 10. Histogram of the change in volume of the relaxed tetrahedron formed by atoms surrounding the Ga or As vacancy in GaAs. Results are calculated by DFT for two densities of k points in the Brillouin zone, and expressed as a percentage change compared to the ideal volume.

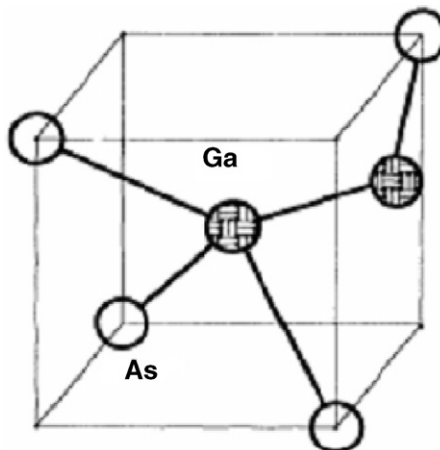


Fig. 11. The two-fold coordinated bridge-bond geometry of the Ga interstitial that is supposedly favored for the (1+) charge state of the defect.

3.5% [281,295]. For As_i , debate has continued over the relative energies of the $\langle 1\ 1\ 0 \rangle$ -split interstitial and tetrahedral configurations; As_i^0 and As_i^{1-} most likely exist as a split-interstitial centered on an arsenic lattice site while As_i^{1+} consists of an As atom and a Ga atom sharing a Ga lattice site [281,296,297]. For the split-interstitial, the As–As bond expands by 3.5% and contracts by 3% in comparison to the neutral state bond length when the system is allowed to relax in the (1–) and (1+) charge states, respectively [296]. The split-interstitial configuration as computed by Schick et al. is shown in Fig. 12.

The arsenic antisite defect, which is illustrated in Fig. 13, has received a great deal of attention in conjunction with the oft-observed EL2 defect in GaAs, with which it has been associated [114,298–306]. The defect can exist in two different forms: stable and metastable. Dabrowski and Scheffler identified the basic mechanism of EL2 metastability with that of the $\text{As}_{\text{Ga}} \leftrightarrow \text{V}_{\text{Ga}}\text{As}_i$ structural transition [307]. Further discussion of the metastable EL2 defect appears elsewhere [301]. The stable EL2 defect has T_d symmetry in all charge states and, upon relaxation, the distance to the next nearest neighbors increases by 4.7% for As_{Ga}^0 and decreases by 3 and 1.4% for $\text{As}_{\text{Ga}}^{1+}$ and $\text{As}_{\text{Ga}}^{2+}$, respectively [301,306].

The gallium antisite is stable in both the neutral and (2–) state; the cation antisite defect is a negative-U system. Ga_{As}^0 prefers to adopt a three-fold-coordinated broken-bond configuration, while $\text{Ga}_{\text{As}}^{2-}$ is most stable in a

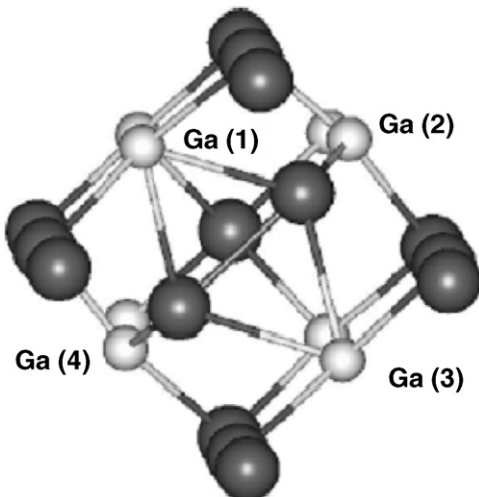


Fig. 12. The neutral As–As defect in GaAs from the DFT calculations of Schick et al. [296]. The larger dark spheres represent As atoms, and the smaller light spheres represent Ga atoms.

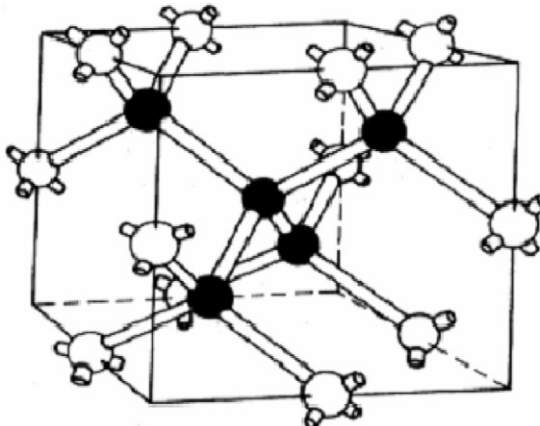


Fig. 13. Atomic geometry of the isolated arsenic antisite. Solid circle are As atoms and open circles are Ga atoms.

four-fold-coordinated substitutional configuration [308]. Large outward bond relaxations of 34% that, in turn, lead to the destabilization of $\text{Ga}_{\text{As}}^{1-}$, are calculated for the neutral charge state. T_d symmetry, with small inward relaxations, is predicted for the (2-) charge state of Ga_{As} [297,308–310]. The two geometries for the defect are depicted in Fig. 14.

5.1.4. Other III–V semiconductors

While some structural similarities exist between charged defects in GaAs and those in other III–V semiconductors, many differences are also observed. These differences are not only restricted to those compounds that contain a second row element such as boron or nitrogen. This discussion will focus on gallium antimonide, gallium nitride, and boron nitride, the primary III–V semiconductors for which a significant defect literature exists.

The gallium vacancy in GaSb is stable in the (1–), (2–), and (3–) charge states. For the (1–) and (2–) charge states of the defect, symmetry-breaking distortions cause a transition to $\sim T_d$ and $\sim D_{2d}$ symmetry, respectively [310]. In contrast, an inward relaxation of 12% preserves T_d symmetry for $\text{V}_{\text{Ga}}^{3-}$ [310]. As a reminder, the inward structural relaxation of the gallium vacancy in GaAs is almost independent of charge state, with a magnitude of 13.5–14.5% that preserves T_d symmetry in all cases [291–293]. Similarly to V_{As} , however, the point-symmetry and relaxations of the antimony vacancy states $\text{V}_{\text{Sb}}^{1-}$, V_{Sb}^0 , or $\text{V}_{\text{Sb}}^{1+}$, depend strongly upon the charge state of the defect. The singly negatively charged vacancy exhibits a very strong inward relaxation of about 20% to D_{2d} symmetry, similar to that found for the $\text{V}_{\text{As}}^{1-}$ in GaAs [291,310]. On the other hand, for $\text{V}_{\text{Sb}}^{1+}$, the symmetry group is $\sim T_d$ with a small inward relaxation of 5% [310]. The tetrahedral interstitial configuration is hypothesized to be the most favorable for all stable interstitial charge states in the band gap, Ga_i^{1+} , Sb_i^{1+} , and Sb_i^{3+} [310]. The (1–) gallium antisite defect, $\text{Ga}_{\text{Sb}}^{1-}$, relaxes inwards by 9% to preserve T_d symmetry; in GaAs, $\text{Ga}_{\text{As}}^{2-}$ is also stable in a four-fold-coordinated substitutional

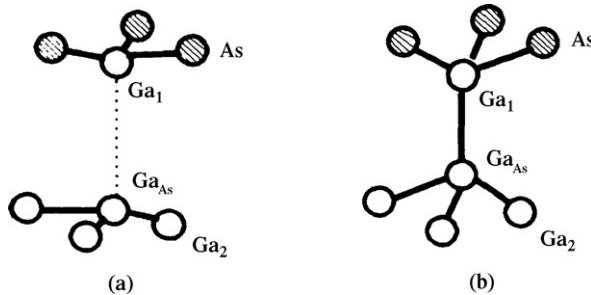


Fig. 14. Structural models for the Ga antisite in GaAs determined by Zhang and Northrup [297], where (a) is the broken-bond configuration for Ga_{As}^0 and (b) is the four-fold coordinated substitutional site model for the negative charge state.

configuration [308,310]. Conversely, Sb_{Ga} behaves quite differently than the comparable antisite in GaAs and InP. Only the neutral charge state, which displays T_d symmetry and outward relaxations of approximately 11%, is stable; there are no stable configurations of $\text{Sb}_{\text{Ga}}^{2+}$, $\text{Sb}_{\text{Ga}}^{1+}$, $\text{Sb}_{\text{Ga}}^{2-}$, or $\text{Sb}_{\text{Ga}}^{1-}$ within the band gap [310].

For gallium nitride and boron nitride, which both contain a second row element, the formation energies of antisite defects in these compounds are prohibitively large. Although those of cation self-interstitials also make their spontaneous formation unlikely, the structure of the more energetically favorable anion (or nitrogen) interstitial will be discussed in brief. GaN has the wurtzite structure rather than the zinc-blende. Conflicting results exist in the literature regarding the relaxations of the stable charge states of the gallium vacancy, V_{Ga}^0 , $\text{V}_{\text{Ga}}^{1-}$, $\text{V}_{\text{Ga}}^{2-}$, and $\text{V}_{\text{Ga}}^{3-}$. Neugebauer and Van de Walle indicated that the $\text{V}_{\text{Ga}}^{3-}$ –N bond length increases by 10.6–11.8%, while Limpijumong et al. found that the N atoms move outward from $\text{V}_{\text{Ga}}^{3-}$ by only about 4% of the ideal bond length [311,312]. In an even earlier work, the former authors suggested charge state-dependent relaxations of the defect, with distances between the vacancy center and the furthest N atom of 3.7, 6.3, 8.3, and 10% for the (0), (1 $-$), (2 $-$), and (3 $-$) charge states, respectively [311,313]. In contrast, the relaxations of the boron vacancy in wurtzite BN are independent of charge state, and closer to the magnitude of those for $\text{V}_{\text{Ga}}^{3-}$, or about 10% [314]. But when the charge state of the nitrogen vacancy in GaN changes from (1 $+$) to (3 $-$), the direction of the relaxation changes from outward (V_{N}^{1+}) to inward (V_{N}^{1-} , V_{N}^{2-} , V_{N}^{3-}), with an associated switch from T_d to D_{2d} symmetry [312,315,316]. The nitrogen vacancy in BN exhibits exclusively outward relaxations that decrease in magnitude from 19.8 to 7.7% for the charge states (3 $+$) to (0), with only slight distortions from the T_d symmetry [314].

In GaN, the gallium interstitial favors a site near the octahedral interstitial site for both stable charge states, Ga_i^{1+} and Ga_i^{3+} [312]. This configuration differs considerably from the split–interstitial and tetrahedral geometries that are observed for Ga_i in GaAs and GaSb. Also, a small increase in the distance to the nearest-neighbor nitrogen atoms, on the order of 0.1 Å, is observed when the charge state decreases from (3 $+$) to (1 $+$). The boron interstitial in BN assumes two different lowest-energy configurations depending on the charge state of the defect. For the (1 $+$) and (2 $+$) charge states, the interlayer B atom is in line with the N and B atoms of the adjacent planes, while for the neutral, (1 $-$), and (2 $-$) charge states, the B interstitial binds with a B atom of the first layer and a B–N pair of the second layer; the latter charge states are associated with large distortions [252]. For the nitrogen interstitial in GaN, on the other hand, a split–interstitial configuration arises in which N_i forms a bond with one of the nitrogen host atoms, sharing its lattice site (Fig. 15). The gallium atoms relax outwards by a distance equal to 25% of the bulk Ga–N bond length for the (3 $+$) charge state, while an *inward* relaxation of 6.1% is observed for N_i^{1-} [312].

5.1.5. Titanium dioxide

The structures associated with the charged defects in TiO_2 are not nearly as well described as for those in group IV and III–V semiconductors. The effect of variable charge states on defect configuration and relaxation is not often explored in conjunction with titanium dioxide; the charged titanium interstitial (Ti_i^{3+} and Ti_i^{4+}) is one exception. As for the remaining point defects, only the (2 $+$) oxygen vacancy, the (4 $-$) titanium vacancy, and the neutral oxygen interstitial have been considered. The defect chemistry of TiO_2 is typically described in terms of either Schottky or Frenkel disorder. Intrinsic disorder of the Schottky type leads to the presence of a lone $\text{V}_{\text{Ti}}^{4-}$ defect and two V_{O}^{2+}

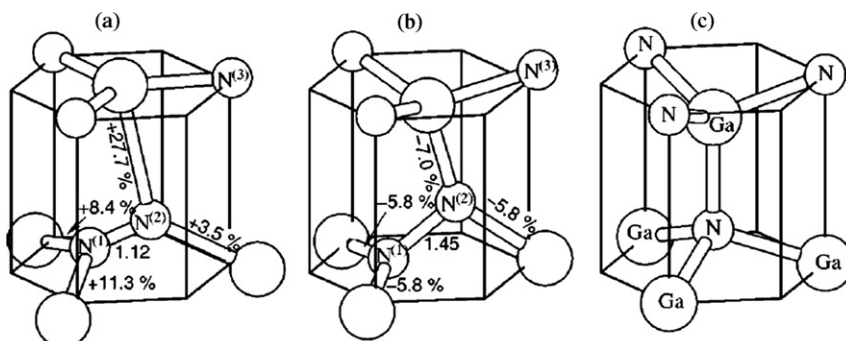


Fig. 15. Ball-and-stick model of atomic configurations of (a) N_i^{3+} and (b) N_i^{1-} defects in GaN in comparison to (c), the undefected GaN crystal lattice. N_i is depicted in a split–interstitial configuration for both charge states.

defects within the crystal. Frenkel type disorder implies the formation of a vacancy and an interstitial of the same atom; in TiO_2 , the Frenkel defect is comprised of Ti_i^{4+} and $\text{V}_{\text{Ti}}^{4-}$.

When it comes to describing the structure and geometry of both anion and cation vacancy defects in TiO_2 , a clear void exists in the literature. Instead, the only commonly available information about the structure of V_{O}^{2+} and $\text{V}_{\text{Ti}}^{4-}$ is related to their tendency to form energetically favorable complexes. As early as 1995, Yu and Halley used a semi-empirical tight-binding method to illustrate the preferential clustering of individual point defects in bulk titania [317]. He et al. have confirmed that when Schottky disorder dominates for rutile TiO_2 , the (2+) oxygen vacancy prefers to form a clustered configuration with the other V_{O}^{2+} and lone $\text{V}_{\text{Ti}}^{4-}$ formed within the unit cell [318]. Due to the positive charge on the defect, it is not surprising that the surrounding Ti cations are displaced outward and the O anions shifted inward toward the vacancy site [319]. Using the modified semi-empirical intermediate neglect of differential overlap (INDO) and first-principles methods, relaxations from 0.1 to 0.3 Å have been calculated, or approximately 5–15% of the bulk Ti–O bond length of 1.95 Å [319,320].

The titanium interstitial, whose charge state of (3+) or (4+) has been the subject of much controversy, is preferentially located at an unoccupied octahedral site adjacent to its original lattice site [317,318,320]. Configurations in which the Ti atom moves in the $\langle 1\ 0\ 0 \rangle$ or $\langle 0\ 1\ 0 \rangle$ direction to form the defect are more favorable than those in which the Ti interstitial moves along the $\langle 0\ 0\ 1 \rangle$ direction [318] (Fig. 16). The presence of the interstitial titanium atoms causes additional distortion of the octahedra within the unit cell. Due to the open structure of the rutile phase along the $\langle 0\ 0\ 1 \rangle$ direction, relatively small relaxations are found around the Ti interstitial compared to the case of the oxygen vacancy. A first-principle study performed by Cho et al. found that the closest Ti atoms relax away from the interstitial site by 13% of the bulk Ti–O bond length, while the nearest four O atoms pull in toward the cation interstitial by 10% [320].

The oxygen interstitial and its associated geometry have not received a great amount of attention in the literature due to its high formation energy at Ti-rich, or reduced, conditions [321]. Although, in principle, the interstitial could contribute to the defect chemistry of TiO_2 at high oxygen partial pressures, it exhibits a strong tendency to bind to lattice oxygen, which causes O_2 dimers to substitute for O lattice sites. Consequently, the presence of O_i is indicated by the neutral substitutional diatomic molecule $(\text{O}_2)_\text{O}$ that forms on the O site [321]. The defect is reminiscent of the split-interstitial that occurs in silicon, although first-principles calculations show that its diatomic bond length, wave functions, and stretch frequencies better resemble those of a free molecule [322]. No significant relaxation of the neighboring atoms is expected, as the charge neutral O_2 is electrostatically equivalent to any O atom on a lattice site and the rutile structure is open enough to accommodate the diatomic molecule.

To touch briefly upon the defect chemistry in anatase versus rutile TiO_2 , a recent paper by Na-Phattalung et al. addresses several features of the defect geometry in anatase that remain unexplored for rutile TiO_2 . The three nearest-neighbor Ti atoms of the oxygen vacancy in anatase experience outward relaxations away from V_{O}^{2+} and towards its five remaining O neighbors [321]. $\text{V}_{\text{Ti}}^{4-}$, a defect that arises in small concentrations, causes the surrounding O atoms to relax outwards substantially to a point halfway between its two remaining Ti neighbors [321]. When Ti_i^{4+} is situated at an octahedral site, one vertical O neighbor moves towards the defect, while the surrounding Ti atoms relax outward as a result of the electrostatic repulsion between positively charged Ti ions. In anatase TiO_2 , the substitutional O_2

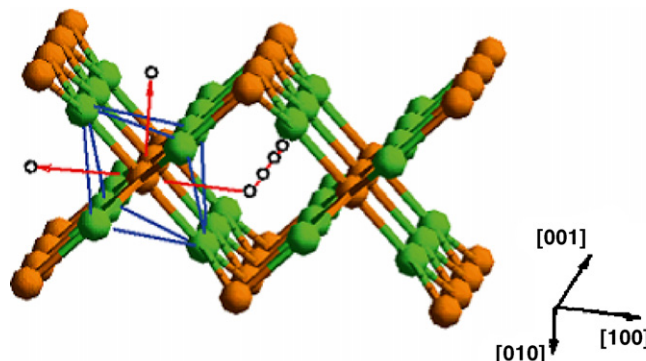


Fig. 16. Possible geometries for octahedral Ti interstitial sites in rutile TiO_2 .

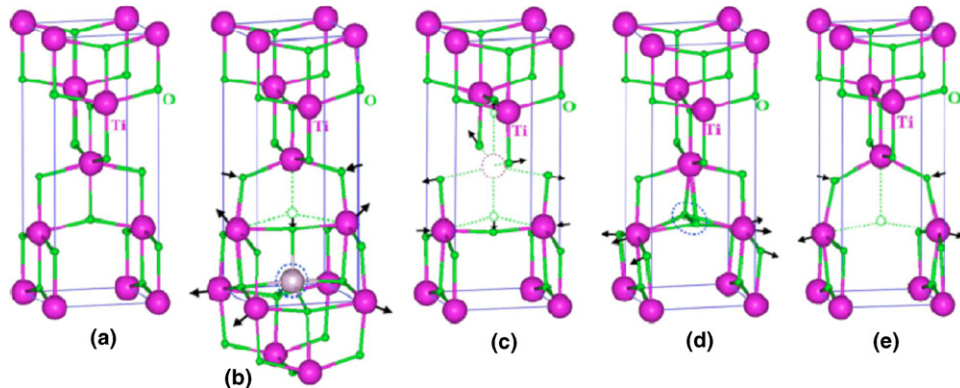


Fig. 17. Atomic structures of (a) bulk anatase TiO_2 ; (b) Ti_i^{+4} ; (c) $\text{V}_{\text{Ti}}^{4-}$; (d) $(\text{O}_2)\text{O}$; (e) V_O^{2+} defects. The large spheres are the Ti atoms and the small spheres are the O atoms. Relaxation directions of neighboring atoms are indicated by the arrows. In some cases, ideal positions of the atoms before relaxation or removal are shown by dashed circles.

molecule induces a small outward relaxation of the neighboring Ti atoms. The defect has a bond length of 1.46 \AA , or about 21% greater than the bond length of free O_2 , 1.21 \AA [321]. The geometries of all of the aforementioned defects in anatase TiO_2 , along with the relaxation directions of neighboring atoms, are depicted in Fig. 17.

5.1.6. Other oxide semiconductors

The structure and geometry of the defects in other oxide semiconductors such as ZnO , UO_2 , and CoO have been explored in a similar fashion to those in groups IV and III–V semiconductors [323–325]. Especially in UO_2 and CoO , a full understanding of defect configuration has yet to be obtained. ZnO , on the other hand, has been characterized with more success; especially recently, its point defects have been explored in more detail than those in TiO_2 .

When an oxygen atom is removed from the wurtzite ZnO lattice, an almost perfect tetrahedron of Zn atoms forms around the vacancy site. The magnitude and direction of the relaxations are highly dependent upon the charge state of the defect. Although both V_O^0 and V_O^{2+} experience large displacements, V_O^0 displays an inward relaxation of the Zn atoms of approximately 11–12%, while V_O^{2+} experiences an outward relaxation of about 19–23% [325,326] due to electrostatic repulsion (Fig. 18). The large relaxation associated with the formation of V_O^{2+} in ZnO substantially reduces the formation energy of the defect with respect to V_O^{1+} , making the oxygen vacancy observed under zinc-rich conditions a negative-U defect [326]. The (1+) vacancy causes the four Zn nearest neighbors to be displaced outwards by only by 2% [326].

In contrast to the relaxations surrounding V_O , Erhart et al. found that those induced by V_{Zn} are almost independent of charge state. The (0), (1–), and (2–) charge states of the zinc vacancy defect exhibit a symmetric 14% outward relaxation of the nearest O neighbors, while relaxations of farther neighbors are negligible [325].

Unlike in TiO_2 , the structures of isolated oxygen interstitials as well as substitutional diatomic oxygen have been examined. Limpijumnong has considered the first of these two species, which is stable only in the neutral charge state; the defect will not exist in any appreciable concentration, as it has a formation energy far higher than that of O_i in both

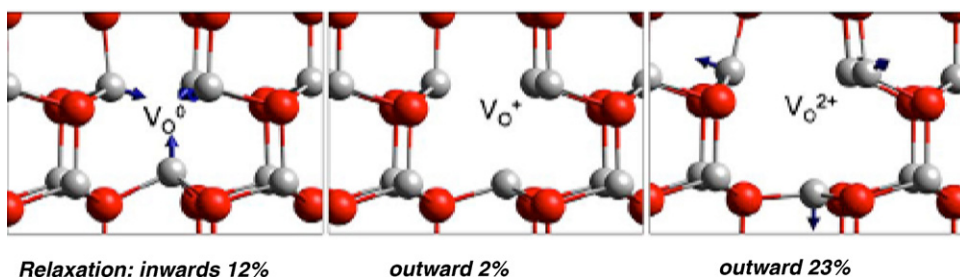


Fig. 18. Ball and stick representation of the local atomic relaxations around the oxygen vacancy in ZnO in the (0), (1+), (2+) charge states.

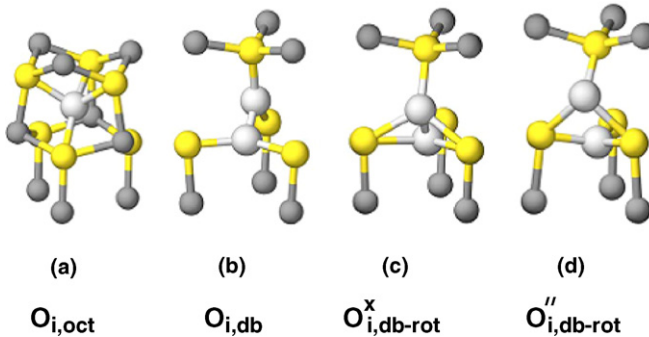


Fig. 19. Overview of possible oxygen interstitial configurations in ZnO. The yellow and dark gray spheres are the zinc and lattice oxygen atoms, respectively. The interstitial oxygen atom(s) are colored in light gray. The (a) octahedral and (b) dumbbell configurations are shown for the neutral charge state. The rotated dumbbell geometry that occurs for (c) the neutral charge state is also shown for (d) the (2+) charge state.

zinc- and oxygen-rich material [322]. In oxygen-rich material with Fermi levels in the lower part of the band gap, however, the neutral dumbbell-shaped oxygen interstitial is the dominant point defect. Before arriving at this conclusion, Erhart et al. considered the relative importance of three O_i geometries, octahedral, dumbbell, and rotated dumbbell, as a function of charge states ranging from (2+) to (2−) [325]. The octahedral defect is stable in the (0), (1−), and (2−) charge states, the dumbbell in the (0) charge state, and the rotated dumbbell in the (0) and (2−) charge states, respectively [325] (Fig. 19). The dumbbell interstitial is characterized by two oxygen atoms that form a homonuclear bond and jointly occupy a regular oxygen lattice site; it is conceptually similar to the well-known dumbbell interstitial defect in silicon and the nitrogen interstitial in GaN [221,312,325]. The rotated dumbbell is related to the non-rotated dumbbell by a rotation of the oxygen bond about the $\langle 1\ 0\ -1\ 0 \rangle$ axis by an angle of 105°; each oxygen atom is bonded to three, rather than four zinc atoms.

5.2. Surface defects

Point defect geometries on semiconductor surfaces have an additional complication not present in the bulk; surfaces often reconstruct to reduce the number of dangling bonds. These reconstructions can differ greatly among the various crystallographic orientations and may have complicated geometries themselves. Defect geometries differ accordingly among the crystal planes, and relatively few generalizations can be made.

5.2.1. Silicon

The Si(1 0 0) surface that is technologically relevant to integrated circuit fabrication exhibits a reconstruction with (2×1) periodicity, creating rows of surface atoms bonded to each other as dimers. The dimers buckle slightly from a perfectly symmetric configuration, although they typically oscillate back and forth between the two mirror-image buckled configurations. If a single-atom vacancy forms, the atom that was previously dimerized with the missing atom tends to leave the dimer row fairly rapidly, transforming the missing-atom vacancy into a missing-dimer vacancy. Such divacancies (or “dimer vacancies”) dominate on the Si(1 0 0)-(2 × 1) reconstruction near and below room temperature [327–334]. These defects stabilize the oscillatory dimer buckling of the silicon surface by pinning the dimers into one or the other asymmetric buckling orientation [335]. By STM imaging the Si(1 0 0) surface, Hamers et al. observed the single dimer vacancy as well as two other types of defects, a double dimer vacancy (“B”) and a defect that appears as two half-dimers [329]. The latter defect, the so-called “type C” vacancy, is best described as two adjacent Si atoms missing along a $\langle 1\ -1\ 0 \rangle$ direction. In contrast, the dimer vacancy involves the removal of two Si atoms along a $\langle 1\ 1\ 0 \rangle$ symmetry, and has mirror symmetry with respect to reflection in both $\langle 1\ 1\ 0 \rangle$ and $\langle 1\ -1\ 0 \rangle$ planes. Several DFT calculations have considered the dimer vacancy in detail [28,333,334,336], although only Chan et al. considered charging effects.

The divacancy induces the adjacent pairs of atoms in the underlying layer to relax toward and rebond to each other along the row to partially fill the void, as shown in Fig. 20. Although the distances between these pairs are identical in the undefected structure, upon divacancy formation the extent of rebonding differs. The distance under the lower atom of the original dimer contracts nearly 0.5 Å more than the corresponding distance under the upper atom. The degree of

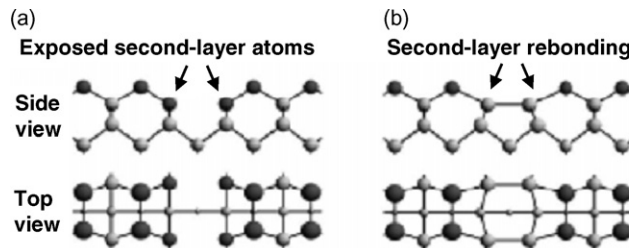


Fig. 20. Ball and stick models of single dimer vacancy defects on Si(1 0 0) including the (a) nonbonded and (b) rebonded geometries. Silicon atoms that have a dangling bond are shaded black.

relaxation of the neighboring atoms does not change significantly with charge state—less than about 0.1 Å [28]. This change is smaller than comparable charge-induced changes for the bulk divacancy, which exceed 0.5 Å.

Regarding adatoms (or “surface interstitials”), Ihara et al. initially suggested a model involving *interstitial* dimers recessed into the Si(0 0 1) surface [337]. Three years later, however, Wang et al. readdressed this hypothesis to show that the interstitial dimer leads to a density of states at odds with experimental observations; in contrast to the bulk, the self-interstitial is not a dominant defect on the Si(1 0 0) surface [334].

The Si(1 1 1) plane is the natural cleavage plane of Si, and it reconstructs below roughly 1000 K into a complicated (7×7) structure shown in Fig. 21. The dominant defect is the monovacancy. Four vacancy locations on the (1 1 1) surface have been explored in the literature: the unfaulted corner (UFC), unfaulted edge (UFE), faulted corner (FC), and faulted edge (FE) [60,255]. The different vacancy types, which are shown in Fig. 21, arise from the unusual adatom surface arrangement, where the local geometry of Si(1 1 1)-(7 × 7) is described by unfaulted and faulted triangular units of six adatoms. However, the effects of charging on these various vacancy locations are likely to be similar [60]. In fact, the UFE vacancy can have dominant charge states of (2−), (1−), and (0), but structural rearrangements due to charging are negligible [60].

Above roughly 1000 K, Si(1 1 1) exists in a “1 × 1” phase that does not have the simple bulk-terminated structure. Experiments employing second harmonic generation (SHG) [338], scanning tunneling microscopy (STM) [339], and reflection high-energy electron diffraction (RHEED) [340,341] have deduced that the “1 × 1” surface has a relaxed bulk-like structure with adatom coverage of about 0.25 monolayers (ML). At the temperatures where the “1 × 1” is observed, the adatoms move quickly and therefore do not reside in single sites for very long. However, a useful static model of this dynamic surface is one in which adatoms are placed in a (2 × 2) periodicity, thereby reproducing the 0.25 ML coverage as shown in Fig. 22 [236]. Quantum calculations by Meade and Vanderbilt [342] have indicated that this configuration is second only to the (7 × 7) in stability at room temperature. The vacancies can have dominant charge states of (1−), (0) or (1+) [236], and as with the (7 × 7) reconstruction, structural relaxation effects due to vacancy charging are negligible.

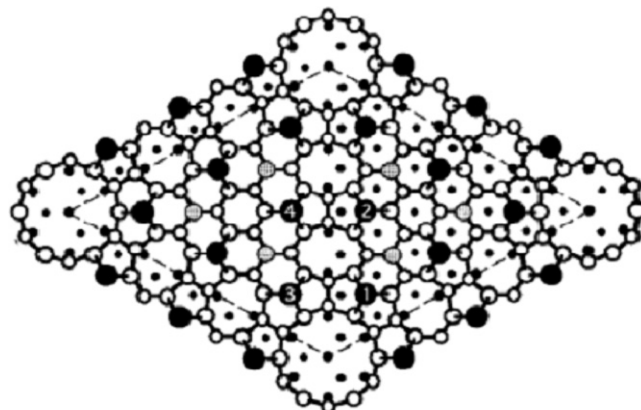


Fig. 21. Top view of the Si(1 1 1)-(7 × 7) reconstruction. The four nonequivalent types of adatoms are labeled (1) unfaulted corner; (2) unfaulted edge; (3) faulted corner; (4) faulted edge.

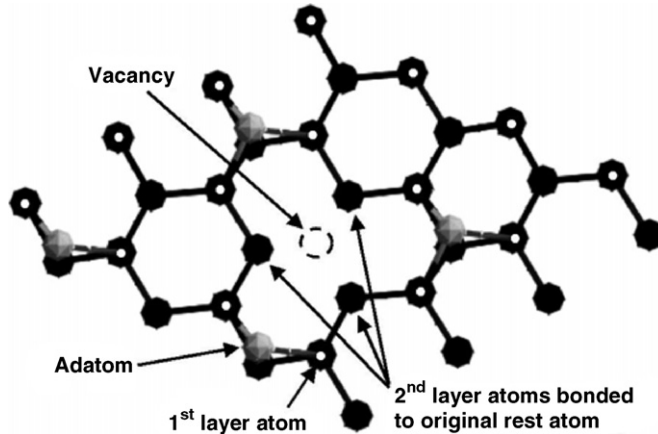


Fig. 22. Diagram of the Si(1 1 1) – “1 × 1” slab including a vacancy before relaxation. Only the first two surface layers and the adatom layer are shown for clarity.

5.2.2. Germanium

The types of charged vacancies on germanium are roughly similar to those observed on silicon, although their formation is far less favorable [343,344]. In this case, the evidence is exclusively experimental. For example, although Ciobanu et al. recently performed empirical-potential calculations to compare the dimer vacancy defects on Ge(0 0 1) to those on Si(0 0 1), they only considered neutral defects [345]. When Ge divides along its natural (1 1 1) cleavage plane, single atom vacancies, as well as defects due to antiphase shift, are the dominant point defects [178,346]. On the other hand, dimer vacancy defects are far more likely to arise on the Ge(1 0 0) face. The antiphase shift vacancy discussed by Lee et al. is a point defect generated by a shift of an adatom row by a half period in the row direction; it perturbs the $c(2 \times 8)$ reconstruction and causes a line stacking fault, or antiphase domain boundary [178]. The asymmetric dimer reconstruction adopted by Ge(0 0 1) at room temperature does not require the formation of stabilizing vacancy-type defects, but dimer-vacancy defects are still often seen on the surface with STM [347,348]. STM images obtained by Yang et al. reveal a majority of negatively charged dimer vacancy defects, as well as complexes consisting of a single missing dimer, a twin missing dimer, and a shared or “split-off dimer,” on Ge(0 0 1) [348].

5.2.3. Gallium arsenide

Vacancies on GaAs have been studied in considerable detail by both experimental and computational means. GaAs(1 1 0) is decorated with charged arsenic vacancies under gallium-rich gas-phase conditions, and with charged gallium vacancies and adatoms under arsenic-rich conditions [174]. The configurations of the gallium vacancies on GaAs(1 1 0) have not been explored in depth, however, although it is suggested based on DFT calculations employing the LDA that the defect is stable in the (1+), (0), and (1-) charge states and is characterized by a comparatively large relaxation (0.5 Å) of the surface nearest-neighbor atoms into the surface [197]. In contrast, V_{As} exhibits negative-U behavior with only a (1+/1-) ionization level within the band gap. This vacancy also induces similarly large nearest-neighbor relaxations (0.3 Å), however [197].

Arsenic vacancies on the GaAs surface behave differently from those in the bulk of the semiconductor; the charge state of the surface species can vary from (1+) to (1-), and their geometry depends strongly on the Fermi energy [241,349]. When relaxed, the GaAs(1 1 0) surface maintains its (1 × 1) periodicity, but the electrons in the Ga dangling bonds transfer to the As, leading to the formation of five-fold-coordinated As and three-fold-coordinated Ga atoms. Kim and Chelikowsky have suggested that the three non-rebonded Ga atoms around V_{As}^{1+} relax symmetrically inward with respect to the (1 1 0) plane [237,350] (Fig. 23). Zhang and Zunger found, however, that a nonsymmetric rebonded structure reduces the total energy by an additional 0.16 eV for V_{As}^{1+} [241] (Fig. 24). The same nonsymmetric, rebonded configuration was found to be 0.17 eV more stable by Schwarz et al. [197]. Neither of these static equilibrium vacancy configurations exactly match experimental STM observations, and it is suggested that, at room temperature, the vacancy rapidly flips between the two energetically favorable configurations with an associated

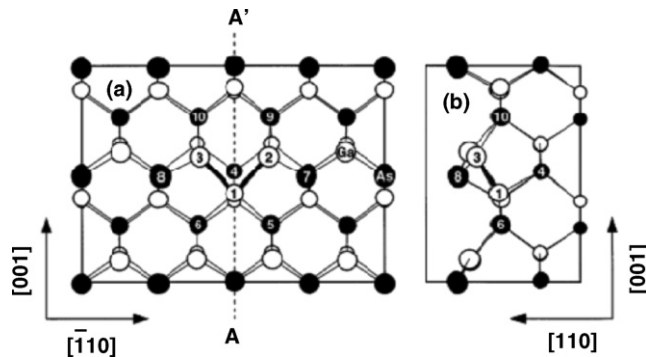


Fig. 23. The relaxed geometry of the singly positive As vacancy on the GaAs(1 1 0) surface including (a) top view and (b) cross-sectional view of the top four layers. The solid and open circles denote the As and Ga ions, respectively. The nearest and the next nearest neighbors to the vacancy site are indexed from 1 to 10.

energy barrier of ~ 0.08 eV [174,181]. In the neutral and $(1-)$ charge states, DFT investigations indicate that a *symmetric* rebonded configuration is always preferred [238,241,242].

In contrast to bulk gallium arsenide, in which charged As_{Ga} and Ga_{As} defects are well characterized, antisite defects on the GaAs surface have received considerably less attention [197,351]. It is suggested, however, that they are most stable in the neutral charge state and have no ionization levels within the band gap, in contrast to those in the bulk,

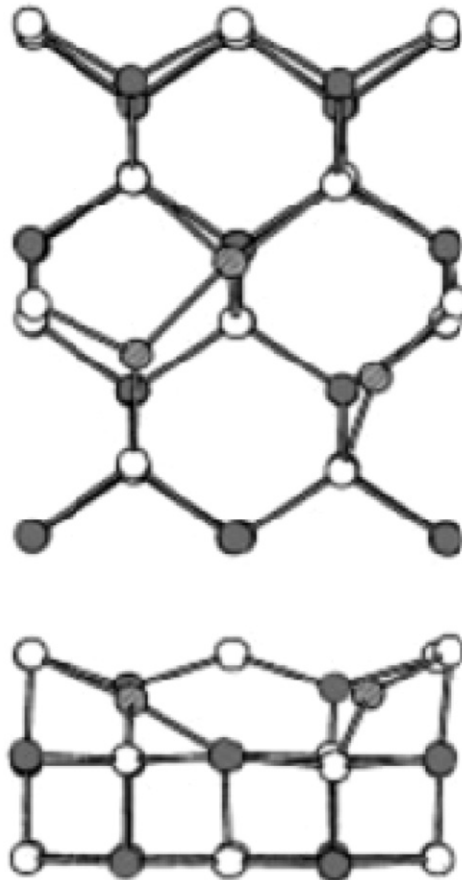


Fig. 24. Top and side view of the relaxed GaAs(1 1 0) surface with $\text{V}_{\text{As}}^{1+}$ in the rebonded configuration. Open and shaded circles denote As and Ga atoms, respectively.

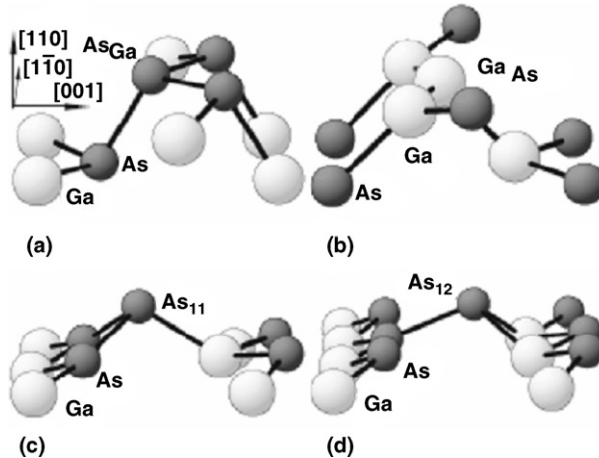


Fig. 25. Atomic relaxations of surface point defects on GaAs(110) including antisites (a and b) and adatoms (c and d).

which are known to have a charge of (2−) (Ga_{As}) or (2+) (As_{Ga}) [197]. There are two possible configurations for the anion adatom: one in which the adatom is bonded to the surface anions (As₁¹⁺, As₁⁰, As₁^{1−}), and one in which it is bonded to the surface cations (As₂⁰ and As₂^{1−}). The former is located 1.1 Å above the surface, while the latter is at 0.8 Å above the surface [197]. The suggested geometries of both the antisite and adatom defects on GaAs(110) are depicted in Fig. 25.

5.2.4. Other III–V semiconductors

Published work for the indium-containing semiconductors InP, InAs, and InSb focuses exclusively on vacancies. Much of the discussion related to the geometry of the charged vacancy on InP, InAs, and InSb centers around the existence (or lack) of symmetry around the defect site. Similar to GaAs, the stable atomic structure depends critically on the vacancy charge state [349,352]. For InP and InAs, the surface anion vacancy is stable in the (1+), (0), and (1−) charge states; for InSb, on the other hand, the (1−) charge state is stable for all Fermi energies within the band gap [239]. For V_P, V_{As}, or V_{Sb}, the general trend is for the surrounding In atoms to relax inward. In analogy to the symmetry associated with V_{As} on GaAs(110), the positively charged anion vacancy has a nonsymmetric configuration with one rebonded dimer, while both the neutral and (1−) charged vacancies show a symmetric configuration with one loosely rebonded trimer [197,238–242].

These classifications were initially considered to be at odds with early STM investigations, V_P¹⁺ on p-type InP(110) was observed to have a symmetric image, whereas V_P^{1−} on n-type InP(110) and V_S^{1−} on n-type InSb(110) had asymmetric geometries [239,240,349,353,354]. But the STM observations can be explained in terms of thermal flipping between two degenerate defects configurations [240] (Fig. 26). For the (1+) charge state, thermal flipping prompts the reaction path to pass through a saddle point with a symmetric configuration. For the (1−) charge state, the anion vacancy actually has two local minima, one corresponding to a symmetric geometry and the other to a nonsymmetric geometry, although the former has a lower energy [239].

Qian et al. also looked at the relaxations associated with the stable anion surface vacancies [239]. In the nonsymmetric configuration adopted by V_A¹⁺, one of the surface In ions forms a dimer with the subsurface In ion. The three nearest-neighbor In atoms relax substantially inwards by different amounts. On InAs, the surface indium ion, the subsurface indium ion with which it dimerizes, and the surface indium ion that becomes two-fold coordinated relax by 11.2, 20.9, and 41.9% of the bulk bond length, respectively. Around the symmetric V_A⁰ and V_A^{1−} sites with rebonded trimer, the two surface In atoms neighboring the defect move inward, while the subsurface In atom shifts toward the vacancy. For V_A⁰, relaxations on the order of 15.9–27.1% of the bulk bond length now take place, with the relaxation of the surface atom typically being slightly larger than that of the subsurface atom, i.e. 21.1% versus 17.8% in InAs. In going from the (0) to (1−) charge state, the surface indium atoms relax further towards the vacancy site along both the [001] and [110] directions. For example, the surface and subsurface atoms in InAs experience net displacements of 25.2 and 22.1%, respectively.

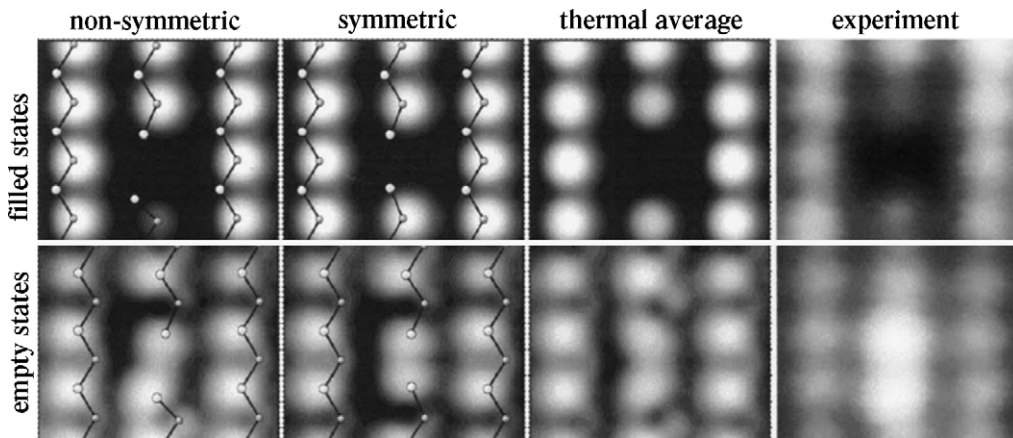


Fig. 26. Simulated STM images above the surface of a (1+) charged P vacancy on InP(1 1 0) surface for different atomic configurations. The simulation shows images for the nonsymmetric and symmetric rebonded configurations, as well as a time average of the two.

The relaxations of the (1 1 0) surface of zinc-blende III–V semiconductors containing nitrogen differ greatly from those of GaAs [355–359]. For GaAs both the anion and cation are displaced along the z -axis, but for GaN, only the surface cation experiences large shifts [356]. The main relaxation consists of a contraction of the GaN bond in the surface layer and a slight buckling rehybridization with N atoms tending to adopt p^3 coordination and Ga atoms adopting an sp^2 configuration [360]. The rotation angles (θ) associated with atomic relaxation in InN, GaN, and AlN are nearly half those for GaAs, while the bond contractions (C_B) for the same compounds are appreciable, in contrast to those in GaAs [356–358,361]. Filippetti et al. predicted that materials with small cohesive energies and ionicities will tend to have large rotations, whereas very ionic and strongly bound solids will tend towards small rotations. Rotation angles of between 11.7° and 21.7° are calculated for the nitride semiconductors, in contrast to the approximately 30° found for GaAs [356,357,362,363]. The bond contractions in AlN, InN, and GaN, which are about five times larger than those in GaAs, correlate well with cation size: $C_{B,\text{InN}} > C_{B,\text{GaN}} > C_{B,\text{AlN}}$ [355,356,362,364]. Using Hartree–Fock *ab initio* calculations, Jaffe et al. found that the relatively large surface bond contractions in the nitrides correlate with hybridization effects of cation d states with anion-derived valence states [355].

5.2.5. Titanium dioxide

The two-fold coordinated oxygen atoms on the $\text{TiO}_2(1\ 1\ 0)-(1\times 1)$ surface are extremely susceptible to removal during thermal annealing. As suggested by Henrich and Kurtz [365], this process generates a defect in the row of bridging O atoms on the crystal surface [83,365,366]. Oxygen atoms in the same plane as the Ti atoms on $\text{TiO}_2(1\ 1\ 0)$ can also be removed from the surface, leading to the formation of in-plane oxygen vacancies (POV) rather than bridging oxygen vacancies (BOV) [367]. For both the BOV and the POV, the coordination of the cations adjacent to the O vacancy is reduced, as is the screening between the cations [368].

For all BOV charge states, BOV^0 , BOV^{1+} , and BOV^{2+} , there is a slight ($\sim 0.01\ \text{\AA}$) outward relaxation of the bond between the five-fold-coordinated titanium atom and the in-plane oxygen atom. The Ti-bridging oxygen bond changes from $2.023\ \text{\AA}$ for the undefected surface to 1.990 , 1.991 , and $1.968\ \text{\AA}$ in the presence of BOV^0 , BOV^{1+} , and BOV^{2+} [246]. The Ti-Ti distance across the vacancy increases from 2.959 to $3.305\ \text{\AA}$ after the BOV formation; it is lowered to 3.200 and $3.239\ \text{\AA}$ when the vacancy gains a (1+) or (2+) charge, respectively. The $0.14\ \text{\AA}$ expansion of the six-fold-coordinated Ti atoms away from BOV^{2+} can be compared to the 0.28 – $0.30\ \text{\AA}$ outward displacement of titanium atoms from VO^{2+} in bulk TiO_2 [246,320]. The changes in bond lengths associated with the formation of an in-plane oxygen vacancy on the $\text{TiO}_2(1\ 1\ 0)$ surface, POV^0 , POV^{1+} , and POV^{2+} , as well as those of the BOV, are illustrated in Fig. 27.

5.2.6. Other oxide semiconductors

Oxygen vacancies are the predominant surface defects on other oxide semiconductors such as ZnO , UO_2 , and CoO . For example, several oxygen-derived surface defects on $\text{ZnO}(1\ 0\ 1\ 0)$ have been considered: an oxygen vacancy within the surface Zn–O dimer, an oxygen vacancy in the second layer of the material, and a whole dimer vacancy [369,370]. The formation energy of the latter is lowest when linear vacancies form in the [0 0 1] direction [370]. On

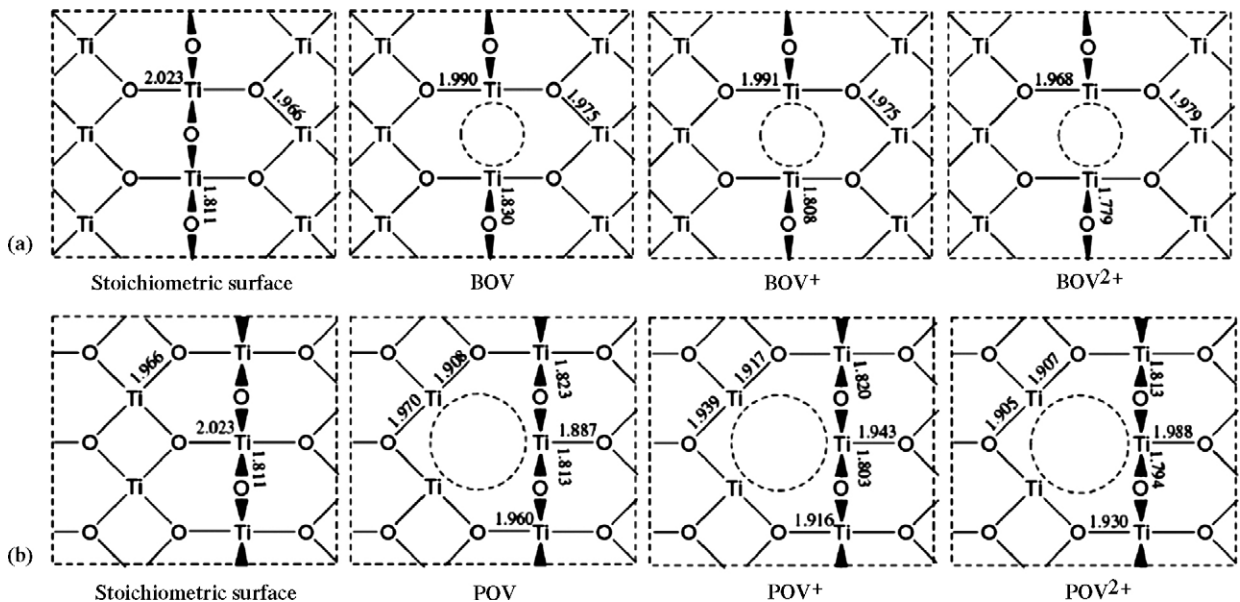


Fig. 27. Top view of the perfect: (a) bridging-oxygen and (b) in-plane-oxygen defect sites on the rutile $\text{TiO}_2(1\ 1\ 0)$ two-layer model surfaces.

ionic cobaltous oxide, it has been shown that 500 eV Ar^+ -ion bombardment leads to a removal of about 4% of the monolayer of surface oxygen ions [371,372]. For the unrelaxed vacancy defect on the surface, the shielding between cations adjacent to the defect is greatly reduced compared to the stoichiometric surface [372]. The existence of charged cation vacancies on zinc oxide is mentioned briefly in the literature. For example, the compensation of ionic excess charge on polar $\text{ZnO}(1\ 0\ 0\ 0)$ may occur, in part, through the formation of doubly positively charged zinc vacancies at the Zn-terminated surface [373]. Dulab et al. have found that the removal of Zn atoms happens through the formation of triangular shaped reconstructions [373,374].

6. Energetics and ionization levels of charged defects

6.1. Bulk defects

6.1.1. Silicon

Silicon has a band gap of about 1.1 eV at 300 K. Most experimental determinations of defect ionization levels in silicon have come from deep-level transient spectroscopy, electron paramagnetic resonance, and diffusion measurements. Numerous calculations of ionization levels have also been published, although many conflict with each other and experimentally obtained values. Some of the deviation may be due to the fact that DFT numbers are all at 0 K, whereas transient enhanced diffusion measurements, for example, are carried out above 1200 K. Acceptor levels, which track the temperature variation of the conduction band minimum, move from their 0 K positions by more than 0.4 eV at 1200 K. As a ground-state theory, DFT has other inherent shortcomings, namely the need to incorporate boundary conditions due to the use of the supercell approximation and the band gap problem, where Kohn–Sham eigenvalues significantly underestimate the fundamental band gap. These issues lead to problems even when considering neutral point defects in semiconductors. Understandably, when density-functional theory is employed to consider charged defects, additional difficulties arise. Few authors address these issues, let alone make move to compensate for them. One exception to this rule is Schultz, who recently presented a novel modification to DFT that enforces electrostatic boundary conditions that account for net charge effects, eliminates the need for *ad hoc* procedures to calibrate the electron chemical potential for each charged defect calculation, and handles defect dispersion with a new occupation scheme for populating states [53]. Using this modification to the supercell method, Schultz obtains ionization levels for an assortment of silicon defects, some of which will be discussed momentarily, that span the experimental band gap, i.e. exhibit no band gap problem. More importantly, however, he draws attention to the fact that DFT must be coupled with modifications in order to replicate experimentally observed charged defect

levels, a concept that is still taking off in the silicon defect engineering community, let alone the Ge, III–V, and oxide semiconductor communities.

The stability of the Si vacancy in the (2+), (1+), (0), (1−), (2−), and (4−) charge states has been considered. The existence of negative-U behavior for the donor states, i.e. the instability of V_{Si}^{1+} , has long been debated; it has been observed experimentally yet has been both confirmed and denied in computational works. While some have claimed that the (1−/2−) ionization level is resonant in the conduction band, others have posited the stability of V_{Si}^{2-} , and even V_{Si}^{4-} for Fermi energies within the band gap. One can at least be fairly certain that V_{Si}^0 is stable for most Fermi energies in the middle third of the band gap. The formation of the donor and acceptor vacancies in silicon is described by



and



Or, if negative-U behavior of the vacancy is to be believed:



The vacancy donor levels are still not fully established in bulk silicon. EPR investigations performed by Watkins and co-workers in the 1960s led to the first identification of vacancy ionization levels [102,104,375,376]. These authors proposed that the vacancy could exist in a doubly negative charge state and, along with Newton et al., established a level at $E_v + 0.13$ eV for V^{2+} and $E_v + 0.05$ for V^{1+} [270,377]. Watkins et al. found experimental evidence in support of the negative-U behavior for V_{Si} , as predicted by Baraff, Kane, and Schluter, where upon capture of the first hole, the energy barrier of the vacancy for capturing a second hole is lowered instead of raised [269,270,378,379]. This means that, for all values of the Fermi energy, V^{1+} is unstable in comparison to either V^0 or V^{2+} . Emtsev et al. performed Hall-effect measurements on gamma-irradiated samples to obtain first and second donor ionization levels of 0.028 and 0.128 eV above the valence band maximum [380]. Comparable ionization levels have been found from an assortment of theoretical methods. In early Green's-function total energy calculations, Car et al. found V_{Si}^{2+} to be stable below $E_v + 0.12$ eV, with a switch to V_{Si}^0 for $0.12 < E_F < 1.06$ eV [213]. 216- and 256-atomic-site supercell calculations locate the $\epsilon(2+/0)$ at $E_v + 0.15$ eV [194] and $E_v + 0.1$ eV [271], respectively. Mueller et al. also observed negative-U behavior for the defect using a 216-atom supercell and a plane-wave-basis set with a kinetic-energy cutoff of 12 Ry; the corrected (2+/1+) and (1+/0) ionization levels are at 0.30 and 0.08 eV above the valence band maximum, respectively [381]. On a plot of defect formation energy versus electron chemical potential, the suggested negative-U behavior manifests as a direct transition between the (2+) and (0) charge states of the defect, as shown in Fig. 28.

In contrast, the more recent LDA calculations of Centoni et al. and Schultz, both of which use similar supercell sizes and k -point sampling, have failed to reproduce the observed negative-U behavior in the positive charge states of the vacancy; the difference between the (0/1+) and (1+/2+) ionization levels is only ~ 0.1 eV, however. Centoni et al. obtained only a single donor level $\epsilon(1+/0)$ at $E_v + 0.09$ eV, while Schultz, who used a novel modification method in his computation, placed $\epsilon(1+/0)$ and $\epsilon(2+/1+)$ at 0.19 and 0.07 eV, respectively [27,53].

Even in comparison to silicon vacancy donor levels, the acceptor ionization levels for the defect are poorly understood. Troxell and Watkins concluded that the acceptor ionization levels for (0/1−) and (1−/2−) had to be more than 0.17 eV below the conduction band based on DLTS investigations [382], meaning below $\sim E_v + 0.9$ eV at 300 K. In contrast, Car's Green's function calculations, revealed V_{Si}^{1-} to be stable for all Fermi energies above $\sim E_v + 1.06$ eV to the conduction band minimum, i.e. the defect has no (1−/2−) level within the band gap [213]. Subsequent DLTS experiments indicated that the levels (0/1−) and (1−/2−) were located around the midgap and in the upper part of the gap, respectively [103]. A single ionization level $\epsilon(0/1-)$ was also proposed to lie below the middle of the band gap by Mäkinen et al., who carried out positron-annihilation studies of electron irradiated Si samples [383]. Several authors have proposed the existence of a second negative-U system for V^0 , V^{1-} , and V^{2-} , a

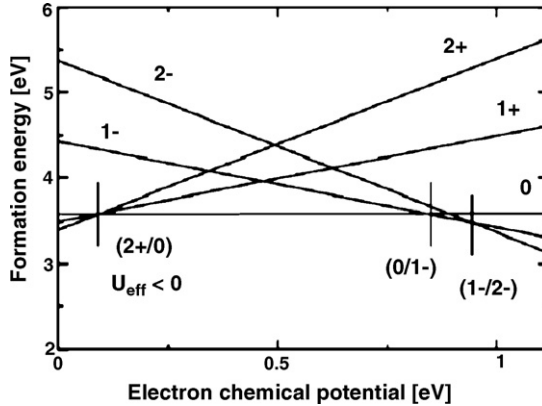


Fig. 28. Formation energy of the Si vacancy in charge states from (2+) to (2-) as a function of the electron chemical potential. The positions of the ionization levels are shown as vertical full lines. Negative-U behavior exists near a chemical potential of 0.15 eV involving a direct transition between the neutral and (2+) states.

feature that has not been clearly observed experimentally [194,384]. Γ -point 64-atomic-site and 216-atomic-site supercell calculations respectively yield effective negative-U levels (0/2-) at 0.65 and 0.49 eV above the valence band maximum [194]. Boyarkina et al. interpreted experimental results to suggest the existence of single and double acceptor levels respectively at $E_c - 0.09$ eV and $E_c - 0.39$ eV (meaning $\sim E_v + 1.0$ eV and $E_v + 0.7$ eV at 300 K) [384]. 256-atomic supercell local density approximation computations locate $\epsilon(0/1-)$ at $E_v + 0.85$ eV, with a subsequent switch to V_{Si}^{2-} for Fermi energies above 0.93 eV [271]. Using the plane-wave pseudopotential code VASP with a supercell of 216 atoms, Mueller et al. have calculated corrected values for the single and double acceptor ionization levels at $E_v + 0.66$ eV and $E_v + 0.77$ eV [381]. More surprisingly, these authors have suggested a second negative-U phenomenon for the hitherto unconsidered (3-) and (4-) charge states of the lattice vacancy defect. Instead of considering the split vacancy V_B , which has a highest attainable charge of (2-), they consider the lattice vacancy defect V , which can adopt all charge states up to (4-). For a Fermi energy very close to the conduction band minimum, however, the (4-) charged substitutional vacancy is thermodynamically stable, whereas V^{3-} is not. The uncorrected and corrected estimates of the (2-/4-) ionization level are $E_v + 0.66$ eV and $E_v + 0.87$ eV, respectively [381]. Centoni et al. recently published first-principles calculations that explore the ionization levels associated with both the lattice and split vacancy configurations. V^0 and V^{1-} are stable for Fermi energies from ~ 0.1 to 0.65 eV and 0.65 to 0.74 eV, respectively, with a switch to V_B^{2-} for Fermi energies from $E_v + 0.74$ eV to the conduction band minimum [27]. Fig. 29 illustrates how the split vacancy is proposed to have a lower formation energy than the lattice vacancy in n-type material, although it should be noted that these authors do *not* find negative-U behavior for the donor states of the defect. Schultz, using a novel method modification, determined single and double lattice vacancy acceptor levels at $E_c - 0.27$ eV and $E_c - 0.39$ eV (meaning $\sim E_v + 0.83$ eV and $E_v + 0.7$ eV at 300 K) that agree roughly with those determined experimentally [53]. Table 7 summarizes the experimentally and theoretically determined silicon vacancy ionization levels [27,53,115,193,194,213,270,377,380–383,385–401] (Table 7).

Silicon self-interstitials become ionized according to



Unfortunately, the self-interstitial defect has never been experimentally observed by a direct method; its charge states and ionization levels have been inferred from thermally-stimulated capacitance measurements and irradiation studies. Hence, most information regarding ionization levels comes from DFT calculations or indirect experimental determinations. There is considerable debate over the best method to use because the combination of strong and weak bonds in many interstitial configurations poses significant challenges for electronic structure calculations. Consequently, the charge states for Si interstitials in p-type and n-type silicon are still not clearly established. The

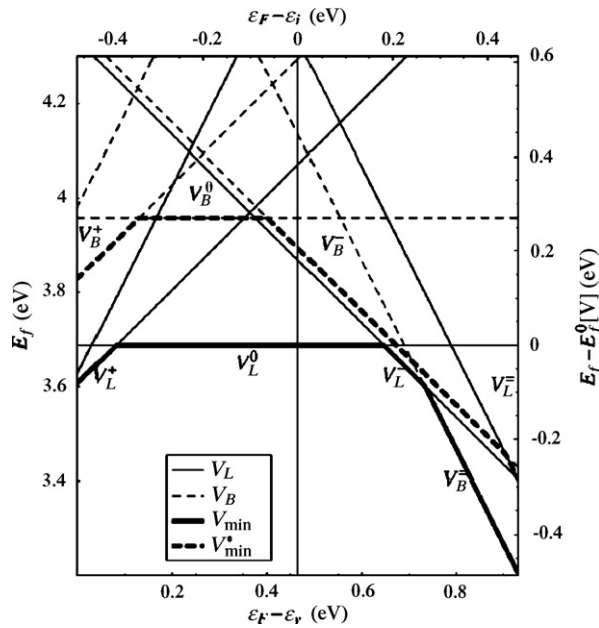


Fig. 29. Formation enthalpies of vacancies in Si vs. Fermi level. The heavy solid line indicates the lowest formation enthalpy at a given Fermi level. Both the lattice vacancy and the split vacancy are shown. The latter is more energetically stable only for the (2-) charge state.

possible candidates [4,27,30,261,282,402–405] include Si_i^{2+} , Si_i^0 , Si_i^{1-} , and Si_i^{2-} [30]. Controversy has arisen, in part, due to the strong dependence of the defect formation energies on local geometric structure. Also, different calculation methods yield highly variable formation energies; the generalized gradient approximation is known to yield higher values than the local density approximation [406–408]. Recent evidence based on diffusion experiments suggests that tetrahedral Si_i^{2+} dominates in p-type silicon, with a switch to neutral Si_i in a $\langle 1\ 1\ 0 \rangle$ -split configuration for weakly n-type material; a $\varepsilon(2+/0)$ ionization level of $E_v + 0.54$ eV, an arithmetic average from multiple investigators, was associated with this ionization level [4]. The formation energies and ionization levels associated with the negative charge states of the self-interstitial in strongly n-doped Si are still poorly characterized.

Electron, alpha particle, and proton irradiation have been used to experimentally study the ionization levels of self-interstitials in silicon. Abdullin et al. assigned (2+/1+) and (1+/0) Si_i ionization levels at $E_c - 0.39$ eV and $E_c - 0.26$ eV (meaning $\sim E_v + 0.7$ eV and $E_v + 0.84$ eV at 300 K), respectively, based on the annealing properties of two traps observed with DLTS [409]. Later, these authors reversed the ordering of the defect ionization levels to suggest negative-U behavior [410]. Subsequent thermally stimulated capacitance measurements performed by Abdullin and Mukashev confirmed a level at $E_c - 0.36$ eV ($E_v + 0.74$ eV) associated with a positively charged defect, presumably the unstable Si_i^+ [411]. In 1996, a center in the EPR spectra of irradiated silicon with T_d point symmetry, the so-called AA12 center, was associated with the same singly positive charge state by Mukashev et al. and Abdullin et al. [412,413]. Based on the analysis of the secondary processes of radiation-induced defect formation in Si crystals, Lukjanitsa recently placed the (2+/0) and (0/1-) ionization levels at $E_v + 0.43$ eV and $E_v + 0.66$ eV, respectively. According to these authors, the singly positive silicon self-interstitial, a negative-U defect with a correlation energy of -0.19 eV, has a (2+/1+) level at $E_v + 0.24$ eV [414].

Computational results from Lee et al., Harrison, and Zhu based on DFT suggest that the ionization levels differ considerably for the three different site configurations available to Si_i [27,30,404,405]. The existence of Si_i^{1+} was first suggested based on transient enhanced diffusion profiles for implanted B in Si [415]. Although Fair originally rationalized these TED profiles in terms of Si_i^{1+} and Si_i^0 , subsequent computational work by DFT and related methods suggest that Si_i^{1+} is destabilized by negative-U behavior at 0 K [4,27,30,213,404,405]. Lee et al. reported that the lowest energy state is Si_i^{2+} in the tetrahedral configuration below $E_v + 0.73$ eV, with a direct switch to Si_i^{1-} in the $[1\ 1\ 0]$ -split configuration at higher Fermi energies. Hakala et al. found the same configurations favorable, but with a charge state switch from Si_i^{2+} to Si_i^0 at $E_v + 0.62$ eV (this value was calculated from the data in their Table 2) [402]. These levels are in relatively good agreement with those obtained by Abdullin and co-workers and Lukjanitsa,

Table 7

Experimentally and computationally determined ionization levels for the vacancy defect in bulk silicon

V_{Si}	Method						Reference
	(2+/1+)	(1+/0)	(2+/0)	(0/1-)	(1-/2-)	(0/2-)	
–	–	–	–	0.2	–	–	Defect formation during gamma irradiation [385]
–	–	–	–	0.78	–	–	Tracer diffusion extrinsic conditions [386]
–	0.44	–	–	0.73	–	–	Carrier removal after electron irradiation [387]
–	0.37	–	–	0.55	1	–	Unspecified [388]
–	0.11	–	–	–	1.03	–	Kinetics after electron irradiation measured by DLTS [389]
–	0.12	–	–	–	–	–	Kinetics after electron irradiation measured by junction capacitance [390]
–	0.35	–	–	0.68	1.01	–	Unspecified [391]
–	–	–	–	≤ 0.95	≤ 0.95	–	DLTS [382]
–	0.14	–	–	–	1.03	–	Kinetics after electron irradiation measured by DLTS [392]
0.13	0.05	–	–	–	–	–	EPR [270]
0.112	0.0567	0.084 ± 0.004	–	–	–	–	Hall effect [393]
0.13	0.05	Yes	–	–	–	–	DLTS [377]
0.128	0.028	0.078 ± 0.002	–	–	–	–	Hall effect [380,394]
–	–	–	–	0.19	0.88	–	Defect introduction by electron irradiation [395]
–	–	–	–	0.39	0.85	–	Unspecified [396]
–	–	0.078	–	0.2–0.5	0.88	–	Defect formation during gamma irradiation [397]
–	–	–	–	0.58–0.65	–	–	Formation of radiation defect [398]
–	–	–	–	0.13–0.56	–	–	PAS [383]
–	–	–	–	1.03	0.73	–	Annealing of Si-E centers [399]
–	–	0.13	–	–	–	–	EPR [115]
–	–	0.118	–	–	–	–	DLTS [400]
–	–	0.15	–	–	0.49	DFT	[194]
–	–	0.12	1.06	–	–	–	Green's function calculations [213]
0.45	0.55	–	0.66	0.92	–	–	Green's function calculations [401]
–	–	0.1	0.85	0.93	–	DFT-LDA	[193]
0.3	0.08	–	0.66	0.77	–	DFT-GGA	[381]
–	0.09	–	0.65	0.74	–	DFT-GGA	[27]
0.07	0.19	–	0.85	0.73	–	DFT-LDA	[53]

All values are in eV and referenced to the valence band maximum.

although the corresponding value from Zhu's DFT calculations is $E_v + 0.45$ eV [405]. Lee et al. [30] reported a further switch to Si_i^{2-} in the $[1\ 1\ 0]$ -split configuration above $E_v + 1.04$ eV, while Zhu found a switch to Si_i^{1-} at $E_v + 1.01$ eV. A recent first-principles study by Centoni et al. finds a transition from tetrahedral Si_i^{2+} to $\langle 1\ 1\ 0 \rangle$ -split Si_i^0 at $\sim E_v + 0.5$ eV, and subsequent ionization of $Si_i,\langle 1\ 1\ 0 \rangle$ to a $(1-)$ charge state for Fermi energies above $E_v + 0.78$ eV [27]. Fig. 30, from this same author, is representative of the manner in which the formation energy of Si self-interstitials, including their geometric configuration, is typically correlated to the Fermi energy within the semiconductor. Fair's TED profile simulation has been revisited by Jung et al., with the finding that experimental data can be accurately described in terms of just Si_i^{2+} and Si_i^0 defects, with an effective negative-U ionization level at $E_v + 0.12 \pm 0.05$ eV [4]. Table 8 summarizes the computational and experimental values proposed for the ionization levels of self-interstitials in silicon [4,27,53,387,398,402,404,405,409,410,414,416–426] (Table 8).

6.1.2. Germanium

Germanium has a band gap of about 0.67 eV at 300 K. The germanium vacancy behaves qualitatively in the same way as the silicon vacancy; it exists in several charge states in the band gap, each of which is characterized by different local lattice relaxations, and exhibits symmetries similar to the ones observed around V_{Si} . Experimental and computational evidence exists for three germanium vacancy charge states within the band gap: V_{Ge}^0 , V_{Ge}^{1-} , and V_{Ge}^{2-} . In contrast to silicon, the vacancy defect in Ge is never a single donor; it has no $(1+/0)$ state in the band gap [266,288]. Also, the defect does not exhibit negative-U behavior, as the energy of correlation between the first and second donor states is not sufficiently negative as to produce a $(0/2+)$ level within the band gap [266].

Van Vechten and Thurmond were among the first to simultaneously consider the possible charge states of the vacancy defect and accurately predict the results of quenching experiments [50]. They found a free energy of vacancy

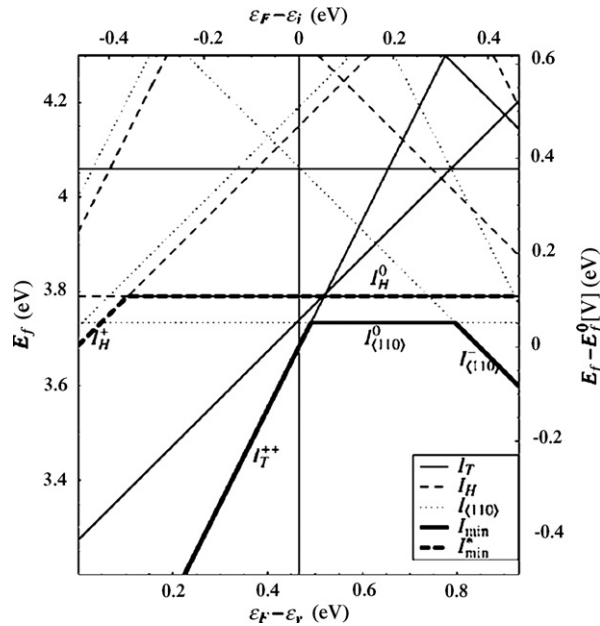


Fig. 30. Formation enthalpies of interstitials in Si vs. Fermi level. The heavy solid line indicates the lowest formation enthalpy at a given Fermi level. The tetrahedral, hexagonal, and split- $\langle 1\ 1\ 0 \rangle$ configurations are shown. The split- $\langle 1\ 1\ 0 \rangle$ is most stable except for the (2+) charge state.

formation in Ge of 2.0 ± 0.2 eV at 0 K with corresponding enthalpies of ionization of 0.51, 0.38, and 0.67 eV for the (1+), (1-), and (2-) charge states, respectively [50]. Most of the other early computational investigations yielded neutral defect formation energies of between 1.9 and 2.52 eV [427–433]. Using perturbed angular correlation spectroscopy (PACS), Haesslein et al. deduced a deep acceptor at 0.2 ± 0.04 eV above the valence band maximum,

Table 8
Experimentally and computationally determined ionization levels for the self-interstitial defect in bulk silicon

Si _i	Method					Reference
(2+/1+)	(1+/0)	(2+/0)	(0/1-)	(1-/2-)		
–	0.315	–	0.695	–	Self-diffusion	[416]
–	0.4	–	0.67	–	Self-diffusion	[417]
–	0.4	–	0.8	–	Quenching of defects	[418]
–	0.46	–	0.73	–	Annealing of irradiation induced defects	[387]
–	0.4	–	0.72	–	Unspecified	[419]
–	–	–	0.63	–	DLTS	[420]
–	0.34	–	1.03	–	OED	[421]
–	0.39	–	1.03	–	IED	[422]
–	0.17	–	1.01	–	OED	[423]
–	0.33	–	–	–	OED	[424]
–	–	0.67–0.69	–	–	Formation of radiation defects	[398]
0.73	0.87	–	–	–	DLTS	[409]
0.87	0.73	–	–	–	DLTS	[410]
–	0.5	–	0.72	0.82	OED	[425]
0.24	–	0.43	0.66	–	Formation of radiation defects	[414]
–	–	0.6	–	–	DFT-LDA	[404]
–	–	0.73 (2+/1-)	–	1.04	DFT-LDA	[426]
–	–	0.45	1.01	–	DFT-LDA	[405]
–	–	0.62	–	–	DFT-LSDA	[402]
–	–	0.5	0.78	–	DFT-GGA	[27]
–	–	0.12 ± 0.05	–	–	Fitting of TED profiles	[4]
0.57	0.68	–	0.93	1.1	DFT-LDA	[53]

All values are in eV and referenced to the valence band maximum.

Table 9

Experimentally and computationally determined ionization levels for the vacancy defect in bulk germanium

V_{Ge}						Method	References
(2+/1+)	(1+/0)	(0/1−)	(1−/2−)	(2−/3−)			
–	–	–	0.29	–	Unspecified	[50]	
–	–	0.33	–	–	DLTS and PAC	[435]	
–	–	0.20 ± 0.04	–	–	PAC	[434,436]	
0.16	0.21	0.27	0.42	0.49	Green's function calculations	[401]	
0.001	0.209	0.373	0.399	–	DFT-LDA	[437]	
0	0.21	0.366	0.395	–	DFT-LDA	[267]	
–	–0.11	0.2	0.2	0.37	DFT-LSDA	[266]	

All values are in eV and referenced to the valence band maximum.

which they attributed to V_{Ge}^{1-} [434]. DFT studies by Coutinho et al. placed the (0/1−) vacancy ionization level between $E_v + (0.17\text{--}0.2 \text{ eV})$, matching the location estimated from the PACS measurements. The (2−) and (3−) charged vacancies in Ge were suggested to have levels at around $E_v + 0.17 \text{ eV}$ and $E_v + 0.37 \text{ eV}$, respectively. Due to the proximity of the ionization levels for V_{Ge}^{1-} and V_{Ge}^{2-} , Coutinho et al. pointed out that the $E_v + 0.2 \text{ eV}$ level inferred from PACS measurements could actually be assigned to a (0/2−) ionization level [266,434]. As the band gap of the semiconductor is around 0.7 eV, the (1−/2−) level falls very close to the (0/1−) level, so the existence of a negative-U correlation energy has not been ruled out. This negative energy is associated with the strong structural relaxation of the neutral and (2−) defects when compared to that of the (1−) vacancy [266]. The same relationship does not hold for the (2+), (1+), and (0) states in Ge. Janotti et al. found that they do not form a negative-U system [268]. The proposed ionization levels of the germanium vacancy are summarized in Table 9 [50,266–268,401,434–436].

The germanium self-interstitial is definitely stable within the band gap in the neutral and (1−) states; conflict exists in the literature as to the stability of the (1+) state, likely due to the assortment of defect geometries that have been considered. The (0/1−) ionization level has been located at approximately 0.30 eV above the valence band maximum by several authors. A (1+/0) transition level above the valence band maximum may exist for the ⟨1 1 0⟩-interstitial kite defect investigated by da Silva et al., but not for the split-⟨1 1 0⟩ configuration considered by Moreira et al. The existence of Ge_i^{1-} and Ge_i^{2-} was first inferred by analyzing the low temperature recovery stages associated with the thermally activated migration of self-interstitials [437]. Shortly thereafter, Seeger and Frank, Trueblood, Saito et al., and Shimotomai et al. identified neutral and (1+) interstitials [417,438–440]. In at least one early quenching study, the interstitial was erroneously predicted to act as a double donor, with an energy level between the vacancy-acceptor level and the middle of the band gap [441]. Quantum calculations of the germanium interstitial charge density have revealed highly delocalized orbitals with a large valence band character [268,287,288]. As such, the (1+/0) donor level must be located close to the top of the valence band, not close to bottom of the conduction band. Some authors have found that the (1+/0) level is resonant within the valence band [287], while others have indicated that the level lies slightly above the valence band maximum [268,288] (Table 10). These results differ from the experimental (1+/0) ionization level at 0.04 eV below the conduction band observed by Haesslein using PACS [434,442]. Moreira et al. suggested that the PACS level introduced by the self-interstitial near the conduction band minimum might actually be an acceptor [287]. From the work of Haesslein et al., da Silva estimates that the (1+/0) level is between 0.11 and 0.16 eV above the top of the valence

Table 10

Computationally determined ionization levels for the self-interstitial defect in bulk germanium

Ge_i			Method	Reference
(1+/0)	(0/1−)			
0.15	–	DFT-LDA	[268]	
−0.08	0.37	DFT-LDA	[287]	
0.07	0.31	DFT-LDA	[288]	
0.63	–	PAC	[434]	

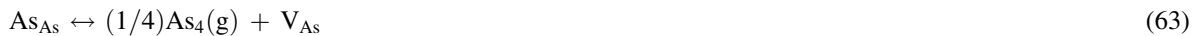
All values are in eV and referenced to the valence band maximum.

band, in agreement with their computational results [288,434]. Calculations for the (0/1 $-$) acceptor ionization level are less varied, and indicate that the level is about 0.31–0.37 eV above the valence band maximum [287,288].

6.1.3. Gallium arsenide

Gallium arsenide has a band gap of 1.43 eV at 300 K [443]. The native point defects in gallium arsenide include vacancies and antisite defects on both sublattices, as well as Ga and As interstitials. The relative contribution of the bulk defects is often correlated to the deviation from exact 1:1 GaAs stoichiometry, where the amount of Ga and As in the sample is determined by electrochemical titration or the average mass of the unit cell [305]. For crystals grown under Ga-rich, or p-type, conditions, the concentrations of As_i and As_{Ga} are negligible. Similarly, for As-rich, or n-type, conditions, V_{Ga} plays a much more important role than V_{As} [305]. The lowest formation energies are found for As_{Ga}²⁺ in p-type and V_{Ga}³⁻ in n-type GaAs under As-rich conditions [293], and for Ga_i³⁺ in p-type and Ga_{As}²⁻ in n-type GaAs under Ga-rich conditions, all respectively [296,297].

Arsenic atoms exit the lattice as interstitials, a process that can be described by both an elementary and overall gas-phase reaction:



Similarly, the formation of gallium vacancies entails:



Both types of vacancies can also be formed by the reaction of vacancies already present within the crystal with antisite defects. For example, a gallium vacancy can be formed from an arsenic vacancy and an arsenic antisite:



All of these defects undergo ionization reactions to donor and acceptor states similar to those laid out for silicon (e.g. Eqs. (54) and (59)). Note that the antisite defect, which was not considered for either silicon or germanium, may also be charged.

The stable charge states for the arsenic vacancy are still a matter of debate. Experiments have suggested V_{As}¹⁺, V_{As}⁰, V_{As}¹⁻, and V_{As}²⁻ as candidates in the bulk, whereas recent theoretical calculations propose negative-U behavior and the subsequent destabilization of the (0) and (1 $-$) charge states. Positron annihilation spectroscopy has been used to identify donor and acceptor ionization levels close to the conduction band minimum. For example, Corbel et al. located the (0/1 $-$) and (1 $-$ /2 $-$) levels at E_v + 1.33 ± 0.02 eV and E_v + 1.395 ± 0.015 eV, respectively (where these values have been converted from the CBM with a band gap of 1.43 eV) [444]. Although several early Green's function and tight-binding studies predicted no negative-U behavior for the defect, more recent density-functional theory investigations have suggested otherwise. Cheong and Chang and Poykko et al. were the first to report the negative-U effect for the (1+1 $-$) ionization level of V_{As} [445,446]. This behavior was confirmed by Chadi, who found the electron capture V_{As}¹⁺ + 2e⁻ → V_{As}¹⁻ to be favored by strong Jahn-Teller distortions, leading to the stability of the (1 $-$) charge state for Fermi energies above midgap [303]. Recently, El-Mellouhi et al. have suggested a shallower (1+1 $-$) ionization level and a second negative-U electron capture at E_v + 1.27 eV with the reaction V_{As}¹⁻ + 2e⁻ → V_{As}³⁻ [293]. In this model, illustrated in Fig. 31, the arsenic vacancy exhibits two successive negative-U transitions, meaning that neither the neutral nor the (2 $-$) states are ever majority species (Fig. 31). The ionization levels of the arsenic vacancy in bulk GaAs are summarized in Table 11 [292,293,295,309,401,444,445,447–452].

Although it has long been known that the gallium vacancy exists in large concentrations in n-type GaAs, the conclusive identification of its charge state in that regime is a relatively recent development. Calculations hinted at the predominance of V_{Ga}³⁻ [292,445,446,453], while diffusion experiments indicated the existence of V_{Ga}¹⁻ or V_{Ga}²⁻ [454]. Positron annihilation results and first-principles calculations have now definitively shown that, for intrinsic and n-type GaAs, V_{Ga}³⁻ has a lower formation energy than V_{Ga}⁰, V_{Ga}¹⁻, or V_{Ga}²⁻ [293,455–457]. Some authors have reported ionization levels lying well below the midgap with no negative-U effect [296,446,453,457], while others have identified defects with ionization levels closer to the center of the band gap [293,309,445], and even negative-U

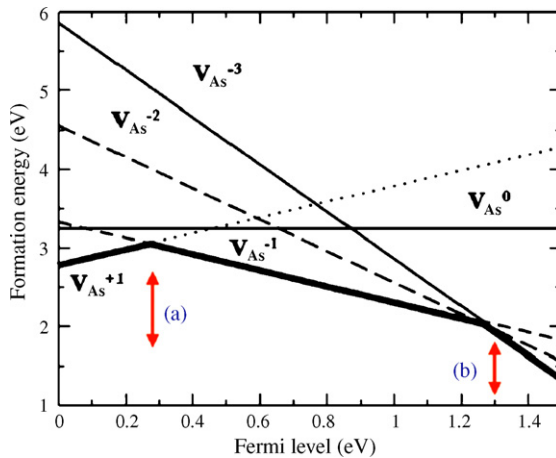


Fig. 31. Formation energies as a function of the Fermi energy of various charge states of As vacancies in GaAs at 0 K. The Fermi level is calculated with respect to the valence band maximum. Arrows point to the location of the (a) (1+/1-) and (b) (1-/3-) ionization levels as suggested by El-Mellouhi and Mousseau [293].

behavior [292]. Recently, in a fashion akin to the investigation of the temperature-dependence of defect ionization levels in silicon performed by Van Vechten, El-Mellouhi and Mousseau revisited the divergent experimental and theoretical findings for V_{Ga} in GaAs [458]. They used LDA results to explore the effects of temperature on the Gibbs free energy of formation and found that the thermal dependence of the Fermi level and ionization levels leads to a reversal of the preferred charge state as the temperature increases. Fig. 32 reveals the minimal effect of temperature on vacancy ionization enthalpies, as well as the linearly increasing entropic term in the Gibbs free energy. With such an analysis, El-Mellouhi and Mousseau were able to reproduce the conflicting experimental results of Bracht et al., Gebauer et al., and Tan et al. [456,459,460]. To summarize, the calculated and experimentally determined ionization levels for the gallium vacancy defect are tabulated in Table 12 [292,293,295,296,309,445,450–453,457,459,461].

Gallium interstitials in the (3+) charge state are the dominant defects in p-type GaAs under Ga-rich conditions [281,294,296,297]. In the early 1990s, investigators focused more heavily upon the (2+) gallium self-interstitial [281,462]; for example, self-consistent pseudopotential calculations performed by Chadi et al. placed the (2+/1+) level of the defect at the valence band maximum. For the [1 1 0] split-interstitial form of the defect, which is favored for the neutral charge state, a (+1/0) ionization level of $E_v + 0.6\text{--}0.7$ eV arises [281]. Also, if acceptor states of the interstitial defect are considered, the neutral defect is less stable than the negatively charged defect; charged Ga interstitials form a negative-U system [281]. Hurle et al. “arbitrarily assigned” levels of $E_v + 0.3$ eV and $E_v + 0.5$ eV to the (2+/1+) and

Table 11
Experimentally and computationally determined ionization levels for the arsenic vacancy defect in bulk GaAs

V_{As}				Method	Reference
(1+/0)	(0/1-)	(1-/2-)	Other		
–	1.33 ± 0.02	1.395 ± 0.015	–	PAS	[445]
1.29	1.4	–	–	PAS	[448]
1.29	1.4	–	–	PAS	[449]
–	1.37 ± 0.01	–	–	PAS	[450]
–	–	–	0.07 (2+/1+)	Green's function calculations	[309]
1.25	1.36	–	–	DFT-LDA	[451]
1.11	1.21	1.3	–	Green's function	[401]
–	1.285	1.342	–	TB calculations	[452]
0.83	1.04	1.15	1.26 (2-/3-)	TB calculations	[295]
–	–	–	0.785 (1+/1-)	First-principles calculations	[446]
1.3	1.428	–	–	TB calculations	[292]
–	–	–	0.86 (1+/1-)	DFT-LDA	[453]
–	–	–	0.27 (1+/1-), 1.27 (1-/3-)	DFT-LDA	[293]

All values are in eV and referenced to the valence band maximum.

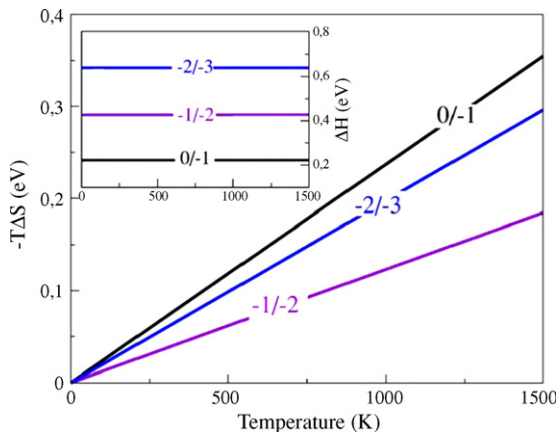


Fig. 32. Entropy and enthalpy (inset) contributions to the free energy of ionization obtained for various charge transitions of V_{Ga} in GaAs. The enthalpy shows little temperature dependence, but the ionization entropy is significant, leading to a substantial entropy contribution to the free energy of ionization that increases linearly with temperature.

(1+/0) charge state transitions, respectively [305]. On the other hand, Northrup et al. found a low formation energy for the (3+) charge state of Ga_i in both intrinsic and p-type material using the LDA and first-principles pseudopotentials [294]. Using a similar calculation method, Zhang et al. obtained both (3+/2+) and (2+/1+) ionization levels slightly below midgap, yet did not cite their exact locations [297].

Under equilibrium conditions, charged arsenic interstitials, which tend to adopt the split-interstitial configuration over the ideal tetrahedral configuration, have formation energies that are much higher than those of antisites and vacancies in bulk GaAs [296,297]. Nevertheless, they are easily created by irradiation and are likely responsible for the deviation from stoichiometry (towards As-rich unless the concentration of Ga in the melt is considerably greater than 50%) observed in melt-grown GaAs [305,463]. Interstitial arsenic defects are difficult to observe experimentally, as even after irradiation or heat treatment, they are often EPR, electrically, and optically invisible [295]. Consequently, most of the insight into their configuration and electronic structure arises from self-consistent semi-empirical tight-binding, pseudopotential, and first-principles molecular-dynamics calculations [281,295,296,464]. In the As-rich limit, the charge on the arsenic split-interstitial transitions from (1+) to (0) to (1-) for increasing Fermi energies within the band gap [296]. This picture is different from that of the defect proposed by Chadi et al. in 1992, which suggested negative-U behavior for the As_i defect with a (1+/1-) transition level at about $E_v + 0.35$ eV [281]. Instead,

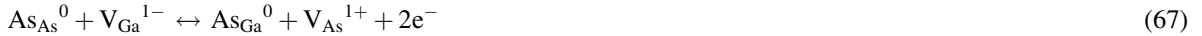
Table 12
Experimentally and computationally determined ionization levels for the gallium vacancy defect in bulk GaAs

V_{Ga}				Method	Reference
(0/1-)	(1-/2-)	(2-/3-)	Other		
0.42	0.6	—	—	Self-diffusion under extrinsic conditions	[460]
0.19	0.49	0.68	—	Green's function calculations	[309]
0.1	0.35	0.5	—	DFT-LDA	[451]
0.283	0.436	0.605	—	TB calculations	[452]
0.25	0.39	0.57	0.13 (1+/0)	TB calculations	[295]
0.19	0.2	0.32	—	DFT-LDA	[454]
—	0.49	0.69	—	First principles calculations	[446]
—	—	—	0.035 (1+/1-), 0.078 (1-/3-)	TB calculations	[292]
0.11	0.22	0.33	—	DFT-LDA	[453]
0.09	0.13	0.2	—	DFT-LDA	[296]
0.39	0.52	0.78	—	DFT-LDA	[462]
0.13	0.15	0.18	—	DFI-LDA	[458]
0.05	0.4	0.55	—	DFT-LDA	[293]

All values are in eV and referenced to the valence band maximum.

recent DFT results obtained by Schick et al. using the LDA with the Ceperley–Alder form for the exchange and correlation potentials as parameterized by Perdew and Zunger reveal (1+/0) and (0/1–) ionization levels for the As split–interstitial located at $E_v + 0.3$ eV and $E_v + 0.5$ eV, respectively [296].

The interaction that leads to the formation of the antisite defect, or the migration of a vacancy to a nearest neighbor, is expressed as



The ionization reaction for the defect, which can exist in a neutral, (1+) or (2+) state is



Based on EPR measurements, Weber et al. assigned ionization levels of $E_v + 0.52$ and $E_c - 0.75$ eV to the (2+/1+) and (1+/0) ionization levels of the stable arsenic antisite in GaAs, respectively [114]. The levels calculated by Bachelet et al. using the local-density approximation were significantly higher, at 0.83 and 1.10 eV for the (2+/1+) and (1+/0) ionization levels, respectively [290]. These calculations, performed in the 1980s, along with others published concurrently, all presented values that are far higher than those obtained experimentally or in more recent computational investigations [295,309]. At present, As_{Ga} , the EL2 defect is assumed to form (1+) and (2+) states located at approximately 0.75 eV below the conduction band edge [465] and 0.54 eV above the valence band edge [305], respectively.

The gallium antisite defect acts as a shallow acceptor in n-type GaAs but as a deep acceptor in p-type GaAs. It arises due to the following chemical and electronic reactions:



Values for the acceptor ionization levels of this defect vary widely; it has been ascertained from deep-level transient spectroscopy experiments that n-type versus p-type doping greatly affects the behavior of the defect [466]. For n-type samples, Boguski et al. determined (0/1–) and (1–/2–) ionization levels at $E_v + 0.20$ eV and $E_v + 0.077$ eV, respectively [466]. Only $\text{Ga}_{\text{As}}^{2-}$ defects were observed, lending support to the suggested negative-U behavior of the defect, with a (0/2–) ionization level at about $E_v + 0.17$ eV. Zhang and Chadi obtained similar ionization levels of $E_v + 0.24$ eV (0/1–) and $E_v + 0.09$ eV (1–/2–) [308]. In p-type GaAs, Bugajski et al. found only a single acceptor level at $E_v + 0.068$ eV, in close agreement with the (0/1–) and (1–/2–) levels at $E_v + 0.078$ eV and $E_v + 0.20$ eV observed by Yu and co-workers [466–468]. On the other hand, Baraff and Schluter and Wang et al., located transition

Table 13

Experimentally and computationally determined ionization levels for both arsenic antisites and gallium antisites in bulk GaAs

As_{Ga}	Ga_{As}			Method	Reference	
	(2+/1+)	(1+/0)	(0/1–)	(1–/2–)		
–	–	0.077	0.23	–	DLTS	[468]
–	–	0.4	0.7	–	DLTS	[470]
–	–	0.077	0.2	–	Transient capacitance spectroscopy	[467]
–	–	0.3	0.62	–	Green's function calculations	[309]
–	–	0.24	0.09	0.17 (0/2–)	DFT-LDA	[308]
0.61	0.89	–	–	–	DLTS	[298]
0.52	0.75	–	–	–	EPR	[114]
–	0.7	–	–	–	Magnetic field dependence of zero-phonon line	[299]
0.83	1.1	–	–	–	Green's function calculations	[471]
0.64	0.87	–	–	–	Defect molecule model	[472]
1.5	1.25	–	–	–	Green's function calculations	[309]
1.2	1.37	–	–	–	Green's function calculations	[295]
1	1.1	–	–	–	DFT-LDA	[296]
0.98	1.18	–	–	–	Green's function calculations	[306]

All values are in eV and referenced to the valence band maximum.

levels considerably above the valence band maximum, $E_v + 0.30$ or 0.40 eV for $\text{Ga}_{\text{As}}^{1-}$ and $E_v + 0.62$ or 0.70 eV for $\text{Ga}_{\text{As}}^{2-}$, all respectively [309,469]. The ionization levels for both arsenic and gallium antisites are summarized in Table 13 [292,293,295,296,309,445,450–453,457,459,461].

6.1.4. Other III–V semiconductors

When the charged defects in the other group III–V semiconductors are compared to those in gallium arsenide, many similarities can be observed. This correspondence is most pronounced for compounds that contain no boron or nitrogen. For example, in gallium phosphide, which has a band gap of 2.26 eV at 300 K, the lowest formation energies are found for $\text{P}_{\text{Ga}}^{2+}$ in p-type and $\text{V}_{\text{Ga}}^{3-}$ in n-type material under P-rich and stoichiometric conditions. Only the charge state of the gallium interstitial that dominates in p-type Ga-rich GaP is different ((2+) versus (3+)); Ga_i^{2+} and Ga_i^{2-} have low formation energies in p-type and n-type material under Ga-rich conditions, respectively [450,470]. Under stoichiometric conditions, there is a small region in the band gap between 0.65 and 0.94 eV where Ga_i^{2-} has a large concentration in the bulk [470]. According to LDA calculations and ESR experiments, the (2+/1+) ionization level for the phosphorus vacancy lies at $E_v + 0.97$ eV and $E_v + 1.25$ eV, respectively [470,471]. For charge states ranging from (1+) to (5–), the phosphorus vacancy exhibits negative-U behavior; only V_P^{1-} and V_P^{3-} are energetically favorable [470]. The formation energy of $\text{V}_{\text{Ga}}^{2-}$ is approximately 0.5 eV higher than that of $\text{V}_{\text{Ga}}^{3-}$, and for Ga-rich conditions, the (2-/3-) ionization level is about 0.20 eV above the valence band maximum [470]. Negative-U behavior is observed for the gallium antisite defect, for which there is only one (0/2–) ionization level inside the band gap [470]. The complexity of the defect chemistry in GaP, as well as a visual representation of how close some of the defect levels are, can be gleaned from Fig. 33.

The ionization levels of charged defects in III–V compounds that contain elements from the second row of the periodic table are different from those in GaAs. In AlN, BN, InN, and GaN, for the most part, only vacancies have low enough formation energies to affect the electronic properties of the bulk under equilibrium conditions. The band gaps of these wide-band gap semiconductors are tabulated in Table 14 [472–475]. Exceptions to this rule occur in BN, where the mismatch between the radii of the boron and nitrogen atoms is comparatively small, and in zinc-blende AlN, where the lattice defects can interact with a greater number of nearest-neighbor atoms; charged antisites and interstitials may occur in these materials [113,251,314]. For conditions rich in the group-III element, it has been suggested that the (3–) charge state of the group-III vacancy is the dominant point defect in n-type material, while the concentration of either $\text{V}_{\text{group V}}^{1+}$ or $\text{V}_{\text{group V}}^{3+}$ becomes significant in p-type material [314,461,476–479]. For all four group-III nitride compounds, according to this model, the nitrogen vacancy exhibits negative-U behavior [311,312,476,480]. Recently, however, Ganchenkova and Nieminen have suggested that negatively charged nitrogen vacancies, which were not even considered in earlier works, dominate in n-type conditions [316]. Progressing from

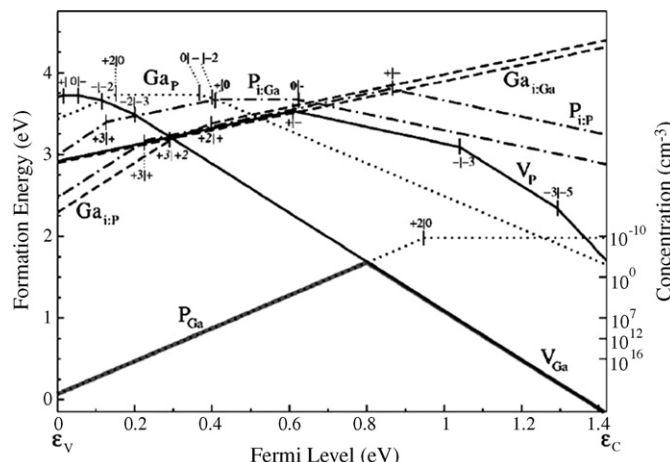


Fig. 33. Formation energies as a function of the Fermi-level for relaxed native defects in GaP under P-rich conditions. The antisite defects are shown as dotted lines, vacancies as full lines, and interstitials as broken lines. The alternative y-axis on the right gives the defect concentration in orders of magnitude at $T = 300$ K.

Table 14

Band gap values at 300 K for the group III-nitrogen semiconductors

Material	Band gap at 300 K (eV)	Reference
AlN	6.026	[473]
BN	6.1–6.4	[474]
GaN	3.2	[475]
InN	0.7	[476]

Fermi energies near the conduction band minimum to those at the valence band maximum, their model proposes that V_N^{3-} , V_N^{1-} , and V_N^{1+} are the dominant defects in the bulk.

The gallium vacancy in GaN is a triple acceptor, much like that in GaAs; in n-type material, V_{Ga} exists in the (3-) charge state. The (0/1-), (1-/2-), and (2-/3-) ionization levels are located at approximately 0.2, 0.7, and 1.1 eV above the valence band maximum [311,312,478]. V_N^{1+} and V_N^{3+} are shallow donors in GaN, and although they have high formation energies under n-type conditions, they can act as compensating centers in the case of p-type doping [113]. Using a larger supercell that allows for better relaxation of V_N^{3+} , Limpijumnong and Van de Walle have placed the (3+/1+) ionization level for V_N at $E_v + 0.59$ eV, or considerably higher than previously published values [312,481–483]. Ganchenkova and Nieminen appear to be the first to have considered the possibility of negatively charged nitrogen vacancies in n-type material [316]. This is surprising, considering as the acceptor ionization levels of V_{As} in GaAs and V_P in GaP have been explored for some time. They suggested that, for n-type material, V_N^{1-} and V_N^{3-} will have smaller formation energies than V_{Ga}^{3-} , and that V_N exhibits negative-U behavior for the newly investigated ionization states; it is unstable in the neutral and (2-) charge states. Using the Zhang-Northrup formalism, Ganchenkova and Nieminen calculated nitrogen vacancy ionization levels at 2.43, 2.58, and 2.60 eV above the valence band maximum for the (1+/1-), (1-/2-), and (2-/3-) ionization levels, respectively. Fig. 34 illustrates the turn-over in defect formation energy that occurs at about 2.5 eV when the (1-) and (3-) charge states are considered. The authors acknowledged that PAS experiments have shown no evidence of nitrogen vacancies in n-type GaN, yet suggested that the signals of the negatively charged vacancies are similar to that of the bulk, and are thus PAS-invisible [477,484–487]. The positron lifetimes for V_N^{1-} and V_N^{3-} are about 131 and 132 ps, respectively, which is essentially the same as in the bulk [316].

Interstitial defects created in GaN upon irradiation can be observed by optically detected electron paramagnetic resonance [488]. Density-functional theory and first-principles calculations have also been employed to predict their electronic structure and defect levels [113,312,313,489]. The interstitial defects in GaN have been suggested to exist in considerably different charge states than those in GaAs. According to density-functional theory calculations performed by Limpijumnong et al., Ga_i is stable only as Ga_i^{3+} and Ga_i^{1+} [312]. The (3+/1+) transition level occurs at

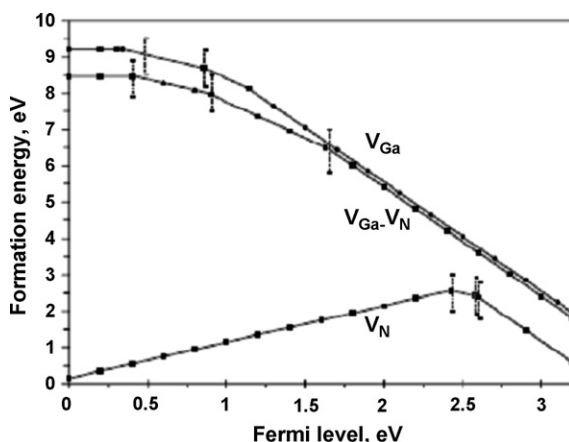


Fig. 34. Formation energies for gallium and nitrogen vacancies and mixed divacancies in GaN. Notice the turn-over in the slope of the V_N line at about 2.5 eV, which suggests that negatively charged nitrogen vacancies may, in fact, contribute to the defect chemistry in bulk GaN.

about 2.5 eV above the valence band minimum. Based on experimental ODEPR measurements, Chow et al. predicted second and third ionization levels for the defect at $E_v + 1.9$ eV and $E_v + 2.25$ eV, respectively [490]. As a reminder, the gallium interstitial in GaAs is stable in charge states ranging from (3+) to (0); none of the donor states are unstable, i.e. no negative-U behavior has been found. Nitrogen interstitials, which can occur in charge states ranging from (3+) to (1−), have high formation energies for all Fermi energies within the band gap, and can be produced in GaN only upon irradiation [113]. Nitrogen interstitials in GaN, in comparison to arsenic interstitials in GaAs, have more stable charge states within the band gap. The (3+/2+), (2+/1+), (1+/0), and (0/1−) ionization levels calculated by Limpijumnong et al. are located at Fermi energies approximately 0.75, 1.0, 1.5, and 1.0 eV above the VBM, respectively. These levels are far higher than those suggested for As_i in GaAs (assuming no negative-U behavior). Schick et al. calculated ionization levels for $\text{As}_i^{1+}/\text{As}_i^0$ at $E_v + 0.30$ eV and $\text{As}_i^0/\text{As}_i^{1-}$ at $E_v + 0.50$ eV [296].

6.1.5. Titanium dioxide

Titanium dioxide is typically an n-type semiconductor whose defect structure involves an excess of metal [258]. Anatase and rutile TiO_2 , the two most studied phases, differ considerably in their electronic properties; at 300 K, rutile has a direct band gap of around 3.03 eV while anatase has an indirect band gap of approximately 3.18 eV [491,492].

To explain the electronic behavior of reduced and stoichiometric rutile and anatase TiO_2 , defect models involving three main types of point defects, Ti^{3+} interstitials, Ti^{4+} interstitials, and O^{2+} vacancies have been proposed [83]. Only one paper in the literature mentions that an alternate Ti^{2+} interstitial defect may exist [320]. Majority opinion now suggests that the predominant defects in non-stoichiometric rutile TiO_{2-x} , where x is the deviation from stoichiometry, are Ti_i^{3+} and V_O^{2+} at low [493–501] and high [502,503] oxygen partial pressures, respectively. For example, for TiO_2 at 1073 K, the concentration of V_O^{2+} in the bulk overtakes that of Ti_i^{3+} for oxygen partial pressures greater than 10^{-9} Pa; the same transition occurs at about 10^{-8} Pa for material at 1473 K [504]. The contribution of Ti_i^{4+} , rather than Ti_i^{3+} , becomes more significant in near-stoichiometric rutile TiO_2 , although the concentration of titanium interstitials is probably always less than that of V_O^{2+} [82,504]. Oxygen vacancies act as intrinsic n-type dopants that shift the Fermi-level towards the conduction-band minimum [320,505]. Based on experimental findings at an assortment of ambient conditions, it seems reasonable to suppose that (2+) oxygen vacancies are the dominant defects at increasing partial pressures of oxygen; only at high oxygen partial pressure (10^5 Pa) would one be able to obtain exactly stoichiometric material [495,506–509]. Alternatively, based on thermogravimetry and electrical conductivity measurements performed in the 1980s, it has been suggested that V_O^{1+} prevails at very high oxygen partial pressure (TiO_{2-x} where $x \leq 0.0001$) [507]. The experimentally observed behavior, however, can also be explained in terms of trivalent impurities such as Al^{3+} and Fe^{3+} that combine with Ti_i^{4+} or V_O^{2+} [510,511]. While a few other authors have considered the possibility of V_O^{1+} , there is no concrete evidence for its existence in titanium dioxide; for the most part, the literature assumes that the oxygen vacancy has no ionization level within the band gap [87,512].

Defect formation and reaction in oxide semiconductors tends to be more complicated than in group IV or III–V semiconductors, and the equations describing these processes often leave out quite a bit of mechanistic detail. One example involves the oxygen vacancy that appears as a product in the Schottky defect formation reaction, which entails the simultaneous creation of both an anion and a cation vacancy:



It is important to keep in mind that the production of an oxygen vacancy must be accompanied by the formation of a corresponding oxygen interstitial according to



The overall Schottky reaction often leaves out this detail. In anatase, the oxygen interstitial can form a substitutional diatomic molecule, $(\text{O}_2)_\text{O}$, a species similar to the split-interstitial in silicon [321]. The oxygen species is presumably important in describing oxygen exchange with the surrounding gas.

Vacancy and interstitial defects are formed by identical chemical and electronic reactions in rutile and anatase TiO_2 . Antisites do not occur, as the large cation–anion size mismatch and strong ionicity cause them to have prohibitively large formation energies [321]. TiO_2 , as well as non-stoichiometric TiO_{2-x} , can undergo reversible reactions with oxygen in the ambient [513]:



The production of neutral oxygen vacancies in the bulk is nominally described by the overall reaction:



Oxygen is lost to the gas phase as a result of the spontaneous binding of interstitial oxygen to oxygen in lattice sites, and subsequent out-diffusion to yield gaseous oxygen [321]. It is likely, though not certain, that the out-diffusing species is interstitial oxygen rather than the diatomic molecule:



Oxygen vacancies are ionized into a (2+) charge state by the following electronic reaction:



Mechanistically, this process is thought to occur by Schottky defect formation, which involves the simultaneous creation of both an anion and a cation vacancy:



The fundamental Schottky equilibrium expression is



The formation of neutral titanium interstitials is represented by the overall reaction:



that is obtained from the following quasi-chemical elementary reactions with the knowledge that oxygen in the TiO_2 lattice is easily reduced:



Also, according to Na-Phattalung et al., as titanium interstitials have low formation energies, they can also be formed when oxygen vacancies react with TiO_2 [321]:



The electronic reactions that lead to the ionization of the titanium interstitials are



In contrast to the Schottky reaction that forms the oxygen vacancy, a Frenkel reaction forms a titanium interstitial. The reaction can be visualized as a titanium lattice ion moving to an interstitial site, leaving a titanium vacancy behind:



This reaction is typically referenced only in respect to the (4+) charge state of the titanium interstitial. Consequently, a parallel reaction for the production of Ti_i^{3+} is generally not discussed.

Debate has long continued over the relative importance of (3+) and (4+) titanium interstitials, as well as (2+) oxygen vacancies, in rutile TiO_2 . The existence of the (3+) [514–516] and (4+) [511,514,517,518] charge states of Ti_i in TiO_{2-x} was first suggested by electron paramagnetic resonance experiments in the 1960s. Mass action laws can be applied to the defect formation reactions in TiO_2 to determine the pressure, and thus stoichiometry, dependence that should be observed in electrical conductivity measurements when a given defect charge state dominates. By

comparing the slopes of experimental quantities such as $\ln(P_{O_2})/\ln(x)$ (where x is the deviation from stoichiometry) or $\ln(P_{O_2})/\ln(e)$ (where e stands for electronic conductivity) with predictions from mass action laws, the existence of Ti_i^{3+} or Ti_i^{4+} can in principle be inferred (accounting for the degree of TiO_2 non-stoichiometry) [82,259,504,509,517,519–521]. Electrical conductivity results suggest that the complete ionization of Ti_i^{3+} ions to Ti_i^{4+} occurs in stoichiometric TiO_2 [87,494]. The relatively small ionization energies observed in TiO_2 corroborate this picture—the activation energy for trapped electrons to be excited into the conduction band is approximately 0.007 eV below 50 K, and about one order of magnitude higher around room temperature [514]. However, numerous authors have also presented computational evidence for the existence of both (3+) and (4+) titanium interstitials [82,318,504,519,522]. Support for the doubly charged titanium interstitial Ti_i^{2+} was inferred by Cho et al. from the delocalized character of doped electrons revealed by first-principles calculations [320]. They cited defect clustering or the inaccuracy of the LDA as possible causes for the discrepancy between their calculations and the typical defect picture, yet presented little explanation for why a single model involving Ti_i^{2+} should replace the many involving Ti_i^{3+} and Ti_i^{4+} [320].

It is necessary to consider the temperature of the ambient when determining the oxygen partial pressure at which the concentration of oxygen vacancies surpasses that of charged Ti interstitials in TiO_2 and TiO_{2-x} . At elevated temperatures, different charge states of interstitials may play a role in the defect chemistry. For example, the relative balance of Ti_i^{4+} versus Ti_i^{3+} depends upon temperature, even in reduced material [82,494,504,507]. It is difficult to select a single reference for a definitive picture of the relative concentrations of V_O^{2+} , Ti_i^{3+} , and Ti_i^{4+} in the bulk as a function of temperature and pressure. However, a relatively recent review article by Bak et al. illustrates the manner in which the contribution of several independent variables to the overall defect equilibria must be considered [82,504,523]. An example of a Brouwer diagram found in this review article is shown in Fig. 35.

The defect chemistry of anatase TiO_2 has received increasing attention in the last decade due to the novel photocatalytic properties associated with the crystal structure. While experimental work suggests that anatase

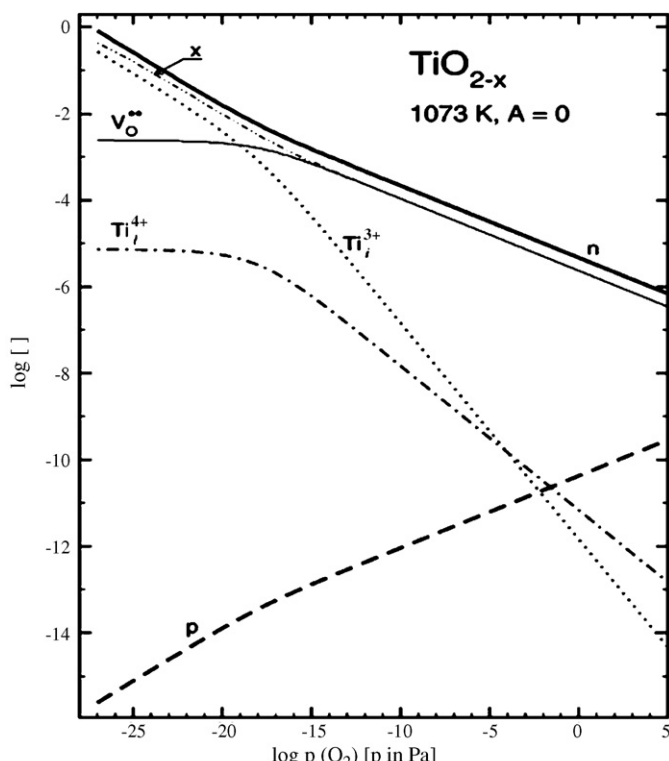


Fig. 35. Defect concentrations in undoped TiO_2 at 1073 K as a function of oxygen partial pressure. Notice that the concentration of (3+) titanium interstitials exceeds that of (2+) oxygen vacancies at low partial pressures. On the other hand, the concentration of V_O^{2+} is larger than that of Ti_i^{3+} and Ti_i^{4+} at high partial pressures.

behaves in a similar fashion to rutile, computational work has recently suggested that the concentration of V_O^{2+} is not appreciable in anatase for any range of ambient oxygen partial pressure. However, experiments using impedance spectroscopy have suggested that V_O^{2+} dominates at low T and high oxygen partial pressures ($10^5 > P_\text{O}_2 > 10 \text{ Pa}$), whereas Ti_i^{4+} becomes important at increasing temperatures and low oxygen partial pressure ($10^{-5} > P_\text{O}_2 > 10^{-19} \text{ Pa}$) [520]. The experimental papers published by these groups do, however, consider nanocrystalline and ceramic TiO_2 , and also differ slightly in their pressure and temperature ranges. Weibel et al. found the transition from Schottky disorder (V_O^{2+} and $\text{V}_{\text{Ti}}^{4-}$) to Frenkel cation disorder (Ti_i^{4+} and $\text{V}_{\text{Ti}}^{4-}$) to occur at 580 °C; the activation energies of the two types of defects are 1.3 ± 0.1 and $2.2 \pm 0.2 \text{ eV}$, respectively. The temperature at which the transition from oxygen vacancy to titanium interstitial dominance occurs is much lower in anatase than in rutile, where interstitial formation is observed only above 1100 °C and under 10^{-1} Pa . The more favorable formation of interstitials in anatase can be attributed to the fact that it has a 10% lower density than rutile [253].

In contrast, the computations of Na-Phattalung et al. indicate V_O^{2+} is not a dominant native defect near equilibrium growth conditions; even at high oxygen deficiencies, the formation of the oxygen vacancy is less favorable than that of the (4+) titanium interstitial [321]. Using a similar computational method to that of He and Sinnott in rutile TiO_2 , the authors confirmed low formation energies for the fundamental native defects (Ti_i , O_i , V_{Ti} , and V_O) and high formation energies for the Ti- and O-antisite defects [321]. None of the four low-energy native defects were found to have ionization levels inside the DFT band gap, as shown in Fig. 36 [321]. For Ti-rich material, $\text{V}_{\text{Ti}}^{4-}$ becomes more energetically favorable than Ti_i^{4+} for Fermi energies about 2.8 eV above the valence band maximum. In O-rich material, the range over which Ti_i^{4+} is likely to exist in substantial concentrations is far smaller; instead, neutral ($\text{O}_2)_0$ and $\text{V}_{\text{Ti}}^{4-}$ have low formation energies for Fermi energies between $E_\text{v} + 0.6$ and $E_\text{v} + 1.35 \text{ eV}$ and from $E_\text{v} + 1.35 \text{ eV}$ to the conduction band minimum, respectively [321]. As Ti_i^{4+} has a negative formation energy for $E_\text{F} < 2.4 \text{ eV}$ and 0.5 eV under Ti-rich and O-rich conditions, respectively, the p-type doping of TiO_2 under equilibrium growth conditions is unlikely [321]. The small formation energy of Ti_i^{4+} makes the following reaction favorable and explains

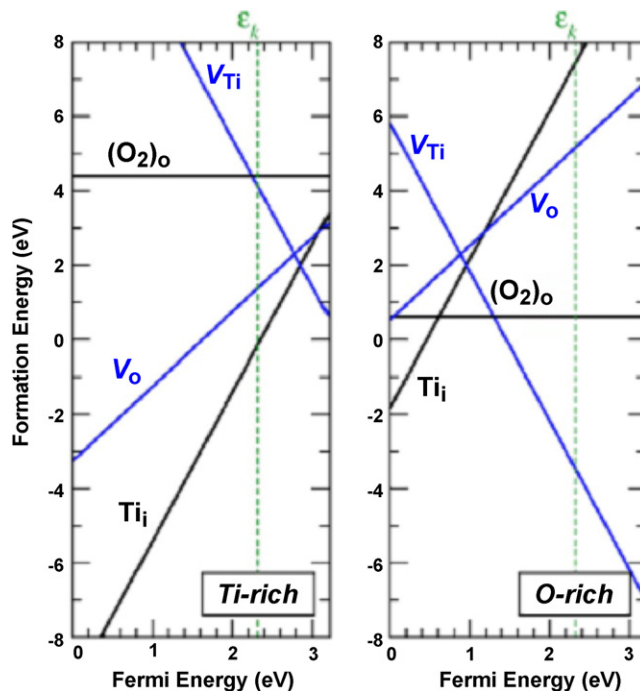


Fig. 36. Defect formation energies as a function of Fermi level under Ti-rich (left panel) and O-rich (right panel) growth conditions. The Fermi energy, referenced to the valence band maximum, is traced all the way up to the experimental band gap. The vertical dotted line is the calculated band gap at the special k -point. Notice the low formation energy proposed for (4-) titanium vacancies in strongly n-type material, especially under O-rich conditions.

the insignificant concentration of V_O^{2+} in the bulk:



6.1.6. Other oxide semiconductors

The ionized point defects in ZnO , UO_2 , and CoO have been investigated by the same pressure dependency measurements as those in TiO_2 , as well as DFT calculations. The band gaps of these materials are respectively 3.2 eV [524], 1.3 eV [525], and 6.0 eV [372]. As ZnO tends towards a reduced state under equilibrium conditions, oxygen vacancies in the (2+) and (0) charge states are the dominant defects under p-type and n-type conditions, respectively. For O-rich conditions, or high oxygen partial pressures, discrepancy exists in the literature as to whether charged zinc vacancies or oxygen interstitials dominate [85,86,88,325]. V_O^{2+} is also the dominant defect in hypostoichiometric UO_{2-x} , whereas O_i^{2-} forms to accommodate the hyperstoichiometry of UO_{2+x} [324]. In CoO , which prefers to exist as Co_{1-x}O , V_{Co}^0 and $\text{V}_{\text{Co}}^{1-}$ are the predominant defects at high oxygen partial pressure, depending upon Fermi energy, while $\text{V}_{\text{Co}}^{2-}$ becomes important at low oxygen partial pressures [84,526]. Implicit in this brief introduction is the implication that the defects in both ZnO and CoO have ionization levels within the band gap. For example, in a recent density-functional theory investigation using the GGA, Zhao et al. identified charge transfer levels for V_O , V_{Zn} , O_i , and Zn_i , as shown in Fig. 37 [85]. It is important to ask why multiple charge states of the oxygen vacancy have been considered in ZnO (2+, 1+, 0) and not in TiO_2 (mostly 2+). In light of the following discussion, it is highly possible that the defect chemistry of latter material is still not fully described.

The defect chemistry of ZnO has been well-studied; ion-gas and electronic reactions and their rate constants have been explored in great detail by Kroger, Hagemark, and Mahan [527–529]. With respect to specific charge states, the following defect species have been considered: oxygen vacancies V_O^{2+} , V_O^{1+} , and V_O^0 ; zinc vacancies V_{Zn}^0 , $\text{V}_{\text{Zn}}^{1-}$, $\text{V}_{\text{Zn}}^{2-}$; and oxygen interstitials O_i^{2+} , O_i^{1+} , O_i^0 , O_i^{1-} , O_i^{2-} . Antisite oxygen, as well as neutral, singly, and doubly ionized zinc interstitials have also been considered in the literature, yet their formation energies are always higher than those of O and Zn vacancies and O interstitials [85,530,531].

The reaction between ZnO and the ambient can be described by the solid–gas reaction:



Oxygen vacancies and interstitials are created by the elementary reaction:



If ZnO behaves like TiO_2 , then interstitial oxygen binds to oxygen in lattice sites and outdiffuses to form gaseous oxygen [321] according to the overall reaction:

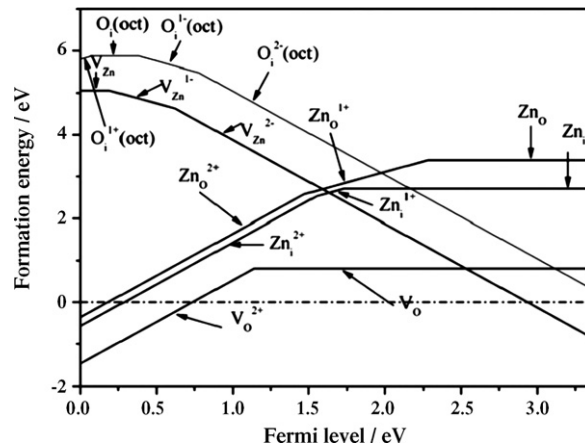
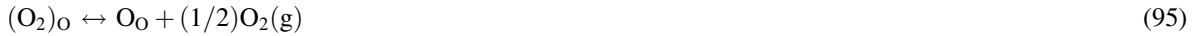


Fig. 37. Calculated defect formation energies for selected vacancy, interstitial, and antisite defects in ZnO as a function of the Fermi level at low oxygen partial pressure.

is formed by summing the following elementary reactions:



Zinc interstitials and vacancies are formed by



All of the defects in ZnO exist in multiple charge states. Their formation can be described by the ionization reactions analogous to those shown earlier for TiO₂.

There exists significant experimental and computational evidence that oxygen vacancies in a neutral or (2+) state are the dominant defects in zinc-rich ZnO [85,326,529,532]. Under p-type conditions, the oxygen vacancy is in the (2+) charge state, while under n-type conditions, the oxygen vacancy is in the neutral charge state [326]. The (1+) charge state is thus never thermodynamically stable in undoped material. The (2+/0) ionization level of the vacancy defect has been placed at approximately $E_v + 2.2$ eV by several authors [86,325,326,532,533]. Most recently, density-functional theory calculations using the GGA for the exchange-correlation potential have instead located this transition level at 1.07 eV above the valence band maximum [85]. These authors do point out, however, the tendency of the GGA to underestimate the band gap and strongly alter the defect formation energies and transition levels.

While the literature agrees that V_{Zn} in the (2-) charge state is the dominant point defect in n-type, O-rich ZnO [85,86,325,326,532,534], its existence at high concentrations as either V_{Zn}^0 or V_{Zn}^{1-} under p-type conditions is controversial [85,86,88,325,535]. Calculations by Zhang et al., Lee et al., and Erhart et al. suggest that V_{Zn}^{2-} is the defect with the lowest formation energy only for Fermi energies above midgap, and that the defect has no ionization levels in the band gap [325,535,536]. On the other hand, Kohan et al., Zhao et al., and Oba et al. find that the formation energy of the zinc vacancy is always lower (even under p-type conditions) than that of the other intrinsic defects in O-rich ZnO. Also, these authors all find at least one charge state transition within the band gap. Kohan et al. and Zhao et al. computed (0/1-) and (1-/2-) ionization levels at 0.2–0.3 and 0.6–0.8 eV above the valence band maximum [85,86,88]. In an earlier first-principles study also using the GGA, Oba et al. ruled out V_{Zn}^0 as a stable defect within the band gap and cited a (1-/2-) level at about 0.05 eV above the VBM [88]. The values published by Zhao et al. in 2006 may be more reliable, however, as they were obtained using a 72-atom supercell with four-k-point sampling and a plane-wave cutoff energy of 400 eV; Oba et al. used only one k-point with a cutoff energy of 380 eV.

The dumbbell oxygen interstitial in the neutral charge state is the alternative defect that has been suggested to have a low formation energy in p-type ZnO under O-rich conditions [325]. O_i can serve as both a donor and acceptor in ZnO with charge states ranging from (2+) to (2-) [85]. The debate over the formation energy of the oxygen interstitial in p-type O-rich ZnO is strongly related to the geometry of the defect. For Fermi energies within 0.5 eV of the valence band, Erhart et al. and Lee et al. claim that $O_{i,db}^0$ is the dominant point defect in the bulk. Although both $O_{i,db}^{2+}$ and $O_{i,db}^{1+}$ are stable, the (2+/1+) and (1+/0) ionization levels for the two defects are right at the valence band maximum [325,536]. This picture is not at odds with prior research, which had always revealed the *octahedral* oxygen interstitial to be a high formation energy defect in both Zn- and O-rich material. $O_{i,oct}$ is an acceptor in ZnO; its (0/1-) and (1-/2-) ionization levels are normally placed at $E_v + 0.3$ –0.6 eV and $E_v + 0.8$ –1.5 eV, respectively [85,86,88,535]. Erhart et al. also calculated formation energies for $O_{i,oct}$, in the (0), (1-), and (2-) charge states in close agreement with these values. A recent density-functional theory investigation may not be justified in claiming that the formation of V_{Zn}^0 is at least 1 eV more favorable than that of O_i^0 , as the work considers the octahedral instead of the dumbbell configuration of the defect [85]. The proposed ionization levels for the oxygen interstitial defects, as well as those for V_O , V_{Zn} , and Zn_i are summarized in Table 15 [85,86,88,326,535–537].

Uranium and oxygen vacancies, as well as oxygen interstitials, occur in undoped UO₂; they arise in the (4-), (2+), and (2-) charge states, respectively. Frenkel pairs, which consist of a vacancy and an interstitial of the same elemental type, V_O^{2+} and O_i^{2-} in this case, are the most stable defect in stoichiometric UO₂ [323,324,538–540]. Based on neutron diffraction studies [541] of interstitials in near-stoichiometric UO₂, Willis et al. proposed an anion Frenkel

Table 15

Experimentally and computationally determined ionization levels for oxygen vacancies, zinc vacancies, oxygen interstitials, and zinc interstitials in bulk ZnO

Defect	(2+/1+)	(1+/0)	(0/1−)	(1−/2−)	Other	Method	Reference
Vo	—	—	—	—	1.2 (2+/0)	Nonlinear spectroscopy	[538]
	—	—	—	—	0.2 (2+/0)	DFT-LDA	[86]
	—	—	—	—	0.5 (2+/0)	DFT-GGA	[88]
	—	—	—	—	1.1 (2+/0)	DFT-LDA	[537]
	—	—	—	—	1.6 (2+/0)	DFT-LDA	[536]
	2.9	1.94	—	—	2.42 (2+/0)	DFT-LDA + U	[326]
	—	—	—	—	1.1 (2+/0)	DFT-GGA	[85]
V _{Zn}	—	—	0.4	0.8	—	DFT-LDA	[86]
	—	—	0.05	—	—	DFT-GGA	[88]
	—	—	—	~0.45	—	DFT-LDA	[537]
	—	—	—	0	—	DFT-LDA	[536]
	—	—	0.2	0.6	—	DFT-GGA	[85]
O _i	—	—	0.27	1	—	DFT-LDA	[86]
	—	—	0.48	0.89	—	DFT-GGA	[88]
	—	0.1	—	—	1.45 (0/2−)	DFT-LDA	[537]
	—	—	0.7	1.7	—	DFT-LDA	[536]
	—	0.1	0.4	0.72	—	DFT-GGA	[85]
Zn _i	0.4	0.5	—	—	—	DFT-LDA	[86]
	—	—	—	—	1.07 (2+/0)	DFT-GGA	[88]
	—	—	—	—	~0.4 (2+/0)	DFT-LDA	[537]
	1.55	1.75	—	—	—	DFT-GGA	[85]

All values are in eV and referenced to the valence band maximum.

disorder model for the crystal (V_O^{2+} and O_i^{2-}); the alternative models of Schottky (V_O^{2+} and V_U^{4-}) or cation Frenkel disorder would have required a cation vacancy structure for the anion excess crystals. A later defect survey of UO_2 initially considered both the singly and doubly charged Frenkel pair [538]. The calculations revealed that the formation energy of the singly charged pair far exceeds that of the doubly charged pair. This result implies that the negatively charged oxygen interstitial provides a considerably deeper electron trap than the ion vacancy, whose effective charge is positive. Support for the predominance of divalent oxygen Frenkel disorder in UO_2 has also been obtained from subsequent diffraction experiments and modeling work [323,538–540]. Most researchers agree that only a small minority of Schottky defects will exist in the bulk [538,542]; recent *ab initio* calculations, for instance, have shown that the formation energies of the oxygen vacancy and interstitial are more than 10 eV lower than that of the uranium vacancy [323,324,543].

The principal point defects to be considered in Co_{1-x}O are cation vacancies and charge compensating electrons or holes; the cation vacancies can exist in the neutral, (1−), or (2−) state [544–551]. While an ideal point-defect model was initially considered suitable to interpret the properties of CoO , more recently, models involving cobalt vacancies and interstitials, oxygen vacancies, antisite defects, and complexes have been proposed [258,552]. The Debye–Hückel model of Nowotny, for example, which neglects the concentrations of neutral and singly ionized vacancies, as well as interstitials, accurately fits the experimental conduction data for Co_{1-x}O for all values of x [552]. The large ionic size of the oxygen atom in CoO serves as the main prohibitive factor to the easy formation of oxygen interstitials in the bulk [526]. In the 1970s, Dieckmann and Koel et al. both showed that V_{Co}^0 or $\text{V}_{\text{Co}}^{1-}$ are important at oxygen pressures around 1 atm, while $\text{V}_{\text{Co}}^{2-}$ becomes the majority defect at lower pressure [526,553]. As CoO under low P_{O_2} , when the concentration of defects is lower than about 0.1 at.%, displays very little non-stoichiometry, it can be assumed that $\text{V}_{\text{Co}}^{2-}$ is important in nearly stoichiometric material [258]. The ionization level for the (1−) vacancy has been predicted to be between 0.45 and 0.65 eV above the valence band maximum by several authors [526,544,546,549]. The slightly higher values obtained by Fryt and Bransky and Wimmer (0.98–1.1 eV) probably considered additional intrinsic defects such as Schottky or Frenkel type defects [547,554,555]. Values of between 0.65 and 0.77 eV above the valence band maximum have been found for the (1−/2−) ionization level of the cobalt vacancy [526,547–549].

6.2. Surface defects

6.2.1. Silicon

The dimer vacancy defect is actually a divacancy, and was first observed on Si(0 0 1) using scanning tunneling microscopy in 1985 [327,328]. Using DFT, Chan et al. have shown that the divacancy can have stable charge states of (0), (1 $-$), and (2 $-$) [28], although STM imaging studies have observed only the positively charged species [177]. It is possible that the failure to observe negatively charged dimer vacancies on Si(0 0 1) via STM or calculate positively charged dimer vacancies on the same surface is related to the rebonding configuration [556]. Also, the experimentally prepared surface might not be sufficiently n-type for negatively charged defects to arise, or tip-induced band bending might obscure the observation of negatively charged dimer vacancies [556]. The literature has also been confused by varying terminology. For example, Hamers and Kohler have designated the “type A” vacancy as a single dimer vacancy [329], and the “type B” vacancy as a double dimer vacancy [329]. However, there is at least one mention in the literature where the single dimer vacancy is referred to as a “type B” defect [177].

The positively charged single dimer vacancy imaged by Brown et al. is shown in Fig. 38. For the n-type material utilized in the experiment, perturbations associated with both positive and negative charge density are visible in empty-state images, whereas only those associated with negative charge density are visible in filled-state images [177].

An assortment of computational methods have been used to calculate the formation and ionization energies of the divacancy on Si(0 0 1) [28,333,334,557,558] as well as those of the monovacancy, which is not considered as frequently due to its high formation energy (0.87–1.50 eV) [28,177,559]. For the divacancy, the formation energies of the positive charge states increase as the Fermi energy moves away from the valence band, while those of the negative states decrease. The Fermi energy on the free Si(0 0 1) surface resides at $E_v + 0.41$ eV, meaning that divacancies should exist predominantly in the neutral charge state at temperatures near absolute zero. Only the neutral, (1 $-$), and (2 $-$) states are stable on the surface, in contrast to the bulk, where positively charged states can also exist for some values of the Fermi energy. The (0/1 $-$) and (1 $-$ /2 $-$) ionization levels of the surface dimer vacancy at 0 K have been calculated to be at 0.62 and 1.06 eV above the valence band minimum, respectively [28].

Dimer pair atoms on Si(1 0 0)-(2 \times 1) are buckled, with the “upper” atom residing slightly further above the surface than the “lower” atom. Hence, two distinct types of monovacancy can form: the upper monovacancy in response to removal of the upper atom, and analogously for the lower monovacancy. The charge state-dependent stability of both the lower and upper monovacancy has been investigated. The lower monovacancy supports only (0) and (1 $-$) states. The upper monovacancy is very similar to that of the bulk silicon vacancy [28] in terms of stable

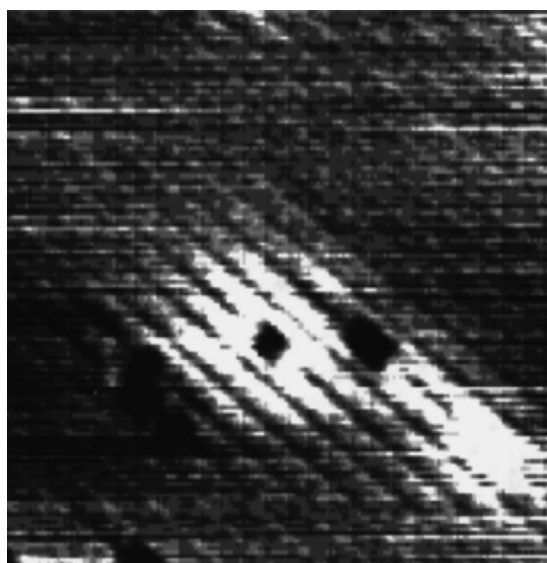


Fig. 38. Empty-state image of defects on Si(1 0 0)-(2 \times 1). The central defect is a divacancy that is positively charged.

Table 16

The ionization levels for the divacancy, lower monovacancy, and upper monovacancy defects on Si(1 0 0)

Si surface defect	(2+/0)	(0/1-)	(1-/2-)
Divacancy	–	0.62	1.06
Lower monovacancy	–	0.82	–
Upper monovacancy	0.07	0.62	1

All values are in eV and referenced to the valence band maximum.

charge states, however. The upper monovacancy exists in four charge states (2+), (0), (1−), and (2−), complete with negative-U defect behavior that leads to metastability of the (1+) charge state [194,270,271,378]. So far this case represents the only known example of negative-U behavior for a surface defect. Table 16 summarizes the findings of Chan et al., which include the ionization levels of the divacancy, lower, and upper monovacancy on Si(1 0 0) [28] (Table 16). Dev et al. estimated the entropy of ionization for the divacancy and monovacancy on Si(0 0 1)-(2 × 1) to predict the behavior of their ionization levels at temperatures between 0 and 1600 K [57]. For both types of defects, increasing the temperature causes a lowering of the ionization levels for negatively charged vacancies. The corresponding levels for positive vacancies remain unchanged, resulting in a decrease in the range of Fermi energies over which the neutral species is stable [57].

Subsequent work examined the unfaulted edge (UFE) vacancy on Si(1 1 1)-(7 × 7). Depending on the position of the Fermi energy, the UFE vacancy is stable in the (0), (1−), and (2−) charge states; positive charge states are not stable for any value of E_F [60]. For comparison, the monovacancy in bulk Si is stable as V²⁺, V⁰, V^{1−}, and V^{2−}, while the lower and upper monovacancies on Si(1 0 0)-(2 × 1) support charges of (0) and (1−), and (2+), (0), (1−), and (2−), respectively [57]. Clearly, there is only a modest correspondence in the number and type of stable charge states among the bulk and various surface crystallographic orientations. In considering the temperature dependence of the UFE vacancy, the (0/1−) level intersects the valence band at about 640 K, implying that UFE⁰ is not stable above this temperature for any value of Fermi energy. If, as reported by Himpel et al., a high density of surface states sets the Fermi energy near midgap for undoped, room temperature Si(1 1 1), Dev et al. suggest that the (2−) charge state of the vacancy dominates under virtually all temperatures and dopant concentrations [60,560–562] (Fig. 39).

6.2.2. Germanium

No computational work exists concerning the ionization levels of Ge(1 0 0) and Ge(1 1 1) surface defects, although several *ab initio* molecular dynamics works have investigated the energetics, geometries, and band structures associated with the undefected germanium surface [563–565]. Defects on the (1 0 0) crystal plane of germanium have not been explored experimentally to the extent of those on Si(1 0 0), in part due to the inherent stability of the (2 × 1) surface reconstruction [347,348]. Yang et al. have observed delocalized contrast surrounding these features on Ge(1 0 0)-(2 × 1), which potentially indicates that the defects are not charged relative to the neutral surface [346–348]. However,

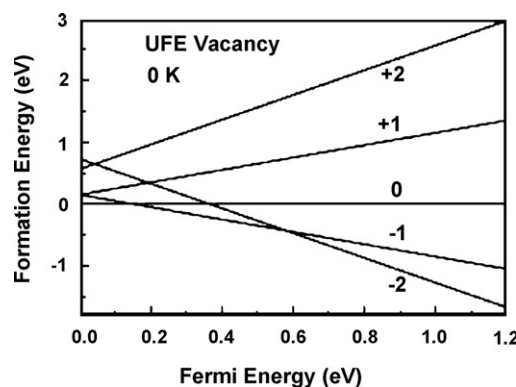


Fig. 39. Formation energies as a function of Fermi energy of various charge states of the UFE vacancies on Si(1 1 1)-(7 × 7) at 0 K. The formation energy is referenced to the neutral vacancy, while the Fermi energy is referenced to the valence band maximum.

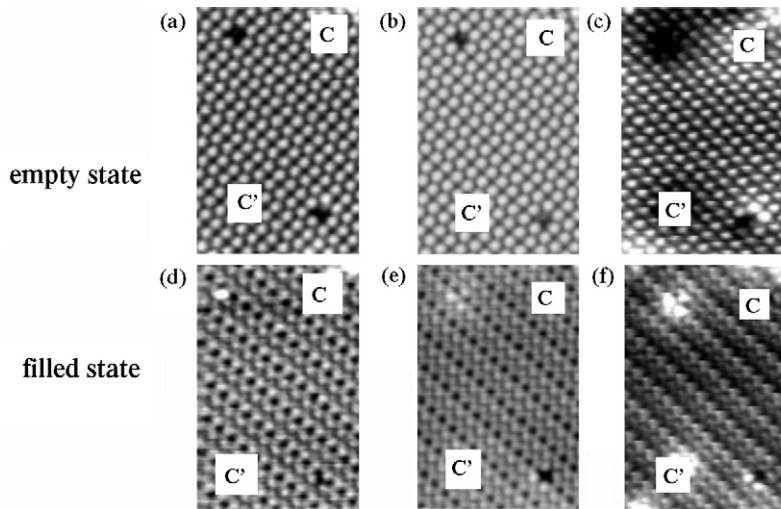


Fig. 40. STM images of the defects labeled as C (adatom vacancy) and C' (rest atom vacancy) on the Ge(1 1 1) surface taken at various sample voltages: (a) +2.5 V; (b) +1.5 V; (c) 0.5 V; (d) -2.0 V; (e) -1.0 V; (f) -0.5 V, respectively.

when Lee et al. put forth this explanation in 2000, they cited a similar absence of charged vacancies on Si(1 1 1)-(7 × 7) and Si(1 0 0)-(2 × 1); the evidence for charged defects on these surfaces is now very strong [28,177].

For Ge(1 1 1) – $c(2 \times 8)$, variable voltage STM has been used to demonstrate the existence of charged surface defects and to provide insight into the local band bending that they cause [178,346,348,566]. Five years after Molinàs-Mata and Zegenhagen first used STM to investigate the defects of the Ge(1 1 1) – $c(2 \times 8)$ reconstruction, Lee et al. revealed the presence of surface defects with a net charge [346,426,567]. The defects on Ge(1 1 1) can be classified into three categories: adsorbed H atoms, Ge atom vacancies, and defects due to antiphase shift [178]. There is no spatial designation assigned to the vacancies, in contrast to those on Si(1 1 1)-(7 × 7), which supports four distinct adatom vacancy locations, the unfaulted corner (UFC), unfaulted edge (UFE), faulted corner (FC), and faulted edge (FE) [60,255]. All of the possible Ge surface defects are voltage-dependent, indicating that they are either charged point defects or neutral composites of defects with opposite charges (Fig. 40). The germanium vacancy on the surface is associated with a bright spot due to the charge localized at the dangling bonds of the three non-bonded first-layer atoms. From the direction of surface band bending, Lee et al. inferred that the adatom vacancy defect is negatively charged; the UFE vacancy on Si(1 1 1) investigated by Dev et al. is also negatively charged [60,178,346]. In some STM images, however, the vacancy appears to be neutral, a phenomenon the authors attribute to neutralization of the negative adatom vacancy by a positively charged rest-atom vacancy, although no individual positively charged rest-atom vacancies were observed [346]. The authors make no mention of the degree of band bending or the concentration of adatom vacancy defects that would be required to lead to Fermi energy pinning over the whole surface.

The antiphase shift vacancy discussed by Lee et al. is a point defect generated by a shift of an adatom row by a half period in the row direction; it perturbs the $c(2 \times 8)$ reconstruction and causes a line stacking fault, or antiphase domain boundary. In some images the point defect is negatively charged, while in others it appears to be neutral relative to the background of the unperturbed surface. No comparable defect is observed on the Si(1 1 1)-(7 × 7) reconstruction.

6.2.3. Gallium arsenide

GaAs(1 1 0) is decorated with charged gallium and arsenic vacancy defects; the observation of these charged defects on n- and p-type material is a result of localized defect states introduced in the band gap by the vacancies [174]. STM has been used extensively to image the vacancies on GaAs, and to determine their charge states [174,175,568–571]. Under gallium-rich conditions, V_{As}^{1+} and V_{As}^{1-} are the dominant defects for p-type and n-type GaAs(1 1 0), respectively, whereas under arsenic-rich conditions, charged gallium vacancies and arsenic adatoms become important [197]. Surface photovoltage measurements and density-functional theory and *ab initio* calculations have been employed to obtain values for defect ionization levels [237,241,572], although the determined positions of these levels vary widely, as well as the degree of band bending they cause [179,566,573–575]. As opposed to bulk gallium arsenide, in which ionized As_{Ga} and Ga_{As} play an important role in the defect chemistry, antisite defects have yet to be

observed on the GaAs surface. From DFT calculations, however, it is known that the surface and near-surface antisite defect has no charge-transfer level within the band gap, and thus, does not alter the electronic properties of the (1 1 0) surface [197,351]. Nevertheless, Schwarz et al. find the surface antisite defects to be most stable in the neutral charge state, in contrast to those in the bulk, which are known to act as either double acceptors (Ga_{As}) or double donors (As_{Ga}) [197].

Arsenic and gallium vacancies at the surface are formed by the following surface-gas reactions:



where there is a noticeable difference in the number of gallium atoms surrounding the vacancy [576]. Scanning tunneling microscopy images reveal the presence of missing arsenic atoms, or charged surface anion vacancies, on Ga(1 1 0) [179,349,577] (Fig. 41). Based on the two bright spots in the cation sublattice observed around the arsenic vacancy, Lengel et al. proposed a $\text{V}_{\text{As}}^{2+}$ defect on p-type GaAs(1 1 0) [179].

Chao et al. used a method based on STM and compensation by ionized dopant atoms to determine an isolated arsenic vacancy charge of (1+) [568,569], in agreement with the work of Zhang et al., who suggested that $\text{V}_{\text{As}}^{2+}$ is 1.4 eV higher in energy than $\text{V}_{\text{As}}^{1+}$ [241]. Yi et al., Kim and Chelikowsky, and Zhang et al. all considered the Fermi energy dependence of the formation energies of $\text{V}_{\text{As}}^{1-}$, V_{As}^0 , and $\text{V}_{\text{As}}^{1+}$ [241,572,578]. *Ab initio* calculations performed by Yi et al. found the (1-) arsenic vacancy to be the predominant surface defect for all Fermi energies within the band gap [241,572,578]. In contrast, the latter two groups identified $\text{V}_{\text{As}}^{1+}$ and $\text{V}_{\text{As}}^{1-}$ as the dominant defects for p-type and n-type GaAs(1 1 0), respectively. They also found that V_{As}^0 is stable only over a narrow energy range, as the (1+/0) ionization level is fairly close to that of (0/1-); more recently, it has also been suggested that the arsenic vacancy behaves as a negative-U center [197,237,241]. The energy levels calculated by Kim and Chelikowsky and Zhang et al. deviate considerably from one another: DFT calculations predicted (1+/0) at $E_v + 0.32$ eV [241] and $E_v + 0.10$ eV [237] and (0/1-) at $E_v + 0.40$ eV [241] and $E_v + 0.24$ eV [237]. Schwarz et al., the authors who proposed a negative-U center for the arsenic vacancy, placed the (1+/1-) level at about 0.22 eV above the valence band maximum [197]. Kim and Chelikowsky have cited the inaccuracy in evaluating the band-maximum line-up of different charge states as a possible reason for the varying ionization level values [237].

Under arsenic-rich conditions, two different types of charged defects become important: gallium vacancies and arsenic adatoms. The surface gallium vacancy bears little resemblance to the bulk gallium vacancy; $\text{V}_{\text{Ga}}^{3-}$ is the

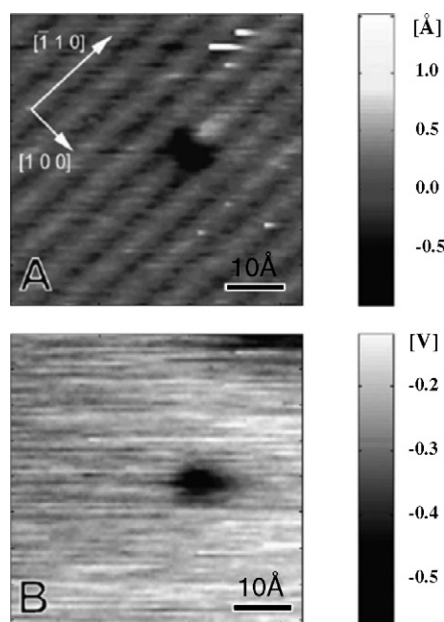


Fig. 41. Topography (A) and surface photovoltage images (B) taken simultaneously at $V_s = -2.8$ V around an arsenic vacancy on GaAs(1 1 0).

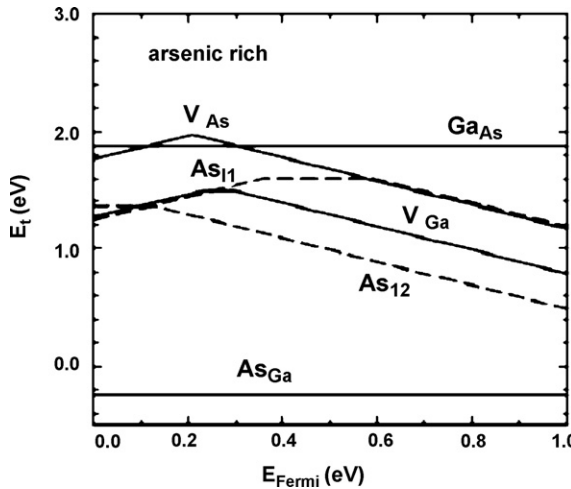


Fig. 42. Formation energies of surface point defects on GaAs(1 1 0) as a function of the surface Fermi level for arsenic-rich conditions.

lowest energy defect in n-type Ga-rich GaAs. On the surface, the (3 $-$) state does not exist, and for n-type Ga-rich GaAs(1 1 0), V_{Ga}^{1-} has a formation energy that is about 1 eV greater than that of V_{As}^{1-} [197]. Normally, without special treatment, gallium vacancies can be observed on the surface of n-type GaAs wafers [243]. They were first identified in filled-state STM images of n-type GaAs(1 1 0) by Lengel et al. [579]. Schwarz et al. calculated ionization levels for the gallium vacancy of $E_v + 0.24$ eV and $E_v + 0.31$ eV for the (1 $+$) and (1 $-$) states, respectively [197]. For p-type material, V_{Ga}^{1+} is almost degenerate in formation energy with the positively charged arsenic adatom [197]. The same authors calculated two ionization levels for the arsenic adatoms As_{11} : (1 $+0$) at $E_v + 0.36$ eV and (1 -0) at $E_v + 0.60$ eV [197]. The cation-bound adatom was predicted to be (1 $-$) for all positions of the Fermi energy except for extremely p-type material, in which the neutral charge state of the defect is stable, as shown in Fig. 42.

6.2.4. Other III–V semiconductors

As revealed in the STM images of Fig. 43, many III–V semiconductor surfaces are decorated with charged defects similar to those on GaAs(1 1 0) [181,182,349,580–583]. For example, under indium-rich conditions, V_{P}^{1+} and V_{P}^{1-} have low formation energies on p-type and n-type InP(1 1 0), respectively [174,180,181,584,585]. Interestingly, antisite defects, rather than indium vacancies or phosphorus adatoms, are predicted to arise under anion-rich conditions [181]. While the morphology and electronic structure of the surfaces of the boron and nitride-containing semiconductors have been investigated, little information exists concerning their charged defects [356,364,586]. Typically, the (1 0 1 0) ZnO surface is used as a reference system for AlN, GaN, and InN [356]. For a more thorough discussion of point defects on compound semiconductor surfaces, Ph. Ebert has published over thirty journal articles on the subject. Two reviews offer a general understanding of the characteristics of charged defects on groups III–V surfaces, including a summary of defects observable using STM, shown in Fig. 43 [45,174].

Valuable insight can be gleaned from comparing the ionization levels of defects on the different indium-group V compounds. For InP and InAs, the anion vacancy ionization levels (1 $+0$) and (0 $1-$) are located around the center of the band gap; for InSb, on the other hand, the (1 $-$) charge state is stable for all Fermi energies within the band gap (Fig. 44). In contrast to the anion vacancy in bulk InP, InAs, and InSb, the surface anion vacancy can be in the (1 $+$), (0), or (1 $-$) charge state [239]. Using combined STM and photoelectron spectroscopy, Ebert et al. obtained a (1 $+0$) ionization level for V_{P} in InP of $E_v + 0.52$ eV and $E_v + 0.45$ eV corresponding to the nonsymmetric and less stable symmetric vacancy, respectively [240]. Qian et al. used density-functional theory to obtain ionization levels of 0.388 and 0.576 eV above the valence band maximum for (1 $+0$) and (0 $1-$) in InP, respectively, with a calculated band gap of 1.11 eV [239]. The same authors also determined the levels for V_{As} on InAs(1 1 0); (1 $+0$) and (0 $1-$) are 0.20 and 0.277 eV above the valence band maximum [239]. For InSb(1 1 0), Qian et al. found no ionization level for the Sb vacancy within the band gap [239]. The anomalous behavior of the antimony vacancy can be explained in terms of the electronic configuration of the defect. Of the three In-based compounds, InSb shows the strongest hybridization, with the localized surface state derived from the valence and conduction states. In order to reduce the total energy when the

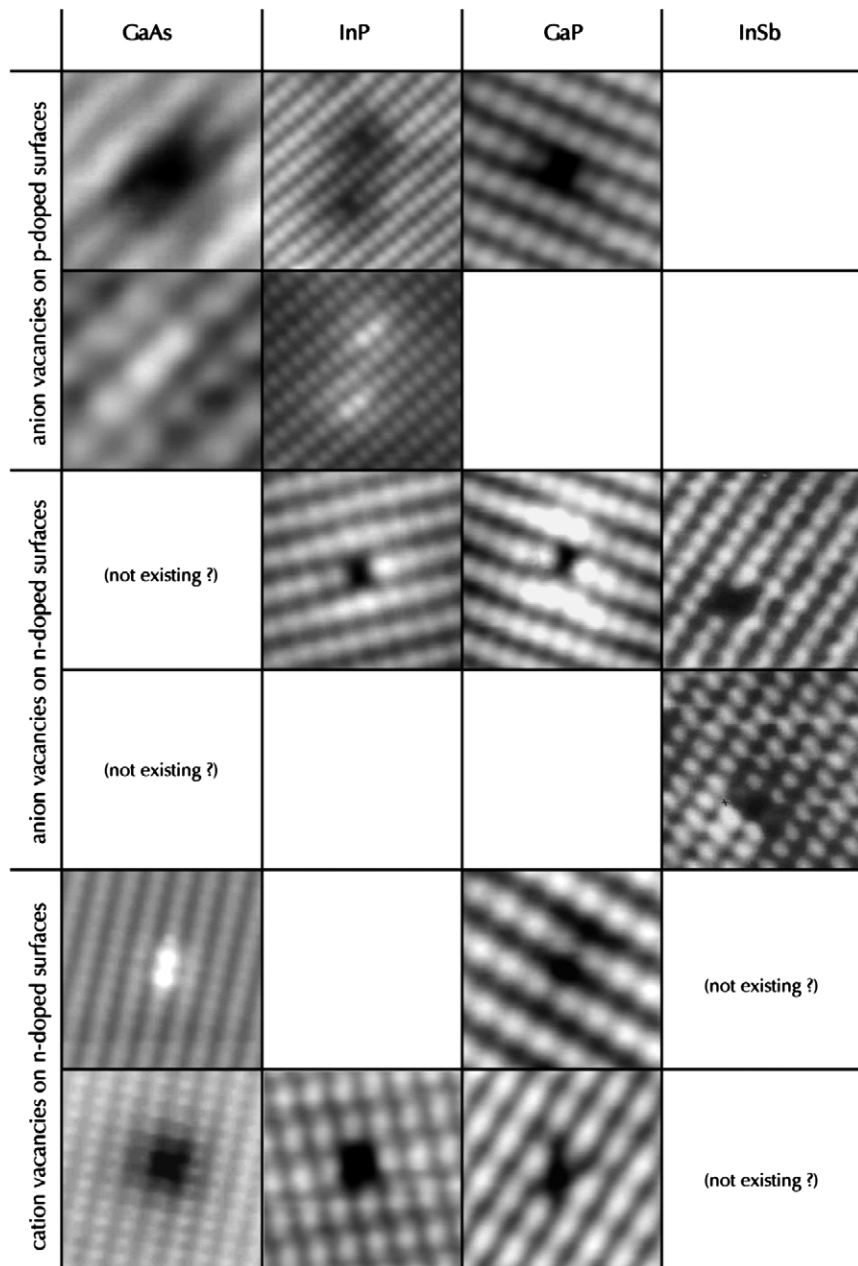


Fig. 43. Anion and cation vacancies on different materials. The upper and lower frames of each vacancy show the occupied and empty state STM images, respectively.

Fermi energy is shifted from the valence band maximum to the conduction band minimum, the vacancy state of InSb, located within the valence band, is always occupied [239].

6.2.5. Titanium dioxide

The bridging (BOV) and in-plane (POV) oxygen vacancies that occur on the rutile $\text{TiO}_2(1\ 1\ 0)$ surface are also easily ionized. It has recently been suggested that these defects can occur as BOV^{2+} , BOV^{1+} , POV^{2+} , and POV^{1+} , in addition to BOV^0 and POV^0 [246,250,367,587]. This phenomenon makes sense, as the existence of positively charged oxygen vacancies in bulk TiO_2 is well known. The low surface free energy of anatase TiO_2 leads to a different tendency

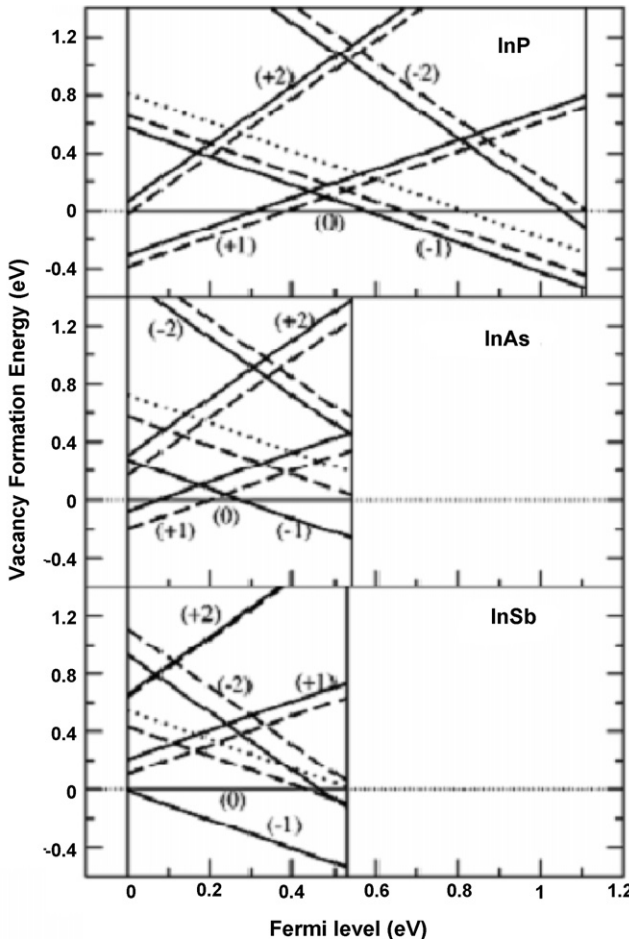


Fig. 44. Fermi-level dependence of the formation energy of different charged anion vacancies on the (1 1 0) surfaces of InP, InAs, and InSb. Solid, dashed, and dotted lines denote the symmetric, nonsymmetric, and one loosely rebonded dimer symmetric configurations.

toward reduction and/or the formation of oxygen vacancies compared to rutile TiO_2 . Despite the fact that several studies have considered the effect of surface defects on adsorbate reactions, the existence and possible structure of the surface oxygen vacancy are still uncertain [588,589].

Using the embedded-cluster numerical discrete variational method, Chen et al. suggested the existence of charged F-type centers, i.e. positively charged oxygen vacancies, on TiO_2 (1 1 0) [250]. Positively charged bridging and in-plane oxygen vacancies can form when negatively charged, rather than neutral, bridging-oxygen ions (O^{1-} and O^{2-}) are removed [246]. Most computational studies of the reduced (1 1 0) TiO_2 -(1 × 1) surface predict gap states, although the published reports do not come to an agreement as to the surface defect structure responsible for these states [590]. This is in contrast to V_{O}^{2+} in bulk TiO_2 , which does not give rise to any defect levels within the band gap [320]. Wang et al. recently compared the energetics behind the formation of in-plane and bridging oxygen vacancies in the neutral, (1+), and (2+) states [246]. The DFT-derived formation energies of all three states of both defects are tabulated in Table 17. The ionization potential for losing one electron to form BOV^{1+} is -0.9 eV, while the second ionization potential to form BOV^{2+} is 1.3 eV; these values indicate the stability of BOV^{1+} [246]. The first and second ionization potential of the POV are -0.7 and 1.1 eV, respectively. These numbers can be compared to the formation energies detailed above for the BOV, revealing a stability order of the oxygen vacancies on the TiO_2 (1 1 0) surface as $\text{BOV}^+ \approx \text{POV}^+ > \text{BOV} \approx \text{BOV}^{2+} > \text{POV} \approx \text{POV}^{2+}$ [246].

In 2000, Heibenstreit reported the first scanning tunneling microscopy study of single-crystal anatase. STM images of anatase surfaces must be interpreted differently from those of rutile surfaces. In the former, the corrugated nature of the surface causes the two-fold-coordinated oxygen atoms at the highest position to be imaged bright, whereas in the

Table 17

The formation energies (in eV) of the neutral and charged vacancies on $\text{TiO}_2(1\ 1\ 0)$ according to Wang et al.

Defect	Formation energy of given charge state (eV)		
	(0)	(1+)	(2+)
BOV	7.9	4.2	8.1
POV	8.3	4.5	8.6

latter, the 3d Ti-derived empty defect states appear brighter [591]. Hebenstreit et al. observed four types of imperfections on anatase (1 0 1), yet were unable to easily associate any of them with the oxygen vacancy that is easily identified in studies of rutile (1 1 0) (Fig. 45). The authors suggested that either the anatase (1 0 1) surface is very stable against the loss of two-fold-coordinated oxygen atoms, or STM is not capable of imaging such vacancies. It is still undetermined as to whether these atomic-scale imperfections are oxygen vacancies. If the imperfections are point defects, they would be present in far lower number densities than are observed on rutile (1 1 0). This low concentration would not, however, be at odds with the general surface science picture of the material; not only is the surface energy of anatase (1 0 1) known to be low, but also Woning and van Santen have predicted the easier reduction of rutile versus anatase titanium dioxide surfaces [83,587,592–594]. Synchrotron photoemission spectroscopy experiments performed by Thomas et al. have indicated that the defects may be surface O vacancies in the form of surface Ti^{3+} . The authors observed the defects to give rise to a state below E_F similar to that seen on the surface of rutile TiO_2 [595]. From the band gap state at 1.1 eV, and associated resonance in the spectrum, they suggested that Ti 3d contributes to the defect state, probably as a result of surface O vacancies [595].

6.2.6. Other oxide semiconductors

The intrinsic surface defects on ZnO , UO_2 , and CoO have not been explored to the same extent as those on titanium dioxide. When the rare natural form of ZnO , zincite, is cleaved, nonpolar (1 0 1 0) surfaces result; for this surface, it is known that the most commonly occurring defects are oxygen vacancies [596–598]. Papers published between 1957 and 1979 by Heiland et al. indicated the existence of donor-type ZnO defects near the surface, with ionization levels at about 0.2 eV below the conduction band minimum [599]. The same picture is not true for the (0 0 0 1)-Zn surface, where one of two processes can occur: either zinc atoms are removed from the lattice, leading to the formation of (2+) zinc vacancies, or oxygen atoms are adsorbed to the surface [373,598,600]. Although oxygen and zinc vacancies in bulk ZnO are known to exist in an assortment of charge states, when they are discussed in relation to the zinc oxide surface, no mention of ionization levels is made.

Defects can be artificially created on UO_2 by ion sputtering; the removal of surface oxygen atoms creates charged oxygen vacancies on the surface [601,602]. In STM images taken by Castell et al., bright lattice positions correspond to uranium sites; point defects in the image simply appear as vacancies, without causing a detectable brightening or darkening of the uranium sites [602] (Fig. 46). Although Muggelberg et al. observed the stabilization of the $\text{UO}_2(1\ 1\ 0)$ surface through the creation of vacancy defects, they make no mention of their charge state [603].

Oxygen vacancy defects are also the predominant surface defects on ionic cobaltous oxide [604]. When a surface O^{2-} ion is removed from the lattice, two electrons must be trapped at the defect site in order to maintain local charge

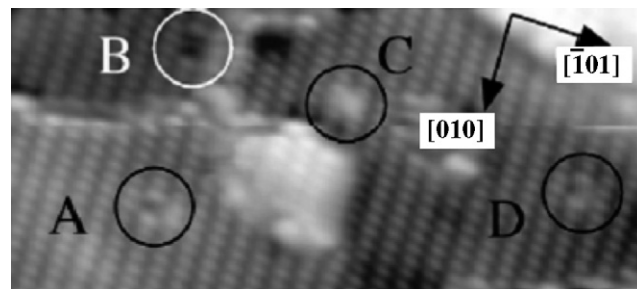


Fig. 45. STM image of an anatase (1 0 1) surface. Four features could possibly represent oxygen vacancies including (A) single black spots; (B) double black spots; (C) bright spots; (D) half black spots.

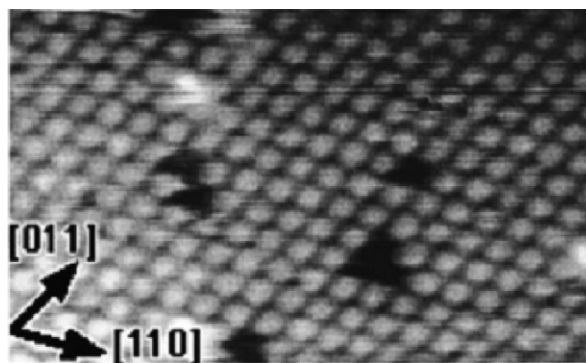


Fig. 46. Empty states STM image of the $\text{UO}_2(1\ 1\ 1)$ surface with a sample bias of 1.9 V. Missing uranium ions do not create an observable perturbation on their neighbors.

neutrality. Investigating the $\text{CoO}(1\ 0\ 0)$ surface with photoemission spectroscopy reveals that the oxygen vacancy is associated with an emission in the bulk band gap just above the valence band maximum [372]. Unusual conductivity behavior arises from the creation of isolated oxygen vacancies on $\text{CoO}(1\ 1\ 1)$, in comparison to other transition-metal oxides. Mackay et al. found that the defective surface was less conducting than the as-cleaved surface, despite the fact that electrons must be trapped at the oxygen vacancies [371,605].

7. Diffusion of charged defects

7.1. Bulk defects

7.1.1. Silicon

Remarkably, considerable debate still surrounds the mechanism of defect diffusion in silicon [75,78,145,403,606–610], the question of whether interstitial atoms are the prime mediators (especially at temperatures below about 900 °C) [75], and the value of the interstitial formation energy. Computational approaches [261–265,396,403,611] have not proven to be sufficiently reliable to resolve these questions, with calculated formation energies ranging from 2.2 to 4.5 eV. Recent experiments by Seebauer et al. have shown [24] that surface chemical bonding state affects the self-diffusion rate in silicon by influencing the concentration of point defects within the solid. Diffusion measurements have typically been made in the presence of surfaces whose dangling bonds are largely saturated with adsorbates of various kinds. However, maintaining an atomically clean surface opens a pathway for native point defect formation at the surface that is much more facile than corresponding pathways within the solid. The surface pathway fosters a much larger solid defect concentration on a several-hour laboratory time scale than in conventional approaches, with correspondingly larger self-diffusion rates, as shown in Fig. 47. Data taken under clean conditions therefore yields substantially lower values for the defect formation energy. Also, these experiments employed a kinetic short-time limit [612]. This short-time limit circumvents a problem of data interpretation that has plagued most experimental work on Si self-diffusion.

The energetics and mechanisms of vacancy and self-interstitial diffusion in silicon have been explored extensively [80,280,613]. Older literature has suggested that self-interstitials mediate diffusion at high temperatures, while vacancies dominate at lower ones. More recent results, including those obtained in this laboratory, argue for the predominance of interstitials at all temperatures [145,612]. Several mechanisms of self-interstitial migration in silicon have been posited: direct-interstitial, interstitial-interchange or “kick-out” (where interstitial atoms exchange with the lattice), and pair-diffusion (where Si interstitials migrate along with Si vacancies) [79,231]. Research from this group, which will be published shortly, definitively reveals the existence of an interstitial-dominated diffusion mechanism at all temperatures, most likely direct diffusion without lattice exchange. Experimental measurements of defect diffusivities, which often yield both a pre-exponential factor and activation energy for site-to-site hopping, have likely been critically affected by adsorbate saturation on the sample surface. Even computational investigations of silicon self-interstitial diffusion by DFT, tight-binding, and quantum-based molecular dynamics methods all exhibit an enormous variance [231]. The theoretical investigation of self-interstitial diffusion is complicated by the assortment of

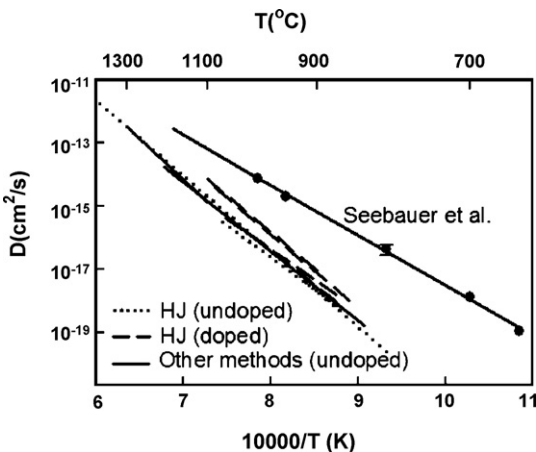


Fig. 47. Self-diffusion coefficients in n-doped Si for the atomically clean (1 0 0) surface measured by Seebauer et al. compared with other literature reports with various methods and doping levels. “HJ” refers to “heterojunction method.” The numbers for the clean surface lie much higher than the others, and imply a correspondingly larger defect concentration that must be caused by the surface.

configurations available to the defect, the stability of which is known to depend upon charge state. For example, some authors believe that the saddle point for the migration of Si_i^0 , Si_i^{1-} , and Si_i^{2-} (all of which prefer the ⟨1 1 0⟩-split configuration) is the tetrahedral site, while others believe that it is the hexagonal site [30]. To further complicate matters, the fraction of time spent in different self-interstitial configurations during migration is a strong function of temperature [81]. In addition, studies differ in the details of the computational method, a result of the debate over which method is most applicable to the combination of strong and weak bonds in many interstitial configurations [53,264,265].

As the energetics of self-interstitial diffusion can only be quantified indirectly, the experimental results reveal a wide variance. Also, the distinction between overall diffusion activation energies, defect formation energies, and migration barriers for site-to-site hopping is also often unclear [79]. In early quenching experiments, Seeber and Frank showed that self-interstitial defects had activation energies of migration of 1.5 eV or more [417]. Taniguchi and Antoniadis inferred an activation energy of 4 eV for the effective diffusion of self-interstitials in silicon from phosphorus-enhanced diffusion [614]. From the in-diffusion of Pt in silicon, Mantovani et al. estimated an activation energy of the self-interstitial diffusion coefficient of 5.1 eV [615]. Stikwijk et al. studied the diffusion of gold in silicon with the aid of a neutron activation analysis to obtain a comparable activation energy of 4.8 eV [616]. Bronner et al., however, obtained a smaller overall activation energy of 2.4 eV from the getting of gold in silicon [617]. This is closer to the recent 1.86 eV value of Wijaranakula based on experiments where oxygen donors were used to trace Si interstitial motion [618]. Tan and Gosele determined a 0.4 eV activation energy for the diffusion of self-interstitials based on the assumption that interstitial-type dislocation loops are formed in the bulk, which they acknowledge as highly controversial [619]. The energy barrier for the site-to-site hopping of the silicon self-interstitial is always considerably smaller. Panteleev et al. characterized the diffusion of self-interstitials with photostimulated electron emission, obtaining a migration energy barrier of 0.12 ± 0.04 eV [620]. By monitoring the disappearance of proton-beam-generated point defects below room temperature, Hallen et al. assigned an migration energy barrier of 0.065 ± 0.015 eV to Si_i [621].

In the early 1980s, Baraff and Schluter, Car et al., and Bar-Yam and Joannopoulos used Green’s function techniques to consider the isolated diffusion of both Si_i^{2+} and Si_i^0 [213,282,622]. For example, the latter authors found a low energy barrier, 1.1 ± 0.3 eV, for the exchange of Si_i^{2+} with a lattice atom; the migration of the tetrahedral self-interstitial to the hexagonal site has an identical energy barrier [282]. The hopping mechanism of the neutral defect is less obvious due to the near degeneracy of the hexagonal, bond-centered, and lattice sites. Exchange of Si_i^0 with a lattice atom is associated with an energy barrier of 1.7 ± 0.4 eV. In early DFT work, Nichols et al. obtained an activation energy for Si_i^0 diffusion of 4.0 eV with a migration energy barrier of 0.4 eV [623]. Kato et al. proposed a combined mechanism of direct-interstitial and interstitial-interchange for the diffusion of Si_i^0 , with an associated energy barrier for migration of 1.2–1.7 eV. Their corresponding value for Si_i^{2+} , which is thought to diffuse solely via site-to-site hopping, is 1.3–2.3 eV [79]. Gilmer et al. employed a classical MD simulation to obtain a result of 0.9 eV

[624]. Zhu et al. reported a barrier of 1.4 eV for Si_i^0 , which decreases to 0.9 and 0.7 eV for Si_i^{1+} and Si_i^{2+} , respectively [625]. A high barrier of 1.37 eV for Si_i^0 has been computed by Tang et al. from tight-binding molecular dynamics simulations for neutral Si [280]. Lee et al. reported a range of 0.15–0.18 eV in LDA for Si_i^0 depending on path, with corresponding values of 0.47–0.59 eV for Si_i^{1+} and a lower bound of 1.0 eV for Si_i^{2+} [30]. These authors also postulated a charge-assisted hopping mechanism in which the interstitial is neutral in the initial and final states, but converts to Si_i^{2-} in the transition state. The barrier for such motion was calculated to be less than 0.05 eV. Leung et al. used DFT to obtain a range of barriers of 0.03–0.15 eV in LDA and 0.18–0.20 eV in the generalized gradient approximation (GGA) for Si_i^0 , with the results depending on diffusion path [264,626]. Needs et al. determined energy barriers for the diffusive jump of the interstitial defect between the hexagonal and split- $\langle 1\ 1\ 0 \rangle$ sites of 0.15 eV (LDA) and 0.20 eV (GGA) [261]. Using maximum likelihood methods and a wide variety of literature reports, this group has estimated a migration energy barrier of 0.72 ± 0.03 eV [231].

Experimentally and computationally determined vacancy diffusion parameters suffer from the same uncertainties as their interstitial counterparts. Watkins was the first to use EPR and DLTS to report diffusion coefficients and migration energies for $\text{V}_{\text{Si}}^{2+}$, V_{Si}^0 , and $\text{V}_{\text{Si}}^{2-}$ [101,103,375]; these charge states were associated with barriers of 0.32 eV [104,375], 0.33 eV [104], and 0.18 ± 0.02 eV [102], respectively. Neutron irradiation studies in p-type and n-type silicon yield similar values of 0.3–0.4 eV and 0.17, in that order [627]. Ershov et al. investigated the Fermi-level dependence of defect annealing kinetics after photo-stimulated electron emission. These authors associated migration energies of 0.48 ± 0.05 , 0.33 ± 0.03 , and 0.18 ± 0.02 eV with V^{1+} , V^0 , and V^{1-} [628]. It can be inferred that they are, in fact, referring to the doubly charged defect species in comparing their values to those from other studies. For example, Panteleev et al. measured a value of 0.18 eV for the migration energy of V^{2-} and one of 0.25 eV for the single negatively charged defect, V^- [620].

Early simulations based on the supercell approximation, Car-Parinello approach, Stillinger–Weber interatomic potential, and empirical tight-binding method all determined migration energies of between 0.3 and 0.43 for V_{Si}^0 [213,277,623,624,629,630]. In 1986 and 1992, Kelly et al. and Sugino and Oshiyama calculated energy barriers for the (2+) vacancy of 0.42 and 0.4 eV, respectively [631,632]. The value that Sugino and Oshiyama proposed for the migration energy of V^{1-} , 0.1 eV, differs considerably from the experimental value of Panteleev and co-workers [620,632]. Using molecular dynamics simulations, Tang et al. obtained a migration energy barrier of only 0.1 eV for V^0 , which they attribute to an error in the calculation method, as the overall activation energy of 4.07 eV compares well with that from experiments [280]. More recent theoretical predictions are in good agreement with almost all of the experimental values, although few authors have considered the diffusion of V^{2-} and V^{2+} [99,100]. Bernstein et al. calculated a migration energy barrier of 0.3 eV for the neutral vacancy with a nonorthogonal tight-binding model Hamiltonian based on the extended Huckel approach [99]. Using the Car-Parinello molecular dynamics code with GGA functional, Kumeda et al. found a migration barrier for V_{Si}^0 of 0.58 eV [100]. El-Mellouhi et al. associated a migration energy barrier of 0.40 ± 0.02 eV with the movement of the V_{Si}^0 along the $\langle 1\ 1\ 1 \rangle$ direction; the defect passes through the metastable split-vacancy site before reassuming the more stable tetrahedral configuration [613].

7.1.2. Photostimulated diffusion in silicon

There is physical reason to suppose that illumination can affect bulk diffusion in semiconductors nonthermally. Both vacancies and interstitials (of Si and dopants) are capable of existing in multiple charge states. The formation energy and entropy [49,50] for the forward reaction and the migration energies [609] of the point defects thus formed can vary with charge state. Since illumination affects the availability of charge carriers and therefore the most favored charge state of the defects, illumination can, in principle, change both the formation and migration energies (and entropies) of point defects [633]. There has long been evidence that photostimulation may nonthermally influence the diffusion in semiconductors such as Si [634–639]. In all these cases, however, heating by the probe light or changes in heating configuration as probe intensity varied cast doubt on the interpretation of the results. More definitive results have awaited experimental configurations in which heating and illumination could be decoupled.

Seebauer et al. have developed a method for decoupling heating and illumination to definitively identify nonthermally stimulated self-diffusion in Si [640]. Fig. 48 compares diffusion profiles for illuminated and unilluminated specimens of n-type material. Illumination increases the diffusivity substantially. By contrast, no such effect could be observed for p-type material in the temperature range 600–900 °C for intensities up to 2 W/cm². The difference in behavior between n and p-type material gives strong evidence that the observed enhancement in n-Si is genuine, and not an artifact of some unknown heating or similar spurious effect. The diffused profiles do not fit the

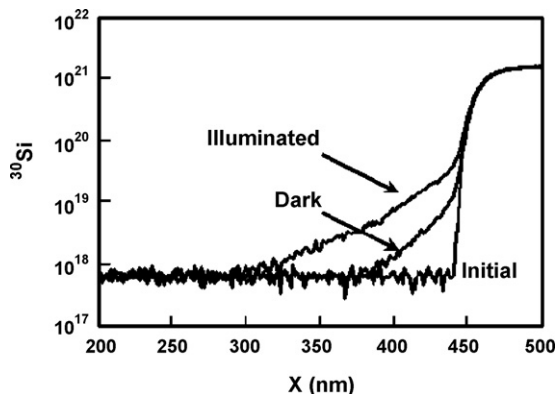


Fig. 48. SIMS profile of ^{30}Si that has diffused in a ^{28}Si matrix, showing nonthermal illumination enhancement of diffusion. Annealing conditions are 800 °C for 1 h in n-type material.

Gaussian form expected for concentration-independent diffusion of a single species. Instead, the profile looks closer to linear on a logarithmic scale, signifying an exponential decay. Such behavior has been observed in the case of boron diffusion in Si [641–643], and offers a signature of diffusion by a quick-moving intermediate species such as an interstitial [612]. Thus, it is the interstitials that are affected by photostimulation.

7.1.3. Germanium

The mechanisms and energetics of self-diffusion in germanium, particularly as they relate to charge state effects, have received less attention than those in silicon. In contrast to silicon, however, it is commonly believed that self-diffusion in germanium occurs via a vacancy mechanism [268,644–647]. Seeger and Chick and Van Vechten both found the formation energy of the germanium interstitial to be prohibitively high; the interstitial is thus unable to influence diffusion at equilibrium [66,648]. Based on the known ionization levels of the defect, it can be inferred that V_{Ge}^0 contributes greatly to self-diffusion in p-type material whereas $\text{V}_{\text{Ge}}^{2-}$ plays a greater role in n-type material. Logically, for intermediate Fermi levels within the band gap, the (1-) germanium vacancy should also contribute to self-diffusion.

The vacancy diffusion process has been studied and analyzed by an assortment of techniques including radioactive tracers, sectioning by grinding or sputtering, and Steigmann's or Gruzin's absorption method; many of these methods yield similar values for the activation energy of site-to-site diffusion, ~3.0 eV, but do not discuss the effect of defect charging [78]. Mayburg and Vanhellemont et al., for example, obtained vacancy formation energies on the order of 2.0 eV and migration energies of approximately 1.1 eV [649,650]. Ershov et al. found migration energies for the neutral and singly charged vacancy in Ge of 0.52 ± 0.05 and 0.42 ± 0.04 eV, respectively [628]. By measuring the effect of dopants on self-diffusion and modeling the dependence of the negatively charged vacancy concentration on the Fermi energy, Werner et al. determined that $\text{V}_{\text{Ge}}^{1-}$ and V_{Ge}^0 are responsible for 77 and 23% of the transport for self-diffusion in intrinsic material at 700 °C, respectively [651]. No experimental data exists for the diffusion of self-interstitials in germanium.

As for silicon, the range of calculated germanium defect formation and migration energies is quite large [652]. Several computational values closely match those obtained from experiment, with formation energies of between 1.9 and 2.07 eV and migration barriers of 0.95–1.0 eV [267,288,430–432,653,654]. On the other hand, Soma et al. and Lauwaert et al. calculate considerably lower vacancy migration energies, 0.17 and 0.31–0.40 eV, respectively [652,655]. More recently, the formation energy of the vacancy has been predicted to be significantly higher, more on the order of 3.1–3.6 eV [652,656,657]. For example, Lauwaert et al., using a molecular dynamics code with a Stillinger–Weber potential, obtained a vacancy formation energy of 3.38 eV and migration energy of 0.17 eV [652]. Coincidentally, these authors confirmed considerably higher values for self-interstitials, 5.81 and 0.42 eV, respectively, confirming that such defects do not contribute to diffusion in germanium.

7.1.4. Gallium arsenide

For gallium arsenide and the other III–V semiconductors whose crystal structure consists of two elemental sublattices, the basic mechanism of self-diffusion is one of migration within a specific sublattice [658]. As illustrated

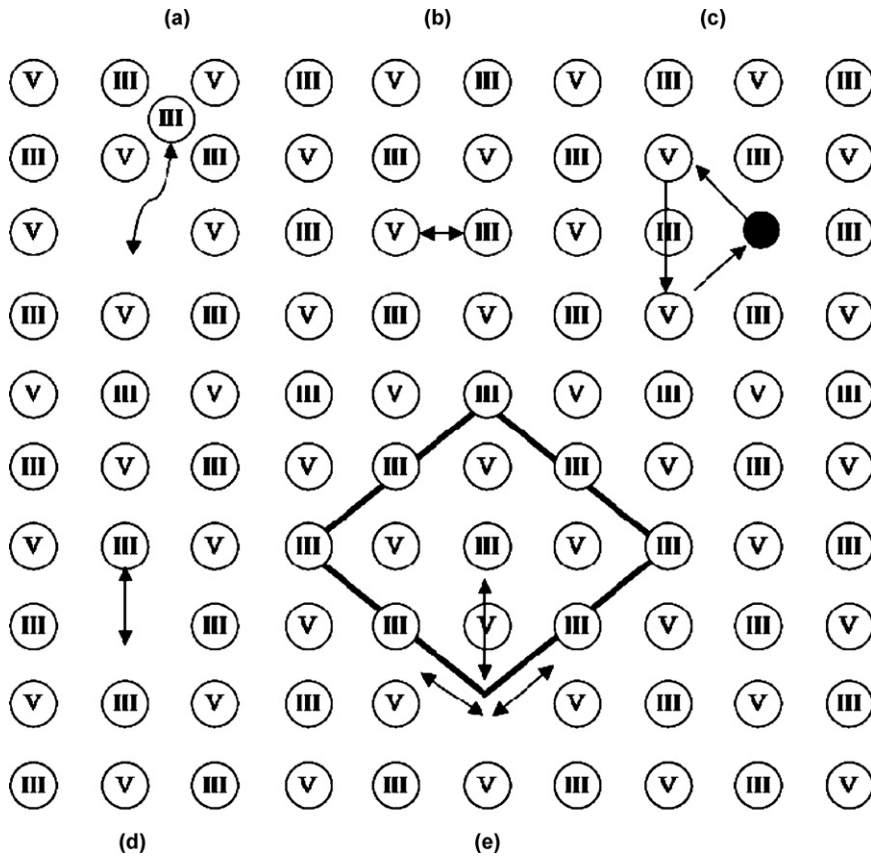


Fig. 49. Schematic illustration of several diffusion mechanisms in a III–V semiconductor. Impurity atoms are shown as filled circles. (a) Interstitial and vacancy generation-recombination via a Frenkel reaction; (b) direct exchange between nearest neighbors on opposite sublattices generating two antisite defects; (c) indirect, concerted exchange through a simple ring on the same sublattice; (d) exchange with nearest-neighbor vacancy on opposite sublattice; (e) exchange with next-nearest-neighbor vacancy (or nearest neighbor on same sublattice). The shaded diamond shows one face of the unit cell. Possible jumps to the vacancy from three (of the nearest 12) group III sites are also shown. Figure adapted from Cohen [659].

in Fig. 49, an assortment of migration mechanism are thought to occur within the bulk of the semiconductor. These include (a) interstitials and vacancies diffusing through the lattice; (b) direct exchange between nearest neighbors on opposite sublattices leading to the generation of two antisite defects; (c) indirect exchange through a ring on the same sublattice; (d) exchange with the nearest-neighbor vacancy on the opposite sublattice; (e) exchange with the next-nearest-neighbor vacancy [659].

In undoped, n-type, and p-type GaAs, gallium self-diffusion is thought to be mediated by gallium vacancies, though various charge states have been suggested to dominate [297,454,660,661]. Vacancies were initially suggested as the primary mediators of Ga diffusion based on micrographs of quantum well interdiffusion versus arsenic partial pressure [662]. By analyzing doping enhanced AlAs/GaAs superlattice disordering data, Tan et al. proposed an activation energy of 6.0 eV for the diffusion of V_{Ga}^{3-} in n-type GaAs under an As-rich ambient [663]. Wang et al. used a Ga tracer isotope technique to explore this defect, which they associated with an activation energy of 4.24 eV, in good agreement with the values calculated by Zhang and Northrup and Walukiewicz et al. of 4.0 ± 0.5 and 4.6 ± 0.3 eV, respectively [297,664,665]. As the stable charge state of the gallium vacancy in n-type material has been under discussion for some time, it is not surprising that V_{Ga}^{1-} and V_{Ga}^{2-} have also been proposed as the mediators of Ga self-diffusion [666–668]. Bracht et al. suggested that only neutral, singly, and doubly charged Ga vacancies mediate self-diffusion in undoped, p-type, and n-type material, with relative contributions that depend on temperature and doping; this model is presented graphically in Fig. 50 [454]. For example, under p-type conditions, the negatively charged vacancies contribute far less to diffusion than neutral vacancies; the concentrations of V_{Ga}^{1-} and V_{Ga}^{2-}

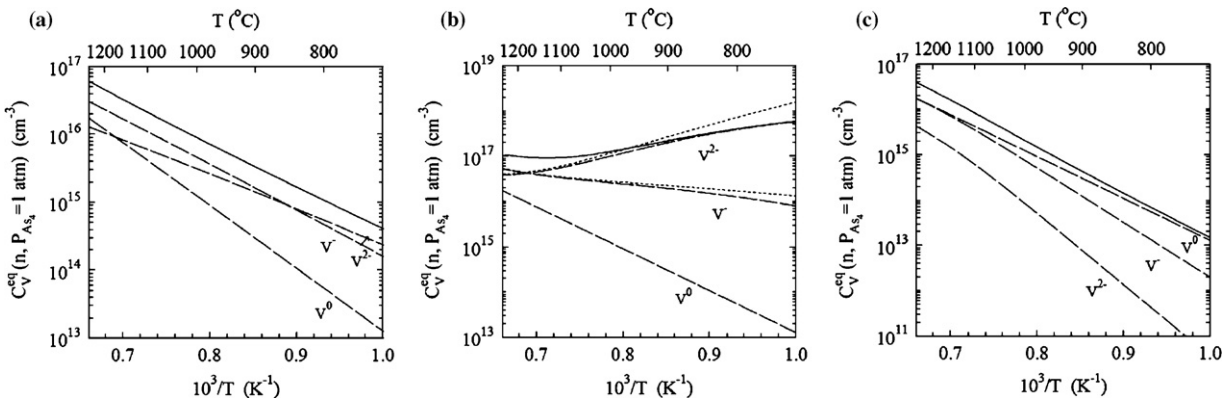


Fig. 50. Temperature dependence of the thermal equilibrium concentrations V_{Ga}^{0} , V_{Ga}^{1-} , and V_{Ga}^{2-} in (a) intrinsic; (b) n-type; (c) p-type GaAs.

decrease even more with decreasing temperature. Under intrinsic conditions, Bracht et al. claim that either V_{Ga}^{1-} or V_{Ga}^{2-} , depending on the temperature, mediate diffusion, with an activation enthalpy of 3.71 eV.

Arsenic diffusion in GaAs is governed by a substitutional–interstitial diffusion mechanism, most likely that of kick-in and kick-out [150,669]. It has not been explored in as much detail as gallium diffusion, probably because at equilibrium, the formation of arsenic interstitials in the bulk is unfavorable in comparison to that of vacancies and antisites. Based on the DFT results of Schick et al., one could infer that As_i^{1+} , As_i^0 , and As_i^{1-} are the primary contributors to As diffusion for Fermi energies from E_v to 0.3, 0.3–0.5, and 0.5 eV to E_c , all respectively [296]. The first estimates of self-diffusion of arsenic in GaAs were obtained by Pashley and Goldstein via the in-diffusion of radioactive arsenic isotopes [658,670]. The instability of these isotopes led to widely differing activation energies and indicated that self-diffusion was governed by a vacancy mechanism [150,151]. More recently, strained GaAsP/GaAs and GaAsSb/GaAs superlattices have proven more useful in studying the self-diffusion coefficient of arsenic [150,151]. Interdiffusion coefficients determined by Egger et al. for these compounds are higher under arsenic-rich conditions than under gallium-rich conditions, pointing to an interstitial-substitutional type of diffusion mechanism [151]. Schutlz et al. found an increase in the effective diffusion coefficient of an arsenic tracer isotope in GaAs for high arsenic vapor pressures, also an indication that interstitial-substitutional migration dominates over vacancy migration [150].

7.1.5. Other III–V semiconductors

In Section 4, a distinction was made between the III–V semiconductors containing elements from the second row of the periodic table, such as GaN and BN, and compounds such as GaAs and GaP. That delineation came into play when discussing the likelihood of interstitial and antisite formation. It also helps to shed light upon the different mechanisms of point defect diffusion that have been observed in several III–V semiconductors. For example, group III vacancy-type defects do not dominate diffusion in GaN for all Fermi energies, as they do in GaAs. Also, as excess nitrogen atoms in the crystal lattice induce significant strains to form the low-symmetry bonding configuration, it is not surprising that nitrogen vacancies, rather than interstitials, mediate nitrogen diffusion in GaN.

For the III–V semiconductors such as GaSb and GaP in which defect diffusion has been explored, many similarities to GaAs exist. According to the model of diffusion in GaSb proposed by Bracht et al., Ga migrates via vacancies whereas Sb migrates via interstitials, in analogy to the diffusion of V_{Ga} and As_i in gallium arsenide [671,672]. Only one mention of positively charged gallium interstitials contributing to self-diffusion has been found in the literature [310]. Hakala et al. suggested a diffusion model involving both V_{Ga} and Ga_i in order to account for diffusion measurements performed in Ga- and Sb-rich ambient conditions. Experiments have conclusively revealed that diffusion in GaSb is mediated by a next-nearest-neighbor diffusion mechanism where migration occurs in two distinct sublattices [671,672]. Migration via a nearest-neighbor diffusion mechanism is associated with strongly asymmetric reaction energies that render the mechanism ineffective in GaSb [310]. Only one direct experimental study of gallium diffusion in GaP exists [665]. The authors felt it premature, without substantial evidence, to attribute Ga self-diffusion to the charged gallium vacancy, although they concluded that diffusion was primarily mediated through one type of simple native defect. They measured an activation energy for diffusion of 4.5 eV in GaP, or about 0.25 eV greater than their value for GaAs, a difference attributed to the stronger Ga–P bond in comparison to the Ga–As bond [665].

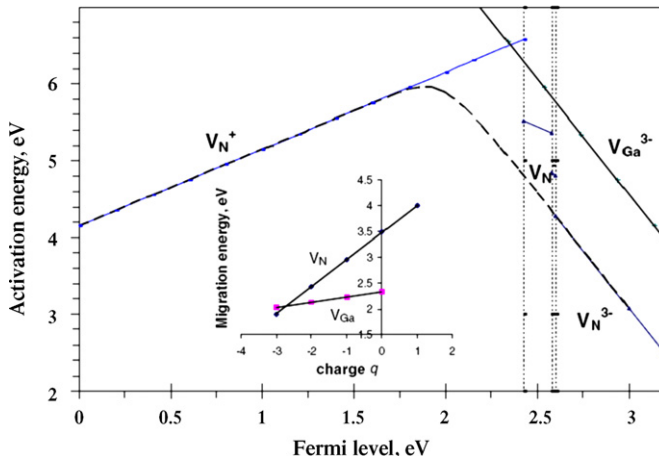


Fig. 51. Activation energies for self-diffusion of gallium and nitrogen vacancies in the GaN sublattice. Solid lines represent the activation energies for the lowest energy charge state of a defect; the dashed line is the effective activation energy for vacancy-mediated self-diffusion. The inset demonstrates the charge dependence of vacancy migration energies.

Defect diffusion in semiconductors containing elements from the second row of the periodic table, such as B and N, is quite different. In p-type material, Limpijumnong et al. suggest that self-diffusion of gallium occurs via Ga_i , since the formation energy of the gallium vacancy is very high [312]. In this regime, the energy barrier for the migration of Ga_i^{3+} is at least 1.0 eV lower than that of V_{Ga}^0 , which is slightly non-intuitive, as one might expect the large radius of the Ga atom to inhibit its movement in the small crystal lattice of GaN [312]. In n-type material, conversely, gallium interstitials are unfavorable and diffusion is mediated by gallium vacancies. The activation energy for self-diffusion of the defect is 3–4 eV, with the formation energy of V_{Ga}^{3-} comprising 1–2 eV. It is suggested that the interstitial defect migrates via a pair-diffusion mechanism [312]. As the formation of nitrogen interstitials in GaN is highly unfavorable, the diffusion of nitrogen is most likely always mediated by vacancy-type defects. Limpijumnong et al. calculated migration barriers of 2.6 eV for V_N^{3+} and 4.3 eV for V_N^{1+} [312]. They attributed the strongly charge state-dependent energies to the saddle-point complexes used to determine the migration barriers. Both contain interstitial nitrogen atoms (in various charge states in order to preserve the total charge of the complex) that have high formation energies for most Fermi energies within the band gap. When Ganchenkova et al. suggested the existence of acceptor-type V_N defects in GaN, they also calculated their site-to-site hopping migration energies. Fig. 51 illustrates how the energy barrier decreases from about 4.0 eV for the (1+) charge state of the defect to ~2.0 eV for the (3-) charge state, as well as the effect of the migration barrier on the overall activation energy of N_i .

7.1.6. Titanium dioxide

The self-diffusion of oxygen [87,512,673–676] and titanium [84,677–679] in rutile TiO_2 has been examined extensively; oxygen migrates via a vacancy diffusion mechanism, whereas excess Ti atoms diffuse through the crystal as interstitials [83]. The diffusion of Ti and O in the rutile crystal lattice have very similar overall activation energies, with values ranging from 2.0 to 2.9 eV [84,498,677–680] and 2.4 to 2.8 eV [512,674,675,681], respectively. In the semiconductors discussed up until this point, especially silicon, the effect of defect charge state upon the migration energy for site-to-site hopping has been discussed. TiO_2 is different for two main reasons: the energy barriers for the site-to-site migration of Ti_i and V_O , as well as the effect of charge state on the energetics of diffusion, are not frequently discussed in the literature.

The self-diffusion of oxygen in non-stoichiometric rutile titanium dioxide has been studied by radioactive tracer and gaseous exchange methods [87,674–676,682]. Haul and Dumbgen were the first to propose that oxygen diffusion occurs via (2+) vacancies, yet the possibility of cooperative motion of both anion and cation defects has also been considered [512,678]. The self-diffusion coefficients of oxygen in TiO_{2-x} have approximately equal activation energies for migration along both the c - and a -axes of the unit cell [681]. Also, these diffusion coefficients grow with increasing non-stoichiometry; oxygen self-diffusion is faster in highly reduced titania [87,683]. Titanium diffuses through titanium dioxide by an interstitial-type mechanism; Ti_i^{3+} and Ti_i^{4+} are likely to contribute more to diffusion at

reduced and stoichiometric conditions, respectively [82,84,504]. From tracer diffusion experiments, the concentration of titanium interstitials will have a $P_{O_2}^{-1/4}$ or $P_{O_2}^{-1/5}$ dependence depending on whether Ti_i^{3+} or Ti_i^{4+} dominates [677]. He et al. considered an assortment of structural Frenkel models to shed light upon the barrier to neutral Ti interstitial diffusion in rutile TiO_2 [318]. They found that it is much easier for the defect to move through the open channel in the $[0\ 0\ 1]$ direction than it is for it to move from a lattice site in the $[1\ 0\ 0]$ or $[0\ 1\ 0]$ direction.

7.1.7. Other oxide semiconductors

The stoichiometry of a metal oxide semiconductor can, in part, provide insight into the mechanisms of defect diffusion at play within the bulk of the crystal. A brief review of terminology is useful, as the terms utilized in the literature tend to vary from report to report. While TiO_{2-x} is typically referred to as “reduced” titanium dioxide, ZnO_{1-x} is described as “Zn-rich” zinc oxide and UO_{2-x} as “hypostoichiometric” uranium dioxide. Similarly, the terms “oxidized,” “O-rich,” and “hyperstoichiometric” can be used interchangeably. It is valuable to become familiar with these conventions, as defect diffusion in the remaining metal oxide semiconductors is often discussed in conjunction with regimes of stoichiometry or chemical potential. Under extreme conditions, e.g. reducing and oxidizing environments, charged vacancies comprised of the deficient species and charged interstitials (and antisites) comprised of the overabundant species tend to preferentially form. Consequently, it is not surprising that in stoichiometric and hypostoichiometric oxides, oxygen always diffuses via a vacancy mechanism. Only under oxygen-rich conditions, e.g. hyperstoichiometric material, does an interstitial-mediated mechanism of anion diffusion come into effect. On the other hand, in the metal oxides that will be discussed shortly, metal cations diffuse as vacancies, rather than interstitials. This naturally prompts the question as to why the diffusion of titanium atoms in TiO_2 has historically been suggested to occur via the migration of metal interstitials; this inquiry will be readdressed at the end of this section.

Oxygen self-diffusion occurs through a vacancy mechanism in Zn-rich ZnO , in which V_O^0 and V_O^{2+} are the dominant point defects [89,90,684–686]. Under oxygen-rich conditions, oxygen diffusion is mediated by interstitials in the (0) or (2-) charge state [90,325,687,688]. The latter mechanism has been observed experimentally, as undoped zinc oxide normally exhibits n-type behavior, and all experiments have been performed under oxygen-rich conditions. Early experimental studies were somewhat unreliable, as they relied on gaseous-exchange techniques [684,689], whereas modern investigators have used secondary ion mass spectroscopy to obtain diffusivities from depth profiles in undoped and doped ZnO samples [89,690]. For example, Haneda et al. and Sabioni saw that extrinsic doping, which leads to the formation of addition O_i^{2-} , increased the oxygen diffusion coefficient [687,688]. Additionally, the diffusion prefactors and activation energies from these studies vary widely. A recent first-principles investigation by Erhart et al. has helped to shed light upon the complex interplay between vacancy and interstitial-mediated diffusion; these authors also explored the effect of defect charge state on the preferred path of O_i through the crystal, as shown in Fig. 52 [691]. The lowest computed energy barrier for migration of O_i^0 (0.81 eV) corresponds to the movement of one of the atoms in the dumbbell to one of the first nearest out-of-plane neighbor positions, and the formation of a new

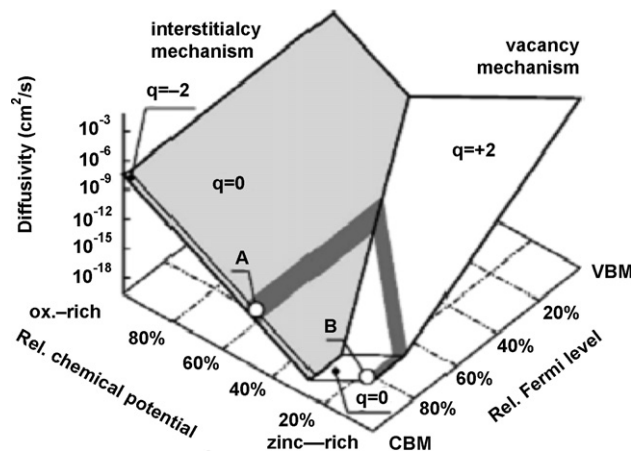


Fig. 52. Dependence of self-diffusion of oxygen in ZnO on chemical potential and Fermi level at 1300 K, illustrating the competition between vacancy and interstitial mechanisms. The dark gray areas indicate the experimental data range around 1300 K obtained by Erhart and Albe [691].

dumbbell interstitial. For intermediary chemical potential, a balance, dependent upon both stoichiometry and Fermi level, occurs between the two migration mechanisms. This occurs as oxygen interstitials have greater formation enthalpies, yet smaller site-to-site migration enthalpies, in comparison to oxygen vacancies.

In contrast to TiO_2 , experiments and computations suggest that cation vacancies, e.g. V_{Zn}^0 , $\text{V}_{\text{Zn}}^{1-}$, and $\text{V}_{\text{Zn}}^{2-}$, are the defect responsible for zinc diffusion in ZnO . This is somewhat non-intuitive, as ZnO falls into the category of a metal-excess, or oxygen-deficient, oxide semiconductor. It could thus be inferred that zinc interstitials, a result of the excess of metal in the crystal, mediate self-diffusion. According to experiments using the method of thin sections performed by Moore and Williams and Kim et al., however, zinc diffuses isotropically in ZnO [689,692]; it is known from computation that zinc interstitials diffuse in an anisotropic manner through the crystal [686]. These results imply that zinc vacancies, rather than interstitials, mediate zinc diffusion in ZnO . Using ^{70}Zn as a tracer isotope and SIMS for data collection, Tomlins et al. also recently confirmed that zinc self-diffusion is controlled by a vacancy mechanism [532]. They briefly discuss the energetics of defect migration; the lowest activation energy for the migration of zinc interstitials (the sum of the formation energy and migration energy of Zn_i^{2-}) is still 0.8 eV higher than that of $\text{V}_{\text{Zn}}^{2-}$. This calculation uses the migration energy of the zinc vacancy obtained by Binks, 0.91 eV, who proposed a “double-jump” model, a combination of two *c*-axis jumps, for the diffusion of the defect [686].

Oxygen self-diffusion in urania occurs in a similar manner to that in ZnO ; in UO_{2+x} , anion mobility occurs by the migration of interstitials [693], while in UO_2 and UO_{2-x} , a vacancy mechanism of anion diffusion dominates [538,693–695]. The hyperstoichiometric and stoichiometric regimes can be likened to O-rich and Zn-rich ZnO , where oxygen interstitials and oxygen vacancies mediate diffusion, respectively. Such behavior has also been found in other alkaline earth fluorites [538,696]. Matthews obtained an activation energy for the migration of O_i^{2-} in UO_{2+x} of 1.3 eV, in comparison to the higher value of 2.8 eV obtained for the diffusion of the same defect in stoichiometric UO_2 [693]. Catlow and coworkers directly compared the energetics of interstitial versus vacancy diffusion in UO_2 ; they obtained a migration enthalpy of ~ 0.52 eV for V_{O}^{2+} , or about 0.5 eV lower than that of O_i^{1-} [694,695]. They also found that the “kick-out” or “interstitialcy” mechanism, where diffusing atoms interchange between substitutional and interstitial sites in the crystal lattice, of interstitial migration is more energetically favorable than the direct migration of anion interstitials [538].

Similar to ZnO , it is suggested that the cation vacancy in the (4-) charge state, V_{U}^{4-} , mediates the diffusion of metal atoms in UO_{2+x} and UO_2 . Catlow, Matthews, and Matzke discovered that the rate of uranium vacancy diffusion increases along with the deviation from stoichiometry in UO_{2+x} [538,693,697]. In UO_{2+x} the overall diffusion coefficient of uranium increases in approximate proportionality with x^2 by roughly five orders of magnitude between UO_2 and $\text{UO}_{2.20}$ at 1400–1600 °C [697]. This fast diffusion is attributed to increased V_{U}^{4-} concentration, since U^{5+} -ions diffuse more slowly than U^{4+} ions. Jackson et al. proposed four different pathways for cation migration; for stoichiometric UO_2 , a mechanism whereby a cation moves into a cation vacancy in the presence of an adjacent oxygen vacancy dominates [698].

In cobaltous oxide, which tends towards Co_{1-x}O , both cobalt and oxygen self-diffuse via a vacancy mechanism [544,553,699]. In 1969, Chen et al. calculated a favorable translational energy at the saddle point associated with the motion of cation vacancies [699]. Tracer diffusion studies place the activation energy for site-to-site hopping of the cation vacancy $\text{V}_{\text{Co}}^{2-}$ at approximately 1.6 eV [544,554,699]. The self-diffusion coefficient of cobalt has a strong dependence on oxygen partial pressure, particularly at low pressures, where the (2-) charge state of V_{Co} dominates. Chen and Jackson also suggested a vacancy-mediated mechanism for oxygen diffusion [699–701]. Assuming that oxygen diffuses via (1+) vacancies, they calculated an activation energy for migration of 4.12 eV at 1429 °C and 0.21 atm [699]. For purposes of comparison, in the temperature range 1000–1600 °C, the activation energy for cation vacancy self-diffusion in CoO is much smaller than that for anion diffusion (1.65 eV for cobalt and 4.12 eV for oxygen) [544,554,555,699].

It is now logical to return to the subject of the predominant cation diffusion mechanism in TiO_2 . In n-type ZnO , UO_2 , and CoO , vacancies in the (2-), (4-), and (2-) charge states mediate the migration of metal atoms within the bulk. Similar behavior has been observed and calculated in BaO , CaO , MgO , NiO , SrO [702,703]. For example, in nickel oxide, the rapid cation self-diffusion relative to anion self-diffusion suggests that excess oxygen ions are accommodated by the formation of cation vacancies in the (1-) and (2-) charge state [702]. As a reminder, Na-Phattalung et al. identified $\text{V}_{\text{Ti}}^{4-}$ as the defect present in high concentrations in O-rich anatase TiO_2 . They were the first group to explore the Fermi energy dependence of the formation energy of the metal vacancy, and not just that of the metal interstitial. When the migration of titanium in TiO_2 via an interstitially-mediated mechanism is discussed, no

mention is even made of V_{Ti}^{4-} (the other defect formed in the Schottky reaction that produces Ti_i^{4+}). As oxygen has a small atomic radius (60 pm), it is not surprising that it diffuses in TiO_2 as an interstitial defect. Titanium, on the other hand, has an atomic radius of 140 pm, or about 5 pm larger than that of Zn and Co. It is left to the reader to ponder whether, in contrast to the other metal oxides discussed in this section, the diffusion of Ti is truly mediated by interstitial defects. Without a doubt, further experimental and computational investigation of the matter is in order.

7.2. Surface defects

Self-diffusion and many kinds of heterodiffusion on metals are typically mediated by native point defects such as vacancies or adatoms, though small adatom clusters sometimes play a role. The rate of mesoscale mass transport depends upon the number of mobile defects on the surface, and also upon the rate at which these defects move from site to site. In the case of a vacancy, the defect moves when an atom within the surface plane shifts into the original vacancy position. In the case of an adatom, site-to-site motion can take place by simple hopping of the atom or by one of various surface exchange mechanisms [64,704]. In simple exchange, for example, the atom “dives” into the surface, simultaneously “pushing” a substrate atom into an adatom position. Atomic motion is much easier to image directly on surfaces than in the bulk. Thus, both site-to-site hopping and mesoscale diffusion over many atomic distances (by continuum methods) have been examined experimentally in considerable detail.

7.2.1. Silicon

Previously, only the diffusion of neutral defects on the $Si(0\ 0\ 1)$ surface had been explored. For example, Kirichenko et al. discussed possible mechanisms for the disappearance of neutral monovacancies on $Si(0\ 0\ 1)$. They proposed four models for this phenomenon, including escape of the remaining atom from the “defect” dimer, diffusion of monovacancies along a dimer row and formation of dimer vacancies, rapid hopping of the remaining atom between two possible energy minima in the “defect” dimer, and diffusion of the surface monocavacancy into the subsurface layer [705]. Kitamura et al. measured the migration of single-dimer vacancies on $Si(0\ 0\ 1)$ using high-T real-time STM, revealing that diffusion is predominantly one dimensional along the dimer row with a corresponding activation barrier of 1.7 ± 0.4 eV [330]. Using first-principles density functional calculations, Zhang et al. and Wang et al. have proposed a barrier to dimer vacancy migration as high as 2.5 eV [334,706]. The former authors also proposed a displacement for the single dimer vacancy consisting of a wavelike displacement with the concerted motion of two second layer and two top layer atoms [706] (Fig. 53).

The diffusion of isolated adatoms on $Si(1\ 0\ 0)$ has also been investigated. Mo et al. obtained an energy barrier of 0.67 eV for their diffusion by comparing island number densities measured with STM with those from simulations [707]. Brocks et al. calculated a comparable activation energy of 0.6–1.0 eV, depending on the path, from first-principles total-energy calculations; diffusion along the dimer rows is more favorable than diffusion perpendicular to the rows [708].

Activation energies for mesoscale diffusion are now available for $Si/Si(1\ 0\ 0)$, $In/Si(1\ 1\ 1)$, $Ge/Si(1\ 1\ 1)$, and $Sb/Si(1\ 1\ 1)$. Webb et al. and Keefe et al. both associated an activation energy of ~ 2.25 with the diffusion of silicon on the $(0\ 0\ 1)$ surface [709,710]. Mo reported the diffusion of Sb dimers on a $Si(0\ 0\ 1)$ surface using a STM whose tip approached the same region before and after sample annealing, giving an activation energy and a prefactor of diffusion of 1.2 eV and $10^{4-}\text{cm}^2/\text{s}$ [707,711].

Measurements of thermal surface diffusion on both $Si(1\ 0\ 0)$ and $Si(1\ 1\ 1)$ have shown a dependence on native defect charge state [29,330,334,706–714]. Recent work has shown that the ionization of surface adatoms and vacancies affects mass transport at the mesoscale [29]. Activation energies obtained for In, Ge, and Sb on the $Si(1\ 1\ 1)$ surface for mesoscale diffusion using second harmonic microscopy range from 1.83 to 2.48 eV. The activation energies for diffusion and diffusion coefficients associated with these surface and adsorbed species are tabulated in Table 18. Since Sb and In have the same valence (three) and roughly the same atomic size, the primary differences in $E_{\text{diff},M}$ should arise from ionization effects associated with either electronegativity or acceptor/donor effects. The diffusional pre-exponential factor comprises the product of the intrinsic prefactor $D_{0,I}$ together with an entropic formation term. The entropic formation term comprises several components analogous to those discussed for ΔH_f . There is a positive chemical entropy of formation ΔS_{fc} associated with lattice mode softening near a terrace vacancy, which decreases local vibrational frequencies [69]. ΔS_{fc} for a terrace vacancy should not be too far from that in the bulk as a first approximation, and both analytical [715,716] and MD [717,718] calculations suggest that this term can be $6R$

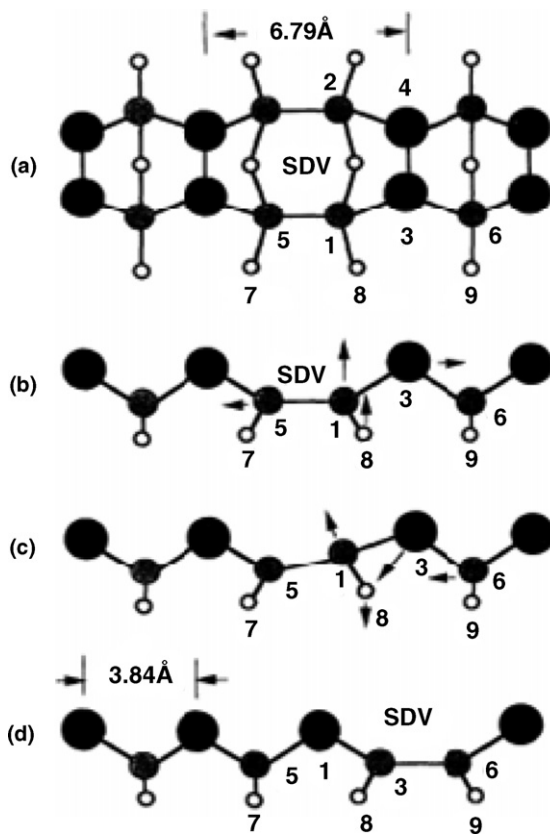


Fig. 53. (a) Schematic diagram of a portion of a dimer row in Si(1 0 0) containing a single-dimer vacancy (top view). The large, medium, and small circles represent atoms in the top, second, and third layers, respectively. A solid line between any two atoms shows a Si-Si bond. Also shown are the (b) initial, (c) transition state and (d) final configurations along the diffusion pathway (side view). The arrows indicate the directions of atom motion leading to the next configuration, with longer arrows indicating larger displacements.

to 11R or higher. Adatoms themselves do not appear to contribute to ΔS_{fc} appreciably (by hardening the lattice, for example). An ionization entropy ΔS_{fi} may also exist because of the band gap. Again, the effect arises from local mode softening, this time due to a charge carrier confined near a charged vacancy or ion core [50]. If the carrier is associated with a hydrogenic donor or acceptor in a semiconductor, the carrier's charge is generally screened by the large dielectric constant of the material and becomes very delocalized. Hence, little contribution to ΔS_{fi} is made. This effect

Table 18

Summary of activation energies for diffusion (in eV) and diffusion coefficients (in cm^2/s) for defects and adsorbed species on Si(1 1 1) and Si(1 0 0)

Species	Surface	E_A (eV)	D (cm^2/s)	Reference
Sb	Si(1 1 1)	2.6 ± 0.13	$6 \times 10^3 \pm 0.7$	[714]
In	Si(1 1 1)	1.82 ± 0.02	$3 \times 10^3 \pm 0.3$	[29]
Ge	Si(1 1 1)	2.48 ± 0.09	$6 \times 10^2 \pm 0.5$	[713]
Si	Si(0 0 1)	2.25 ± 0.04	—	[710]
Si	Si(0 0 1)	2.25 ± 0.04	—	[711]
Si	Si(0 0 1)	0.67 ± 0.08	10^{-3}	[708]
Si	Si(0 0 1)	$0.6-1.0$	—	[709]
Pb	Si(1 1 1)	1.2	2×10^{10} to 8×10^{11}	[712]
Sb	Si(1 0 0)	1.2 ± 0.1	$10^{-4 \pm 1}$	[715]
Single dimer vacancy	Si(1 0 0)	1.7 ± 0.4	—	[330]
Single dimer vacancy	Si(1 0 0)	2.5	—	[707]
Single dimer vacancy	Si(1 0 0)	≥ 2.2	—	[334]

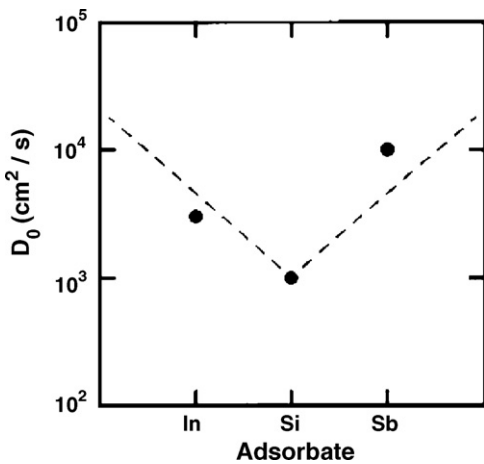


Fig. 54. Comparison of pre-exponential factors for mesoscale surface diffusion of groups III and V adsorbates on Si(1 1 1). The V shape gives evidence for the ionization of surface defects, since the ionization entropy of such defects is positive (and increases the diffusional pre-exponential factor) for both positive and negative defects.

can be seen in the diffusion prefactor for In, Si, and Sb on Si; the quantity is larger for both In and Sb than for Si (Fig. 54).

7.2.2. Photostimulated diffusion on silicon

Akin to bulk diffusion, the hypothesis that charged vacancies affect surface diffusion has also been confirmed by experiments involving photon illumination of the Si(1 1 1) surface. Low-level optical illumination (<2 W/cm²) was shown to either enhance or inhibit diffusion of indium, germanium and antimony on Si by close to an order of magnitude, depending on the doping type (n or p) of the underlying substrate [26]. In that case, the effects seemed to arise primarily from illumination-induced changes in the formation energy for surface vacancies and mobile atoms. When the surface is illuminated, the concentration of charged vacancies varies in response to the generation of photogenerated charge carriers. Illumination of a p-type material makes the surface more n-type, presumably increasing the average negative charge of the vacancies. Adatoms on the Si(1 1 1)-(7 × 7) surface, however, are suggested to have a positive charge, which could result in electrostatic attraction between the negatively charged vacancies and positive adatoms [26]. Under illumination, D_M decreases for p-type material and increases for n-type material due to the contribution of both neutral and positively charged vacancies (Fig. 55). Also, Ditchfield et al. noted a similar temperature for the convergence of the Arrhenius plots and the disappearance of the (7 × 7) reconstruction in the Ge/Si system, offering additional evidence for the importance of ionization on surface diffusion.

7.2.3. Germanium

Although some researchers have explored the diffusion of adatoms and vacancies on the Ge(1 1 1) surface with STM, their behavior is not as well characterized as that of similar defects on Si(1 1 1). Also, no computational work exists concerning the ionization levels of surface defects, so the effect of charge state on the energetics of diffusion has not been discussed in any theoretical investigations.

From the direction of surface band bending in STM images, Lee et al. inferred that the adatom vacancy defect on the Ge(1 1 1) – c(2 × 8) occurs in both the neutral and negative charge state [178]. Molinas-Mata et al., Mayne et al. and Brihuega et al. observed the thermal diffusion of vacancies and vacancy complexes with scanning tunneling microscopy, yet did not mention defect charge state [719–721]. They have shown that, by the thermally activated hopping of neighboring adatoms to a vacancy site, the vacancy, presumably either in the neutral or (1–) charge state, can diffuse on the surface [719]. Artificially generated single vacancies can either switch to a different lattice site or split into two so-called “semivacancies.” The semivacancies are separated by a variable number of Ge adatoms in metastable T₄ positions and can diffuse or eventually merge back into a single vacancy. Mayne et al. considered the mechanisms of both single vacancy hopping and the hopping of two vacancies occupying adjacent surface sites, although without regard to vacancy charge state [720] (Fig. 56). Brihuega et al. also observed isotropic diffusion of the

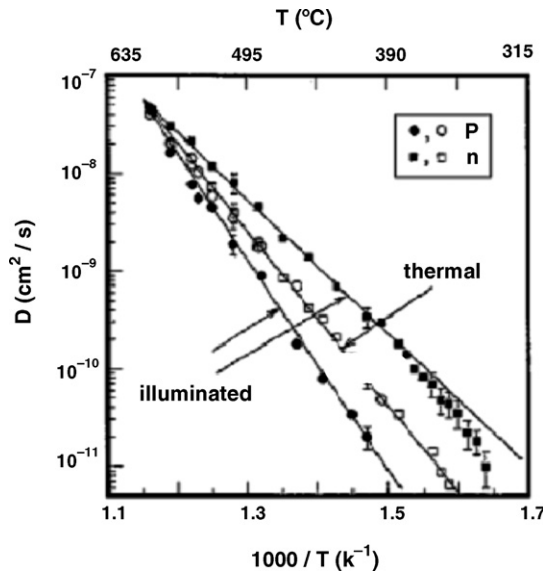


Fig. 55. Arrhenius plots for In diffusion on n-type and p-type Si(1 1 1) at about 10^{18} cm^{-3} doping under dark and illuminated conditions. Error bars derive from standard error analysis of the diffused profiles, while lines represent least-squares fits. For diffusion in the dark, n-type and p-type material yield identical fits. For n-type illuminated material, the least-squares fit includes only data about 390 K. The drop-off in D below 390 K appears to represent a true change in slope.

single vacancy to take place via a typical two-dimensional random walk pattern. The process is thermally activated with an effective energy barrier for the migration of the neutral defect of $E_d = 0.89 \pm 0.01$ and 0.88 ± 0.02 eV according to Mayne et al. and Brihuega et al., respectively [720,721]. At room temperature, the diffusion coefficient along [1 1 0] is more than twice the value obtained along [1 1 2], indicating that the diffusion processes leading to single vacancy migration on the surface are slightly anisotropic [721].

7.2.4. Gallium arsenide

Scanning tunneling microscopy has also been used to investigate the diffusion mechanisms of anion and cation vacancies on the surface of GaAs(1 1 0) [243]. The injection of minority carriers by the STM tip serves as a catalyst for vacancy motion; under gallium-rich conditions, V_{As}^{1+} and V_{As}^{1-} are the dominant defects for p-type and n-type GaAs(1 1 0), respectively, whereas under arsenic-rich conditions, charged gallium vacancies and arsenic adatoms become important [197]. Gwo et al. and Lengel et al. both investigated the directional movement of gallium and arsenic on the GaAs surface, yet made no mention of the effect of defect charge state on migration mechanism [243,579,722]. *Ab initio* calculations on the energetics and dynamics of surface vacancies on GaAs(1 1 0) performed

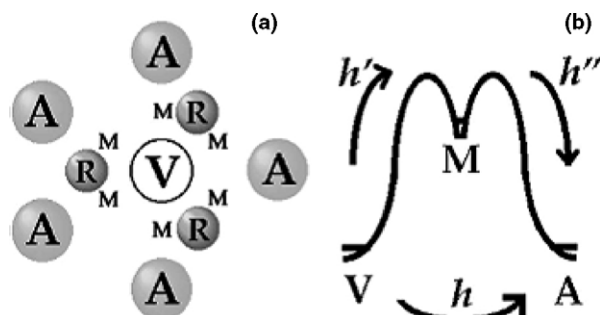


Fig. 56. Schematic diagrams of diffusional hopping of a single vacancy on Ge(1 1 1) – $c(2 \times 8)$. Diagram (a) shows a two dimensional view with the vacancy surrounded by restatoms (R) and adatoms (A) together with metastable sites (M) to which it can hop. In (b), the 1D simplification is shown with the approximate hopping rates.

by Yi et al. found that the diffusion of gallium and arsenic vacancies on the surface is more likely to occur via motion along the zig-zag chains, rather than between them [578]. The diffusional barrier heights for neutral V_{Ga} and V_{As} are 2.5 and 1.5 eV, respectively, while those for the same singly negatively charged vacancies are 1.9 and 2.5 eV. These activation energies imply that V_{Ga}^{1-} diffuses more easily than the neutral vacancy, whereas charging impedes the motion of V_{As}^{1-} compared to the neutral defect [578]. The considerable barrier height for the diffusion of V_{As}^{1-} is due to the high stability of the vacancy when it is charged. No mention is made in the literature of the diffusion of the singly positively charged V_{As}^{1+} and V_{Ga}^{1+} that are hypothesized to exist in high concentrations on p-type GaAs(1 1 0) under Ga-rich and As-rich conditions, respectively.

Some experimental and computational information exists on the diffusion of cations on the GaAs(0 0 1)- β 2 surface [723–728]. The experimentally deduced migration barriers for Ga adatoms vary over a wide range from 1.1 to 4.0 eV [725–728]. These studies were undertaken mainly to provide a model for surface growth during molecular beam epitaxy, and thus neglect to mention the relative contribution of the arsenic adatom in the (1+), (0), and (1-) states. Kley et al. identified two diffusion channels that affect the migration of adatoms: in one channel the adatom jumps across the surface dimers and leaves the dimer bonds intact, while in the other, the dimer bond is broken [723].

7.2.5. Other III–V semiconductors

Few studies exist regarding the diffusion of charged defects on the remaining III–V semiconductor surfaces. In particular, little is known about the migration of electrically active defects on semiconductors containing elements from the second row of the periodic table, such as BN and GaN. In the literature that does exist, Ebert et al. explored the diffusion of phosphorus vacancies on InP(1 1 0) and GaP(1 1 0) with scanning tunneling microscopy. The migration is most likely triggered by the STM tip, as the probability of diffusion is significantly higher when the tip contacts the surface. Under indium-rich conditions, V_P^{1+} and V_P^{1-} have low formation energies on p-type and n-type InP(1 1 0), respectively [174,180,181,584,585]. Jumps of vacancies in both the [1 -1 0] and [0 0 1] directions are observed; jumps in the former direction occur three times more frequently than those in the latter direction. The authors estimate the diffusion coefficient of the V_P^{1+} as 10^{-18} cm²/s [729]. On GaP, diffusion can lead to the recombination of neutral adatoms with charged vacancies and the formation of adatom clusters [729].

7.2.6. Titanium dioxide

Experimental and theoretical evidence has revealed a mechanism of adsorbate-mediated vacancy diffusion on rutile (1 1 0) [245,730–733]. Two molecular configurations and one dissociated (atomic) configuration of O₂ adsorption can occur on defected surfaces, whereas no adsorption takes place on stoichiometric TiO₂(1 1 0) [732]. The model has been discussed only in the context of neutral oxygen vacancies, yet based on calculations by Wang et al., it is possible that the (1+) and (2+) charge states of BOVs and POVs also contribute to the phenomenon [246]. In 2003, Schaub et al. found experimental STM evidence for O vacancy diffusion along the [1 1 0] direction, or perpendicular to the bridging O rows of the TiO₂(1 1 0) surface [730]. The phenomenon was observed for surfaces with 0.1–1 Langmuir coverage at temperatures ranging from 180 to 300 K. The authors proposed a diffusion mechanism whereby adsorbed O₂ molecules mediate vacancy mobility through a cyclic process involving the loss of an oxygen atom to a vacancy and sequential capture of a bridging oxygen atom [730]. This model has been questioned by Thompson et al., who failed to detect any isotopic exchange with lattice O following photodesorption and thermal desorption of adsorbed ¹⁸O₂ on TiO₂(1 1 0), implying that surface vacancy diffusion cannot occur via the dissociation of adsorbed molecular oxygen adjacent to a surface vacancy [731]. Subsequent density-functional theory calculations performed by Wang et al., on the other hand, confirm a moderate energy barrier for molecular O₂ to jump across an oxygen vacancy and diffuse along a Ti(5c) row [733].

Four different diffusion paths, all involving two metastable, intermediate states, an O₂ molecule bound to an oxygen vacancy, and a single O atom located on a Ti site neighboring the initial vacancy position, were observed on TiO₂(1 1 0) by Schaub et al. [730]. Indirect evidence for the first intermediate state can be extracted from work by Henderson et al., who found that complexes formed of vacancies and diatomic oxygen O₂ are unstable at temperatures above 150 K [734]. Schaub et al. point out that oxygen vacancy diffusion is not observed without direct intervention of O₂; O vacancies are immobile on the adsorbate-free surface, as later corroborated by the 4 eV barrier calculated by Rasmussen et al. for the unassisted diffusion of a bridging oxygen atom from a bridging row to a titanium row [245,730]. Wu et al. proposed that oxygen-assisted O vacancy diffusion results from transformations among several different O₂ adsorption states, which have comparable energies and separated reasonable energy barriers (1.1–3.4 eV);

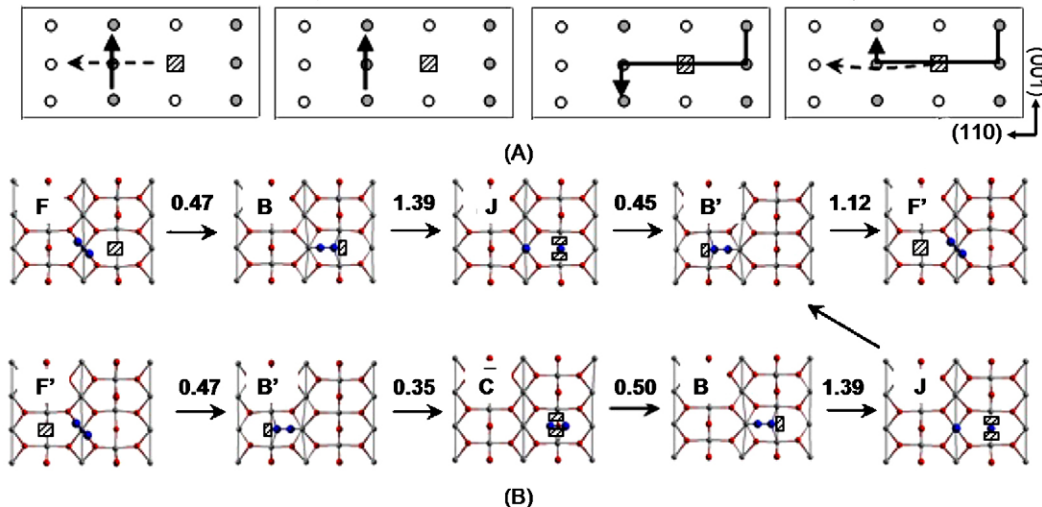


Fig. 57. (A) O_2 -mediated vacancy diffusion mechanisms on the rutile $\text{TiO}_2(1\ 1\ 0)$ surface as observed by Schaub et al. [730], where the solid and dotted lines represent O_2 and O-vacancy movement, respectively. (B) Dominant processes proposed by Wang et al. [733] for vacancy diffusion, with energy barriers in eV. The prime (') represents the symmetric configuration with respect to the vacancy site. The vacancy site is indicated by hatched squares. The large blue balls and the small black and gray balls represent the adsorbed O_2 and the surface O and Ti atoms, respectively. (For interpretation of the references to color in this figure legend, the reader is referred to the web version of the article.)

the process is especially favorable when the O vacancy concentration is larger than that of adsorbed O_2 [732]. These findings support the experimental observations of Schaub et al., yet the authors suggest the need for a revised pathway whereby oxygen adatoms play a central role, but not to the extent that has been suggested by STM images [732]. Rasmussen et al. find the key stage in the mechanism proposed by Schaub et al. to be highly dependent on the vacancy coverage of the surface, as neighboring vacancies hugely enhance the ability of O_2 to dissociate at a vacancy [245]. According to these authors, the fairly high energy barriers of 0.7 and 1 eV obtained for the detachment of O_2 from a vacancy and the process of O_2 dissociation at a vacancy, respectively, indicate the need to consider an alternative mechanism than that proposed by Schaub et al. [245]. DFT calculations by Wang et al. predict that O_2 dissociation at the defect site is the rate limiting step for O_2 -mediated vacancy diffusion, with a barrier of 1.39 eV, which is overestimated in comparison to the 10^{2-} to 10^{1-} Hz vacancy hopping frequencies observed by Schaub et al. (Fig. 57). Their computational results do, however, explain vacancy diffusion across bridging oxygen rows in terms of the ease of O–O recombination, vacancy density increase upon atomic O deposition, and the temporal and spatial correlation of vacancy diffusion [733].

8. Summary

Defects in semiconductors have been studied for many years, ultimately with a view toward controlling their behavior through various forms of “defect engineering.” For example, the rates of defect-mediated diffusion, both in the bulk and on the surface, depend upon the charge state of these isolated or clustered species. Different types of charged defects mediate the diffusion process depending upon the temperature, position of the Fermi level, chemical potential or ambient oxygen pressure of the system. Despite the significance of defect charging, much remains unknown about point defect structure and ionization behavior. Many bulk and surface defects have charge state-dependent structural forms. On surfaces, charged defects can either lower the energy of the cleaved plane or induce energetically favorable surface reconstructions.

Atomic properties and concepts of chemical equilibrium can often be invoked to justify why certain defects occur in specific semiconductors or under deviations from stoichiometry. The type of charged defects that occur in group III–V semiconductors containing boron and nitrogen are inherently different from those in GaAs, for example. The small lattice parameters and ionicity of BN, GaN, etc. lead to high self-interstitial and antisite formation energies; only vacancies have formation energies that are low enough to ensure that their concentration affects the electronic properties in the bulk. For compound and oxide semiconductors, the chemical potential and oxygen partial pressure of

the system impact the type of charged bulk and surface defects that arise. Under extreme conditions, e.g. reducing and oxidizing environments, charged vacancies comprised of the deficient species and charged interstitials (and antisites) comprised of the overabundant species tend to preferentially form.

Although much has been learned about defect charging up to now, for most of the materials discussed here no consensus has been reached as to which defect charge states are stable within the band gap, or the values of the Fermi energies at which charge state transitions occur. Experimental determination of this information is often difficult, as defects exist in low concentrations in solids and may be invisible to common detection techniques. Computational methods are still unreliable; extensive modifications are necessary if density functional theory is going to accurately predict charged defect behavior. It is inadvisable to predict the charged defect behavior of a given semiconductor by comparing it to a similar material; for example, vacancies and self-interstitials in silicon and germanium do not display charge state-dependent relaxations of comparable magnitudes or the same set of stable charge states. Also, little correlation exists between the defect charge states that are stable in the bulk versus those on the surface. There are typically fewer stable charge states on the surface than in the bulk. More study is clearly needed.

Acknowledgements

The authors gratefully acknowledge the support of the National Science Foundation through a graduate fellowship award to MCK. This work was also partially supported by the Petroleum Research Fund of the American Chemical Society (43651-AC5).

References

- [1] S.M. Hu, Mater. Sci. Eng. R 13 (1994) 105–192.
- [2] H. Bracht, MRS Bull. 25 (2000) 22–27.
- [3] N. Dasgupta, A. Dasgupta, *Semiconductor Devices: Modeling and Technology*, Prentice-Hall, New Delhi, 2004.
- [4] M.Y.L. Jung, C.T.M. Kwok, R.D. Braatz, E.G. Seebauer, J. Appl. Phys. 97 (2005) 063520.
- [5] P.M. Fahey, P.B. Griffin, J.D. Plummer, Rev. Mod. Phys. 61 (1989) 289–384.
- [6] S. Guha, J.M. Depuydt, M.A. Haase, J. Qiu, H. Cheng, Appl. Phys. Lett. 63 (1993) 3107–3109.
- [7] W.W. Chow, S.W. Koch, *Semiconductor-Laser Fundamentals: Physics of the Gain Materials*, Springer, Berlin, 1999.
- [8] G. Lutz, *Semiconductor Radiation Detectors*, Springer, Berlin, 1999.
- [9] J.W. Fergus, J. Mater. Sci. 38 (2003) 4259–4270.
- [10] Y. Zhang, A. Kolmakov, S. Chretien, H. Metiu, M. Moskovits, Nano Lett. 4 (2004) 403–407.
- [11] W. Baiqi, J. Liqiang, Q. Yichun, L. Shudan, J. Baojiang, Y. Libin, X. Baifu, F. Honggang, Appl. Surf. Sci. 252 (2006) 2817–2825.
- [12] M.A. Green, Conference on Optoelectronic and Microelectronic Materials and Devices Proceedings, IEEE, Canberra, Australia, December 8–11, (1996), pp. 1–7.
- [13] S.R. Kurtz, A.A. Allerman, E.D. Jones, J.M. Gee, J.J. Banas, B.E. Hammons, Appl. Phys. Lett. 74 (1999) 729–731.
- [14] E.C. Jones, E. Ishida, Mater. Sci. Eng. R 24 (1998) 1–80.
- [15] R.M. Cohen, G. Li, C. Jagadish, P.T. Burke, M. Gal, Appl. Phys. Lett. 73 (1998) 803–805.
- [16] P.D. Townsend, P.J. Chandler, L. Zhang, *Optical Effects of Ion Implantation*, Cambridge University Press, Cambridge, 1994.
- [17] S.J. Pearton, F. Ren, S.N.G. Chu, W.S. Hobson, C.R. Abernathy, T.R. Fullowan, J.R. Lothian, R.G. Elliman, D.C. Jacobson, J.M. Poate, Nucl. Instrum. Methods Phys. Res., Sect. B 79 (1993) 648–650.
- [18] Z.L. Wang, Q.T. Zhao, K.M. Wang, B.R. Shi, Nucl. Instrum. Methods Phys. Res., Sect. B 115 (1996) 421–429.
- [19] E.G. Roth, O.W. Holland, V.C. Venezia, B. Nielsen, J. Electron. Mater. 26 (1997) 1349–1354.
- [20] J.S. Williams, Mater. Sci. Eng. A 253 (1998) 8–15.
- [21] S. Pizzini, M. Acciarri, S. Binetti, D. Narducci, C. Savigni, Mater. Sci. Eng. B 45 (1997) 126–133.
- [22] S.P. Wilks, J. Phys. D: Appl. Phys. 35 (2002) R77–R90.
- [23] K. Dev, M.Y.L. Jung, R. Gunawan, R.D. Braatz, E.G. Seebauer, Phys. Rev. B 68 (2003) 195311.
- [24] E.G. Seebauer, K. Dev, M.Y.L. Jung, R. Vaidyanathan, C.T.M. Kwok, J.W. Ager, E.E. Haller, R.D. Braatz, Phys. Rev. Lett. 97 (2006) 055503.
- [25] R. Ditchfield, D. Llera-Rodriguez, E.G. Seebauer, Phys. Rev. Lett. 81 (1998) 1259–1262.
- [26] R. Ditchfield, D. Llera-Rodriguez, E.G. Seebauer, Phys. Rev. B 61 (2000) 13710–13720.
- [27] S.A. Centoni, B. Sadigh, G.H. Gilmer, T.J. Lenosky, T.D. de la Rubia, C.B. Musgrave, Phys. Rev. B 72 (2005) 195206.
- [28] H.Y.H. Chan, K. Dev, E.G. Seebauer, Phys. Rev. B 67 (2003) 035311.
- [29] C.E. Allen, R. Ditchfield, E.G. Seebauer, J. Vac. Sci. Technol. A 14 (1996) 22–29.
- [30] W.C. Lee, S.G. Lee, K.J. Chang, J. Phys.: Condens. Mat. 10 (1998) 995–1002.
- [31] J. Tersoff, Phys. Rev. Lett. 65 (1990) 887–890.
- [32] P. Mascher, S. Dannefaer, D. Kerr, Phys. Rev. B 40 (1989) 11764–11771.
- [33] M.J. Puska, C. Corbel, R.M. Nieminen, Phys. Rev. B 41 (1990) 9980–9993.
- [34] P.W. Tasker, A.M. Stoneham, J. Phys. C: Solid State Phys. 10 (1977) 5131–5140.

- [35] E.G. Seebauer, in: Proceedings of the Fourth International Conference on Solid-State and Integrated Circuit Technology, IEEE, Beijing, China, (2004), pp. 1032–1037.
- [36] Z.M. Jarzebski, Oxide Semiconductors, Pergamon Press, New York, 1973.
- [37] J. Nishizawa, Y. Oyama, Mater. Sci. Eng. R 12 (1994) 273–426.
- [38] A.M. Stoneham, Adv. Phys. 28 (1979) 457–492.
- [39] T. Sinno, E. Dornberger, W. von Ammon, R.A. Brown, F. Dupret, Mater. Sci. Eng. R 28 (2000) 149–198.
- [40] P. Pichler, Intrinsic Point Defects, Impurities, and their Diffusion in Silicon, Springer-Verlag/Wein, New York, 2004.
- [41] R.M. Cohen, Conference on Optoelectronic and Microelectronic Materials and Devices Proceedings, IEEE, Canberra, Australia December 8–11, (1996), pp. 107–113.
- [42] D.M. Smyth, The Defect Chemistry of Metal Oxides, Oxford University Press, New York, 2000.
- [43] K. Kosuge, Chemistry of Non-Stoichiometric Compounds, Oxford Science Publications, New York, 1994.
- [44] V.E. Henrich, The Surface Science of Metal Oxides, Cambridge University Press, Cambridge, 1994.
- [45] P. Ebert, Curr. Opin. Solid State Mater. Sci. 5 (2001) 211–250.
- [46] J. Nowotny, L.C. DuFour (Eds.), Surface and Near-Surface Chemistry of Oxide Materials, Elsevier, Amsterdam, 1988.
- [47] F.A. Kroger, H.J. Vink, J. Phys. Chem. Solids 5 (1958) 208–223.
- [48] J.A. Van Vechten, A simple man's view of the thermochemistry of semiconductors, in: S.P. Keller (Ed.), Handbook on Semiconductors, vol. 3, North-Holland, New York, 1980, pp. 1–111.
- [49] J.A. Van Vechten, C.D. Thurmond, Phys. Rev. B 14 (1976) 3539–3550.
- [50] J.A. Van Vechten, C.D. Thurmond, Phys. Rev. B 14 (1976) 3551–3557.
- [51] J.C. Bourgoin, M. Lannoo, Point Defects in Semiconductors, Springer, Berlin, 1981.
- [52] R.A. Swalin, J. Phys. Chem. Solids 23 (1962) 154–156.
- [53] P.A. Schultz, Phys. Rev. Lett. 96 (2006) 246401.
- [54] H.J. Queisser, E.E. Haller, Science 281 (1998) 945–950.
- [55] Y.P. Varshni, Physica 34 (1967) 149–154.
- [56] C.D. Thurmond, J. Electrochem. Soc. 122 (1975) 1133–1141.
- [57] K. Dev, E.G. Seebauer, Phys. Rev. B 67 (2003) 035312.
- [58] G.E. Jellison Jr., F.A. Modine, Phys. Rev. B 27 (1983) 7466–7472.
- [59] P. Lautenschlager, M. Garriga, L. Vina, M. Cardona, Phys. Rev. B 36 (1987) 4821–4830.
- [60] K. Dev, E.G. Seebauer, Surf. Sci. 538 (2003) 495–499.
- [61] K. Sasaki, J. Maier, J. Appl. Phys. 86 (1999) 5422–5433.
- [62] K. Sasaki, J. Maier, J. Appl. Phys. 86 (1999) 5434–5443.
- [63] G. Brouwer, Phillips Res. Rep. 9 (1954) 366–376.
- [64] C.M. Chang, C.M. Wei, S.P. Chen, Phys. Rev. B 54 (1996) 17083–17096.
- [65] L. Fu-Hsing, Comput. Mater. Sci. 14 (1999) 48–55.
- [66] A. Seeger, K.P. Chik, Phys. Status Solidi B 29 (1968) 455–542.
- [67] S.M. Hu, Phys. Status Solidi B 60 (1973) 595–604.
- [68] H.C. Casey Jr., B.I. Miller, E. Pinkas, J. Appl. Phys. 44 (1973) 1281–1287.
- [69] C. Zener, J. Appl. Phys. 22 (1951) 372–375.
- [70] G.H. Vineyard, J. Phys. Chem. Solids 3 (1957) 121–127.
- [71] S.A. Rice, Phys. Rev. 112 (1958) 804–811.
- [72] C.P. Flynn, Phys. Rev. 171 (1968) 682–698.
- [73] R. Gomer, Surface Diffusion, Plenum Press, London, 1996.
- [74] E.G. Seebauer, M.Y.L. Jung, Surface Diffusion of Adsorbates on metals, Alloys, Oxides and Semiconductors, Springer-Verlag, New York, 2001.
- [75] A. Ural, P.B. Griffin, J.D. Plummer, Phys. Rev. Lett. 83 (1999) 3454–3457.
- [76] A. Ural, P.B. Griffin, J.D. Plummer, Phys. Rev. Lett. 85 (2000) 4836–14836.
- [77] H. Bracht, E.E. Haller, Phys. Rev. Lett. 85 (2000) 4835.
- [78] B.L. Sharma, Diffus. Defect Data, Pt. A 70/71 (1990) 1–102.
- [79] K. Kato, J. Phys.: Condens. Mat. 5 (1993) 6387–6406.
- [80] L.J. Munro, D.J. Wales, Phys. Rev. B 59 (1999) 3969–3980.
- [81] B. Sahli, W. Fichtner, Phys. Rev. B 72 (2005) 245210.
- [82] T. Bak, J. Nowotny, M. Rekas, C.C. Sorrell, J. Phys. Chem. Solids 64 (2003) 1043–1056.
- [83] U. Diebold, Appl. Phys. A 76 (2003) 681–687.
- [84] K. Hoshino, N.L. Peterson, C.L. Wiley, J. Phys. Chem. Solids 46 (1985) 1397–1411.
- [85] Z. Jun-Liang, Z. Wenqing, L. Xiao-Min, F. Ji-Wei, S. Xun, J. Phys.: Condens. Mat. 18 (2006) 1495–1508.
- [86] A.F. Kohan, G. Ceder, D. Morgan, C.G. van de Walle, Phys. Rev. B 61 (2000) 15019–15027.
- [87] F. Millot, C. Picard, Solid State Ionics 28–30 (1988) 1344–1348.
- [88] F. Oba, S.R. Nishitani, S. Isotani, H. Adachi, I. Tanaka, J. Appl. Phys. 90 (2001) 824–828.
- [89] G.W. Tomlins, J.L. Routbort, T.O. Mason, J. Am. Ceram. Soc. 81 (1998) 869–876.
- [90] P. Erhart, K. Albe, Appl. Phys. Lett. 88 (2006) 201918.
- [91] T. Doi, M. Ichikawa, S. Hosoki, K. Ninomiya, Surf. Sci. 343 (1995) 24–30.
- [92] H.P. Bonzel, Structure and Properties of Metal Surfaces, Maruzen Co., Ltd., Tokyo, 1973.

- [93] E.G. Seebauer, C.E. Allen, *Prog. Surf. Sci.* 49 (1995) 265–330.
- [94] B. Mills, P. Douglas, G.M. Leak, *Trans. Met. Soc. AIME* 245 (1969) 1291–1296.
- [95] E.W. Plummer, T.N. Rhodin, *J. Chem. Phys.* 49 (1968) 3479–3496.
- [96] V.T. Binh, P. Melinon, *Surf. Sci.* 161 (1985) 234–244.
- [97] A. Tsoga, P. Nikolopoulos, *J. Am. Ceram. Soc.* 77 (1994) 954–960.
- [98] K. Fukutani, *Surf. Sci.* 281 (1993) 285–295.
- [99] N. Bernstein, M.J. Mehl, D.A. Papaconstantopoulos, N.I. Papanicolaou, M.Z. Bazant, E. Kaxiras, *Phys. Rev. B* 62 (2000) 4477–4487.
- [100] Y. Kumeda, D.J. Wales, L.J. Munro, *Chem. Phys. Lett.* 341 (2001) 185–194.
- [101] G.D. Watkins, *Phys. Rev.* 155 (1967) 802–815.
- [102] G.D. Watkins, Inst. Phys., Freiburg, West Germany, 1975, pp. 1–22.
- [103] G.D. Watkins, *Mater. Sci. Forum* 10–12 (1986) 953–960.
- [104] G.D. Watkins, J.R. Troxell, A.P. Chatterjee, Inst. Phys., Nice, France, 1979, pp. 16–30.
- [105] M.K. Sheinkman, N.I. Kashirina, V.V. Kislyuk, International Semiconductor Conference Proceedings, IEEE, Sinaia, Romania, (1998), pp. 89–92.
- [106] A. El-Hdiy, G. Salace, C. Petit, M. Jourdain, D. Vuillaume, *J. Appl. Phys.* 74 (1993) 1124.
- [107] H. Ness, A.J. Fisher, G.A.D. Briggs, *Surf. Sci.* 380 (1997) L479–L484.
- [108] L. David, J. Bernard, M. Orrit, P. Kottis, *Chem. Phys.* 132 (1989) 31–39.
- [109] F. Baumberger, T. Greber, J. Osterwalder, *Phys. Rev. B* 62 (2000) 15431–15434.
- [110] I.M. Vitomirov, G.D. Waddill, C.M. Aldao, S.G. Anderson, C. Capasso, J.H. Weaver, *Phys. Rev. B* 40 (1989) 3483.
- [111] T.A. Kirichenko, S.K. Banerjee, G.S. Hwang, *Phys. Status Solidi B* 241 (2004) 2303–2312.
- [112] R. Vaidyanathan, E.G. Seebauer, H. Graoui, M.A. Foad, *Appl. Phys. Lett.* 89 (2006) 152114.
- [113] C.G. Van de Walle, J. Neugebauer, *J. Appl. Phys.* 95 (2004) 3851–3879.
- [114] E.R. Weber, *Physica* 116B (1983) 398–403.
- [115] G.D. Watkins, *Mater. Sci. Semicond. Process* 3 (2000) 227–235.
- [116] L.G. Rowan, *J. Electron. Mater.* 19 (1990) 633–636.
- [117] B. Stich, S. Greulich-Weber, J.M. Spaeth, *J. Appl. Phys.* 77 (1995) 1546–1553.
- [118] T.A. Kennedy, N.D. Wilsey, in: Proceedings of the 13th International Conference on Defects in Semiconductors, Metallurgical, AIME, Soc., Warrendale, PA, (1985), p. 929.
- [119] K.L. Brower, *Rev. Sci. Instrum.* 48 (1977) 135–141.
- [120] M. Eldrup, B.N. Singh, *J. Nucl. Mater.* 251 (1997) 132–138.
- [121] A. Seeger, F. Banhart, *Helv. Phys. Acta* 63 (1990) 403–428.
- [122] M.J. Puska, R.M. Nieminen, *Rev. Mod. Phys.* 66 (1994) 841–897.
- [123] H. Kauppinen, Identification of point defect structures in semiconductors by positron annihilation: application to silicon and compound semiconductors, Ph.D. dissertation, Helsinki Univ. Technol., Espoo, Finland, 1997.
- [124] R. Krause-Rehberg, H.S. Leipner, *Positron Annihilation in Semiconductors: Defect Studies*, Springer-Verlag, 1999,, p. 339.
- [125] A. Dupasquier, A.P. Mills, *Positron Spectroscopy of Solids*, IOS, Amsterdam, 1995.
- [126] S. Dutta, M. Chakrabarti, S. Chattopadhyay, D. Jana, D. Sanyal, A. Sarkar, *J. Appl. Phys.* 98 (2005) 053513.
- [127] K. Saarinen, *Acta Polytech. Scand., Appl. Phys. Ser.* (1991) 1–36.
- [128] J. Mäkinen, P. Hautajarvi, C. Corbel, *J. Phys.: Condens. Mat.* 4 (1992) 5137–5154.
- [129] M. Alatalo, M.J. Puska, R.M. Nieminen, *J. Phys.: Condens. Mat.* 5 (1993) L307–L314.
- [130] V.J. Ghosh, M. Alatalo, P. Asoka-Kumar, B. Nielsen, K.G. Lynn, A.C. Kruseman, P.E. Mijnarends, *Phys. Rev. B* 61 (2000) 10092–10099.
- [131] D.V. Lang, *J. Appl. Phys.* 45 (1974) 3023–3032.
- [132] F.D. Auret, M. Nel, *Meas. Sci. Technol.* 2 (1991) 623–627.
- [133] D. Stievenard, D. Vuillaume, *J. Appl. Phys.* 60 (1986) 973–979.
- [134] P. Kaminski, *Mater. Sci. Eng. B* 20 (1993) 221–224.
- [135] F. Auret, P. Deenapanray, *Crit. Rev. Solid State Mater. Sci.* 29 (2004) 1–44.
- [136] B.G. Svensson, C. Jagadish, A. Hallen, J. Lalita, *Nucl. Instrum. Methods Phys. Res., Sect. B* 106 (1995) 183–190.
- [137] Z. Su, J.W. Farmer, *J. Appl. Phys.* 68 (1990) 4068–4070.
- [138] K. Dmowski, *J. Appl. Phys.* 71 (1992) 2259–2269.
- [139] W.A. Doolittle, A. Rohatgi, *J. Appl. Phys.* 75 (1994) 4560–4569.
- [140] A.A. Istratov, *Rev. Sci. Instrum.* 68 (1997) 3861–3865.
- [141] M. Hanine, M. Masmoudi, J. Marcon, *Mater. Sci. Eng. B* 114–115 (2004) 322–329.
- [142] C.D. Beling, S. Fung, H.L. Au, C.C. Ling, C.V. Reddy, A.H. Deng, B.K. Panda, *Appl. Surf. Sci.* 116 (1997) 121–128.
- [143] J.H. Evans-Freeman, N. Abdulgader, *Gettinger and Defect Engineering in Semiconductor Technology 95–96* (2004) 135–140.
- [144] H. Fujikawa, T. Sekiya, Y. Kuzuoka, M. Oshima, H. Usuda, N. Hirashita, M. Niwa, *Appl. Phys. Lett.* 85 (2004) 413–415.
- [145] H. Bracht, E.E. Haller, R. Clark-Phelps, *Phys. Rev. Lett.* 81 (1998) 393–396.
- [146] K. Compaan, Y. Haven, *J. Chem. Soc., Faraday Trans.* 54 (1958) 1498–1508.
- [147] K. Compaan, Y. Haven, *J. Chem. Soc., Faraday Trans.* 52 (1956) 786–801.
- [148] U. Gosele, W. Frank, A. Seeger, *Solid State Commun.* 45 (1983) 31–33.
- [149] P. Fahey, G. Barbuscia, M. Moslehi, R.W. Dutton, *Appl. Phys. Lett.* 46 (1985) 784–786.
- [150] M. Schultz, U. Egger, R. Scholz, O. Breitenstein, U. Gosele, T.Y. Tan, *J. Appl. Phys.* 83 (1998) 5295–5301.
- [151] U. Egger, M. Schultz, P. Werner, *J. Appl. Phys.* 81 (1997) 6056–6061.

- [152] M.A. Van Hove, W.H. Weinberg, C.-M. Chan, Low-Energy Electron Diffraction, Experiment, Theory and Surface Structure Determination, Springer, Berlin, 1986.
- [153] B.A. Joyce, J.H. Neave, P.J. Dobson, P.K. Larsen, J. Zhang, *J. Vac. Sci. Technol. B* 3 (1985) 562.
- [154] S. Clarke, D.D. Vvedensky, *J. Appl. Phys.* 63 (1988) 2272–2283.
- [155] H.H. Farrell, C.J. Palmstrom, *J. Vac. Sci. Technol. B* 8 (1990) 903–907.
- [156] L.H. Dubois, B.R. Zegarski, B.N.J. Persson, *Phys. Rev. B* 35 (1987) 9128–9134.
- [157] T.S. Jones, *Vacuum* 43 (1992) 177–183.
- [158] G. Salace, C. Petit, D. Vuillaume, *J. Appl. Phys.* 91 (2002) 5896–5901.
- [159] C. Petit, G. Salace, D. Vuillaume, *Solid State Electron.* 47 (2003) 1663–1668.
- [160] C.F. Huang, B.Y. Tsui, P.J. Tzeng, L.S. Lee, M.J. Tsai, *Appl. Phys. Lett.* 88 (2006) 262909.
- [161] W.K. Lye, E. Hasegawa, T.P. Ma, R.C. Barker, Y. Hu, J. Kuehne, D. Frystak, *Appl. Phys. Lett.* 71 (1997) 2523–2525.
- [162] P. Balk, S. Ewert, S. Schmitz, A. Steffen, *J. Appl. Phys.* 69 (1991) 6510–6516.
- [163] W. He, T.P. Ma, *Appl. Phys. Lett.* 83 (2003) 2605–2607.
- [164] Y. Borensztein, *Phys. Status Solidi A* 202 (2005) 1313–1324.
- [165] O. Palumbo, F. Cordero, R. Cantelli, F. Trequattrini, B. Molinas, G.M. Guadalupi, *Mater. Sci. Eng. B* 91 (2002) 498–502.
- [166] G. Margaritondo, A. Franciosi, *Annu. Rev. Mater. Sci.* 14 (1984) 67–93.
- [167] Y. Borensztein, N. Witkowski, *J. Phys.: Condens. Mat.* 16 (2004) S4301–S4311.
- [168] C.R. Carlson, W.F. Suechter, F. One-Ibranim, E.G. Sesbauer, *J. Chem. Phys.* 99 (1993) 7190.
- [169] K. Dev, E.G. Seebauer, *Surf. Sci.* 550 (2004) 185–191.
- [170] K. Dev, E.G. Seebauer, *Surf. Sci.* 583 (2005) 80–87.
- [171] D. Stievenard, *Mater. Sci. Eng. B* 71 (2000) 120–127.
- [172] B. Lagel, I.D. Baikie, U. Petermann, *Surf. Sci.* 435 (1999) 622–626.
- [173] Y. Rosenwaks, R. Shikler, T. Glatzel, S. Sadewasser, *Phys. Rev. B* 70 (2004) 085320.
- [174] P. Ebert, *Appl. Phys. A* 75 (2002) 101–112.
- [175] X. de la Broise, C. Delerue, M. Lannoo, B. Grandidier, D. Stievenard, *Phys. Rev. B* 61 (2000) 2138–2145.
- [176] J.A. Kubby, J.J. Boland, *Surf. Sci. Rep.* 26 (1996) 61–204.
- [177] G.W. Brown, H. Grube, M.E. Hawley, S.R. Schofield, N.J. Curson, M.Y. Simmons, R.G. Clark, *J. Appl. Phys.* 92 (2002) 820–824.
- [178] G. Lee, H. Mai, I. Chizhov, R.F. Willis, *Surf. Sci.* 463 (2000) 55–65.
- [179] G. Lengel, R. Wilkins, G. Brown, M. Weimer, J. Gryko, R.E. Allen, *Phys. Rev. Lett.* 72 (1994) 836.
- [180] U. Semmler, P. Ebert, K. Urban, *Appl. Phys. Lett.* 77 (2000) 61–63.
- [181] P. Ebert, P. Quadbeck, K. Urban, B. Henninger, K. Horn, G. Schwarz, J. Neugebauer, M. Scheffler, *Appl. Phys. Lett.* 79 (2001) 2877–2879.
- [182] P. Ebert, G. Cox, U. Poppe, K. Urban, *Ultramicroscopy* 42–44 (1992) 871–877.
- [183] K.A. Schultz, I.I. Suni, C.E. Allen, E.G. Seebauer, *Surf. Sci.* 276 (1992) 40–49.
- [184] K.A. Schultz, I.I. Suni, E.G. Seebauer, *J. Opt. Soc. Am. B: Opt. Phys.* 10 (1993) 546–550.
- [185] R.O. Jones, O. Gunnarsson, *Rev. Mod. Phys.* 61 (1989) 689–746.
- [186] J. Hafner, C. Wolverton, G. Ceder, *MRS Bull.* 31 (2006) 659–665.
- [187] C.W.M. Castleton, A. Hoglund, S. Mirbt, *Phys. Rev. B* 73 (2006) 035215.
- [188] D. Eaglesham, *Phys. World* 8 (1995) 41–45.
- [189] W. Windl, T.J. Lenosky, J.D. Kress, A.F. Voter, *Nucl. Instrum. Methods Phys. Res., Sect. B* 141 (1998) 61–65.
- [190] M.C. Payne, M.P. Teter, D.C. Allan, T.A. Arias, J.D. Joannopoulos, *Rev. Mod. Phys.* 64 (1992) 1045–1097.
- [191] J.R. Chelikowsky, N. Troullier, Y. Saad, *Phys. Rev. Lett.* 72 (1994) 1240–1243.
- [192] J. Shim, E.K. Lee, Y.J. Lee, R.M. Nieminen, *Phys. Rev. B* 71 (2005) 245204.
- [193] J. Lento, J.L. Mozos, R.M. Nieminen, *J. Phys.: Condens. Mat.* 14 (2002) 2637–2645.
- [194] M.J. Puska, S. Poykko, M. Pesola, R.M. Nieminen, *Phys. Rev. B* 58 (1998) 1318–1325.
- [195] G.D. Watkins, The lattice vacancy in silicon, in: S.T. Pantelides (Ed.), Deep Centers in Semiconductors, Gordon and Breach, New York, 1986 p. 147.
- [196] J.P. Perdew, A. Zunger, *Phys. Rev. B* 23 (1981) 5048–5079.
- [197] G. Schwarz, J. Neugebauer, M. Scheffler, in: Proceedings of the 25th International Conference on the Physics of Semiconductors, Springer, Berlin, Osaka, Japan, (2000), pp. 1–3.
- [198] G. Makov, M.C. Payne, *Phys. Rev. B* 51 (1995) 4014–4022.
- [199] L.N. Kantorovich, I.I. Tupitsyn, *J. Phys.: Condens. Mat.* 11 (1999) 6159–6168.
- [200] P.A. Schultz, *Phys. Rev. B* 60 (1999) 1551–1554.
- [201] P.A. Schultz, *Phys. Rev. Lett.* 84 (2000) 1942–1945.
- [202] A. Castro, A. Rubio, M.J. Stott, *Can. J. Phys.* 81 (2003) 1151–1164.
- [203] H. Nozaki, S. Itoh, *Phys. Rev. E* 62 (2000) 1390–1396.
- [204] R. Price, P.M. Platzman, *Phys. Rev. B* 44 (1991) 2356.
- [205] C.W.M. Castleton, S. Mirbt, *Phys. Rev. B* 70 (2004) 195202.
- [206] W. Kohn, L.J. Sham, *Phys. Rev.* 140 (1965) A1133.
- [207] M.C. Payne, M.P. Teter, D.C. Allan, *J. Chem. Soc., Faraday Trans.* 86 (1990) 1221–1226.
- [208] T.D. de la Rubia, *Annu. Rev. Mater. Sci.* 26 (1996) 613–649.
- [209] V. Heine, *Surf. Sci.* 53 (1975) 408.

- [210] D. Vogel, P. Kruger, J. Pollmann, Phys. Rev. B 55 (1997) 12836–12839.
- [211] M. Stadele, M. Moukara, J.A. Majewski, P. Vogl, A. Gorling, Phys. Rev. B 59 (1999) 10031–10043.
- [212] R. Car, P.J. Kelly, A. Oshiyama, S.T. Pantelides, in: Proceedings of the 17th International Conference on the Physics of Semiconductors, Springer-Verlag, New York, (1985), p. 55.
- [213] R. Car, P.J. Kelly, A. Oshiyama, S.T. Pantelides, Phys. Rev. Lett. 52 (1984) 1814–1817.
- [214] G.A. Baraff, M. Schluter, G. Allan, Phys. Rev. B 27 (1983) 1010–1016.
- [215] G. Wachutka, A. Fleszar, F. Maca, M. Scheffler, J. Phys.: Condens. Mat. 4 (1992) 2831–2844.
- [216] I. Gorczyca, C. Skierbiszewski, T. Suski, N.E. Christensen, A. Svane, Phys. Rev. B 66 (2002) 081106.
- [217] I. Gorczyca, A. Svane, N.E. Christensen, MRS Internet J. Nitride Semicond. Res. 2 (18) (1997).
- [218] I. Gorczyca, A. Svane, N.E. Christensen, Phys. Rev. B 60 (1999) 8147–8157.
- [219] D.D. Nolte, Phys. Rev. B 58 (1998) 7994–8001.
- [220] A.P. Horsfield, A.M. Bratkovsky, J. Phys.: Condens. Mat. 12 (2000) R1–R24.
- [221] L. Colombo, Annu. Rev. Mater. Res. 32 (2002) 271–295.
- [222] M. Elstner, D. Porezag, G. Jungnickel, J. Elsner, M. Haugk, T. Frauenheim, S. Suhai, G. Seifert, Phys. Rev. B 58 (1998) 7260–7268.
- [223] D.W. Jenkins, J.D. Dow, Phys. Rev. B 39 (1989) 3317–3329.
- [224] D.W. Jenkins, J.D. Dow, M.H. Tsai, J. Appl. Phys. 72 (1992) 4130–4133.
- [225] M.E. Law, G.H. Gilmer, M. Jaraiz, MRS Bull. 25 (2000) 45–50.
- [226] M.M. Bunea, S.T. Dunham, J. Comput. Aided Mater. Des. 5 (1998) 81–88.
- [227] I. Martin-Bragado, P. Castrillo, M. Jaraiz, R. Pinacho, J.E. Rubio, J. Barbolla, Phys. Rev. B 72 (2005) 035202.
- [228] I. Martin-Bragado, P. Castrillo, M. Jaraiz, R. Pinacho, J.E. Rubio, J. Barbolla, V. Moroz, J. Appl. Phys. 98 (2005) 053709.
- [229] D. Alfe, M.J. Gillan, Phys. Rev. B 71 (2005) 220101(R).
- [230] J.V. Beck, K.J. Arnold, Parameter Estimation in Engineering and Science, Wiley, New York, 1977.
- [231] M.Y.L. Jung, R. Gunawan, R.D. Braatz, E.G. Seebauer, AIChE J. 50 (2004) 3248–3256.
- [232] C.T.M. Kwok, K. Dev, R.D. Braatz, E.G. Seebauer, J. Appl. Phys. 98 (2005) 013524.
- [233] M.Y.L. Jung, R. Gunawan, R.D. Braatz, E.G. Seebauer, J. Electrochem. Soc. 150 (2003) G838–G842.
- [234] R. Gunawan, M.Y.L. Jung, E.G. Seebauer, R.D. Braatz, AIChE J. 49 (2003) 2114–2123.
- [235] Z. Wang, E.G. Seebauer, Phys. Rev. Lett. 95 (2005) 015501.
- [236] K. Dev, E.G. Seebauer, Surf. Sci. 572 (2004) 483–489.
- [237] H. Kim, J.R. Chelikowsky, Phys. Rev. Lett. 77 (1996) 1063–1066.
- [238] G. Cox, K.H. Graf, D. Szynka, U. Poppe, K. Urban, Vacuum 41 (1990) 591–595.
- [239] M.C. Qian, M. Gothelid, B. Johansson, S. Mirbt, Phys. Rev. B 66 (2002) 155326.
- [240] P. Ebert, K. Urban, L. Aballe, C.H. Chen, K. Horn, G. Schwarz, J. Neugebauer, M. Scheffler, Phys. Rev. Lett. 84 (2000) 5816–5819.
- [241] S.B. Zhang, A. Zunger, Phys. Rev. Lett. 77 (1996) 119–122.
- [242] C. Domke, M. Heinrich, P. Ebert, K. Urban, J. Vac. Sci. Technol. B 16 (1998) 2825–2832.
- [243] G. Lengel, J. Harper, M. Weimer, Phys. Rev. Lett. 76 (1996) 4725–4728.
- [244] M. Menetrey, A. Markovits, C. Minot, G. Pacchioni, J. Phys. Chem. B 108 (2004) 12858–12864.
- [245] M.D. Rasmussen, L.M. Molina, B. Hammer, J. Chem. Phys. 120 (2004) 988–997.
- [246] S.G. Wang, X.D. Wen, D.B. Cao, Y.W. Li, H.G. Wang, H.J. Jiao, Surf. Sci. 577 (2005) 69–76.
- [247] H. Fox, A.P. Horsfield, M.J. Gillan, J. Chem. Phys. 124 (2006) 134709.
- [248] J.P. Perdew, K. Burke, M. Ernzerhof, Phys. Rev. Lett. 77 (1996) 3865–3868.
- [249] J.P. Perdew, J.A. Chevary, S.H. Vosko, K.A. Jackson, M.R. Pederson, D.J. Singh, C. Fiolhais, Phys. Rev. B 46 (1992) 6671–6687.
- [250] J. Chen, L.B. Lin, F.Q. Jing, J. Phys. Chem. Solids 62 (2001) 1257–1262.
- [251] C. Stampfl, C.G. Van de Walle, Phys. Rev. B 65 (2002) 155212.
- [252] W. Orellana, H. Chacham, Phys. Rev. B 63 (2001) 125205.
- [253] A. Weibel, R. Bouchet, P. Knauth, Solid State Ionics 177 (2006) 229–236.
- [254] G.P. Srivastava, Rep. Prog. Phys. 60 (1997) 561–613.
- [255] H. Lim, K. Cho, R.B. Capaz, J.D. Joannopoulos, K.D. Brommer, B.E. Larson, Phys. Rev. B 53 (1996) 15421–15424.
- [256] M. Ferhat, A. Zaoui, M. Certier, H. Aourag, Physica B 252 (1998) 229–236.
- [257] A. Zaoui, F.E. Hassan, J. Phys.: Condens. Mat. 13 (2001) 253–262.
- [258] T. Bak, J. Nowotny, C.C. Sorrell, Key Eng. Mater. 125–126 (1997) 1–80.
- [259] J. Nowotny, M. Radecka, M. Rekas, J. Phys. Chem. Solids 58 (1997) 927–937.
- [260] A. Antonelli, E. Kaxiras, D.J. Chadi, Phys. Rev. Lett. 81 (1998) 2088–2091.
- [261] R.J. Needs, J. Phys.: Condens. Mat. 11 (1999) 10437–10450.
- [262] S.J. Clark, G.J. Ackland, Phys. Rev. B 56 (1997) 47–50.
- [263] S. Goedecker, T. Deutscher, L. Billard, Phys. Rev. Lett. 88 (2002) 235501.
- [264] W.K. Leung, R.J. Needs, G. Rajagopal, S. Itoh, S. Ihara, Phys. Rev. Lett. 83 (1999) 2351–2354.
- [265] L.A. Marques, L. Pelaz, P. Castrillo, J. Barbolla, Phys. Rev. B 71 (2005) 085204.
- [266] J. Coutinho, R. Jones, V.J.B. Torres, M. Barroso, S. Öberg, P.R. Briddon, J. Phys.: Condens. Mat. 17 (2005) L521–L527.
- [267] A. Fazzio, A. Janotti, A.J.R. da Silva, R. Mota, Phys. Rev. B 61 (2000) R2401–R2404.
- [268] A. Janotti, R. Baierle, A.J.R. da Silva, R. Mota, A. Fazzio, Physica B 273–274 (1999) 575–578.
- [269] G.A. Baraff, E.O. Kane, M. Schluter, Phys. Rev. Lett. 46 (1979) 956–959.
- [270] G.D. Watkins, J.R. Troxell, Phys. Rev. Lett. 44 (1980) 593–596.

- [271] J. Lento, R.M. Nieminen, *J. Phys.: Condens. Mat.* 15 (2003) 4387–4395.
- [272] J.C. Bourgoin, J.W. Corbett, IOP Conference, Institute of Physics, Bristol, (1974), p. 149.
- [273] J.A. Van Vechten, *Phys. Rev. B* 38 (1988) 9913–9919.
- [274] E. Tarnow, *J. Phys.: Condens. Mat.* 5 (1993) 1863–1876.
- [275] S. Öğüt, H. Kim, J.R. Chelikowsky, *Phys. Rev. B* 56 (1997) 11353–11356.
- [276] S.K. Streicher, *Phys. Status Solidi B* 217 (2000) 513–532.
- [277] D. Maroudas, R.A. Brown, *Phys. Rev. B* 47 (1993) 15562–15577.
- [278] D. Maroudas, R.A. Brown, *Appl. Phys. Lett.* 62 (1993) 172–174.
- [279] P.J. Ungar, T. Halicioglu, W.A. Tiller, *Phys. Rev. B* 50 (1994) 7344–7357.
- [280] M.J. Tang, L. Colombo, J. Zhu, T.D. de la Rubia, *Phys. Rev. B* 55 (1997) 14279–14289.
- [281] D.J. Chadi, *Phys. Rev. B* 46 (1992) 9400–9407.
- [282] Y. Bar-Yam, J.D. Joannopoulos, *Phys. Rev. Lett.* 52 (1984) 1129–1132.
- [283] S. Balboni, E. Albertazzi, M. Bianconi, G. Lulli, *Phys. Rev. B* 66 (2002) 045202.
- [284] S. Öğüt, J.R. Chelikowsky, *Phys. Rev. B* 64 (2001) 245206.
- [285] A.J.R. da Silva, R. Baierle, R. Mota, A. Fazzio, *Physica B* 302–303 (2001) 364–368.
- [286] H.R. Schober, *Phys. Rev. B* 39 (1989) 13013–13015.
- [287] M.D. Moreira, R.H. Miwa, P. Venezuela, *Phys. Rev. B* 70 (2004) 115215.
- [288] A.J.R. da Silva, A. Janotti, A. Fazzio, R.J. Baierle, R. Mota, *Phys. Rev. B* 62 (2000) 9903–9906.
- [289] S. Birner, J.P. Goss, R. Jones, P.R. Briddon, S. Oberg, International Workshop on Defect Engineering of Advanced Semiconductor Devices, Stockholm, Sweden, (2000), pp. 1–4.
- [290] G.B. Bachelet, G.A. Baraff, M. Schluter, *Phys. Rev. B* 24 (1981) 915–925.
- [291] K. Laasonen, R.M. Nieminen, M.J. Puska, *Phys. Rev. B* 45 (1992) 4122–4130.
- [292] S. Hyangsuk, L.J. Lewis, *Phys. Rev. B* 52 (1995) 5675–5684.
- [293] F. El-Mellouhi, N. Mousseau, *Phys. Rev. B* 71 (2005) 125207.
- [294] J.E. Northrup, S.B. Zhang, *Phys. Rev. B* 50 (1994) 4962–4964.
- [295] C. Delerue, *Phys. Rev. B* 44 (1991) 10525–10535.
- [296] J.T. Schick, C.G. Morgan, P. Papoulias, *Phys. Rev. B* 66 (2002) 195302.
- [297] S.B. Zhang, J.E. Northrup, *Phys. Rev. Lett.* 67 (1991) 2339–2342.
- [298] J. Lagowski, H.C. Gatos, J.M. Parsey, K. Wada, M. Kaminska, W. Walukiewicz, *Appl. Phys. Lett.* 40 (1982) 342–344.
- [299] M. Kaminska, M. Skowronski, W. Kuszko, *Phys. Rev. Lett.* 55 (1985) 2204–2207.
- [300] M. Skowronski, J. Lagowski, H.C. Gatos, *Phys. Rev. B* 32 (1985) 4264–4267.
- [301] J. Dabrowski, M. Scheffler, *Phys. Rev. Lett.* 60 (1988) 2183–2186.
- [302] D.J. Chadi, K.J. Chang, *Phys. Rev. Lett.* 60 (1988) 2187–2190.
- [303] D.J. Chadi, *Phys. Rev. B* 68 (2003) 193204.
- [304] H. Hausmann, A. Pillukat, P. Ehrhart, *Phys. Rev. B* 54 (1996) 8527–8539.
- [305] D.T.J. Hurle, *J. Appl. Phys.* 85 (1999) 6957–7022.
- [306] H. Overhof, J.M. Spaeth, *Phys. Rev. B* 72 (2005) 115205.
- [307] J. Dabrowski, M. Scheffler, *Phys. Rev. B* 40 (1989) 10391–10401.
- [308] S.B. Zhang, D.J. Chadi, *Phys. Rev. Lett.* 64 (1990) 1789–1792.
- [309] G.A. Baraff, M. Schluter, *Phys. Rev. Lett.* 55 (1985) 1327–1330.
- [310] M. Hakala, M.J. Puska, R.M. Nieminen, *J. Appl. Phys.* 91 (2002) 4988–4994.
- [311] J. Neugebauer, C.G. Van de Walle, *Appl. Phys. Lett.* 69 (1996) 503–505.
- [312] S. Limpijumnong, C.G. Van de Walle, *Phys. Rev. B* 69 (2004) 035207.
- [313] J. Neugebauer, C.G. van de Walle, *Phys. Rev. B* 50 (1994) 8067–8070.
- [314] W. Orellana, H. Chacham, *Appl. Phys. Lett.* 74 (1999) 2984–2986.
- [315] A. Gulans, R.A. Evarestov, I. Tale, C.C. Yang, *Phys. Status Solidi C* 2 (2005) 507–510.
- [316] M.G. Ganchenkova, R.M. Nieminen, *Phys. Rev. Lett.* 96 (2006) 196402.
- [317] N. Yu, W. Halley, *Phys. Rev. B* 51 (1995) 4768–4776.
- [318] J. He, S.B. Sinnott, *J. Am. Ceram. Soc.* 88 (2005) 737–741.
- [319] A. Stashans, S. Lunell, R.W. Grimes, *J. Phys. Chem. Solids* 57 (1996) 1293–1301.
- [320] E. Cho, S. Han, H.-S. Ahn, K.-R. Lee, S.K. Kim, C.S. Hwang, *Phys. Rev. B* 73 (2006) 193202.
- [321] S. Na-Phattalung, M.F. Smith, K. Kwiseon, D. Mao-Hua, W. Su-Huai, S.B. Zhang, S. Limpijumnong, *Phys. Rev. B* 73 (2006) 125205.
- [322] S. Limpijumnong, X. Li, S.-H. Wei, S.B. Zhang, *Appl. Phys. Lett.* 86 (2005) 211910–211913.
- [323] T. Petit, C. Lemaignan, F. Jollet, B. Bigot, A. Pasturel, *Phil. Magn. B* 77 (1998) 779–786.
- [324] J.P. Crocombe, F. Jollet, L.T. Nga, T. Petit, *Phys. Rev. B* 64 (2001) 104107.
- [325] P. Erhart, A. Klein, K. Albe, *Phys. Rev. B* 72 (2005) 085213.
- [326] A. Janotti, C.G. Van de Walle, *Appl. Phys. Lett.* 87 (2005) 122102.
- [327] R.M. Tromp, R.J. Hamers, J.E. Demuth, *Phys. Rev. Lett.* 55 (1985) 1303–1306.
- [328] R.J. Hamers, R.M. Tromp, J.E. Demuth, *Phys. Rev. B* 34 (1986) 5343–5357.
- [329] R.J. Hamers, U.K. Kohler, *J. Vac. Sci. Technol. A* 7 (1989) 2854–2859.
- [330] N. Kitamura, M.G. Lagally, M.B. Webb, *Phys. Rev. Lett.* 71 (1993) 2082–2085.
- [331] J.H.G. Owen, D.R. Bowler, C.M. Gorringe, K. Miki, G.A.D. Briggs, *Surf. Sci.* 341 (1995) 1042–1047.

- [332] K.C. Pandey, Proc. Indian Natl. Sci. Acad. A 51 (1985) 17–26.
- [333] N. Roberts, R.J. Needs, Surf. Sci. 236 (1990) 112–121.
- [334] J. Wang, T.A. Arias, J.D. Joannopoulos, Phys. Rev. B 47 (1993) 10497–10508.
- [335] A. Cricenti, D. Purdie, B. Reihl, Surf. Sci. 331–333 (1995) 1033–1037.
- [336] S.R. Schofield, N.J. Curson, J.L. O'Brien, M.Y. Simmons, R.G. Clark, N.A. Marks, H.F. Wilson, G.W. Brown, M.E. Hawley, Phys. Rev. B 69 (2004) 085312.
- [337] S. Ihara, S.L. Ho, T. Uda, M. Hirao, Phys. Rev. Lett. 65 (1990) 1909–1912.
- [338] U. Hofer, L. Leping, G.A. Ratzlaff, T.F. Heinz, Phys. Rev. B 52 (1995) 5264–5268.
- [339] Y.N. Yang, E.D. Williams, Phys. Rev. Lett. 72 (1994) 1862–1865.
- [340] S. Kohmoto, A. Ichimiya, Surf. Sci. 223 (1989) 400–412.
- [341] Y. Fukaya, Y. Shigeta, Phys. Rev. Lett. 85 (2000) 5150–5153.
- [342] R.D. Meade, D. Vanderbilt, Phys. Rev. B 40 (1989) 3905–3913.
- [343] S.J. Chey, D.G. Cahill, Surf. Sci. 380 (1997) 377–384.
- [344] H.J.W. Zandvliet, Phys. Rep. 388 (2003) 1–40.
- [345] C.V. Ciobanu, D.T. Tambe, V.B. Shenoy, Surf. Sci. 556 (2004) 171–183.
- [346] G. Lee, H. Mai, I. Chizhov, R.F. Willis, Appl. Surf. Sci. 166 (2000) 295–299.
- [347] J.A. Kubby, J.E. Griffith, R.S. Becker, J.S. Vickers, Phys. Rev. B 36 (1987) 6079–6093.
- [348] W.S. Yang, X.D. Wang, K. Cho, J. Kishimoto, S. Fukatsu, T. Hashizume, T. Sakurai, Phys. Rev. B 50 (1994) 2406–2408.
- [349] P. Ebert, K. Urban, M.G. Lagally, Phys. Rev. Lett. 72 (1994) 840–843.
- [350] H. Kim, J.R. Chelikowsky, Surf. Sci. 409 (1998) 435–444.
- [351] Y. Iguchi, T. Fujiwara, A. Hida, K. Maeda, Phys. Rev. B 71 (2005) 125328.
- [352] B. Engels, P. Richard, K. Schroeder, S. Blugel, P. Ebert, K. Urban, Phys. Rev. B 58 (1998) 7799–7815.
- [353] M. Heinrich, P. Ebert, A.M. Simon, K. Urban, M.G. Lagally, J. Vac. Sci. Technol. A 13 (1995) 1714–1718.
- [354] L.J. Whitman, J.A. Stroscio, R.A. Dragoset, R.J. Celotta, Phys. Rev. Lett. 66 (1991) 1338–1341.
- [355] J.E. Jaffe, R. Pandey, P. Zapol, Phys. Rev. B 53 (1996) 4209–4212.
- [356] A. Filippetti, V. Fiorentini, G. Cappellini, A. Bosin, Phys. Rev. B 59 (1999) 8026–8031.
- [357] R. Miotti, G.P. Srivastava, A.C. Ferraz, Surf. Sci. 426 (1999) 75–82.
- [358] R. Pandey, P. Zapol, M. Causa, Phys. Rev. B 55 (1997) 16009–16012.
- [359] B.K. Agrawal, P. Srivastava, S. Agrawal, Surf. Sci. 405 (1998) 54–61.
- [360] J.E. Northrup, J. Neugebauer, Phys. Rev. B 53 (1996) 10477–10480.
- [361] P. Zapol, R. Pandey, J.D. Gale, J. Phys.: Condens. Mat. 9 (1997) 9517–9525.
- [362] U. Grossner, J. Furthmüller, F. Bechstedt, Phys. Rev. B 58 (1998) 1722–1725.
- [363] C.A. Swarts, T.C. McGill, W.A. Goddard III, Surf. Sci. 110 (1981) 400–414.
- [364] N. Ooi, J.B. Adams, Surf. Sci. 574 (2005) 269–286.
- [365] V.E. Henrich, R.L. Kurtz, Phys. Rev. B 23 (1981) 6280–6287.
- [366] I.A. Kuyanov, D.J. Lacks, U. Diebold, Phys. Rev. B 68 (2003) 233404.
- [367] K. Fukui, H. Onishi, Y. Iwasawa, Phys. Rev. Lett. 79 (1997) 4202–4205.
- [368] V.E. Henrich, Prog. Surf. Sci. 14 (1983) 175–199.
- [369] A. Wander, N.M. Harrison, Surf. Sci. 457 (2000) 342–346.
- [370] L. Whitmore, A.A. Sokol, R.A. Catlow, Surf. Sci. 498 (2002) 135–146.
- [371] J.L. Mackay, V.E. Henrich, Phys. Rev. B 39 (1989) 6156–6168.
- [372] S.P. Jeng, Z.M. Zhang, V.E. Henrich, Phys. Rev. B 44 (1991) 3266–3271.
- [373] G. Kresse, O. Dulub, U. Diebold, Phys. Rev. B 68 (2003) 245409.
- [374] O. Dulub, U. Diebold, G. Kresse, Phys. Rev. Lett. 90 (2003) 016102.
- [375] G.D. Watkins, J. Phys. Soc. Jpn. 18 (1963) 22–27.
- [376] G.D. Watkins, J.W. Corbett, Phys. Rev. 134 (1964) A1359–A1377.
- [377] J.L. Newton, A.P. Chatterjee, R.D. Harris, G.D. Watkins, Physica B 116 (1983) 219–223.
- [378] G.A. Baraff, E.O. Kane, M. Schlüter, Phys. Rev. B 21 (1980) 5662–5686.
- [379] G.A. Baraff, E.O. Kane, M. Schlüter, Phys. Rev. B 21 (1980) 3563–3570.
- [380] V.V. Emtev, T.V. Mashovets, A.V. Dabagyan, Sov. Phys. Semicond. 21 (1987) 1143–1146.
- [381] D.C. Mueller, E. Alonso, W. Fichtner, Phys. Rev. B 68 (2003) 045208.
- [382] J.R. Troxell, G.D. Watkins, Phys. Rev. B 22 (1980) 921–931.
- [383] J. Mäkinen, C. Corbel, P. Hautojärvi, P. Moser, F. Pierre, Phys. Rev. B 39 (1989) 10162–10173.
- [384] N.I. Boyarkina, A.V. Vasil'ev, Semiconductors 34 (2000) 166–170.
- [385] K. Matsui, R.R. Hasiguti, J. Phys. Soc. Jpn. 20 (1965) 487–490.
- [386] J.M. Fairfield, B.J. Masters, J. Appl. Phys. 38 (1967) 3148–3154.
- [387] J.A. Naber, C.E. Mallon, R.E. Leadon, in: Proceedings of the International Conference on Radiation Damage and Defects in Semiconductors, Institute of Physics, Reading, England, (1973), pp. 26–33.
- [388] J.A. Van Vechten, International Conference on Lattice Defects in Semiconductors Institute of Physics, Freiburg, West Germany, July 22–25, (1975), pp. 212–220.
- [389] L.C. Kimerling, in: Proceedings of the International Conference on Radiation Effects in Semiconductors, Institute of Physics, Dubrovnik, Yugoslavia, (1977), pp. 221–230.

- [390] J.C. Brabant, M. Pugnet, J. Barbolla, M. Brousseau, International Conference on Radiation Effects in Semiconductors, Institute of Physics, Dubrovnik, Yugoslavia, (1977), pp. 200–206.
- [391] R.B. Fair, Electrochemical Society Spring Meeting, Electrochem. Soc., Philadelphia, PA, (1977), pp. 598–600.
- [392] L.C. Kimerling, P. Blood, W.M. Gibson, Inst. Phys. Conf. Ser. (1979) 979.
- [393] B.N. Mukashev, V.V. Frolov, L.G. Kolodin, Phys. Lett. A 91A (1982) 358–360.
- [394] V.V. Emtsev, M.A. Margaryan, T.V. Mashovets, Sov. Phys. Semicond. 18 (1984) 950–951.
- [395] V.I. Gubskaya, P.V. Kuchinskii, V.M. Lomako, Phys. Status Solidi A 85 (1984) 585–590.
- [396] J.A. Van Vechten, Phys. Rev. B 33 (1986) 2674–2689.
- [397] V.V. Emtsev, T.V. Mashovets, V.V. Mikhovich, N.A. Vitovskii, Radiat. Eff. Defects Solids 111–112 (1989) 99–118.
- [398] P.F. Lugakov, T.A. Lukashevich, Sov. Phys. Semicond. 23 (1989) 365.
- [399] N.I. Boyarkina, Semiconductors 34 (2000) 410–414.
- [400] N. Zangenberg, J.J. Goubet, A. Nylandsted Larsen, Nucl. Instrum. Methods Phys. Res., Sect. B 186 (2002) 71–77.
- [401] M.J. Puska, J. Phys.: Condens. Mat. 1 (1989) 7347–7366.
- [402] M. Hakala, M.J. Puska, R.M. Nieminen, Phys. Rev. B 61 (2000) 8155–8161.
- [403] P.E. Blochl, E. Smargiassi, R. Car, D.B. Laks, W. Andreoni, S.T. Pantelides, Phys. Rev. Lett. 70 (1993) 2435–2438.
- [404] W.A. Harrison, Phys. Rev. B 57 (1998) 9727–9735.
- [405] Z.Y. Zhu, M.D. Hou, Y.F. Jin, C.L. Liu, Y.S. Wang, J. Han, Nucl. Instrum. Methods Phys. Res., Sect. B 135 (1998) 260–264.
- [406] N. Bernstein, E. Kaxiras, Phys. Rev. B 56 (1997) 10488–10496.
- [407] K. Jeongnim, F. Kirchhoff, J.W. Wilkins, F.S. Khan, Phys. Rev. Lett. 84 (2000) 503–506.
- [408] K. Jeongnim, F. Kirchhoff, W.G. Aulbur, J.W. Wilkins, F.S. Khan, G. Kresse, Phys. Rev. Lett. 83 (1999) 1990–1993.
- [409] K.A. Abdullin, B.N. Mukashev, M.F. Tamendarov, T.B. Tashenov, Phys. Lett. A 166 (1992) 40–42.
- [410] K.A. Abdullin, B.N. Mukashev, M.F. Tamendarov, T.B. Tashenov, Electronic levels and properties of the self-interstitials in irradiated silicon, in: S. Ashok, J. Chevallier, K. Sumino, E. Weber (Eds.), Defect Engineering in Semiconductor Growth, Processing and Device Technology, vol. 262, Mat. Res. Soc. Symp. Proc., 1992, pp. 1109–1113.
- [411] K.A. Abdullin, V.N. Mukashev, Semiconductors 28 (1994) 1012–1017.
- [412] K.A. Abdullin, B.N. Mukashev, Y.V. Gorelkinskii, Semicond. Sci. Technol. 11 (1996) 1696–1703.
- [413] B.N. Mukashev, K.A. Abdullin, Y.V. Gorelkinskii, S.Z. Tokmoldin, Mater. Sci. Eng. B 58 (1999) 171–178.
- [414] V.V. Lukjanitsa, Semiconductors 37 (2003) 404–413.
- [415] R.B. Fair, J. Electrochem. Soc. 137 (1990) 667–671.
- [416] K.P. Chik, Radiat. Eff. Defects Solids (1970) 33–37.
- [417] A. Seeger, W. Frank, in: Proceedings of the International Conference on Radiation Damage and Defects in Semiconductors, Institute of Physics, Reading, UK, (1973), pp. 262–268.
- [418] W. Leskoschek, H. Feichtinger, G. Vidrich, Phys. Status Solidi A 20 (1973) 601–610.
- [419] W. Frank, International Conference on Lattice Defects in Semiconductors, Institute of Physics, Freiburg, West Germany, (1975), pp. 23–43.
- [420] H. Lefevre, Appl. Phys. A 22 (1980) 15–22.
- [421] M.D. Giles, IEEE Transactions on Computer-Aided Design of Integrated Circuits and Systems 8 (1989) 460–467.
- [422] M.D. Giles, Appl. Phys. Lett. 58 (1991) 2399–2401.
- [423] J.P. John, M.E. Law, J. Electrochem. Soc. 140 (1993) 1489–1491.
- [424] D. Tsoukalas, P. Chenevier, Phys. Status Solidi A 100 (1987) 461–465.
- [425] D.J. Roth, J.D. Plummer, J. Electrochem. Soc. 141 (1994) 1074–1081.
- [426] G. Lee, H. Mai, I. Chizhov, R.F. Willis, J. Vac. Sci. Technol. A 16 (1998) 1006–1009.
- [427] C.J. Hwang, L.A.K. Watt, Phys. Rev. 171 (1968) 958–969.
- [428] R.R. Hasiguti, K. Tanaka, S. Takahashi, in: Proceedings of the Santa Fe Conference on Radiation Effects in Semiconductors, Plenum, Santa Fe, NM, (1968), pp. 89–96.
- [429] T. Soma, A. Morita, J. Phys. Soc. Jpn. 32 (1972) 357–364.
- [430] J.C. Phillips, J.A. Van Vechten, Phys. Rev. Lett. 30 (1973) 220–223.
- [431] A. Scholz, A. Seeger, Phys. Stat. Sol. A 3 (1963) 1480.
- [432] R.A. Swalin, J. Phys. Chem. Solids 18 (1961) 290–296.
- [433] R.A. Logan, Phys. Rev. 101 (1956) 1455–1459.
- [434] H. Haesslein, R. Sielemann, C. Zistl, Mater. Sci. Forum 258–263 (1997) 59–64.
- [435] C. Zistl, R. Sielemann, H. Haesslein, S. Gall, D. Braeunig, J. Bollmann, Mater. Sci. Forum 258–263 (1997) 53–58.
- [436] H. Haesslein, R. Sielemann, C. Zistl, Phys. Rev. Lett. 80 (1998) 2626–2629.
- [437] R.C. Frank, J.E. Thomas, J. Phys. Chem. Solids 16 (1960) 144.
- [438] H. Saito, N. Fukuoka, Y. Tatsumi, Radiat. Eff. 8 (1971) 171–175.
- [439] M. Shimotomai, R.R. Hasiguti, Radiat. Eff. 9 (1971) 47–49.
- [440] D.L. Trueblood, Phys. Rev. 161 (1967) 828–833.
- [441] J.N. Hobstetter, C.A. Renton, J. Appl. Phys. 33 (1962) 600–605.
- [442] R.H. Miwa, P. Venezuela, A. Fazzio, Phys. Rev. B 67 (2003) 205315–205317.
- [443] S. Adachi, Properties of Group-IV, III–V, and II–VI Semiconductors, John Wiley & Sons Ltd., Chichester, 2005.
- [444] C. Corbel, M. Stucky, P. Hautojarvi, K. Saarinen, P. Moser, Phys. Rev. B 38 (1988) 8192–8208.
- [445] C. Byoung-Ho, K.J. Chang, Phys. Rev. B 49 (1994) 17436–17439.
- [446] S. Poykko, M.J. Puska, M. Alatalo, R.M. Nieminen, Phys. Rev. B 54 (1996) 7909–7916.

- [447] K. Saarinen, P. Hautojarvi, P. Lanki, C. Corbel, Phys. Rev. B 44 (1991) 10585–10600.
- [448] R. Ambigapathy, A.A. Manuel, P. Hautojarvi, K. Saarinen, C. Corbel, Phys. Rev. B 50 (1994) 2188–2199.
- [449] S. Kuisma, K. Saarinen, P. Hautojarvi, C. Corbel, C. LeBerre, Phys. Rev. B 53 (1996) 9814–9830.
- [450] R.W. Jansen, O.F. Sankey, Phys. Rev. B 39 (1989) 3192–3206.
- [451] X. Hongqi, U. Lindefelt, Phys. Rev. B 41 (1990) 5979–5990.
- [452] S. Poykko, M.J. Puska, R.M. Nieminen, Phys. Rev. B 53 (1996) 3813–3819.
- [453] J.E. Northrup, S.B. Zhang, Phys. Rev. B 47 (1993) 6791–6794.
- [454] H. Bracht, Physica B 274 (1999) 981–986.
- [455] M. Bockstedte, M. Scheffler, Z. Phys. Chem. 200 (1997) 195–207.
- [456] J. Gebauer, M. Lausmann, F. Redmann, R. Krause-Rehberg, H.S. Leipner, E.R. Weber, P. Ebert, Phys. Rev. B 67 (2003) 235207.
- [457] A. Janotti, S.-H. Wei, S.B. Zhang, S. Kurtz, C.G. Van de Walle, Phys. Rev. B 67 (2003) 161201.
- [458] F. El-Mellouhi, N. Mousseau, J. Appl. Phys. 100 (2006) 083521.
- [459] H. Bracht, M. Norseng, E.E. Haller, K. Eberl, M. Cardona, Solid State Commun. 112 (1999) 301–304.
- [460] T.Y. Tan, H.M. You, U. Gösele, Appl. Phys. A: Mater. Sci. Process. V56 (1993) 249–258.
- [461] I. Gorceyca, N.E. Christensen, A. Svane, Phys. Rev. B 66 (2002) 075210.
- [462] T.Y. Tan, S. Yu, U. Gösele, J. Appl. Phys. 70 (1991) 4823–4826.
- [463] J.C. Bourgoin, H.J. von Bardeleben, D. Stievenard, J. Appl. Phys. 64 (1988) R65–R92.
- [464] J.I. Landman, C.G. Morgan, J.T. Schick, P. Papoulias, A. Kumar, Phys. Rev. B 55 (1997) 15581–15586.
- [465] J.M. Baranowski, P. Trautman, Properties of Gallium Arsenide, INSPEC, London, 1996.
- [466] M. Bugajski, K.H. Ko, J. Lagowski, H.C. Gatos, J. Appl. Phys. 65 (1989) 596–599.
- [467] P.W. Yu, W.C. Mitchel, M.G. Mier, S.S. Li, W.L. Wang, Appl. Phys. Lett. 41 (1982) 532–534.
- [468] P.W. Yu, Solid State Commun. 43 (1982) 953–956.
- [469] K.L. Wang, G.P. Li, Solid State Commun. 47 (1983) 233–235.
- [470] A. Hoglund, C.W.M. Castleton, S. Mirbt, Phys. Rev. B 72 (2005) 195213.
- [471] U. Kaufmann, J. Schneider, R. Worner, T.A. Kennedy, N.D. Wilsey, J. Phys. C 14 (1981) 951–955.
- [472] W. Guo, A. Yoshida, Jpn. J. Appl. Phys. 33 (1994) 2453–2456.
- [473] S.L. Rumyantsev, M.E. Levinshtein, A.D. Jackson, S.N. Mohammad, G.L. Harris, M.G. Spencer, M.S. Shur, in: M.E. Levinshtein, S.L. Rumyantsev, M.S. Shur (Eds.), Properties of Advanced Semiconductor Materials GaN, AlN, InN, BN, SiC, SiGe, John Wiley & Sons, New York, 2001, pp. 67–92.
- [474] V. Bougov, M.E. Levinshtein, S.L. Rumyantsev, A. Zubrilov, in: M.E. Levinshtein, S.L. Rumyantsev, M.S. Shur (Eds.), Properties of Advanced Semiconductor Materials GaN, AlN, InN, BN, SiC, SiGe, John Wiley & Sons, New York, 2001.
- [475] V.Y. Davydov, A.A. Klochikhin, V.V. Emtsev, A.V. Sakharov, S.V. Ivanov, V.A. Vekshin, F. Bechstedt, J. Furthmüller, J. Aderhold, J. Graul, A.V. Mudryi, H. Harima, A. Hashimoto, A. Yamamoto, J. Wu, H. Feick, E.E. Haller, SPIE-Int. Soc. Opt. Eng., St. Petersburg, Russia, (2003), pp. 68–71.
- [476] C. Stampfl, C.G. Van de Walle, D. Vogel, P. Kruger, J. Pollmann, Phys. Rev. B 61 (2000) 7846–7849.
- [477] P. Boguslawski, E.L. Briggs, J. Bernholc, Phys. Rev. B 51 (1995) 17255–17258.
- [478] T. Mattila, R.M. Nieminen, Mater. Sci. Forum 258–263 (1997) 1119–1123.
- [479] A. Fara, F. Bernardini, V. Fiorentini, J. Appl. Phys. 85 (1999) 2001–2003.
- [480] C. Stampfl, C.G. Van de Walle, Phys. Rev. B 57 (1998) 15052–15055.
- [481] J. Neugebauer, C.G. Van de Walle, Festkörperprobleme/Advances in Solid State Physics, Vieweg, Braunschweig/Wiesbaden, 1996.
- [482] C.H. Park, D.J. Chadi, Phys. Rev. B 55 (1997) 12995–13001.
- [483] A.F. Wright, T.R. Mattsson, J. Appl. Phys. 96 (2004) 2015–2022.
- [484] T. Mattila, R.M. Nieminen, Phys. Rev. B 55 (1997) 9571–9576.
- [485] K. Saarinen, T. Laine, S. Kuisma, J. Nissila, P. Hautojarvi, L. Dobrzynski, J.M. Baranowski, K. Pakula, R. Stepniewski, M. Wojdak, A. Wysmolek, T. Suski, M. Leszczynski, I. Grzegory, S. Porowski, Phys. Rev. Lett. 79 (1997) 3030–3033.
- [486] J. Oila, V. Ranki, J. Kivioja, K. Saarinen, P. Hautojarvi, J. Likonen, J.M. Baranowski, K. Pakula, T. Suski, M. Leszczynski, I. Grzegory, Phys. Rev. B 63 (2001) 045205.
- [487] K. Saarinen, T. Suski, I. Grzegory, D.C. Look, Physica B 308–310 (2001) 77–80.
- [488] K.H. Chow, G.D. Watkins, A. Usui, M. Mizuta, Phys. Rev. Lett. 85 (2000) 2761–2764.
- [489] F. Gao, E.J. Bylaska, W.J. Weber, Phys. Rev. B 70 (2004) 245208.
- [490] K.H. Chow, L.S. Vlasenko, P. Johannessen, C. Bozdog, G.D. Watkins, A. Usui, H. Sunakawa, C. Sasaoka, M. Mizuta, Phys. Rev. B 69 (2004) 045207.
- [491] J.G.E. Jellison, L.A. Boatner, J.D. Budai, B.S. Jeong, D.P. Norton, J. Appl. Phys. 93 (2003) 9537–9541.
- [492] Y. Jin, G. Li, Y. Zhang, Y. Zhang, L. Zhang, J. Phys.: Condens. Mat. 13 (2001) L913–L918.
- [493] M. Aono, R.R. Hasiguti, Phys. Rev. B 48 (1993) 12406–12414.
- [494] L.A. Bursill, M.G. Blanchin, J. Solid State Chem. 51 (1984) 321–335.
- [495] L.A. Bursill, M.G. Blanchin, A. Mebarek, D.J. Smith, Radiat. Eff. 74 (1983) 253–265.
- [496] L.A. Bursill, D.J. Smith, Nature 309 (1984) 319–321.
- [497] M.G. Blanchin, L.A. Bursill, Phys. Status Solidi A 86 (1984) 101–109.
- [498] K. Kitazawa, T. Kuriyama, K. Fueki, T. Mukaibo, J. Am. Ceram. Soc. 60 (1977) 363–366.
- [499] N. Ait-Younes, F. Millot, P. Gerdanian, Solid State Ionics 12 (1984) 437–442.
- [500] N. Ait-Younes, F. Millot, P. Gerdanian, Solid State Ionics 12 (1984) 431–436.

- [501] F. Millot, J. Mater. Sci. Lett. 4 (1985) 902–903.
- [502] H. Miyaoka, G. Mizutani, H. Sano, M. Omote, K. Nakatsui, F. Komori, Solid State Commun. 123 (2002) 399–404.
- [503] R.G. Breckenridge, W.R. Hosler, Phys. Rev. 91 (1953) 793.
- [504] T. Bak, J. Nowotny, M. Rekas, C.C. Sorrell, J. Phys. Chem. Solids 64 (2003) 1057–1067.
- [505] M. Batzill, E.H. Morales, U. Diebold, Phys. Rev. Lett. 96 (2006) 026103.
- [506] J. Yahia, Phys. Rev. 130 (1963) 1711–1719.
- [507] J.F. Marucco, J. Gautron, P. Lemasson, J. Phys. Chem. Solids 42 (1981) 363–367.
- [508] C. Picard, P. Gerdanier, J. Solid State Chem. 14 (1975) 66.
- [509] F. Millot, M.G. Blanchin, R. Tetot, J.F. Marucco, B. Poumellec, C. Picard, B. Touzelin, Prog. Solid State Chem. 17 (1987) 263–293.
- [510] R.N. Blumenthal, J. Coburn, J. Baukus, W.M. Hirthe, J. Phys. Chem. Solids 27 (1966) 643–654.
- [511] D.S. Tannhauser, Solid State Commun. 1 (1963) 223–225.
- [512] R. Haul, G. Dumbrgen, J. Phys. Chem. Solids 26 (1965) 1–10.
- [513] J.W. DeFord, O.W. Johnson, J. Appl. Phys. 44 (1972) 3001–3007.
- [514] H.P.R. Frederikse, J. Appl. Phys. 32 (1961) 2211–2215.
- [515] C.G. Young, A.J. Shuskus, O.R. Gilliam, Bull. Am. Phys. Soc. 6 (1961) 248.
- [516] P.F. Chester, J. Appl. Phys. 32 (1961) 2233–2236.
- [517] P. Kofstad, J. Phys. Chem. Solids 23 (1962) 1579–1586.
- [518] R.N. Blumenthal, J. Baukus, W.M. Hirthe, J. Electrochem. Soc. 114 (1967) 172–176.
- [519] N. Capron, G. Boureau, Int. J. Quantum Chem. 99 (2004) 677–684.
- [520] P. Knauth, H.L. Tuller, J. Appl. Phys. 85 (1999) 897–902.
- [521] C.J. Kevane, E.L. Holverson, R.D. Watson, J. Appl. Phys. 34 (1963) 2083–2087.
- [522] A. Hallil, R. Tetot, F. Berthier, I. Braems, J. Creuze, Phys. Rev. B 73 (2006) 165406.
- [523] T. Bak, J. Nowotny, M. Rekas, C.C. Sorrell, J. Phys. Chem. Solids 64 (2003) 1069–1087.
- [524] S.J. Pearson, C.R. Abernathy, M.F. Overberg, G.T. Thaler, D.P. Norton, N. Theodoropoulou, A.F. Hebard, Y.D. Park, F. Ren, J. Kim, L.A. Boatner, J. Appl. Phys. 93 (2003) 1–13.
- [525] G.V. Samsonov, The Oxide Handbook, IFI Plenum, New York, 1982.
- [526] R. Dieckmann, Z. Physik. Chem. 107 (1977) 189–210.
- [527] F.A. Kroger, The Chemistry of Imperfect Crystals, North-Holland, Amsterdam, 1964, p. 691.
- [528] K.I. Hagemark, J. Solid State Chem. 16 (1976) 293–299.
- [529] G.D. Mahan, J. Appl. Phys. 54 (1983) 3825–3832.
- [530] L. Bixia, F. Zhuxi, J. Yunbo, Appl. Phys. Lett. 79 (2001) 943–945.
- [531] D.C. Reynolds, D.C. Look, B. Jogai, H. Morkoc, Solid State Commun. 101 (1997) 643–646.
- [532] G.W. Tomlins, J.L. Routbort, T.O. Mason, J. Appl. Phys. 87 (2000) 117–123.
- [533] W.-J. Lee, J. Kang, K.J. Chang, Physica B 376–377 (2006) 699–702.
- [534] F. Tuomisto, V. Ranki, K. Saarinen, D.C. Look, Phys. Rev. Lett. 91 (2003) 205502.
- [535] S.B. Zhang, S.H. Wei, A. Zunger, Phys. Rev. B 63 (2001) 075205.
- [536] E.-C. Lee, Y.S. Kim, Y.G. Jin, K.J. Chang, Phys. Rev. B 64 (2001) 085120.
- [537] V. Gavryushin, G. Raciukaitis, D. Juodzbalis, A. Kazlauskas, V. Kubertavicius, J. Cryst. Growth 138 (1994) 924.
- [538] C.R.A. Catlow, Proc. R. Soc. London, Ser. A 353 (1977) 533–561.
- [539] R.A. Jackson, C.R.A. Catlow, A.D. Murray, J. Chem. Soc., Faraday Trans. 83 (1987) 1171–1176.
- [540] M.T. Hutchings, J. Chem. Soc., Faraday Trans. 83 (1987) 1083–1103.
- [541] B.T.M. Willis, J. Phys. Radiat. 25 (1964) 431–439.
- [542] K. Tharmalingam, Phil. Magn. 23 (1971) 181.
- [543] M. Freyss, T. Petit, J.-P. Crocombe, J. Nucl. Mater. 347 (2005) 44–51.
- [544] R.E. Carter, F.D. Richardson, J. Met. 6 (1954) 1244–1257.
- [545] A.I. Shelykh, K.S. Artemov, V.E. Shvaiko-Shvaikovskii, Fiz. Tverd. Tela 8 (1966) 883–887.
- [546] N.G. Eror, J.B. Wagner Jr., J. Phys. Chem. Solids 29 (1968) 1597–1611.
- [547] I. Bransky, J.M. Wimmer, J. Phys. Chem. Solids 33 (1972) 801–812.
- [548] H. le Brusq, J.P. Delmaire, Revue Internationale des Hautes Temperatures et des Refractaires 10 (1973) 15–26.
- [549] B. Fisher, D.S. Tannhauser, J. Chem. Phys. 44 (1966) 1663–1672.
- [550] C. Wagner, E. Koch, Z. Physik. Chem. B 31 (1936) 439.
- [551] A. Dusquesnoy, F. Marion, C. R. Acad. Sci. 256 (1963) 2862.
- [552] J. Nowotny, M. Rekas, J. Am. Ceram. Soc. 72 (1989) 1199–1207.
- [553] G.J. Koel, P.J. Gellings, Oxidat. Met. 5 (1972) 185–203.
- [554] E. Fryt, S. Mrowec, T. Walec, Oxidat. Met. 7 (1973) 117–130.
- [555] E. Fryt, Oxidat. Met. 10 (1976) 311–327.
- [556] G. Brown, personal communication, 2003.
- [557] N. Roberts, R.J. Needs, J. Phys.: Condens. Mat. 1 (1989) 3139–3143.
- [558] L. Nurminen, F. Tavazza, D.P. Landau, A. Kuronen, K. Kaski, Phys. Rev. B 67 (2003) 035405.
- [559] G.W. Brown, H. Grube, M.E. Hawley, S.R. Schofield, N.J. Curson, M.Y. Simmons, R.G. Clark, J. Vac. Sci. Technol. A 21 (2003) 1506–1509.
- [560] M. McCellistrem, G. Haase, D. Chen, R.J. Hamers, Phys. Rev. Lett. 70 (1993) 2471–2474.
- [561] R.J. Hamers, R.M. Tromp, J.E. Demuth, Phys. Rev. Lett. 56 (1986) 1972–1975.

- [562] F.J. Himpel, T. Fauster, G. Hollinger, *Surf. Sci.* 132 (1983) 22–30.
- [563] N. Takeuchi, A. Selloni, E. Tosatti, *Phys. Rev. B* 49 (1994) 10757–10760.
- [564] L. Pasquali, S. Nannarone, M. Canepa, L. Mattera, *Phys. Rev. B* 57 (1998) 2507–2513.
- [565] F. Bechstedt, A.A. Stekolnikov, J. Furthmüller, P. Kackell, *Phys. Rev. Lett.* 87 (2001) 016103.
- [566] J.A. Stroscio, R.M. Feenstra, A.P. Fein, *Phys. Rev. Lett.* 58 (1987) 1668–1671.
- [567] P. Molinas-Mata, J. Zegenhagen, *Surf. Sci.* 281 (1993) 10–20.
- [568] K.J. Chao, A.R. Smith, C.K. Shih, *Phys. Rev. B* 53 (1996) 6935–6938.
- [569] K.J. Chao, A.R. Smith, C.K. Shih, *J. Vac. Sci. Technol. B* 14 (1996) 948–952.
- [570] C. Domke, P. Ebert, M. Heinrich, K. Urban, *Phys. Rev. B* 54 (1996) 10288–10291.
- [571] Y. Ishikawa, N. Tsurumi, T. Fukui, H. Hasegawa, *J. Vac. Sci. Technol. B* 16 (1998) 2387–2394.
- [572] J.Y. Yi, J.Y. Koo, S. Lee, J.S. Ha, E.H. Lee, *Phys. Rev. B* 52 (1995) 10733–10736.
- [573] N.D. Lang, *Phys. Rev. Lett.* 58 (1987) 45–48.
- [574] S. Aloni, I. Nevo, G. Haase, *Phys. Rev. B* 60 (1999) R2165–R2168.
- [575] S. Aloni, I. Nevo, G. Haase, *J. Chem. Phys.* 115 (2001) 1875–1881.
- [576] S.Y. Chiang, G.L. Pearson, *J. Appl. Phys.* 46 (1975) 2986–2991.
- [577] R.M. Feenstra, A.P. Fein, *Phys. Rev. B* 32 (1985) 1394–1396.
- [578] J.Y. Yi, J.S. Ha, S.J. Park, E.H. Lee, *Phys. Rev. B* 51 (1995) 11198–11200.
- [579] G. Lengel, R. Wilkins, G. Brown, M. Weimer, *J. Vac. Sci. Technol. B* 11 (1993) 1472–1476.
- [580] G.S. Khoo, C.K. Ong, *Phys. Rev. B* 47 (1993) 9346–9349.
- [581] M. Heinrich, C. Domke, P. Ebert, K. Urban, *Phys. Rev. B* 53 (1996) 10894–10897.
- [582] P. Ebert, X. Chen, M. Heinrich, M. Simon, K. Urban, M.G. Lagally, *Phys. Rev. Lett.* 76 (1996) 2089–2092.
- [583] A. Schwarz, W. Allers, U.D. Schwarz, R. Wiesendanger, *Phys. Rev. B* 61 (2000) 2837–2845.
- [584] S. Morita, M. Abe, K. Yokoyama, Y. Sugawara, *J. Cryst. Growth* 210 (2000) 408–415.
- [585] J. Kanasaki, *Physica B* 376 (2006) 834–840.
- [586] R. Miotti, G.P. Srivastava, A.C. Ferraz, *Phys. Rev. B* 59 (1999) 3008–3014.
- [587] U. Diebold, J. Lehman, T. Mahmoud, M. Kuhn, G. Leonardi, W. Hebenstreit, M. Schmid, P. Varga, *Surf. Sci.* 411 (1998) 137–153.
- [588] A. Tilocca, A. Selloni, *J. Chem. Phys.* 119 (2003) 7445–7450.
- [589] A. Tilocca, A. Selloni, *J. Phys. Chem. B* 108 (2004) 4743–4751.
- [590] P.J.D. Lindan, N.M. Harrison, M.J. Gillan, J.A. White, *Phys. Rev. B* 55 (1997) 15919–15927.
- [591] E.L.D. Hebenstreit, W. Hebenstreit, U. Diebold, *Surf. Sci.* 461 (2000) 87–97.
- [592] M.A. Henderson, *Surf. Sci.* 355 (1996) 151–166.
- [593] A. Vittadini, A. Selloni, F.P. Rotzinger, M. Gratzel, *Phys. Rev. Lett.* 81 (1998) 2954–2957.
- [594] J. Woning, R.A. Van Santen, *Chem. Phys. Lett.* 101 (1983) 541–547.
- [595] A.G. Thomas, W.R. Flavell, A.R. Kumarasinghe, A.K. Mallik, D. Tsoutsou, G.C. Smith, R. Stockbauer, S. Patel, M. Gratzel, R. Hengerer, *Phys. Rev. B* 67 (2003) 035110.
- [596] W. Gopel, R.S. Bauer, G. Hansson, *Surf. Sci.* 99 (1980) 138–158.
- [597] W. Gopel, L.J. Brillson, C.F. Brucker, *J. Vac. Sci. Technol. B* 17 (1980) 894–898.
- [598] A. Wander, N.M. Harrison, *Surf. Sci.* 529 (2003) L281–L284.
- [599] G. Heiland, D. Kohl, *Phys. Status Solidi A* 49 (1978) 27–37.
- [600] N. Jedrecy, M. Sauvage-Simkin, R. Pinchaux, *Appl. Surf. Sci.* 162 (2000) 69–73.
- [601] C.R. Stanek, M.R. Bradford, R.W. Grimes, *J. Phys.: Condens. Mat.* 16 (2004) S2699–S2714.
- [602] M.R. Castell, A.S.L. Dudarev, C. Muggelberg, A.P. Sutton, G.A.D. Briggs, D.T. Goddard, *J. Vac. Sci. Technol. A* 16 (1998) 1055–1058.
- [603] C. Muggelberg, M.R. Castell, G.A.D. Briggs, D.T. Goddard, *Surf. Sci.* 404 (1998) 673–677.
- [604] J.M. McKay, M.H. Mohamed, V.E. Henrich, *Phys. Rev. B* 35 (1987) 4304–4309.
- [605] V.E. Henrich, *Rep. Prog. Phys.* 48 (1985) 1481–1541.
- [606] H. Bracht, N.A. Stolwijk, H. Mehrer, *Phys. Rev. B* 52 (1995) 16542–16560.
- [607] B.J. Masters, J.M. Fairfield, *Appl. Phys. Lett.* 8 (1966) 280–281.
- [608] W. Frank, U. Gosele, H. Mehrer, A. Seeger, *Diffusion in Crystalline Solids*, Academic Press, New York, 1984.
- [609] R.B. Fair, Physics and chemistry of impurity diffusion and oxidation of silicon, in: D. Kahng (Ed.), *Silicon Integrated Circuits, Part B*, Academic Press, New York, 1981.
- [610] K.C. Pandey, *Phys. Rev. Lett.* 57 (1986) 2287–2290.
- [611] T. Sinno, Z.K. Jiang, R.A. Brown, *Appl. Phys. Lett.* 68 (1996) 3028–3030.
- [612] R. Vaidyanathan, M.Y.L. Jung, R.D. Braatz, E.G. Seebauer, *AIChE J.* 52 (2006) 366–370.
- [613] F. El-Mellouhi, N. Mousseau, P. Ordejon, *Phys. Rev. B* 70 (2004) 205202.
- [614] K. Taniguchi, D.A. Antoniadis, *Appl. Phys. Lett.* 46 (1985) 944–946.
- [615] S. Mantovani, F. Nava, C. Nobili, G. Ottaviani, *Phys. Rev. B* 33 (1986) 5536–5544.
- [616] N.A. Stolwijk, B. Schuster, J. Holzl, *Appl. Phys. A* 33 (1984) 133–140.
- [617] G.B. Bronner, J.D. Plummer, *J. Appl. Phys.* 61 (1987) 5286–5298.
- [618] W. Wijaranakula, *J. Appl. Phys.* 67 (1990) 7624–7627.
- [619] T.Y. Tan, U. Gosele, *Appl. Phys. A* 37 (1985) 1–17.
- [620] V.A. Panteleev, S.N. Yershov, V.V. Cheryakhovskii, S.N. Nagurnykh, *Zhurnal Eksperimental'noi i Teoreticheskoi Fiziki*, Pis'ma v Redaktsiyu 23 (1976) 688–691.

- [621] A. Hallen, N. Keskitalo, L. Josyula, B.G. Svensson, *J. Appl. Phys.* 86 (1999) 214–216.
- [622] G.A. Baraff, M. Schluter, unpublished work, Bell Laboratories, 1984.
- [623] C.S. Nichols, C.G. Vandewalle, S.T. Pantelides, *Phys. Rev. B* 40 (1989) 5484–5496.
- [624] G.H. Gilmer, T.D. Delarubia, D.M. Stock, M. Jaraiz, *Nucl. Instrum. Methods Phys. Res., Sect. B* 102 (1995) 247–255.
- [625] J. Zhu, T.D. de la Rubia, L.H. Yang, C. Mailhot, G.H. Gilmer, *Phys. Rev. B* 54 (1996) 4741–4747.
- [626] W.K. Leung, R.J. Needs, G. Rajagopal, S. Itoh, S. Ihara, *VLSI Des.* 13 (2001) 229–235.
- [627] B.L. Gregory, C.E. Barnes, in: *Proceedings of the Santa Fe Conference on Radiation Effects in Semiconductors*, Plenum, Santa Fe, NM, (1968), pp. 124–135.
- [628] S.N. Ershov, V.A. Panteleev, S.N. Nagornyykh, V.V. Chernyakhovskii, *Sov. Phys. Solid State* 19 (1977) 187.
- [629] P.B. Rasband, P. Clancy, M.O. Thompson, *J. Appl. Phys.* 79 (1996) 8998–9011.
- [630] L. Shao, J.R. Liu, Q.Y. Chen, W.K. Chu, *Mater. Sci. Eng. R* 42 (2003) 65–114.
- [631] P.J. Kelly, R. Car, S.T. Pantelides, *Mater. Sci. Forum* 10–12 (1986) 115–120.
- [632] O. Sugino, A. Oshiyama, *Phys. Rev. B* 46 (1992) 12335–12341.
- [633] M.Y.L. Jung, R. Gunawan, R.D. Braatz, E.G. Seebauer, *ECS* (2000) 15.
- [634] E. Wieser, H. Syhre, F.G. Rudenauer, W. Steigner, *Phys. Stat. Sol. A* 81 (1984) 247.
- [635] Y. Ishikawa, M. Maruyama, *Jpn. J. Appl. Phys.* 36 (1997) 7433–7436.
- [636] Gyulai, J., Ryssel, H., Biro, L.P., Frey, L., Kuki, A., Kormany, T., Serfozo, G., Khanh, N.Q., 1994. Athermal effects in ion implanted layers. In: *Radiation Effects and Defects in Solids*, vol. 127. Taylor and Francis, Reading, UK, p. 397.
- [637] S. Noel, L. Ventura, A. Slaoui, J.C. Muller, B. Groh, R. Schindler, B. Froeschle, T. Theiler, *J. Electron. Mater.* 27 (1998) 1315–1322.
- [638] R.B. Fair, S. Li, *J. Appl. Phys.* 83 (1998) 4081–4090.
- [639] B. Lojek, M. Whiteman, R. Ahrenkiel, *Advanced Thermal Processing of Semiconductors 9th International Conference on RTP 2001*, IEEE, (2001), pp. 125–131.
- [640] M.Y.L. Jung, E.G. Seebauer, *Fourth International Workshop on Junction Technology*, Fudan University Press, Shanghai, China, (2004), pp. 87–89.
- [641] N.E.B. Cowern, K.T.F. Janssen, C.G. Van de Walle, D.J. Gravesteijn, *Phys. Rev. Lett.* 65 (1990) 2434–2437.
- [642] N.E.B. Cowern, C.G. Van de Walle, P.C. Zalm, D.J. Oostra, *Phys. Rev. Lett.* 69 (1992) 116–119.
- [643] N.E.B. Cowern, C.G. Van de Walle, D.J. Gravesteijn, C.J. Vriezema, *Phys. Rev. Lett.* 67 (1991) 212–215.
- [644] M.W. Valenta, C. Ramasastri, *Phys. Rev.* 106 (1957) 73–75.
- [645] D.R. Campbell, *Phys. Rev. B* 12 (1975) 2318–2324.
- [646] H.D. Fuchs, W. Walukiewicz, E.E. Haller, W. Dondl, R. Schorer, G. Abstreiter, A.I. Rudnev, A.V. Tikhomirov, V.I. Ozhogin, *Phys. Rev. B* 51 (1995) 16817–16821.
- [647] H. Letaw Jr., W.M. Portnoy, L. Slifkin, *Phys. Rev.* 102 (1956) 636–639.
- [648] J.A. Van Vechten, *Phys. Rev. B* 10 (1974) 1482–1506.
- [649] S. Mayburg, *Phys. Rev.* 95 (1954) 38.
- [650] J. Vanhellemont, T. Fujiwara, J. Lauwaert, O. De Gryse, P. Vanmeerbeek, D. Poelman, P. Spiewak, I. Romandic, A. Theuwis, P. Clauws, *Solid State Phenom.* 108–109 (2005) 683–690.
- [651] M. Werner, H. Mehrer, H.D. Hochheimer, *Phys. Rev. B* 32 (1985) 3930–3937.
- [652] J. Lauwaert, S. Hens, P. Spiewak, D. Wauters, D. Poelman, I. Romandic, P. Clauws, J. Vanhellemont, *Physica B* 376 (2006) 257–261.
- [653] K.H. Bennemann, *Phys. Rev.* 137 (1965) A1497–A1514.
- [654] F. Bailly, in: R.R. Hasiguti (Ed.), *Lattice Defects in Semiconductors*, University of Tokyo Press, Tokyo, 1968, p. 231.
- [655] T. Soma, M. Saeki, A. Morita, *J. Phys. Soc. Jpn.* 35 (1973) 146–148.
- [656] N. Bernstein, M.J. Mehl, D.A. Papaconstantopoulos, *Phys. Rev. B* 66 (2002) 075212.
- [657] V.A. Panteleev, *Fiz. Tverd. Tela* 19 (1977) 2801.
- [658] B. Goldstein, *Phys. Rev.* 118 (1960) 1024–1027.
- [659] R.M. Cohen, *Mater. Sci. Eng. R* 20 (1997) 167–280.
- [660] T.Y. Tan, U. Gosele, *Mater. Sci. Eng. B* 1 (1988) 47–65.
- [661] R.A. Morrow, *Appl. Phys. Lett.* 57 (1990) 276–278.
- [662] R.W. Kaliski, D.W. Nam, D.G. Deppe, N. Holonyak, K.C. Hsieh, R.D. Burnham, *J. Appl. Phys.* 62 (1987) 998–1005.
- [663] T.Y. Tan, *Mater. Chem. Phys.* 40 (1995) 245–252.
- [664] W. Walukiewicz, *Phys. Rev. B* 41 (1990) 10218–10220.
- [665] L. Wang, L. Hsu, E.E. Haller, J.W. Erickson, A. Fischer, K. Eberl, M. Cardona, *Phys. Rev. Lett.* 76 (1996) 2342–2345.
- [666] P. Mei, T. Venkatesan, S.A. Schwarz, N.G. Stoffel, J.P. Harbison, D.L. Hart, L.A. Florez, *Appl. Phys. Lett.* 52 (1988) 1487–1489.
- [667] W.M. Li, R.M. Cohen, D.S. Simons, P.H. Chi, *Appl. Phys. Lett.* 70 (1997) 3392–3394.
- [668] K. Muraki, Y. Horikoshi, *J. Cryst. Growth* 175 (1997) 162–167.
- [669] M. Noack, K.W. Kehr, H. Wenzl, *J. Cryst. Growth* 178 (1997) 438–444.
- [670] H.D. Palfrey, M. Brown, A.F.W. Willoughby, *J. Electron. Mater.* 12 (1983) 863–877.
- [671] H. Bracht, S.P. Nicols, E.E. Haller, J.P. Silveira, F. Briones, *J. Appl. Phys.* 89 (2001) 5393–5399.
- [672] H. Bracht, S.P. Nicols, W. Walukiewicz, J.P. Silveira, F. Briones, E.E. Haller, *Nature* 408 (2000) 69–72.
- [673] R. Haul, G. Dummbgen, *Z. Elektrochem.* 66 (1962) 636–641.
- [674] D.J. Derry, D.G. Lees, J.M. Calvert, *J. Phys. Chem. Solids* 42 (1981) 57–64.
- [675] M. Arita, M. Hosoya, M. Kobayashi, M. Someno, *J. Am. Ceram. Soc.* 62 (1979) 443–446.
- [676] A.N. Bagshaw, B.G. Hyde, *J. Phys. Chem. Solids* 37 (1976) 835–838.

- [677] J.R. Akse, H.B. Whitehurst, *J. Phys. Chem. Solids* 39 (1978) 457–465.
- [678] D.A. Venkata, L.E. Poteat, *Mater. Sci. Eng.* 5 (1970) 258–262.
- [679] T.S. Lundy, R.A. Padgett, M.D. Banus, *Metall. Trans. A* 4 (1973) 1179–1180.
- [680] H. Sawatari, E. Iguchi, R.J.D. Tilley, *J. Phys. Chem. Solids* 43 (1982) 1147–1155.
- [681] E. Iguchi, K. Yajima, *J. Phys. Soc. Jpn.* 32 (1972) 1415–1421.
- [682] V.I. Barbanell, V.N. Bogomolov, S.I. Budarina, *Fiz. Tverd. Tela* 13 (1971) 1251–1252.
- [683] T.B. Gruenwald, G. Gordon, *J. Inorg. Nucl. Chem.* 33 (1971) 1151–1155.
- [684] J.W. Hoffman, I. Lauder, *J. Chem. Soc., Faraday Trans.* 66 (1970) 2346–2353.
- [685] W.C. Mackrodt, R.F. Stewart, J.C. Campbell, I.H. Hillier, *J. Phys. Colloque* 41 (1980) 6–64.
- [686] D.J. Binks, Computational modelling of zinc oxide and related oxide ceramics, Ph.D. Dissertation, University of Surrey, 1994.
- [687] A.C.S. Sabioni, *Solid State Ionics* 170 (2004) 145–148.
- [688] H. Haneda, J. Tanaka, S. Hishita, T. Ohgaki, N. Ohashi, *Key Eng. Mat.* 157–158 (1999) 221–226.
- [689] W.J. Moore, E.L. Williams, *Crystal Imperfections and the Chemical Reactivity of Solids*, The Faraday Society, Aberdeen, Scotland, 1959 p. 86.
- [690] D. Hallwig, H.G. Sockel, C. Monty, Oxygen diffusion in NiO and ZnO, in: *Reactivity of Solids*, Elsevier, New York, 1976, pp. 631–634.
- [691] P. Erhart, K. Albe, *Phys. Rev. B* 73 (2006) 115206.
- [692] K.S. Kim, Ph.D. Dissertation, Massachusetts Institute of Technology, 1971.
- [693] J.R. Matthews, *Mechanical Properties and Diffusion Data for Carbide and Oxide Fuels. Ceramics Data Manual Contribution*, United States, 1974, p. 49.
- [694] C.R.A. Catlow, A.B. Lidiard, M.J. Norgett, *J. Phys. C* 8 (1975) 435–438.
- [695] G.E. Murch, C.R.A. Catlow, *J. Chem. Soc., Faraday Trans.* 83 (1987) 1157–1169.
- [696] R.A. Jackson, A.D. Murray, C.R.A. Catlow, *Physica* 131B+C (1985) 136–138.
- [697] H. Matzke, *J. Chem. Soc., Faraday Trans.* 83 (1987) 1121–1142.
- [698] R.A. Jackson, A.D. Murray, J.H. Harding, C.R.A. Catlow, *Phil. Magn. A* 53 (1986) 27–50.
- [699] W.K. Chen, R.A. Jackson, *J. Phys. Chem. Solids* 30 (1969) 1309–1314.
- [700] J.L. Routbort, *Solid State Ionics* 12 (1984) 383.
- [701] A. Dominguez-Rodriguez, M. Sanchez, R. Marquez, *Phil. Magn. A* 46 (1982) 411–418.
- [702] N.L. Peterson, C.L. Wiley, *J. Phys. Chem. Solids* 46 (1985) 43–52.
- [703] W.C. Mackrodt, R.F. Stewart, *J. Phys. C: Solid State Phys.* 12 (1979) 5015–5036.
- [704] Z. Jun, L. Lei, *Phys. Rev. B* 59 (1999) 13278–13284.
- [705] T.A. Kirichenko, S.K. Banerjee, G.S. Hwang, *Surf. Sci.* 555 (2004) 187–192.
- [706] Z.Y. Zhang, H. Chen, B.C. Bolding, M.G. Lagally, *Phys. Rev. Lett.* 71 (1993) 3677–3680.
- [707] Y.W. Mo, J. Kleiner, M.B. Webb, M.G. Lagally, *Phys. Rev. Lett.* 66 (1991) 1998–2001.
- [708] G. Brocks, P.J. Kelly, R. Car, *Phys. Rev. Lett.* 66 (1991) 1729–1732.
- [709] M.B. Webb, F.K. Men, B.S. Swartzentruber, R. Kariotis, M.G. Lagally, *Surf. Sci.* 242 (1991) 23–31.
- [710] M.E. Keefe, C.C. Umbach, J.M. Blakely, *J. Phys. Chem. Solids* 55 (1994) 965–973.
- [711] H. Hibino, T. Ogino, *Phys. Rev. B* 54 (1996) 5763–5768.
- [712] C.E. Allen, R. Ditchfield, E.G. Seebauer, *Phys. Rev. B* 55 (1997) 13304–13313.
- [713] C.E. Allen, E.G. Seebauer, *Langmuir* 11 (1995) 186–190.
- [714] Y.W. Mo, *Phys. Rev. Lett.* 71 (1993) 2923–2926.
- [715] M. Lannoo, G. Allan, *Phys. Rev. B* 25 (1982) 4089–4101.
- [716] M. Lannoo, G. Allan, *Phys. Rev. B* 33 (1986) 8789–8790.
- [717] I.I. Suni, E.G. Seebauer, *Surf. Sci.* 301 (1994) L235–L238.
- [718] I.I. Suni, E.G. Seebauer, *Thin Solid Films* 272 (1996) 229–234.
- [719] P. Molinas-Mata, A.J. Mayne, G. Dujardin, *Phys. Rev. Lett.* 80 (1998) 3101–3104.
- [720] A.J. Mayne, F. Rose, C. Bolis, G. Dujardin, *Surf. Sci.* 486 (2001) 226–238.
- [721] I. Brihuega, O. Custance, J.M. Gomez-Rodriguez, *Phys. Rev. B* 70 (2004) 165410.
- [722] S. Gwo, A.R. Smith, C.K. Shih, *J. Vac. Sci. Technol. A* 11 (1993) 1644–1648.
- [723] A. Kley, P. Ruggerone, M. Scheffler, *Phys. Rev. Lett.* 79 (1997) 5278–5281.
- [724] M. Kawabe, T. Sugaya, *Jpn. J. Appl. Phys., Part 2* 28 (1989) 1077–1079.
- [725] T. Nishinaga, C. Kyoung-Ik, *Jpn. J. Appl. Phys., Part 2* 27 (1988) 12–14.
- [726] J.H. Neave, P.J. Dobson, B.A. Joyce, J. Zhang, *Appl. Phys. Lett.* 47 (1985) 100–102.
- [727] T. Shitara, T. Suzuki, D.D. Vvedensky, T. Nishinaga, *Materials Research Society Symposium Proceedings*, MRS, Boston, MA, (1993), pp. 131–134.
- [728] K. Ohta, T. Kojima, T. Nakagawa, *J. Cryst. Growth* 95 (1989) 71–74.
- [729] P. Ebert, K. Urban, *Ultramicroscopy* 49 (1993) 344–353.
- [730] R. Schaub, E. Wahlstrom, A. Ronnau, E. Laegsgaard, I. Stensgaard, F. Besenbacher, *Science* 299 (2003) 377–379.
- [731] T.L. Thompson, O. Diwald, J.T. Yates, *Chem. Phys. Lett.* 393 (2004) 28–30.
- [732] W. Xueyuan, A. Selloni, M. Lazzari, S.K. Nayak, *Phys. Rev. B* 68 (2003) 241402.
- [733] Y. Wang, D. Pillay, G.S. Hwang, *Phys. Rev. B* 70 (2004) 193410.
- [734] M.A. Henderson, *Surf. Sci.* 419 (1999) 174–187.